ICE FORCES ON A MULTIFACETED CONICAL STRUCTURE

ZHIGUO WANG

ICE FORCES ON A MULTIFACETED CONICAL STRUCTURE

© Zhiguo Wang , B.E., M.E.

A thesis submitted to the School of Graduate
Studies in partial fulfilment of the
requirements for the degree of
Doctor of Philosophy

Faculty of Engineering & Applied Science
Memorial University of Newfoundland
June 1997

St. John's, Newfoundland, Canada

Acknowledgements

I owe a great deal to many individuals who made this work possible. My most heartfelt thanks go to my supervisor Dr. Derek Muggeridge who introduced me into the faceted cone test program and has financially and academically supported me during my study. His friendly and thoughtful advice and guidance have benefited me not only for this study but also for many aspects of my life.

I wish to express my gratitude to my co-supervisor Dr. A.S.J. Swamidas. His encouragement played a major role in the progress of this work; his careful reading and correcting of the manuscript significantly polished it. Dr. Swamidas' support for printing all copies of this thesis and related materials are also gratefully appreciated.

The author wishes to extend his sincere gratitude to Professor Ken Croasdale, and Dr. Richard McKenna, members of the supervisory committee, for their encouragement and helps in various aspects. Professor Croasdale offered his experience to guide this research and he provided support for the last semester of my study. Dr. McKenna helped to obtain the permission for use of the discrete element code, DECICE, and his intellectual support has helped the progress of the research.

Special thanks are addressed to Dr. J.J. Sharp, Associate Dean of Engineering, for his

encouragement for completion of this program and help with respect to financial support and teaching assistantships which partly ensured the completion of this program. Sincere appreciation is extended to the School of Graduate Studies for the fellowships awarded throughout this program.

The author wishes to express his gratitude to the Institute for Marine Dynamics (IMD) of the National Research Council of Canada for permission to use the DECICE code, and for the use of computing facilities. Deep thanks go to Dr. Stephen Jones and Mr. Donald Spencer, research officers of IMD, and Mr. L. Bruce Schooley, system manager of IMD's computer system, for their assistance, patience, and help in using the software and facilities.

Sincere thanks go to all team members of the multifaceted cone test program for their effort to make the data accessible.

Last, but not least, my unbounded thanks are expressed to my wife Wei-Zhong Zheng and my daughter Zhen Chao for their understanding, love, and support throughout this program.

Abstract

To simplify fabrication and reduce costs of conical structures for arctic offshore development, a multifaceted conical shape was proposed to replace the conventional smooth cone. This raised a number of concerns about the mechanisms for ice interaction with this multifaceted conical structure (MCS) and the validity of analytical models which were developed for the smooth conical structure (SCS). A vertical neck at the top of the MCS was proposed for a prototype and industry has desired a large size for this neck, i.e., its diameter to be only slightly smaller than water-line diameter. This raised another concern: what was the effect of this vertical neck on ice loads ?

To address these concerns, a university-industry joint program (NSERC file # 661-119/88) was initiated to carry out a series of test program. The program involved three series of tests carried out in three Canadian test facilities (ESSO Resources Canada, Calgary; NRCC's Institute for Mechanical Engineering, Ottawa; and NRCC's Institute for Marine Dynamics, St. John's) with structural models at scales of 1:50 to 1:10 and at a cost about 1.3 million Canadian dollars. The results of these tests were presented in test reports published by each facility; while presenting these test results no detailed analysis was carried out to understand the ice/structure interaction in a comprehensive manner. The data contained in these test reports have been used in this study to understand in depth the various interaction scenarios possible between a multi-year ice ridge and the MCS.

The direct analysis of the test data, presented in this study, covers answers to most of the concerns raised by the offshore industry but is not limited to them. Besides the ice failure mechanisms involved in the process of ice interaction with the MCS models, the parameters analyzed include neck size, structural orientation, ridge width, and the events that caused the maximum ridge loads. In the analysis of the ice failure mechanisms, three ridge failure patterns are identified. Both ridge cracking and ridge segment ride up processes are recognized to be events causing the maximum ridge loads. The influence of a number of factors on ice cracking pattern and ice loads exerted on the MCSs are considered in the data analysis.

To provide an insight into the interaction process and the ice failure mechanisms, a series of numerical simulations are carried out using a commercial discrete element code (DECICE). DECICE is capable of realistically simulating the ice breaking processes accompanied by broken ice pieces riding up on the structural surface. This overcomes the disadvantage of the conventional finite element analysis in which the ride-up forces are to be approximately computed under an unrealistic assumption that only one layer of ice rides up. The simulations using DECICE show the broken ice pieces to be actively involved in the breaking process of impinging ice. The effect of neck size on ridge and sheet ice loads is also studied using DECICE.

An analytical model is developed which takes the particular feature of the MCSs and ridge length into account; this model should provide designers with a simple estimation of ridge cracking loads. This analytical model is given in the form of a set of equations covering the

initial crack event and hinge crack event for both finite length (short) and infinite length (long) ridges. Three loading conditions for hinge cracks in an infinite ridge are considered in the equations. The most conservative loading condition for the hinge cracks is chosen for short ridges to give a conservative estimation of the maximum ridge loads. The equations for long ridges are expressed in a general form with different coefficients for various crack events and loading conditions.

An extensive comparison of the experimental results given in this thesis, for level ice fields, has been made with the analytical models that were develped for prediction of level ice loads on SCSs. The results show Nevel's analytical model for sheet ice load estimation to be fairly valid for use in estimation of sheet ice loads on MCSs though it was developed for smooth cones. Ralston's model is also acceptable for MCSs if appropriate parameters are chosen for inputs to this model.

Of the various analytical models available for ridge load estimation, the model developed in this thesis gives the best prediction (closest to the measured loads). As a second choice, Wang's plasticity model which has been widely accepted for smooth cones is also applicable to the case of MCSs.

Contents

Acknowledgements i
Abstract iii
Contents vi
List of Figures xi
List of Tables xiv
Nomenclature xv

1 Introduction 1
1.1 Background of the Test Program 1
1.2 Background of This Study 3
1.3 Objectives 4
1.4 Organization of the Thesis 6

2 Literature Review 8
2.1 Experimental Studies of Ice Ridge Forces 8
2.1.1 Failure Process and Forces of Broadside Ridges 10
2.1.2 Effect of Ridge Orientation on Failure Process and Peak Loads 11
2.1.3 Effects of Sheet Thickness and Strength on Failure Process and Peak Loads 13
2.1.4 Ratio of Horizontal to Vertical Forces 13
2.1.5 Effect of Ridge Length on Peak Forces 14
2.2 Analytical Models for Ridge Force Estimation 15
2.2.1 Croasdale Model and Abdelnour Model 15
2.2.2 Kim and Kotras Model 17
2.2.3 Ride-up Model 18
2.2.4 Plasticity Method 19
2.2.5 Comparison of Models and Discussions 20
2.3 Ice Sheet Interaction with a SCS 21
2.4 Analytical Models for Ice Sheet and SCS Interaction 22
2.4.1 Ralston Model 23
2.4.2 Croasdale Model 23
2.4.3 Nevel Model 24
2.4.4 Comparison of Models and Discussions 25

2.5 Numerical Analysis 26
2.5.1 Finite Element Analysis 26
2.5.2 Discrete Element Analysis 28

3 Faceted Cone Test Program 33
3.1 Test Facilities 33
3.1.1 ERC's Ice Basin 33
3.1.2 IMD's and IME's Ice Tanks 34
3.2 Structures and Instrumentation 35
3.2.1 Prototype Structures and Test Models 35
3.2.2 Instrumentation 38
3.2.3 Coordinate System 39
3.3 Test Matrices 39
3.3.1 Overall Scope 39
3.3.2 Test Matrices 41
3.4 Tested Ice 50
3.4.1 The Ice for ERC's Tests 50
3.4.2 The Ice for IME's and IMD's Tests 52
3.5 Test Results 54

4 Analysis of the Tests 60
4.1 Typical Interaction Scenario 60
4.1.1 The Process of Sheet Ice and MCS Interaction 61
4.1.2 Ridge Failure Pattern I 62
4.1.3 Ridge Failure Pattern II 66
4.1.4 Ridge Failure Pattern III 67
4.2 Ridge Crack Loads and Maximum Loads 68
4.2.1 What Causes the Maximum Loads ? 69
4.2.2 Horizontal and Vertical Ridge Forces 72
4.3 Influence of Various Parameters on Ridge Failure Process and Forces 74
4.3.1 Effect of Ridge Width 75
4.3.2 Effect of Structural Orientation 80
4.3.3 Effect of Neck Size 85
4.4 Analysis of Sheet Ice Forces 91
4.4.1 Approach for the Analysis 91
4.4.2 Effect of Structural Orientation on Sheet Ice Forces 94
4.4.3 Effect of Neck Size on Sheet Ice Forces 96

5 Numerical Simulation 100
5.1 The Approach for Numerical Simulation 101
5.1.1 DECICE Program and the Procedures for Problem Solving 101
5.1.2 Structure and Ice Modelling 103
5.1.3 Failure Criteria and Ice Strengths 106
5.2 Simulation of Sheet Ice and Structure Interaction 109
5.2.1 Ice Configuration and Elements 109
5.2.2 Overview of Simulation Results 111
5.2.3 Effect of Element Size 113
5.2.4 Interaction of Sheet with Small Neck Structure 118
5.3 Simulation of Ridge and Structure Interaction 126
5.3.1 The Ridge, Sheet, and Their Discretization 126
5.3.2 Comparison of Simulation with Test 128
5.3.3 Relation of Interaction Process and Global Forces 131
5.4 Numerical Study on the Effect of Neck Size 137
5.4.1 Ice Sheet Interaction with Large Neck Structure 139
5.4.2 Ice Ridge Interaction with Large Neck Structure 141
5.4.3 Discussions of Neck Size Effect 144

6 Analytical Studies 146
6.1 The Problem and Its Simplification 146
6.2 Loading Conditions 151
6.3 Bending Moment and Crack Locations for Infinite Ridges 155
6.3.1 Bending Moment and Crcak Location for Initial Crack 155
6.3.2 Bending Moment and Crack Location for Hinge Crack under Uniformly Distributed Load Condition 158
6.3.3 Bending Moment and Crack Location for Hinge Crack under Concentrated Load Condition 159
6.3.4 Bending Moment and Crack Location for Hinge Crack under Triangular Load Condition 162
6.4 Formulae for Estimation of the Loads Exerted by Infinite Ridges 164
6.5 Consideration of Ridge Length Effect 168
6.5.1 Initial Crack Load of a Finite Length Ridge 169
6.5.2 Hinge Crack Load of a Finite Length Ridge under a Concentrated Load 171
6.6 Discussion about the Analytical Model 173
6.6.1 Effect of Facet Length on the Loads and

Crack Locations of Infinite Ridges 174
6.6.2 Effect of Ridge Length on Crack Loads 177
6.6.3 Short, Finite, and Long Ridges 179
6.6.4 The Maximum Ridge Crack Loads 180
6.7 Ride-up Forces and Total Forces 181

7 Validation of Analytical Models 184
7.1 Verification of the Present Analytical Model 184
7.1.1 Comparison of Computed and Measured Loads 185
7.1.2 Analysis of the Prediction 189
7.2 Validation of Other Analytical Models for Ridge Load Estimation 196
7.2.1 The Load Prediction 197
7.2.2 Evaluation of the Analytical Models 201
7.3 Validation of the Theoretical Models for Sheet Ice Load prediction 206
7.3.1 The Models and the Inputs 206
7.3.2 Computation Results 208
7.3.3 Analysis of Prediction 213

8 Conclusions and Recommendations 220
8.1 Conclusions Regarding Ice Failure Mechanisms and Maximum Loads 220
8.1.1 Ice Ridge and Sheet Crack patterns 221
8.1.2 The Events Generating Maximum Loads 221
8.1.3 Effect of Structural Orientation 221
8.2 Conclusions Regarding the Effect of Neck Size 223
8.2.1 Effect of Neck Size on Ice Ridge Loads 223
8.2.2 Effect of Neck Size on Ice Sheet Loads 223
8.3 Conclusion Regarding Validation of Load Equations 224
8.3.1 Validation of Ridge Ice Load Equations 224
8.3.2 Validation of Sheet Ice Load Equaons 225
8.4 Contribution of This Work 225
8.5 Recommendations for Future Work 227

References 229

Appendices 236
Appendix A Assumption for Ice Behaviour 236
Appendix B Estimate of Parameters for Mohr-Coulomb Criterion 242

Appendix C Simplification of Ridge Crack Problem 247
Appendix D Functions A(y), B(y), C(y), D(y) and Their Operations 256
Appendix E Multi-Year Ice Characteristics for Beaufort and Chukchi Seas 260

List of Figures

3.1 The Prototype Structure with Small Neck 36
3.2 The Prototype Structure with Large Neck 36

4.1 Vertical Ridge Forces on Large Neck Structures 78
4.2 Horizontal Ridge Forces on Large Neck Structures 78
4.3 Vertical Ridge Forces on Small Neck Structures 79
4.4 Horizontal Ridge Forces on Small Neck Structures 79
4.5 Vertical Ridge Forces on Face-on Structures 87
4.6 Horizontal Ridge Forces on Face-on Structures 88
4.7 Vertical Ridge Forces on Edge-on Structures 89
4.8 Horizontal Ridge Forces on Edge-on Structures 90
4.9 Effect of Structural Orientation on Horizontal Sheet Forces 95
4.10 Effect of Structural Orientation on Vertical Sheet Forces 96
4.11 Effect of Neck Size on Vertical Sheet Ice Forces 98
4.12 Effect of Neck Size on Horizontal Sheet Ice Forces 98
4.13 Zoomed Plotting of Vertical Forces against C_p 99

5.1 Simulated Small Neck MCS Structure 103
5.2 Simulated Ice, Basin Walls and the Structure 104
5.3 Ice Sheet and Elements 110
5.4 Simulated and Measured Global Sheet Loads 111
5.5 Ice Sheet/MCS Interaction Scenario at the 78th Second 112
5.6 Interaction of Structure with Fine Meshed Ice Sheet at the 78th Second 113
5.7 Effect of Element Mesh on Global Sheet Loads 114
5.8 Measured Sheet Loads and the Simulation with Fine Mesh 115
5.9A Displacements of Ice Sheet Element 27 119
5.9B Rotations of Ice Sheet Element 27 120
5.10 Cracks of Front Elements 121
5.11 Side View of Ice Sheet/ MCS Interaction Situation at the 9th Second 121
5.12 Side View of Ice Sheet/MCS Interaction Situation at the 22.5th Second 122
5.13 Side View of Ice Sheet/MCS Interaction Scenario at the 48th Second 124
5.14 Side View of Ice Sheet/MCS Interaction Scenario at the 78th Second 124
5.15 Time History of Simulated and Measured Global Ridge Loads 128
5.16 Measured and Simulated Ridge Crack Patterns 129
5.17 Simulated Ridge/MCS Interaction Scenario at the 116th Second 129
5.18 Ridge Crack Pattern of Y1T1R2 130
5.19 Ridge/MCS Interaction Scenario at the 72nd Second 132
5.20 Ridge/MCS Interaction Scenario at the 82nd Second 133
5.21 Crack Pattern immediately after Event "d" 134
5.22 Crack Pattern during Event "e" 135

5.23 The Ridge-Sheet Ice Clearing Process 137
5.24 Simulated Sheet Loads for Large and Small Neck Structures 139
5.25 A Scenario of Sheet Ice Interaction with the Large Neck structure 140
5.26 Simulated Ridge Ice Loads on the Large and Small Neck Structures 142
5.27 An Interaction Scenario of the Ridge Interacting with the Large Neck Structure 142
5.28 Side View of a Scenario of Ridge Clearing Process 143

6.1 Cross Section of Ridge Beam with Ice Sheet Flanges 148
6.2A Contact Condition for Initial Crack 152
6.2B Loading Condition for Initial Crack 152
6.3A Corner Contact for Hinge Crack 153
6.3B Concentrated Loads for Hinge Crack 154
6.4 Triangular Loads for Hinge Crack 154
6.5 Normalized Crack Location of Initial and Hinge Cracks 157
6.6 Load Functions of Infinite Ridges 166
6.7 Contact and Loading Conditions for Hinge Cracks in a Finite Ridge 169
6.8 Load Function for the Central Crack in a Finite Length Ridge 170
6.9 Load Function for a Hinge Cracks in a Finite Length Ridge 173

7.1 Vertical Predicted and Measured Ridge Loads 186
7.2 Horizontal Predicted and Measured Ridge Loads 186
7.3 Vertical Ridge Loads of the ERC Tests 190
7.4 Horizontal Ridge Loads of the ERC Tests 190
7.5 Vertical Ridge Loads of IMD Tests 191
7.6 Horizontal Ridge Loads of IMD Tests 191
7.7 Vertical Ridge Loads of the IME Tests 192
7.8 Horizontal Ridge Loads of the IME Tests 192
7.9 Vertical Loads from Three Models for the ERC Tests 198
7.10 Horizontal Loads from Three Models for the ERC Tests 198
7.11 Vertical Loads from Three Models for the IMD Tests 199
7.12 Horizontal Loads from Three Models for the IMD Tests 199
7.13 Vertical Loads from Three Models for the IME Tests 200
7.14 Horizontal Loads from Three Models for the IME Tests 200
7.15 Vertical Sheet ice Loads, NIL, RCL, and CCL 210
7.16 Horizontal Sheet ice Loads, NIL, RCL, and CCL 210
7.17 Vertical Sheet ice Loads, NIL, RIL, and CIL 211
7.18 Horizontal Sheet ice Loads, NIL, RIL, and CIL 211
7.19 Vertical Sheet ice Loads, NIL, RCN, and CCN 212
7.20 Horizontal Sheet ice Loads, NIL, RCN, and CCN 212
7.21 Predicted Vertical Sheet ice Loads with NNA and NNP 217
7.22 Predicted Horizonal Sheet ice Loads with NNA and NNP 217

A.1 Strains for ERC test Y1T1R1 239
A.2 Strains for ERC test Y1T1R2 239

C.1 Forces on a Ridge 248
C.2 Equivalent Forces on the Ridge 250
C.3 Idealized Geometry of Multi-year Ridges 251

List of Tables

3.1 Overall Scope of The Test Program 40
3.2 Test Matrix for ERC's Year-One Tests 42
3.3 Test Matrix of ERC's Year-Two Tests 43
3.4 Test Matrix for IME's Ice Sheet Tests 46
3.5 Test Matrix of IME's Ridge Tests 47
3.6 Test Matrix for IMD's Tests with 1:25 Scale Large Neck Model 48
3.7 Test Matrix of IMD's Tests with 1:25 Scale Small Neck Model and 1:50 Scale Large Neck Model 49
3.8 Ice Properties for the ERC Tests 51
3.9 Ice Properties of IMD Tests 53
3.10 ERC Test Results 56
3.11 IME Test Results 57
3.12 IMD Test Results 59

4.1 Crack Loads and Maximum Load for the ERC tests 70
4.2 Ridge Crack Loads and Maximum Loads for the IMD Tests 71
4.3 Horizontal and Vertical Ridge Forces for all the Tests 73
4.4 Crack Location of the ERC Ridges 82
4.5 Crack Location of the IME Ridges 83
4.6 Statistical Measurements of the Neck Size Effect 86

6.1 Coefficients of $F(2l/L_e)$ 167

7.1 Statistical Measures of the Predicted Ridge Loads 188
7.2 Statistical Measures of Vertical Loads for the Three Models 201
7.3 Statistical Measures of Horizontal Loads for the Three Models 202
7.4 Overall Statistical Measures of Prediction of the Three Models 205
7.5 Overall Statistical Measures of sheet Ice Load Prediction 213
7.6 Statistical Measures for Vertical Sheet Load Prediction 214
7.7 Statistical Measures for Horizontal Sheet Load Prediction 214
7.8 Statistical Measures of NNA and NNP Predictions 216

A.1 Parameters for Sinha's Model 238
A.2 Strains for Y1T1R1 and Y1T1R2 at 20th Second of Loading 240
B.1 Estimated Compressive and Tensile Strengths 244
C.1 Ridge Dimension 249
E.1 Multi-Year Ice Characteristics 260
E.2 Ridge Characteristic Length 262

Nomenclature

B_e	effective width of ice sheet attached to a ridge
B_s	slope of best fitting line for predicted vs. measured forces
B_t	ridge top width
CCL, CCN, CIL	Refer to section 7.3.2
C_p	$= D_w^2 \rho_i g / (\sigma_f h)$ (refer to Equation (4.3))
DECICE	the name of a discrete element computer program
DEM	Discrete Element Method
D_T	cone top diameter for SCSs, circumscribed neck diameter for MCSs
D_w	waterline (circumscribed, for MCSs) diameter
edge-on	refer to Section 3.3.1
ERC	Esso Resources Canada Ltd.
E_r	Young's modulus for ridge ice
E_s	Young's modulus for sheet ice
face-on	refer to Section 3.3.1
FEM	Finite Element Method
$F_C(2l/L_e)$	load function for the hinge crack of an infinite length ridge under concentrated loads (MCS).
$F_D(2l/L_e)$	load function for the hinge crack of an infinite length ridge under uniform loads (MCS).
$F_T(2l/L_e)$	load function for the hinge crack of an infinite length ridge under triangular loads (MCS).
$F_I(2l/L_e)$	load function for the initial crack of an infinite length ridge against a MCS.
$F_0(L_n, l_n)$	load function for the initial crack of a finite length ridge against a MCS.
$F_H(L_n, l_n)$	load function for the hinge crack of a finite length ridge against a MCS.
F_{HS}	load function for the hinge crack of a finite length ice ridge against a SCS.
F_{IS}	load function for the initial (central) crack of a finite length ice ridge against a SCS.
F_{mx}	X component of the measured maximum ice load on a MCS
F_{my}	Y component of the measured maximum ice load on a MCS
F_{mz}	Z component of the measured maximum ice load on a MCS
F_x	general symbol for the X component of the ice load on a MCS
F_z	general symbol for the Y component of the ice load on a MCS
g	acceleration due to gravity

h	thickness of ice sheet
H_k	ice ridge keel depth
I	moment of inertia of an ice ridge and attached ice sheet
I_f	moment of inertia of the ice sheet attached to ice ridge
I_r	moment of inertia an ice ridge without ice sheet attached
IMD	Institute for Marine Dynamics of National Research Council of Canada (in St. John's, Newfoundland)
IME	Institute for Mechanical Engineering of National Research Council of Canada (in Ottawa, Ontario)
k	foundation modulus, see Equation (6.1)
L	a half length of an ice ridge
l	a half of facet width of a MCS at waterline
L_c	characteristic length of an ice ridge including the attached ice sheet
l_s	characteristic length of an ice sheet
L_n	$= L/L_c$
l_n	$= l/L_c$
MCS	Multi-faceted Conical Structure
$M(y)$	bending moment along the Y axis
M_{max}	general symbol for the maximum bending moment
M_i , M_d , M_c , M_t	the maximum bending moments in an infinite length ridge for the initial crack (M_i) and hinge cracks under uniform (M_d), concentrated (M_c), and triangular (M_t) loads, respectively
$M_0(L_n , l_n)$	bending moment at the center line (perpendicular to Y axis) of a finite length ridge
NIL	refer to Section 7.3.2
NNA, NNP	Nevel model (sheet ice) considering "active action" and "passive action", respectively, refer to Section 7.3.3
p_c	concentrated load for the hinge crack of an infinite length ridge
p_{cs}	concentrated load for the hinge crack of a finite length ridge
P_H , P_v	general symbols for the horizontal and vertical forces
P_{iv} , P_{hv}	vertical ridge forces for the initial crack and hinge crack, respectively
P_I , P_D , P_C , P_T	the maximum crack forces of an infinite length ridge for the initial crack (P_I) and hinge cracks under uniform (P_D), concentrated (P_C), and triangular P_T) loads, respectively
P_{IS} , P_{HS}	the initial crack and hinge crack forces of a finite length ridge
q_d	intensity of uniform load for hinge crack of an infinite length ridge

q_i	intensity of uniform load for central crack of an infinite length ridge
q_{is}	intensity of uniform load for central crack of a finite length ridge
q_t	maximum value of the intensity of triangular load for hinge crack of an infinite length ridge
R	correlation coefficient of measured and predicted ice forces
RCL, RCN. RIL	refer to Section 7.3.2
R_P	mean ratio of predicted to measured ice forces
RMS	Root Mean Square of relative error of force prediction
SCS	Smoothly-curved Conical Structure (i.e., smooth cone)
S_P	standard deviation of force ratio, R_P
X_I , X_H	horizontal forces for initial and hinge cracks, respectively
Z_I , Z_H	vertical forces for initial and hinge cracks, respectively
z_b , z_t	the distance from the centroid of a ridge cross section to its top fibre and its bottom fibre, respectively
z	freeboard of a SCS for Equation (2.8)
α	slope angle of main cone (from horizontal)
φ	internal friction angle
μ	friction coefficient between ice and structural surface
μ_0	internal friction coefficient of ice, $\mu_0 = tan\ \varphi$
ρ_i , ρ_w	ice and water densities, respectively
ρ_r , ρ_s	density of ice ridge and ice sheet, respectively
ρ_b , ρ_{rb}	buoyancy of ice sheet and ice ridge, respectively
σ	normal stress
σ_1 , σ_2	maximum and minimum principal stresses, respectively
σ_b	total bending stress
σ_c	compressive stress
σ_f	flexural strength of ice
σ_{rb} , σ_{rt}	flexural strength of ice ridge with bottom or top in tension, respectively
σ_{sb} , σ_{st}	flexural strength of ice sheet with bottom or top in tension, respectively
τ, τ_s	shear stress and shear strength, respectively
ν	Poisson's ratio

Chapter 1 Introduction

1.1 Background of the Test Program

Up to the early 1990's, many significant geological structures in the Canadian frontier areas have been drilled and tested for oil and gas at a total cost of over 15 billion Canadian dollars. Discoveries have been significant as the oil reserves (including discovered and potential) in the Grand Banks and Beaufort Sea areas alone are about 8 billion barrels (Croasdale, 1991). However, Hibernia and Terra Nova are the only frontier oil projects being or to be developed to date. The high cost for safe exploration and production is the main reason for slow progress with the frontier oil developments.

Conical shaped structures can induce ice bending failure and this mode will exert much lower loads on the structure compared to ice loads from a crushing failure mode. Therefore conical shaped structures are preferred for arctic oil and gas exploration/production operations. The conical structures designed till the 1990's have been of smoothly curved surfaces and have assumed steel construction. The difficulties encountered in manufacturing a smooth surface lead to a higher cost of construction, consequently making the total cost of oil and gas development projects higher. For ease of fabrication and savings in the cost of construction, Exxon Production Research Company proposed the development of a multifaceted surface to approximate the smooth surface (Weiss, 1988). This newly proposed configuration of the

structure will be referred to as the *multifaceted conical structure* (MCS) in the rest of this thesis, and the conventional *smoothly curved conical structure* will be referred to as SCS.

Utilization of such a structure raised several new concerns about ice load estimation. The main concerns are described as follows:

1. The mechanism of ice failure. The multifaceted surface may affect the ice failure process and make the process quite different from that for a smoothly-curved conical structure (SCS); hence the ice loads on the multifaceted surface may be different.
2. The effect of ice interaction with the vertical neck (refer to Figures 3.1 and 3.2). Designers preferred the diameter of the vertical neck to be only slightly smaller than the water-line diameter (Weiss 1988) but were afraid a large neck could lead to a higher ice load. The ice load formulae and procedures given in the design codes up to that time did not account for ice interaction with a normal vertical neck, let alone this large neck.
3. The methods or procedures for estimation of ice loads on this type of MCSs. All the existing formulae and procedures for ice load estimation in design codes have been supported by and/or based on tests with SCSs; hence it was questionable whether these formulae and procedures could still be used for MCSs.

To study the new features of ice interaction with a MCS and help understand the ice failure mechanisms and develop proper ice load estimation formulae, a NSERC University-Industry collaborative research program (NSERC file # 661-119/88) was initiated. This program, with a funding of 1.3 million Canadian dollars was carried out by Memorial

University of Newfoundland (MUN), ESSO Resources Canada Ltd. (ERC) (on behalf of Imperial Oil Resources and its industry partners including Exxon Production Research and Mobil Oil Ltd.), and National Research Council of Canada (NRCC). The program involved three series of tests carried out in the three facilities : ERC's outdoor ice basin at Calgary and the indoor ice tanks of NRCC's Institute for Marine Dynamics (IMD) at St. John's, Newfoundland, and Institute for Mechanical Engineering (IME) in Ottawa.

ERC's tests were done during the winter of 1988-1989 (to be referred to as *Year One Tests*) and the winter of 1989-1990 (to be referred to as *Year Two Tests*), respectively. The IME and IMD tests were completed during the spring and the summer of 1992, respectively.

1.2 Background of This Study

Each of the test teams documented their results in separate test reports (Metge and Weiss 1989, Metge and Tucker 1990, Irani *et al* 1992, Lau *et al* 1993). These reports mainly recorded the test conditions and the physical measurements for each individual tests. No theoretical analysis was done during presentation of these test reports; the present research work is the first comprehensive study carried out on the experimental results documented in these test reports.

Since concerns 1 and 2 presented in the last section could not be answered without an overall analysis of test results, such an analysis of these test results became vital and important. Moreover widely used analytical models for ice load estimation, available earlier, were based

on test conducted with SCSs; hence concern 3 required an extensive evaluation of the validity of theses models for the newly proposed MCS. Considering the difference in the loading conditions between a SCS and a MCS, new analytical models accounting for the characteristic interaction of ice ridge with MCSs were found to be desirable for estimating ice ridge loads on MCSs. Another concern, i.e., the effect of neck size, could have been better addressed if the conditions of two tests were kept the same except for structure's neck size. Unfortunately, no single pair of such tests could be found in all the test series. Therefore, a set of numerical simulations with the same parameters were undertaken for this purpose. Numerical simulations were helpful in understanding the mechanism of ice failure (concern 1). All studies carried out to address these aspects and the conclusions obtained from these studies are presented in this thesis. Except for the test results obtained from the test reports, all the graphical plots, analysis and conclusions presented in this thesis were obtained as a part of the investigation carried out for this thesis work.

1.3 Objectives

The principal objectives of the present study are to get an insight into the ice/MCS interaction and to provide theoretical and practical results for designers to consider in their structural design or for researchers' further study. The study will focus on the concerns raised by industry. It is divided into the following tasks:

1. Identification of the relationship between the ice loads and the ice cracking process under test conditions. The task will be fulfilled by thoroughly analyzing all the test data

including both the load records and the video records. A numerical analysis will also be performed to assist in the completion of this task. This is expected to help in the further understanding of ice-structure interaction and to aid in the development of theoretical models for ice cracking load estimation.

2. A study of the effects of structural parameters and orientations on the ice crack pattern and the ice loads on the structure. These include neck size (one of the factors of concern, to industry), the relative orientation between a structural facet face and sheet ice motion, the ridge orientation, etc. This task will be completed by means of analysis of the tests and numerical simulation.

3. Development of a theoretical model for easy estimation of ice ridge cracking loads on a MCS. This is considered as a separate item because the ice ridge cracking load is the most important consideration for structural designers and no analytical or semi-empirical models are available for a MCS.

4. Evaluation of the suitability of existing analytical models for estimation of ice loads on a MCS. Due to the reasons described in Section 1.2, an evaluation of the validity of existing SCS models for a MCS became a necessity. Since the MCS has two diameters (inscribed and circumscribed) and a vertical neck which are not accounted for in these existing analytical models, determination of which geometrical dimension(s) is (are) appropriate to be used as inputs to these existing models is another work that had be done.

1.4 Organization of the Thesis

This thesis consists of eight chapters and its main contents can be divided into four parts. The first part that follows this introduction is a literature review given in Chapter 2. The review focuses on the ridge tests with SCSs that can be considered as a counterpart of the present tests. Another area of literature reviewed is on typical analytical models developed earlier by other researchers.

The second part is a single chapter, Chapter 3, which presents a summary of the tests and their results. The materials given in this chapter provide a data base for the analysis in the chapters that follow.

The third part consists of two chapters: Chapter 4 and Chapter 5. The first portion of Chapter 4 summarizes the key scenarios of the ice-structure interaction process, which is followed by an analysis of the effect of neck size and the structural orientation on the sheet ice loads and on the ridge ice loads. Chapter 5 presents a series of numerical simulations carried out using a discrete element code. The simulation mainly focuses on the identification of the relationship between ice loads and ice cracking process. The effect of neck size is also analyzed by the numerical studies presented in Chapter 5. This part directly addresses concerns 1 and 2 or tasks 1 and 2 given earlier.

Chapters 6 and 7 contribute the fourth part of this thesis. Chapter 6 is dedicated to the

presentation of the newly developed theoretical model for the estimation of ice ridge cracking loads on MCSs. Its verification using test data is given in Chapter 7. Chapter 7 also contains the examination of other earlier theoretical models available. These models were developed for estimation of either ridge ice loads or sheet ice loads on SCSs. This part is expected to address concern 3 or tasks 3 and 4 given earlier.

Finally, an additional but more important chapter, Chapter 8, is arranged to summarize the conclusions obtained and contributions made in the course of this study and to give recommendations for further studies in this area.

Chapter 2 Literature Review

Before the present research program, there have been few theoretical and/or experimental studies on MCS reported in the open literature. The literature that is reviewed in this chapter is part of the large literature available on ice interaction with SCSs. In addition, this review will also cover some important developments and conclusions arrived from earlier research on ice interaction with SCSs.

During the past two decades, many excellent review papers and reports (Chao 1992a & 1992b, Wessels and Kato 1989, Marcellus *et al* 1988, Sodhi 1987, Nessim *et al* 1987, Krankkala and Maattanen 1984, Croasdale 1975 & 1980, Cammaert and Muggeridge 1988) have been published on ice-structure interaction. In these publications, the results and progress in the studies of ice sheet loads on SCSs were extensively reviewed. However, the SCS and ice ridge interaction have received lesser attention. Therefore, the emphasis in this chapter will be given to review the studies of ridge/SCS interaction.

2.1 Experimental Studies of Ice Ridge Forces

So far, only a few test data for ice ridge forces exist in the open literature. In the following, several typical model test programs are reviewed. A brief introduction to these test programs will be followed by a summary of the test results which are organized into five subsections.

Lewis and Croasdale (1978) reported one of the earlier test programs on ridge-cone interaction. The tests were conducted with a 45° conical structure model and saline ice ridges at a test scale of about 1:50. Eleven ridges were successfully tested for structure/ridge interaction. The ridges were built from ice sheets and could be considered as pressure ridges or layer ridges. The results have been used to support analytical models (Croasdale 1975 & 1980, Kim and Kotras 1973).

Kamesaki and Yoshimura (1988) conducted a new series of tests with two cone models at a scale of 1:100. The slope angles at waterline for these two models were 45° and 40.7°, respectively. The ratio of ridge keel depth and ice sheet thickness, ridge length, and ridge orientation were changed to investigate their effects.

Abdelnour (1988) presented a summary of two extensive test programs, based on the work carried out by Abdelnour and Teh (1976) and Edwards and Abdelnour (1977). A total of sixty ridges were tested against a 45° cone with a waterline diameter of 0.61 meters. The ridges and the surrounding sheet ice were modeled using a synthetic material to simulate natural ice at scales between 1:50 and 1:75. Besides the broadside and 45° skewed orientation, an end-on orientation of the ridges (the ridge axis was parallel to its moving direction) was also tested. Ridge length varied from 0.38 meters, to simulate very short ridges, to 4.1 meters, to simulate infinite ridges. The experimental data from these tests have been used to develop and verify analytical models (Wang 1984, Abdelnour 1988).

2.1.1 Failure Process and Forces of Broadside Ridges

The typical ridge failure sequence observed and described by Lewis and Croasdale (1978) can be presented in four steps as follows:

1. When the ridge is initially approaching the cone the ice sheet between the ridge and the cone breaks. The corresponding force is quite low (compared to the maximum force), and is at the level of the ice sheet force.
2. As the ridge moves further forwards, the cone encounters the underwater leading edge of the ridge and begins to lift the ridge slightly, causing an initial crack in the ridge, usually at the center of the ridge, often referred to as initial crack or center crack; it has also been observed that the crack could extend through the ridge into the ice sheet. The magnitude of force increases sharply until the crack forms and then levels off. The magnitude of the force at this instant may not be at its maximum but it is much higher than the earlier peaks associated with the breaking of the ice sheet.
3. As the motion continues, the ice sheet is separated from the ridge by a tensile failure. The ridge is now noticeably deflected upwards and the initial crack is widened and extends further into the ice sheet. The magnitude of the force continues to increase but has not reached its maximum.
4. The ridge continues to be deflected upwards until a second crack (hinge crack) occurs at some distance away from the center crack. Then, the ridge and ice sheet fail simultaneously, and the surrounding sheet ice which have been deflected considerably upwards begins to settle back into the water. The force is at its peak magnitude.

The above failure sequence is typical only for relatively long and broadside ridges surrounded by a moderately thick ice sheet. In fact, the mode of ridge failure is dependent on the type of interaction, ridge length, sheet thickness, and many other factors. Abdelnour (1988) summarized four distinct failure processes observed for the broadside ridges of various lengths.

1. Complete separation of the ridge from the ice sheet followed by interaction of the advancing ice cover with the ridge
2. Complete separation of the ridge from the ice sheet followed by a central crack in the ridge and clearing of the ridge around the cone.
3. Separation of the ridge from the ice sheet ahead of the ridge (side of ridge nearest to the cone) and at the ridge ends followed by central cracking of ridge and occasionally by hinge cracks.
4. Ridge failure at the center followed by hinge cracks. No apparent ridge/sheet separation; either or both ends of ridges still firmly embedded in ice sheet.

The average ratio of hinge crack force to initial crack force was 1.73 on average for Lewis and Croasdale's tests (1978). This ratio for Abdelnour's results was estimated to be close to 1.

2.1.2 Effect of Ridge Orientation on Failure Process and Peak Loads

Kamesaki and Yoshimura (1988) observed that the end-on ridges were broken like a semi-infinite beam loaded at the end. The broken beams, approximately the size of the ridge width, frequently

piled up in front of the cone.

Abdelnour (1988) reported two distinct failure processes observed for the interaction of end-on ridges with a SCS.

- Complete separation of the ridge from the ice sheet followed by interaction of the ridge with the advancing ice sheet.
- Separation of the ridge from the ice sheet at both sides with a sequential hinge failure.

The failure process for the 30° and 45° skewed ridges was observed to be similar to the ones for broadside interaction scenario. However, after the occurrence of the center crack and hinge crack, the ridge could come in contact with the cone once more and could produce another hinge crack (Abdelnour 1988, Kamesaki and Yoshimura 1988). Kamesaki and Yoshimura's tests also showed that the 60° skewed ridges failed in a quite different way: the portion of the ridge between its leading edge and the center crack was not broken, and the portion between its trailing edge and the center crack was completely cracked along the moving direction.

Abdelnour's (1988) results showed that the broadside orientation yielded an average load that was at least twice as large as that for the end-on orientation. However, Kamesaki and Yoshimura's results (1988) indicated that the loads for these two orientations were roughly at the same level.

2.1.3 Effects of Sheet Thickness and Strength on Failure Process and Peak Loads

Thickness of the ice sheet strongly affects the failure process, and hence the ice loads (Abdelnour, 1988). If the ice sheet was sufficiently thin (compared to the ridge keel depth), the ridge tended to rotate in its plane after a center crack developed. If the surrounding ice sheet was sufficiently thick, a local bending failure or a circumferential crack was likely to occur in the centre of the ridge because of the high confinement effect of the surrounding ice sheet (Kamesaki and Yoshimura, 1988). Abdelnour (1988) pointed out that an increase in ice thickness by a factor of two resulted in an increase in the force by at least two to four times for most cases of his tests.

Another important effect of the ice sheet was to increase the global force through the ride-up scenario. Wang (1979) summarized the peak forces of the ridges with and without ice sheet ride-up (the data were quoted from Edwards and Abdelnour's tests (1977)). The results showed that the sheet ice ride-up action increased the average vertical and horizontal peak forces by 31% and by 29%, respectively.

2.1.4 Ratio of Horizontal to Vertical Forces

The mean ratio of the horizontal to vertical peak forces for the 27 tested ridges, summarized by Abdelnour (1988), was 1.18. The corresponding value for Lewis and Croasdale's tests was 1.66,

and for Kamesaki and Yoshimura's tests was 1.97. All these data were for 45° cones.

The ratio of horizontal and vertical forces on a cone can be theoretically expressed as (Croasdale, 1975, 1980):

$$P_H / P_V = \frac{\sin\alpha + \mu\cos\alpha}{\cos\alpha - \mu\sin\alpha} \tag{2.1}$$

where P_H and P_V are the horizontal and vertical forces, respectively, α is the cone slope angle from the horizontal, and μ is the ice/cone surface friction coefficient.

While applying equation (2.1) to the above tests, one will find the ratio should vary from 1.15 to 1.56 as coefficient of friction μ varies from 0.1 to 0.2. It is obvious that Kamesaki and Yoshimura's tests yield a ratio much higher than the one predicted by equation (2.1). The same conclusion could also be drawn from the results of other test programs. This difference could be due to the fact that this formula is valid only for two-dimensional cases and also may be due to the error in coefficient of friction measurement as pointed out by Abdelnour (1988).

2.1.5 Effect of Ridge Length on Peak Forces

Abdelnour (1988) used a dimensionless ridge length $2L/L_c$ to measure the effect of the ridge length, where L is the half ridge length, and L_c is the characteristic length of a ridge in water. He concluded that a ridge with the dimensionless length between 1 and 1.5 exerted a higher vertical force than a ridge with a dimensionless length below or above this range. These

relatively short ridges may exhibit forces twice as high as an infinite ridge.

Kamesaki and Yoshimura (1988) plotted the peak forces against a ratio of $2L/H_k$, where H_k is ridge keel depth. The plot showed that the force increased with the increase of $2L/H_k$ until $2L/H_k$ reached a value of 20; when $2L/H_k$ ratio increased beyond 20 (where the ridge might be regarded as infinite) the peak force became almost a constant.

2.2 Analytical Models for Ridge Force Estimation

2.2.1 Croasdale Model and Abdelnour Model

Croasdale (1975 & 1980) applied the theory of an beam on an elastic foundation, developed by Hetenyi (1946), to estimate the maximum force of a ridge on a cone. It was assumed that ice ridge will crack when the tensile stress at its outer fibre equals the ice flexural strength. The formulae for vertical forces were derived and given in the form:

$$P_{iv} = \frac{4\ \sigma_{rt}\ I}{z_t\ L_c} \qquad P_{hv} = \frac{6.2\ \sigma_{rb}\ I}{z_b\ L_c} \tag{2.2}$$

where P_{iv} and P_{hv} are vertical forces for center and hinge cracks, respectively; z_t and z_b are the distance from centroidal axis of the ridge to its top and bottom layers; σ_{rt} and σ_{rb} are ridge flexural strength for top and bottom in tension, respectively; L_c is characteristic length of the

ridge and attached ice sheets and I is moment of inertia of ridge cross section. The horizontal forces can be calculated using Equation (2.1).

In this model, the ridge was assumed to be infinite, and the effect of the attached sheet ice was not taken into consideration. Moreover, a concentrated load acting at the ridge/cone contact point was assumed, that is, the effect of the load distribution along the contact edge was not taken into account.

Abdelnour (1981, 1988) also applied Hetenyi's theory to the ridge/cone problem. His expression of load formula including the effect of ridge length and attached sheet ice was considered, is rewritten with the notations used in this thesis as follows:

$$P_{iv} = \frac{\sigma_{rt} I}{z_t L_c} F_{IS} \qquad P_{hv} = \frac{\sigma_{rb} I}{z_b L_c} F_{HS} \tag{2.3}$$

where F_{IS} and F_{HS} are load functions for initial (cental) and hinge cracks, respectively, and they can be expressed as

$$F_{IS} = \frac{4\left(\sinh\frac{2L}{L_c} + \sin\frac{2L}{L_c}\right)}{\cosh\frac{2L}{L_c} - \cos\frac{2L}{L_c}} \tag{2.4}$$

$$F_{HS} = \frac{2\left(\sinh^2\frac{L}{L_c} - \sin^2\frac{L}{L_c}\right)}{\sinh\frac{L}{L_c}\sin\frac{Y}{L_c}\sinh\frac{L-Y}{L_c} - \sin\frac{L}{L_c}\sinh\frac{Y}{L_c}\sin\frac{L-Y}{L_c}} \tag{2.5}$$

where $2L$ represents full ridge length. Y is the location where the maximum moment occurs or where ridge failure happens and it can be obtained by differentiating the moment equation and equating it to zero. The bending moment for a hinge crack can be written as follows:

$$M(y) = -P_{hv}L_c \frac{\sinh\frac{L}{L_c}\sin\frac{y}{L_c}\sinh\frac{L-y}{L_c} - \sin\frac{L}{L_c}\sinh\frac{y}{L_c}\sin\frac{L-y}{L_c}}{2\left(\sinh^2\frac{L}{L_c} - \sin^2\frac{L}{L_c}\right)} \tag{2.6}$$

For convenience, Equation (2.2) together with Equation (2.3) will be referred to as the Croasdale-Abdelnour model in this thesis.

2.2.2 Kim and Kotras Model

Kim and Kotras (1973) developed a sequentially straightforward approach, also based on the Lewis and Croasdale's observation and Hetenyi's theory. The ridge and the surrounding ice sheet were treated as an elastic beam and plate on an elastic foundation, respectively. Their approach used in determining the failure sequence can be summarized in seven steps, which was later coded into a computer program by Semeniuk (1975). The first four steps are for initial (or center) crack and the rest are for analysis of the hinge cracks.

1. After the ridge contacts the cone, the ridge's upwards deflection, W_0, at the contact point can be calculated for a given penetration distance X. For this W_0, the ridge and sheet deflection W(x,y) is approximately determined using beam and plate theory.
2. Determine the vertical force required to lift the ice to the deflection W(x,y).
3. Check both shear and bending stresses at the interface between the ridge and the attached ice sheet to see if the ridge is separated from the sheet.
4. Check to see if the center crack occurs. If the ice sheet was not separated from the ridge, the ridge/sheet combination was idealized as a beam with attached flanges. Compare the stresses at the center of the ridge with ridge flexural strength to see if failure (center crack) occurs. If no failure occurs, increase the penetration and repeat steps 1 through 4 until the initial crack occurs.
5. As the ridge (and sheet, if it was not separated from the ridge) moves further forwards, update its deflection and the required forces.
6. Check the separation at sheet/ridge interface again. After the initial (or center) crack, the sheet, if not separated from the ridge before the initial crack, could be detached from the ridge just before hinge cracks.
7. Check the stress to see if the hinge cracks occur (similar to Step 4).

2.2.3 Ride-up Model

The Croasdale-Abdelnour model and Kim and Kotras model are only for infinite ridges which do not account for the possible ride-up process. Winkler and Nordgren (1986) developed a

model for calculation of the ridge force during the ride-up process with the assumption that the ridge is free-floating within a surrounding ice floe.

The ride-up problem of a ridge was analyzed in two steps. The ridge first was modeled as a rigid body undergoing large rotation and translation in its cross-sectional plane. The forces acting on the ridge consist of the force exerted by the cone, buoyancy force, gravity load, and a force transmitted from the ice floe behind. For each stage of the ride-up process (i.e. for a certain rotation angle of the ridge), the ridge force on the cone can be calculated by solving the equilibrium equation of the force system. Then the ridge was treated as an elastic beam on the cone. A maximum ridge force for flexural failure can be determined at each stage of the ride-up process. The maximum force over the entire ride-up process gives the overall maximum ridge force for a given ridge cross section.

The approach was also extended to include the effects of dynamics and local crushing (Nordgren and Winkler 1989), and to probabilistic analysis (Winkler and Reece 1986).

2.2.4 Plasticity Method

All the above models are based on elasticity theory, and are likely to under-estimate the actual forces. To estimate an upper bound of ridge forces, Wang (1979 & 1984) developed a model based on plasticity theory.

In this model, the ice ridge and ice sheet were assumed to be elastic-perfectly plastic and resting on an elastic-perfectly plastic foundation. The ice sheet in front of the leading edge of the ridge was assumed to be separated from the ridge before the ridge cracked. Then, the upper bound theorem was applied to this sheet-ridge-cone system. Five components of the rate of energy dissipation were considered, viz., the rates of energy dissipation due to ice sheet and ridge bending, ice sheet and ridge weight (or buoyancy) and friction between the ridge and the cone. Five types of admissible velocity fields were considered, two of which were designed for long ridges with center and hinge cracks, another two for short ridges with a center crack only, and one for very short ridges without crack at all. Each of these five velocity fields gave an upper bound for the ridge force. Among the five bounds, the smallest was selected as the calculated value.

This model has been widely used in ridge force estimation and analysis (Schreiber *et al* 1989). Nevel (1991) simplified the force equation for the long ridge type I velocity field which is the most likely breaking pattern for long ridges.

2.2.5 Comparison of Models and Discussions

Comparison of these analytical models with experimental data has been carried out by many researchers (Wang 1979, Marcellus *et al* 1988, Kamesaki and Yoshimura 1988, and Chao 1992b, etc). The latest and the most extensive one was done by Chao (1992b). These comparisons share a common conclusion: *the elasticity methods generally underestimate the*

ridge loads on a cone, while the plasticity methods may over-predict the loads.

The plasticity model and the Kim and Kotras model are theoretically the most elegant ones because they simulate the real situations more completely than other models. Compared with the Kim and Kotras model, Wang's plasticity model covers more situations in terms of ridge length and possible crack patterns (velocity fields). Wang (1979) did an extensive comparison of these two models using the results of fifty ridge tests and showed the plasticity model predicted the loads better, while Kim and Kotras model under-predicted the loads.

The Croasdale-Abdelnour model is quite simple and easy to apply for ridge load estimation. This model does not include the forces due to the sheet ice pieces riding up, neither does the Winkler and Nordgren model (1986).

2.3 Ice Sheet Interaction with a SCS

Numerous test programs have been carried out to study the ice sheet/cone interaction (see the reviews: Croasdale 1980, Sodhi 1987, Wessels and Kato 1989). The observed failure process and modes are summarized as follows.

As the ice sheet first encounters a cone, local crushing occurs on the underside edge of the ice sheet, which causes an interaction force normal to the surface of the structure. The force, which increases as the crushing area increases, will deflect the ice sheet. If the ice speed is low

and the cone diameter is small compared to the thickness of the ice, radial cracks will initiate the ice-sheet failure. Peak interaction force, however, occurs when circumferential cracks develop around the cone, leading to the formation of wedge-shaped broken ice pieces. If the cone diameter is relatively large, the maximum tensile stresses of the ice cover change from the circumferential direction to the radial direction. This process causes an ice sheet to fail first circumferentially and thereafter radially. The cracked ice pieces will be pushed up on the surface of the structure, which has been termed *ride-up*, then will slide over the surface and down into water or on the ice cover.

Many factors could affect the ice failure mode. Increasing roughness of the cone surface, or increasing ice thickness could gradually alter the failure mode from bending to shear. With increasing speed of ice/structure interaction, the distance between the circumferential cracks would decrease, and finally, the ice-sheet failure would change abruptly from bending to shear, resulting in a lower peak force due to the dynamic effect.

2.4 Analytical Models for Ice Sheet and SCS Interaction

There exist many analytical models and empirical (or semi-empirical) equations developed for estimation of sheet ice forces on SCSs (Chao 1992a). In terms of the theory the models were based on, they can be divided into two categories: elasticity models and plasticity models. This section reviews two typical elasticity models and one plasticity model.

2.4.1 Ralston Model

Ralston (1978 & 1980) applied the technique of plastic limit analysis to the case of ice/cone interaction and developed an analytical model to estimate the maximum ice sheet forces on a cone. The derived formulae for horizontal force P_H and vertical force P_V are given by:

$$\begin{aligned} P_H &= A_4 [A_1 \sigma_f h^2 + A_2 \rho_w g h D_w^2 + A_3 \rho_w g h (D_w^2 - D_T^2)] \\ P_V &= B_1 P_H + B_2 \rho_w g h (D_w^2 - D_T^2) \end{aligned} \tag{2.7}$$

where σ_f and h are flexural strength and thickness of ice sheet, respectively; D_T and D_w are top and waterline diameters of a cone, respectively; A_1, A_2, A_3, A_4, B_1, and B_2 are the coefficients determined by solving complete elliptic integral equations and by optimizing the bound for the failure force (refer to Ralston 1978).

2.4.2 Croasdale Model

Croasdale (1980) presented a simple elasticity analysis model. The ice sheet was treated as a semi-infinite elastic beam on an elastic foundation subjected to a vertical load P_V and a horizontal load P_H at one end. The ice forces on the structure were given by:

$$P_H = (c_1 D_w \sigma_f \sqrt[4]{\rho_w g h^5} + c_2 z h D_w \rho_i g) \Gamma \tag{2.8}$$

where

$$c_1 = 0.68\,\xi\ , \qquad c_2 = \xi(\sin\alpha + \mu\cos\alpha) + (\sin\alpha + \mu\cos\alpha)/\tan\alpha \tag{2.9}$$

$$\Gamma = 1 + \frac{\pi^2 L_s}{4D}$$

Γ is a modification coefficient (for a 2D structure, $\Gamma=1$), L_s is characteristic length of sheet ice, ξ is a function of slope angle of the cone (α) and friction coefficient (μ) and is equal to P_V/P_H as given in equation (2.1). P_V can be determined using equation (2.1). Recently, Croasdale and his associates have modified this model to include the effect of ice rubble in front of a cone (Croasdale *et al*, 1994, Croasdale and Cammaert, 1993).

2.4.3 Nevel Model

Nevel (1992) presented a rigorous model based on elasticity theory and his earlier theoretical studies. The model treated the ice floe as a series of truncated wedges which were formed as a result of radial cracking. It was based on the following observation from physical tests: as the wedges move against the cone, they may break due to the bending failure at the bottom of the wedges; in the mean time the smaller ice pieces broken from the wedges during the preceding interaction process are pushed further up on the cone surface. The model assumes that the ice pieces completely cover the front half of the cone. The impinging wedges subjected to both vertical and horizontal (in plane) loads may break simultaneously or sequentially. For the sequential break, the model assumed that the maximum load occurs when the center wedge breaks.

The greatest contribution of this model is its formulation of the forces due to ice riding up on the cone surface. The model is capable of dealing with the computation of sheet ice loads on a SCS with a number of conical sections, including a vertical neck. Two action conditions were considered in the model: passive action and active action. As the author stated in his paper (Nevel, 1992), "active ice action is defined when the broken ice pieces on the surface of the cone slide into the section above", and "passive ice action is defined when the broken ice pieces do not slide into the section above". In an application, users of this model can choose either of these two action conditions.

2.4.4 Comparison of Models and Discussions

Chao (1992a) and Marcellus *et al* (1988) compared the various analytical models and empirical formulae. A general conclusion from the comparison is that Ralston's model which was based on plasticity theory overestimates the failure loads while the models based on elasticity theory, including the Croasdale model, underestimate the load. These comparisons and conclusions do not cover the Nevel model because it was published later.

Chao (1992a) and Macellus *et al* (1988) also analyzed the crack and ride-up components of the predicted failure load. They stated that the difference between the predicted loads from the plasticity model (Ralston's model) and elasticity models was mainly due to the difference in predicted crack loads. The crack loads predicted from Ralston's model is much larger than those from elasticity models, while the ride-up loads from all the models are relatively close to each

other. This might be because the ice sheet under plasticity theory could stand larger forces.

Many of the offshore drilling structures, proposed for use in the Arctic, have sides with multiple slopes or at least vertical upper walls (like the neck in the MCS to be shown in the next chapter) to reduce the chance of high ice ride-up and to maximize the working surface with respect to the base diameter. When the broken ice pieces ride up to the corner of two slopes the leading ice piece cannot go further. This leading piece could either be crushed or lifted. This, if it occurs, could increase the load on the upper slope or upper vertical wall and also increase the total load. Coon *et al* (1985) and Izumiyama *et al* (1994) studied this aspect and gave a set of formulae accounting for this additional load. Of the three models reviewed above, the Nevel model is the only one accounting for this effect.

2.5 Numerical Analysis

2.5.1 Finite Element Analysis

Bercha (1973, APOA # 57) carried out one of the earliest finite element analysis (FEA) of an ice ridge with attached ice sheet against a cone using a commercial code ANSYS in the early 1970s. The ice was assumed to be a fast brittle, isotropic, homogeneous, linear elastic material. The simulation for a long ice ridge (4000 feet long) showed a crack pattern similar to the one observed by Lewis and Croasdale (1978), and the peak load was also reached during the hinge crack process. His simulation also showed that the maximum force for the short ridge was about

30% lower than that for the long ridge.

Maattanen and Hoikkanen (1990) applied the finite element method to determine ice sheet loads on a cone. The ice sheet was subjected to edge load due to the resistance of the cone and distributed loads on the upper surface of the ice cover due to the weight of the piled-up ice pieces. The ice sheet was treated as an elastic wedge on an elastic foundation. They compared the predictions with their full-scale measurements (Maattanen and Mustamaki 1985) and the predictions from Ralston's model. The results showed that their model yielded a better agreement. Maattanen (1986) also applied this approach to the case of sloping walls.

Derradji-Aouat (1994a & 1994b) implemented a nonlinear and time-dependent constitutive model, i.e. Sinha's model (Sinha 1984 & 1988), into a finite element program to compute sheet ice loads on a cone. He took the ride-up ice into account, but assumed the thickness of ride-up ice to be the same as the parent ice floe. It has been recognized that the total thickness of the ride-up ice (more than one layer) could be much bigger (McKenna and Spencer 1994).

The above FEAs are based on a number of assumpations some of which are not fully realistic. For example, the assumption of tight contact along the ice/cone contact line may be valid only for the very small structure and relatively soft ice (Sanderson 1988). For a large structure, this assumption may result in an overestimation of the ice crack load. The assumption is not realistic even for small structures if the ice is quite brittle. As many tests have shown, the cracks of brittle ice usually form a front such that only part of it can contact the cone for the

next crack. Another example is that most of FEAs consider the effect of the ice rubble on the cone and on the top of the ice sheet by adding their force (due to their gravity loads) to the total ice loads. As pointed out by some researchers (McKenna and Spencer 1994), the rubble, besides their positive contribution to the total loads, could also assist in the failure of the ice sheet.

2.5.2 Discrete Element Analysis

The discrete element technique is a powerful tool that has been widely used in rock mechanics and many other areas including ice mechanics (Mustoe *et al* 1989, Williams and Mustoe 1993). The theory of this technique was given by Williams (Williams *et al* 1985, Pande *et al* 1990). A distinct feature of the Discrete Element Method (DEM) is that each element is considered as a distinct body which communicates with its surrounding elements via face, edge, and corner interaction forces that change as the bodies move and/or deform.

Compared with the finite element technique, the discrete element technique is more suitable for the analysis of multiple, interacting, deformable, discontinuous or fractured bodies undergoing large motions and rotations, which is the case of ice interaction with conical shaped structure. In addition, the analysis with DEM can realistically and fully account for the effect of rubble ice which FEM can only partially take into account.

There are many kinds (although similar) of discrete element approaches available in the literature and many computer codes have been developed. Evgin and Sun (1990) gave an

extensive review of these approaches. The most elegant one was developed by Hocking and his co-workers (Hocking *et al* 1985a, 1985b, 1985c) and coded in a computer program first named CICE and later on changed to DECICE.

DECICE formulation is based upon an internal discretization of Simply Deformable Finite Elements (SDFE). In other words, the linear shape function is implemented for the elements in DECICE. The detailed formulation of DEM is given in DECICE Theoretical Manual (by Intera Information Technologies). An overview of DECICE will be presented in Chapter 5. Only a few applications of DEM to ice/sloping structure interaction will be briefly reviewed in this section.

Rigid elements were used in early development of discrete element technique. The typical approach using a rigid element was proposed by Kawai (1977 & 1979), termed as Rigid Body-Spring Model (RBSM). This model consists of a finite number of small rigid bodies (elements) connected with springs distributed over the contact area of neighbouring bodies. Displacement components of an arbitrary point in that rigid element are expressed in terms of the displacement components of the element center of gravity. The problem is reduced to solving a set of simultaneous linear equations similar to FEM but in terms of displacements of the center of gravity of all elements at each load increment step.

Watanabe and Kawai (1980) first applied this approach to analyze the bending collapse problem of level ice against an ice-breaker bow model with emphasis on the prediction of ice

crack pattern. The stress-strain law in their analysis was elastic-perfectly plastic. The results showed that the calculated and experimental crack patterns coincided with each other well. Later, Yoshimura and Kamesaki (1981) adopted the same method to analyze the crack pattern of the ice sheet in front of a cone, but they considered the stress relief accompanied with the initiation of cracks. Shibue and his associates (Shibue and Kato 1988, Shibue *et al* 1994) introduced a thick-walled shell element into the RBSM. They analyzed the failure process of ice sheets as well as ice ridges against conical structures and inclined indenters. The stress-strain relationship used in their analysis was identified by simulation of ice property tests.

Although the predictions from RBSM were claimed to give good agreement with experimental results, the disadvantage of this approach is obvious. Firstly, it is assumed that the element used in RBSM is rigid and element deformability is not considered; thus, this approach is only appropriate for studying the brittle behaviour of ice. The creep and ductile behaviour cannot be considered in this approach. The reason that good agreement was obtained between the prediction and experimental results could be that the events studied involved mainly brittle behaviour of ice. Secondly, generation of the element mesh largely depends on prior analysis experience. It has a great influence on the ice collapse pattern since failure occurs only at element edges which are linked with springs to the surrounding elements. Thus, a fine mesh is required in the failure zone in order to get typical failure patterns.

In the CICE or DECICE program, the DEM has been generalized to the case of element deformability, i.e., SDFEs are used. Depending on the constitutive behaviour applied to the ice,

this approach allows modelling of ice behaviour from brittle fracturing to creep failure. This improvement overcomes the disadvantage of the RBSM mentioned above.

This approach and the corresponding code DECICE have been verified and validated for ice (both sheet and ridges) interaction with a conical structure and/or a sloping structure (Hocking *et al* 1985a & 1985b). The computation showed that the approach could properly simulate the ice failure process. The ice sheet ride-up and pile-up on a stepped slope artificial island have also been analyzed using DECICE. The ice sheet was discretized using beam bending elements, and the island was modelled as a single rigid element. The elements of the ice sheet were locked together initially to simulate the completely crack-free ice. With the ice sheet moving against the island, the ice experiences fracturing. Whenever a fracture was judged to have occurred according to stress condition and chosen criterion, the element (if the crack went through it) would be broken into two to model the crack. This work together with the computation of interaction forces between elements were done automatically. The calculation was carried out with a time increment; thus the time history of the ride-up and pile-up process could be simulated. Predicted forces were in the same level as those measured. This work demonstrated the power of DECICE in simulating of ice ride-up and pile-up event. It was recommended to be a unique numerical approach for this kind of simulation (Evgin and Sun 1990).

DECICE has also been applied to other areas of ice mechanics; for example, dynamic impact of ice on an offshore structure (Hocking *et al* 1985c), identification of ice properties

(Intera Technology Inc. 1986a), analysis of ice spray platform (Applied Mechanics Inc. 1985), and ice ridging loads (Intera Technology Inc. 1986b), etc.

Chapter 3 Faceted Cone Test Program

A five year test program initiated in 1988 as a joint university-industry project was carried out by Memorial University of Newfoundland (MUN), ESSO Resources Canada (ERC) representing Imperial Oil Resources, Exxon Production Research, Mobil Research and Development, and National Research Council of Canada's Institute for Marine Dynamics (IMD) and Institute for Mechanical Engineering (IME). Three series of tests with structural models at scales varying from 1:10 to 1:50 were conducted in three Canadian ice basins: Esso Resources Canada (ERC)'s outdoor ice basin in Calgary, IMD's large ice tank in St. John's, Newfoundland, and IME's tank in Ottawa (Croasdale and Muggeridge 1993). These tests generated one of the largest data bases in the world for ice-cone interaction. As a member of the research team, I was involved in carrying out part of the tests at NRCC's IMD indoor ice basin at St. John's during the summer of 1992. The description of the various ice basins and the reporting of all the earlier test results are done to make the presentation complete and comprehensive. In addition, the earlier presentation of test results contained some errors which had to be assessed and corrected after a proper review of the videos and computer records of the test results.

3.1 Test Facilities

3.1.1 ERC's Ice Basin

The outdoor ice basin at the ERC's Research Laboratory in Calgary is the widest ice testing

basin in the world. It is capable of allowing near full-scale tests to be carried out against which ice load algorithms can be evaluated (Robbins *et al* 1975).

This basin is 30 meters wide by 55 meters long, with a water depth varying from 1.4 meters (in the area for ice formation) to 3.0 meters (in the area for a test structure to be mounted). The maximum useful ice field run length is in the order of 35 meters. A test structure can be mounted on a three point support system (one more support was added for these faceted cone tests). A floating towing boom is attached to trolleys which travel on rails along the edges of the basin; when the boom is towed, it pulls the ice against the structure. The basin is equipped with refrigeration mats and compressors which are capable of maintaining the temperature at 10° to 20° C below ambient air temperature depending on the number of mats connected.

The water depth of 3 meters in this basin is ideal for the tests on 1:10 scale model structures whose full-scale counterparts are proposed for the Beaufort and Chuchki Sea exploratory drilling operation in about 30 m of water (Weiss 1988).

3.1.2 IMD's and IME's Ice Tanks

IMD's ice tank is the longest indoor ice testing tank in existence. This ice basin is 96 m long by 12 m wide, with an useful ice length of about 76 meters. The water depth is 3 meters. Unlike ERC's ice basin, IMD's ice tank is equipped with a towing carriage, from which a test model is towed to move against ice. The towing carriage is capable of speeds up to 4 meters per second

and has a Micro Vax computer for data collection, and a set of video cameras for recording test runs above and below the water surface from several angles. The refrigeration system in IMD's tank is computer-controlled to ensure that the air temperature is uniform near the water surface. Air temperature can be controlled from -30° C to 15° C.

IME's tank is 21 m long by 7 m wide and 1.2 m deep. Similar to IMD's tank, the IME's tank also has a towing carriage which spans the tank and can travel the length of the tank to tow a structure through ice, with maximum possible speeds up to 65 cm/s. The temperature in the insulated room which houses the tank can be controlled to as low as -20° C.

3.2 Structures and Instrumentation

3.2.1 Prototype Structures and Test Models

The proposed prototype structures are shown in Figures 3.1 and 3.2. The structures consist of three sections: a main cone (the lower portion of the structure), a vertical neck, and a collar, each of which has six facets. The difference between these two structures is their neck size. The structure shown in Figure 3.1 has a relatively smaller neck size; thus its models will be termed as "small neck" model. Similarly, the models of the structure shown in Figure 3.2 will be termed as "large neck" models because of their large sized neck. The slope for all the sides of the main cone is 5:6 (vertical to horizontal) or 39.8 degrees for both structures. Side slope of the collar that sits on the top of the main cone and under the neck is 2:1. A real production platform could be 50 percent larger (Weiss, 1988).

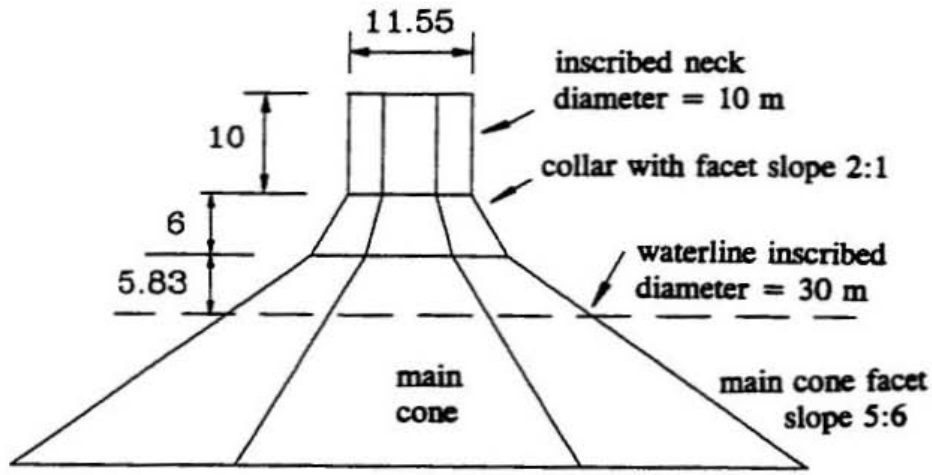

Dimensions are given in meters, slopes given by vertical to horizontal

Figure 3.1 The Prototype Structure with Small Neck

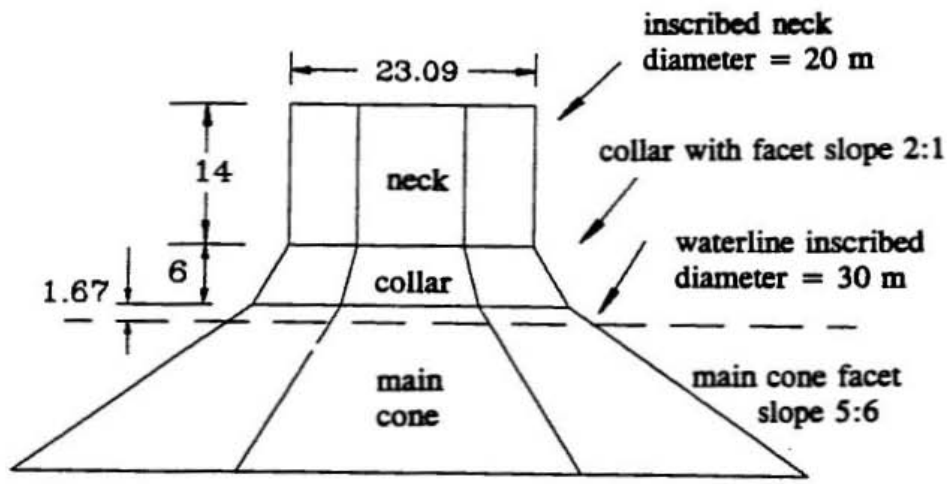

Dimensions are given in meters, slopes given by vertical to horizontal

Figure 3.2 The Prototype Structure with Large Neck

In much of the earlier tests with SCSs, the diameter of the waterline was three or more times the diameter of the neck. Consequently, the ice formulae and the procedure given in the design codes were also based on those tests with small neck structures. The tests with this small neck MCS model were expected to examine the validity of those formulae and to compare with the "large neck" tests. On the other hand, designers have found it advantageous to make the waterline diameter only slightly greater than the neck diameter (Weiss, 1988). The ratio of waterline diameter to the neck diameter being 1.2 to 2.0 would be highly desirable. Therefore, the "large neck" prototype having a ratio of 1.5 was proposed.

In ERC's tests, two models were tested in two winters, a 1:10 model with small and large necks was tested in 1988-1989 winter (to be termed as "Year One" tests), and a 1:20 large neck model was tested 1989-1990 winter (Year Two tests). In IMD series also, two models were tested: a 1:25 model with large and small necks, and a 1:50 large neck model. One small neck model with a nominal scale of 1:50 was tested in IME's tank.

The model used in the IME series was not tested with the water surface elevation corresponding to the full-scale waterline inscribed diameter of 30 meters. The model structure was purposely raised out of the water to increase the loads on the main cone and to avoid high ice pile-ups. The scale at waterline varied from test to test, with an average scale about 1:30 (Irani *et al* 1992). It should be kept in mind that the scale of 1:50 which will be mentioned in the following sections of this thesis is only a nominal scale.

3.2.2 Instrumentation

In ERC's tests, four tri-axial load cells were used to measure the global loads and their moments on the cone. These load cells connected the cone structure to four steel columns that were firmly attached to the basin floor. Each of the three components of the global force, F_x, F_y, and F_z, was the sum of the corresponding components output from the four load cells.

The loads on the vertical neck of the ERC's structural models were measured by using four shear pins. Two pins were mounted together with their sensitive directions at right angles to each other to provide load measurements in both X and Y directions in the horizontal plane. X and Y components of the total load on the neck can be calculated from the individual shear pin measurements.

In IMD's tests, the models were similarly instrumented, but with three six-component dynamometers for global load measurements, and two dynamometers for neck load measurements.

In IME's tests, global, neck and collar loads were separately measured, each with a single dynamometer, respectively. Besides, the main cone facets were also instrumented to measure the loads on them. After the transformation of the facet loads from their local coordinate system to the global coordinate system, a vector sum of these facet loads and collar loads as well as neck loads should be very close to the global loads.

3.2.3 Coordinate System

The global coordinate system was defined as follows: the origin of X, Y, Z is located at the intersection of the vertical centerline and the waterline. The X-axis is positive in the direction of ice motion, the positive Z-axis is directed vertically upwards, and the direction of the Y-axis is such that X, Y, Z axes form a right-handed coordinate system.

The forces in all the three facilities were measured and expressed using this coordinate system. To be consistent, this thesis also uses this global coordinate system for analysis and numerical simulation.

3.3 Test Matrices

3.3.1 Overall Scope

From the previous experience in SCS tests, a set of parameters were identified as essential for detailed understanding of ice-MCS interaction and design consideration of ice loads on the proposed MCS prototypes. Some changes were made in the course of the test program, and the parameters finally tested are listed in Table 3.1.

In all the three facilities, some parameters related to test ice were also varied either on

purpose or due to the difficulties in the control of ice formation. These parameters include: ice floe thickness, ridge width and thickness, ice (floe and ridge) strength, etc.

Parameters Varied	ERC's Year One Tests	ERC's Year Two Tests	IME' Tests	IMD's Tests
Model scale	1:10	1:20	1:50	1:25, 1:50
Neck Size	Small, Large	Large	Small	Small, Large
Structural Orientation	No	No	Yes	No
Ridge Orientation	Yes	Yes	No	No
Ice Movement Rate	No	No	Yes	Yes

Table 3.1 Overall Scope of The Test Program

Some technical terms used in Table 3.1 and to be used in the remaining part of this thesis are defined as follows.

1. **Structural Orientation** means the direction of the structure's front facet with respect to the direction of ice motion. A total of three structural orientations were tested, viz.,
   A. *Face-on* Orientation: the front facet faces the ice motion.
   B. *Edge-on* Orientation: a cone's corner between two adjacent facets is head-on the impinging ice.
   C. *Intermediate* Orientation: the front facet is inclined at 15° to the face-on orientation.
2. **Ridge Orientation** means the orientation of the ridge longitudinal axis with respect to

the direction of the ice motion.

A. *Broadside* Orientation: the ridge longitudinal axis was perpendicular to the direction of ice motion.

B. *Oblique* (or Skewed) Orientation: ridge is inclined at an angle of 30° from the broadside orientation (the ERC tests).

3. Ice Movement Rate means ice speed in the ERC tests, and it is carriage's moving (forwards) speed in the IME tests and the IMD tests.

In the IME tests, all the three structure orientations were tested, while in the ERC and the IMD tests, only the face-on orientation was tested. All the ridges were tested in broadside orientation in the IMD and the IME tests, but five ridges inclined at a 30° oblique angle to the broadside orientation were also tested in the ERC series.

3.3.2 Tests Matrices

A total of 126 test runs including 31 ridges were performed in the three facilities: 8 runs with ice ridges and 4 runs with ice sheets in ERC's Year-One tests, and 8 ridges and 7 sheet runs for Year-Two tests; 14 ridges and 18 sheet runs for the IMD tests, and 15 ridges and 52 sheet runs for IME's tests. A brief test matrix for the Year-One and the Year-Two ERC tests is presented in Tables 3.2 and 3.3, respectively.

In Tables 3.2 and 3.3, three letters, Y, T, and R represent "year", 'test" and "run",

respectively. Thus Y1T1R1 means "run 1 of test 1 for Year-One tests". Since Y1T2R1 was aborted, it does not appear in Table 3.3. If not specified in Tables 3.2 and 3.3, all the ridges (usually 2) in each of the tests were embedded in the same ice sheet. All the tests conducted in ERC's ice basin (both the Year-One and the Year-Two tests) were carried out with an ice speed of 6 cm per second. This parameter is not listed in Tables 3.2 and 3.3.

Test No.	Neck Size	Ice Type	Ice Dimension (m)	Ridge Orientation	Test Duration (seconds)
Y1T1R1	Small	Sheet	0.33	-	93
Y1T1R2	Small	Ridge	3.5x1.00	Broadside	97
Y1T1R3	Small	Ridge	3.7x0.90	Broadside	270
Y1T2R2	Large	Sheet	0.34	-	10
Y1T2R3	Large	Ridge	4.5x0.95	Broadside	162
Y1T2R4	Large	Ridge	3.5x1.05	Broadside	202
Y1T3R1	Large	Ridge	3.5x1.10	Oblique 30°	200
Y1T3R2	Large	Sheet	0.27	-	92
Y1T3R3	Large	Ridge	3.5x1.25	Broadside	135
Y1T4R1	Large	Sheet	0.12	-	210
		Ridge	3.5x0.95	Oblique 30°	
Y1T4R2	Large	Ridge	2.5x0.95	Oblique 30°	280

Table 3.2 Test Matrix for ERC's Year-One Tests

Table 3.4 presents the matrices of IME's sheet ice tests, and Table 3.5 shows the matrices for IME's ridge tests. The tests with the 1:25 large neck model of the IMD series are

listed in Table 3.6 with the rest of the tests of this series given in Table 3.7.

Test No.	Ice Type	Ice Dimension (m)	Ridge Orientation	Test Duration (seconds)
Y2T1R1	Sheet	0.25		110
Y2T1R2	Sheet	0.25		26
Y2T2R1	Sheet	0.32		103
	Ridge	3.0x0.90	Oblique 30°	
Y2T2R2	Sheet	0.36		177
	Ridge	2.5x0.95	Oblique 30°	
Y2T3R1	Sheet	0.385		211
	Ridge	2.75x0.86	Broadside	
Y2T3R2	Ridge	2.17x0.90	Broadside	170
Y2T4R1	Sheet	0.41		155
	Ridge	2.6x1.17	Broadside	
Y2T4R2	Ridge	2.6x1.22	Broadside	120
Y2T5R1	Sheet	0.05		160
	Ridge	2.0x0.30	Broadside	
Y2T5R2	Ridge	2.0x0.27	Broadside	73

Table 3.3 Test Matrix of ERC's Year-Two Tests

A few items used in Tables 3.2 through 3.7 are defined as follows.

- *Ice Dimension* are thickness for ice sheets and width by thickness for ridges. The length of the ridges for each test facility equals its ice basin width. There are two numbers for

ridge thickness in Tables 3.5 through 3.7, the first one (outside the parentheses) is the total thickness including the thickness of the soft layer at the bottom of the ridges, and the second one (the number within parentheses), is the thickness of the ridge core. This will be further explained in the next section.

- *Scale Factor* in Tables 3.4 and 3.5 represents the ratio of the prototype's waterline diameter to the model's waterline diameter.
- *N* in column 6 of Table 3.5 means "not available" or "not measured"
- *Ice Sheet No.* in column 3 of Tables 3.4 and 3.5 indicates what tests share the same ice sheet, i.e., those tests share the common ice sheet for different test runs.
- *Ridge Type* in column 5 of Tables 3.6 and 3.7 identifies two different types of ridges which were constructed with "Dump Truck" and "Split Layer" techniques, respectively. The description of these two techniques are given in the next section.
- σ_{st} and σ_{sb} in columns 6 and 7 of Table 3.4 represent the flexural strength for sheet ice with top in tension and bottom in tension, respectively. The same definition applies to column 6 of Table 3.5. σ_{sb} was not measured for many of the IME tests.
- σ_{rt} and σ_{rb} in column 6 of Table 3.5 are the strength for ridges and have meanings parallel to σ_{st} and σ_{sb}. The values of σ_{rt} and σ_{rb} or σ_{st} and σ_{sb} are separated with a forward slash mark. No strength data were available for test C53.

Test No.	Structure Orient.	Ice Sheet No.	Ice Speed (cm/s)	Ice Thk. (cm)	σ_{st} (kPa)	σ_{sb} (kPa)	Test Duration (seconds)	Scale Factor
C01	Interm.	1	2.6	2.6	73	N	80	30
C02	Interm.	1	9.8	2.3	73	N	30	
C03	Interm.	1	4.8	2.3	73	N	30	
C04	Interm.	2	2.2	3.3	166	N	110	35.2
C05	Interm.	2	3.8	3.7	166	N	50	
C06	Interm.	2	6.2	3.7	166	N	20	
C07	Interm.	3	2.0	2.4	29	24	105	
C08	Interm.	3	4.0	2.3	29	24	45	
C09	Interm.	3	6.0	2.2	29	24	40	
C10	Interm.	4	2.2	4.0	67	58	118	
C11	Interm.	4	4.1	3.8	67	58	55	
C12	Interm.	4	6.1	4.1	67	58	30	
C13	Interm.	5	2.0	1.7	67	N	110	
C14	Interm.	5	4.3	1.6	67	N	55	
C15	Interm.	5	6.0	1.8	67	N	40	
C16	Face-on	6	6.0	3.4	72	96	150	32.9
C17	Face-on	7	6.0	2.4	122	73	50	
C18	Face-on	7	6.1	2.1	59	N	30	
C19	Face-on	7	6.2	2.3	21	N	30	
C20	Face-on	8	5.9	5.7	37	N	70	
C21	Face-on	8	5.8	5.7	17	N	60	
C22	Face-on	9	5.9	3.4	134	N	40	32.3
C23	Face-on	9	6.0	3.3	47	N	30	
C24	Face-on	9	5.8	3.4	25	N	30	
C25	Face-on	10	6.0	4.5	125	N	35	
C26	Face-on	10	6.0	4.6	102	N	40	

Table 3.4 Test Matrix for IME's Ice Sheet Tests

Test No.	Structure Orienta.	Ice Sheet No.	Ice Speed (cm/s)	Ice Thk. (cm)	σ_{st} (kPa)	σ_{sb} (kPa)	Test Duration (seconds)	Scale Factor
C27	Face-on	10	6.0	4.7	82	N	50	32.3
C28	Face-on	11	5.7	4.4	81	63	35	
C29	Face-on	11	5.7	4.2	45	N	45	
C30	Face-on	11	5.7	4.5	26	N	45	
C31	Edge-on	12	5.7	2.4	56	22	40	
C32	Edge-on	12	5.7	2.0	27	9	40	
C33	Edge-on	12	5.7	1.8	17	3	40	
C34	Edge-on	13	5.7	3.5	112	71	60	
C35	Edge-on	13	5.7	3.4	44	64	40	
C36	Edge-on	13	5.8	3.4	25	13	75	
C37	Edge-on	14	6.2	5.6	60	41	40	
C38	Edge-on	14	5.9	5.6	40	40	110	
C39	Edge-on	15	6.2	4.9	44	39	45	
C40	Edge-on	15	6.2	5.1	15	14	40	
C41	Edge-on	15	5.9	5.4	12	14	50	
C42	Face-on	16	6.0	3.3	41	40	45	
C43	Interm.	16	6.1	3.0	41	40	45	
C44	Edge-on	16	6.0	3.3	41	40	40	
C50	Face-on	21	6.2	2.8	21	11	50	
C54	Face-on	23	6.1	4.2	80	40	120	
C55	Face-on	24	5.8	3.6	76	27	40	
C56	Face-on	24	5.9	3.5	49	24	50	
C57	Face-on	24	5.9	3.6	25	10	40	
C60	Face-on	26	6.0	3.0	36	9	50	
C61	Interm.	26	5.9	3.1	36	9	40	
C62	Edge-on	26	6.0	3.1	36	9	40	

Table 3.4 Test Matrix for IME's Ice Sheet Tests (cont'd)

Test No.	Struc. Orien.	Ice Speed (cm/s)	Ice Type	Ice Dimension (cm)	σ_{it}/σ_{ib} or σ_{rt}/σ_{rb} (kPa)/(kPa)	Test Dur. (sec.)	Scale Fac.
C45	Edge on	5.9	Ridge	58 x 16 (9)	70/N	120	32.3
			Sheet	2.6	12/7		
C46	Edge on	6.1	Ridge	72 x 15(10)	95/N	100	
			Sheet	2.6	17/11		
C47A	Edge on	5.9	Ridge	67 x 27 (8)	265/N	90	
			Sheet	2.9	20/7		
C47B			Ridge	109 x 25 (8)	114/N	60	
C48	Face on	5.9	Ridge	67 x 13 (7)	156/50	55	
			Sheet	3.0	20/5		
C49	Face on	5.8	Ridge	105 x 16 (8)	155/51	55	
			Sheet	3.4	20/5		
C51	Face on	6.2	Ridge	63 x 17 (8)	82/171	60	
			Sheet	3.0	21/11		
C52	Face on	5.9	Ridge	60 x 15 (6)	137/199	70	
			Sheet	3.2	8/3		
C53	Face on	5.9	Ridge	100 x 20 (9)	N/N	60	
			Sheet	3.0	8/3		
C58	Face on	6.0	Ridge	64 x 25 (6)	334/581	70	
			Sheet	3.7	46/11		
C59			Ridge	100 x 15 (10)	160/110	70	
C63	Edge on	6.0	Ridge	64 x 18 (5)	345/238	50	31.2
			Sheet	3.7	48/22		
C64			Ridge	100 x 20 (8.5)	130/120	70	32.3
C65	Edge on	6.0	Ridge	62 x 35 (9)	231/208	70	31.2
			Sheet	3.3	53/23		
C66			Ridge	100 x 42 (12)	98/125	70	

Table 3.5 Test Matrix of IME's Ridge Tests

Test No.	Ice Speed (cm/s)	Ice Type	Ice Dimension (cm)	Ridge Type	Test Duration (seconds)
M41	1	Sheet	16.0		130
M42	6	Sheet	16.0		80
M43	4	Sheet	16.0		120
M44	4	Sheet	16.0		150
		Ridge	100 x 43.5	Split Layer	
M45	4	Sheet	16.0		150
		Ridge	100 x 32.7	Split Layer	
M46	4	Sheet	16.4		50
M47	4	Sheet	16.4		150
		Ridge	100 x 50 (33.5)	Dump Truck	
M51	1	Sheet	9.5		160
M52	6	Sheet	9.5		80
M53	7	Ridge	100 x 36.8	Split Layer	150
		Sheet	9.5		120
M54	4	Sheet	9.5		150
		Ridge	100 x 50 (28.0)	Dump Truck	
M61	4	Sheet	12.4		150
		Ridge	100 x 33.4	Split Layer	
M62	4	Sheet	12.4		350
M63	1	Sheet	12.4		115
M64	6	Sheet	12.4		120
M65	4	Sheet	12.4		150
		Ridge	100 x 50 (23.8)	Dump Truck	

Table 3.6 Test Matrix for IMD's Tests with 1:25 Scale Large Neck Model

Test No.	Ice Speed (cm/s)	Ice Type	Ice Dimension (cm)	Ridge Type	Test Duration (Seconds)
1:25 Small Neck Model					
M31	1	Sheet	15.8		125
M32	6	Sheet	15.8		100
M33	4	Ridge	100 x 42.0	Split Layer	150
	4	Sheet	15.8		125
M34	4	Sheet	15.8		150
		Ridge	100 x 32.0	Split Layer	
M35	4	Sheet	14.8		50
M36	4	Sheet	14.8		150
		Ridge	100 x 50 (30)	Dump Truck	
M37	4	Sheet	14.8		150
		Ridge	100 x 50 (36.4)	Dump truck	
1:50 Large Neck Model					
M71	1	Sheet	16.0		450
M72	6	Sheet	16.0		60
M73	4	Sheet	16.0		80
M74	4	Sheet	16.0		150
		Ridge	100 x 32.9	Split Layer	
M75	4	Sheet	16.0		150
		Ridge	300 x 32.9	Split Layer	
M76	4	Sheet	16.4		120
M77	4	Sheet	16.4		150
		Ridge	100 x 50 (24)	Dump Truck	

Table 3.7 Test Matrix of IMD's Tests with 1:25 Scale Small Neck Model and 1:50 Scale Large Neck Model

3.4 Tested Ice

3.4.1 The Ice for ERC's Tests

Saline ice was used for the ERC tests. The ridges were constructed utilizing a layering process in which four techniques were used: spray ice, flooding between raised edges, piling up and flooding of snow, and layering down blocks of ice pieces (Metge and Weiss 1989, Metge and Tucker 1990).

Flexural strength and elastic modulus of sheet ice and ridge ice were determined by a number of in situ beam tests. The beams were loaded downwards to submerge and break; therefore, they failed in tension at the bottom. The measured strengths represented by σ_{sb} for sheet ice and σ_{rb} for ridge ice are given in the column 3 of Table 3.8. The related elastic moduli, E_r for ridge ice and E_s for sheet ice, are given in column 4 of the same table. Ridge strength was also measured by the "ridge fragment lift" tests in which a ridge fragment was lifted out of the water until it broke under its own weight. In this case, the ridge failed in tension at the top. This strength, represented by σ_{rt}, is listed in the column 5 of Table 3.8.

Sheet ice density (ρ_s), buoyancy (ρ_b) and friction coefficient μ (between ice and a painted steel surface) were also measured for each test (except for ERC's tests Y2T5R1 and Y2T5R3), and are listed in Table 3.8.

Test No.	Ice Type	σ_{rb}, σ_{sb} (kPa)	E_r , E_s (MPa)	σ_{rt} (kPa)	Ice Salinity (ppt.)	Ice Temp. (°C)	ρ_s/ρ_b (kg/m³)/ (kg/m³)	μ
Y1T1R1	Sheet	165	1136		5.6	-5.0	945/90	.083
Y1T1R2	Ridge	128	352	154	6.0	-5.0		
Y1T1R3	Ridge	116	301		7.3	-5.0		
Y1T2R2	Sheet	183	836			-4.0	913/120	.133
Y1T2R3	Ridge	182	349	115	6.0	-2.7		
Y1T2R4	Ridge	162	295	170	7.3	-3.7		
Y1T3R1	Ridge	86	271	114	6.0	-6.0	932/102	.036
Y1T3R2	Sheet	249	1129			-5.0		
Y1T3R3	Ridge	150	281	113	7.3	-4.0		
Y1T4R1	Sheet	159	1591			-2.0	965/89	.038
	Ridge	119	580	55		-2.0		
Y1T4R2	Ridge	86	106	115		-2.0		
Y2T1R1	Sheet	50	203		10.0	-10.0	917/100	
Y2T1R2	Sheet	50	203		10.0	-10.0		
Y2T2R1	Sheet	35	288		7.8	-2.0	910/103	0.071
	Ridge	25	50		8.0	-2.0		
Y2T2R2	Sheet	141	1154		7.8	-2.0		
	Ridge	40	80	83	3.4	-2.0		
Y2T3R1	Sheet	135	569		19		930/88	0.078
	Ridge	138	659	157		-2.0		
Y2T3R2	Ridge	108		177		0.0		
Y2T4R1	Sheet	141	853		15		930/120	0.085
	Ridge	62	187	122		-4.0		
Y2T4R2	Ridge	39	114	132		-3.0		
Y2T5R1	Sheet				36	-1.0		
	Ridge	20						
Y2T5R2	Ridge	41	263					

Table 3.8 Ice Properties for the ERC Tests

3.4.2 The Ice for IME's and IMD's Tests

IMD used the EG/AD/S model ice (see Timco, 1986 for details), and IME used a modified version of the EG/AD/S model ice (Lau *et al* 1993).

The two methods used in IMD ridge construction are the Split Layer (SL) and the Dump Truck (DT) techniques. In the SL technique, several layers of level ice strips were laid one over the other to form a ridge. The DT technique requires dumping small ice pieces into the ridge area to form a ridge comprised of randomly orientated pieces of broken ice. Besides the DT technique, IME also utilized a combination of the DT and the layering techniques, i.e., dumping a layer of ice pieces and allowing them to solidify before the next layer was dumped. In both IME's ridges and IMD's DT ridges, there was a relatively large unconsolidated layer at the lower part of a ridge. In Tables 3.5 through 3.7, the ridge thickness includes this unconsolidated layer, and the numbers in parentheses are the thicknesses of the consolidated layer.

The ice properties for IMD's tests are given in Table 3.9, and those for IME tests were included in Tables 3.4 and 3.5. In Tables 3.4, 3.5, 3.8, and 3.9, σ_{sb} and σ_{st} represent flexural strength of sheet ice in tension at the bottom and at the top, respectively, and ρ_r and ρ_b are the ridge ice density and buoyancy, respectively. The elastic moduli for IMD's ice can be determined by the ratio of E_s/σ_{st} given in column 4 of Table 3.9. IME's test report does not give any information on the moduli. According to Timco (1986), a value of 2150 might be chosen for the ratio of E_s/σ_{st}.

Test No.	σ_{sb} (kPa)	σ_{st} (kPa)	E_r/σ_{st}	ρ_s/ρ_b (kg/m^3)/(kg/m^3)	σ_{rb} (kPa)	σ_{rt} (kPa)	E_r (MPa)	ρ_r/ρ_{rb} (kg/m^3)/(kg/m^3)	μ
M31	44.4	79.8	4810	916/86					0.11
M32	44.1	79.4	4810	916/86					0.11
M33	43.6	78.7	4810	916/86	99.3	103.7	77.0	899/104	0.11
M34	42.5	77.1	4810	916/86	48.7	77.7	74.5	904/98	0.11
M35	29.4	42.4	3796	921/81					0.09
M36	29.3	42.3	3796	921/81	16.2	16.8	5.9		0.09
M37	28.9	42.1	3796	921/81	32.5	29.3	4.7		0.09
M41	41.1	74.4	5212	914/88					0.09
M42	40.6	73.5	5212	914/88					0.09
M43	40.4	72.9	5212	914/88					0.09
M44	40.2	72.3	5212	914/88	112.2	126.2	105.4	890/112	0.09
M45	39.7	71.2	5212	914/88	69.2	109.8	206.7	901/101	0.09
M46	19.7	39.0	4615	923/79					0.09
M47	19.6	38.8	4615	923/79	26.5	34.5	6.6		0.09
M51	30.7	43.4	3002	928/74					0.09
M52	30.2	41.6	3002	928/74					0.09
M53	29.9	40.8	3002	928/74	80.5	84.4	183.4	905/97	0.09
M54	27.3	32.5	3002	928/74	10.9	20.1	2.4		0.09
M61	22.5	36.5	3213	919/84	65.5	84.4	160.0	896/107	0.08
M62	22.5	36.0	3213	919/84					0.08
M63	22.5	35.4	3212	919/84					0.08
M64	22.5	35.1	3213	919/84					0.08
M65	22.5	34.2	3213	919/84	12.0	17.1	11.0		0.08
M71	33.7	70.2	8494	918/84					0.08
M72	33.2	69.7	8494	918/84					0.08
M73	32.8	69.3	8494	918/84					0.08
M74	32.5	69.0	8494	918/84	135.5	111.7	282.2	897/106	0.08
M75	32.0	68.5	8494	918/84	135.5	111.7	282.2	897/106	0.08
M76	18.7	42.8	5383	920/82					0.08
M77	18.4	41.9	5383	920/82	12.7	15.8	9.6		0.08

Table 3.9 Ice Properties of IMD Tests

3.5 Test Results

The time history of the measured forces and moments for these tests were documented in four test reports (Metge and Weiss 1989, Metge and Tucker 1990, Irani *et al* 1992, Lau *et al* 1993). The maximum values of the forces on tested structural models are listed in Tables 3.10 through 3.12.

The following are some notes for these tables.

- In Tables 3.11 and 3.12, the test numbers followed by the word R in column 1 of these tables are ridge tests.

- F_{mx}, F_{my}, and F_{mz} represent the X, Y, and Z components of the maximum global loads, respectively; f_{mx}, f_{my}, and f_{mz} denote the X, Y, and Z components of the maximum neck loads, respectively; g_{mx}, g_{my}, and g_{mz} represent the X, Y, and Z components of the maximum collar loads, respectively.

- The numbers given in theses tables are the absolute values of the force magnitudes. Under the coordinate system defined in Section 3.2.3, the Z (vertical) components of the loads are negative in sign because their direction (downwards) is opposite to the positive direction of Z axis (upwards). Similarly, the sign for the Y component also varies from test to test.

- A few numbers presented in Table 3.10 are different from those given in the summary of the ERC test reports. The summary of the maximum forces given in ERC's test reports contains a few errors. If the numerical values from the summary, data records, and plotting were the same or were very close, the values given in ERC's summary are adopted here. Otherwise, the values from the plotting and/or data records are given in Table 3.10 with those from ERC's summary included within a parenthesis.

- In Tables 3.11 and 3.12, the numbers labelled with a * are from those records of force history which have a shape jump and give an un-reasonably large value of the maximum forces.

- In some IME tests, ice pieces dropped into the inside of the cone through the open panel where the far back facet should have been located; this caused ice jamming on the supporting frame and affected the output of the main dynamometer which measured global loads, thus causing some errors. To eliminate these errors, as suggested by the IME test team (Irani *et al* 1992), the sum of the forces on the facets, collar, and neck were taken as global forces.

Test No.	Ice Type	Maximum Global Forces			Maximum Neck Forces	
		F_{mx} (kN)	F_{my} (kN)	F_{mz} (kN)	f_{mx} (kN)	f_{my} (kN)
Y1T1R1	Sheet	40	7.9 (0)	50	1.5	1.5
Y1T1R2	Ridge	130	20 (10)	150	7.0	2
Y1T1R3	Ridge	103	33.4 (15)	185.8 (130)	18.0	7.5 (2)
Y1T2R2	Sheet	10	8	8	0.8	0.8
Y1T2R3	Ridge	160	30 (10)	190		
Y1T2R4	Ridge	149.2 (145)	60	170	8.3	1.0
Y1T3R1	Ridge	94.3 (92)	22.2 (18)	116	13.5	3.0 (1.5)
Y1T3R2	Sheet	17	11 (0)	19		
Y1T3R3	Ridge	125	13	138	6.5	2.0 (0)
Y1T4R1	Sheet	12	0	15	0	0
	Ridge	32	15 (12)	40	2	0
Y1T4R2	Ridge	40	21.8 (5)	50	3.5	1.22 (0)
Y2T1R1	Sheet	10	2.1	12.6 (11)	0.7	0.2 (0)
Y2T1R2	Sheet	3.2 (1.5)	6	4	0.5 (0.8)	0.75 (0.3)
Y2T2R1	Sheet	19	7	22	5	0
	Ridge	63	13	40	18	7
Y2T2R2	Sheet	20	5	20	8	2
	Ridge	72	19.6 (18)	60	34	9 (7)
Y2T3R1	Sheet	30	5	38	2.5	0
	Ridge	66.5 (68)	25.9 (28)	72 (70)	19	7.1 (2)
Y2T3R2	Ridge	68	43	83	13	17
Y2T4R1	Sheet	30	0	35	5	0
	Ridge	63	17 (0)	75	6.8	1.0 (0.5)
Y2T4R2	Ridge	83	20	100 (97)	20.5	4 (0.5)
Y2T5R1	Sheet	2	0	4	0	0
	Ridge	7	2.4 (0)	8.5	0.8 (1)	0
Y2T5R2	Ridge	12	2	15	0.3 (0)	0

Table 3.10 ERC Test Results

Test No.	Maximum Global Forces			Max. Neck Forces			Max. Collar Forces		
	F_{mx} (kN)	F_{my} (kN)	F_{mz} (kN)	f_{mx} (N)	f_{my} (N)	f_{mz} (N)	g_{mx} (N)	g_{my} (N)	g_{mz} (N)
C01	0.24	0.07	0.25	30	10	10	40	10	20
C02	0.23	0.08	0.24	40	0	0	30	10	10
C03	0.22	0.05	0.25	30	10	0	40	10	20
C04	0.37	0.08	0.42	40	10	10	40	10	20
C05	0.32	0.12	0.37	30	10	10	30	20	10
C06	0.26	0.13	0.31	30	30	0	30	10	10
C07	0.16	0.05	0.20	10	0	0	20	10	10
C08	0.18	0.05	0.19	10	0	0	20	0	10
C09	0.19	0.06	0.21	10	0	0	40	10	10
C10	0.45	0.11	0.51	40	10	10	50	20	20
C11	1.28 *	0.17	1.11	100 *	30	0	490 *	70	210 *
C12	0.49	0.14	0.60	30	10	0	40	10	20
C13	0.12	0.06	0.16	10	0	10	10	0	10
C14	0.10	0.03	0.13	0	0	0	10	0	0
C15	0.10	0.04	0.13	10	0	0	10	0	0
C16	0.73	0.10	0.61	120 *	10	10	200 *	10	80 *
C17	0.20	0.07	0.25	40	0	10	50 *	10	20
C18	0.16	0.06	0.19	10	10	0	20	0	10
C19	0.18	0.03	0.20	10	0	0	30	0	0
C20	0.63	0.18	0.71	100 *	10	10	120 *	30	50
C21	0.60	0.14	0.62	100 *	10	10	110 *	10	50
C22	0.36	0.13	0.49	30	10	0	30	30	20
C23	0.37	0.13	0.40	40	20	10	90 *	10	40
C24	0.39	0.07	0.39	80 *	10	10	60	10	30
C25	1.81 *	0.30	1.41 *	280 *	20	10	310 *	60	140 *
C26	0.95	0.40	0.98	50	10	0	270 *	10	110 *
C27	0.85	0.24	0.89	50	10	10	70	10	30
C28	0.54	0.17	0.58	50	10	10	90 *	10	40
C29	0.71	0.12	0.65	40	10	10	200 *	10	10
C30	0.37	0.09	0.44	30	0	10	30	10	10
C31	0.10	0.04	0.17	0	0	0	10	0	10
C32	0.09	0.03	0.13	0	0	0	10	0	0
C33	0.08	0.04	0.13	0	0	0	10	0	0

Table 3.11 IME Test Results

Test No.	Maximum Global Forces			Max. Neck Forces			Max. Collar Forces		
	F_{mx} (kN)	F_{my} (kN)	F_{mz} (kN)	f_{mx} (N)	f_{my} (N)	f_{mz} (N)	g_{mx} (N)	g_{my} (N)	g_{mz} (N)
C34	0.25	0.11	0.35	20	10	0	20	10	10
C35	0.24	0.15	0.31	20	10	0	30	10	10
C36	0.19	0.05	0.28	10	0	10	20	0	10
C37	0.67	0.14	0.80	50	10	10	50	20	30
C38	0.67	0.18	0.83	70 *	40	10	80 *	20	40
C39	0.42	0.08	0.57	30	10	0	40	10	20
C40	0.35	0.09	0.45	20	10	10	30	10	20
C41	0.27	0.05	0.41	20	10	20	30	10	10
C42	0.24	0.04	0.22	10	0	0	20	10	10
C43	0.28	0.07	0.27	10	0	10	20	10	10
C44	0.18	0.02	0.18	10	0	0	10	0	10
C45 R	0.53	0.15	0.60	0	0	0	10	10	10
C46 R	0.75	0.31	0.82	0	0	0	10	10	10
C47A R	0.78	0.21	0.74	0	0	0	10	0	10
C47B R	0.93	0.21	1.02	0	0	0	10	0	0
C48 R	0.52	0.08	0.42	10	0	0	20	0	10
C49 R	0.90	0.23	0.78	80 *	10	50	60 *	10	20
C50	0.34	0.04	0.29	10	0	10	10	0	0
C51 R	1.11	0.35	0.91	10	0	0	10	10	20
C52 R	0.96	0.3	0.80	10	10	0	60	50	30
C53 R	1.28	0.47	1.04	10	0	0	20	10	10
C54	0.71	0.16	0.57	50	10	60 *	50	20	20
C55	0.44	0.08	0.35	20	0	10	30	10	10
C56	0.44	0.08	0.34	20	0	10	30	10	10
C57	0.43	0.07	0.38	20	0	20	20	0	10
C58 R	1.57	0.37	1.17	20	10	30	30	10	10
C59 R	2.02	0.40	1.53	10	0	10	40	10	20
C60	0.32	0.05	0.27	10	0	0	20	0	10
C61	0.30	0.06	0.24	10	0	10	20	10	10
C62	0.20	0.05	0.20	10	0	0	10	0	10
C63 R	0.85	0.25	0.79	20	10	10	20	0	10
C64 R	1.17	0.26	1.17	30	20	10	40	20	50
C65 R	0.98	0.34	0.92	10	0	0	10	10	10
C66 R	2.17	0.56	1.77	20	10	10	50	20	20

Table 3.11 IME Test Results (cont'd)

Test No.	Maximum Global Forces			Maximum Neck Forces		
	F_{mx} (kN)	F_{my} (kN)	F_{mz} (kN)	f_{mx} (kN)	f_{my} (kN)	f_{mz} (kN)
M31	4.52	0.81	5.46	0.6	0.08	0.07
M32	5.18	1.25	6.06	0.49	0.05	0.06
M33	5.32	1.29	6.65	0.51	0.06	0.06
M33 R	21.07	1.80	20.75	2.08	0.18	1.27
M34 R	14.57	1.38	14.92	0.74	0.15	0.09
M35	3.42	0.60	4.22	0.36	0.02	0.03
M36 R	9.09	2.25	10.92	1.34 *	0.13	0.19
M37 R	12.43	1.91	12.60	1.43 *	0.46 *	0.18
M41	5.25	1.01	5.37	0.33	0.07	0.05
M42	6.27	1.35	6.57	0.40	0.06	0.06
M43	6.54	1.39	6.94	0.48	0.08	0.06
M44 R	25.51	3.27	23.5	2.01	1.17 *	0.32
M45 R	13.96	1.58	12.69	1.10	0.26	0.25
M46	5.08	0.72	5.07	0.31	0.08	0.07
M47 R	14.84	3.09	13.47	2.84	0.41	0.55
M51	2.16	0.34	2.17	0.10	0.03	0.02
M52	2.38	0.36	3.35	0.45 *	0.04	0.04
M53	2.25	0.34	2.26	0.21	0.04	0.03
M53 R	5.13	0.36	4.74	0.22	0.05	0.03
M54 R	7.68	2.10	7.60	1.19	0.46	0.27
M61 R	10.86	1.01	10.36	1.02	0.16	0.22
M62	3.08	0.65	3.28	0.25	0.04	0.04
M63	2.96	0.25	2.85	0.21	0.03	0.02
M64	3.26	0.45	3.46	0.19	0.03	0.03
M65 R	8.40	1.61	8.83	1.21	0.35	0.24
M71	8.86	1.94	4.10	0.98	0.38	0.13
M72	9.99	2.25	5.80	1.01	0.33	0.13
M73	10.40	2.33	5.56	0.98	0.45	0.14
M74 R	15.17	2.48	14.89	2.83	2.58	0.59
M75 R	19.76	1.90	19.70	2.24	1.08	4.28 *
M76	6.34	1.50	3.68	0.97	0.23	0.12
M77 R	9.14	2.91	7.98	3.82	0.98	0.47

Table 3.12 IMD Test Results

Chapter 4 Analysis of the Tests

This chapter consists of two parts. The first part concerns the interaction mechanism and the causes for the maximum ridge loads, and are presented in Sections 4.1 and 4.2, respectively. The problem about the ratio of the vertical component to the horizontal component of maximum ridge load is also addressed in Section 4.2. Sections 4.3 and 4.4 comprise the second part that discusses the effects of various parameters on the cracking pattern and ice loads. The effects of ridge width, structural (or ridge) orientation, and neck size on ridge forces as well as ridge crack pattern are analyzed in Section 4.3. Section 4.4 focuses on the analysis of the effects of structural orientation and neck size on the sheet ice forces.

4.1 Typical Interaction Scenario

The time history records of the ice forces experienced by the MCS models were compared with the time-synchronized output of a set of video cameras. Several modes of ice sheet and ridge failures have been identified from the video records and the information given in the test reports (Metge and Weiss 1989, Metge and Tucker 1990, Irani *et al* 1992, Lau *et al* 1993) and are summarized in this section.

Following a brief description of the sheet ice failure process in subsection 4.1.1, three failure patterns of the tested ridges will be presented in subsections 4.1.2, 4.1.3, and 4.1.4,

respectively. These descriptions are mainly based on the ERC and IMD tests.

4.1.1 The Process of Sheet Ice and MCS Interaction

The typical process of ice sheet failure is described as follows:

1. When an ice sheet contacts the structure and the sheet begins to be slightly deflected upwards, a pair of radial cracks initiate from the edges (or corners) of the ice sheet in contact with the front facet, forming a series of three truncated wedges against the front facet and the two front-side facets, respectively. This interaction usually generates a local peak value of global sheet ice force on the structure. After this initial crack, the global force may sharply drop to a lower level.
2. As the ice sheet continues to move forwards, it is further deflected upwards and the force continues to increase. At a certain stage, one or more circumferential crack(s) is (are) formed. The global force again drops from another local peak value.
3. The broken ice pieces gradually ride up on the cone. During this period of time, some large ice pieces may also be broken into smaller pieces some of which may fall down either on the approaching ice sheet or into the water. The force record is quite flat or gently increasing.
4. As the above process repeats more or less in a regular rhythmic manner, the ice pieces in front of the structure gradually accumulate to form a rubble pile which helps to prop some larger ice pieces and make them ride up so high that the top of the neck can be reached. This event together with the ongoing cracking process may produce the

maximum global ice sheet force.

The above interaction process is typical only for ERC tests, IMD 1:25 model tests, and part of IME tests with the structural model in face-on orientation. Even in these tests some different events were observed. For instance, in the ERC test Y2T3R1 (sheet ice test) in which the ice sheet had a straight leading edge, the initial crack was a circumferential crack instead of radial crack(s). The ice used in the IMD 1:50 model tests was softer, and the cracks were much closer to one another, forming smaller pieces, and lowered the ride-up height. The ice failed in a mixed mode of shearing and crushing and the structural model appeared to plough its way through the ice sheet with a narrow broken channel behind it.

For a structural model in edge-on orientation, as that in the IME tests, its front edge acted like an inclined wedge to initiate a radial crack. As the ice sheet continued moving, two truncated ice wedges (or more) rode up on the two front facets, forming circumferential cracks. The cone's two front facets were fully covered by small ice pieces which were clearly demarcated in two groups by the front edge line of the structure.

4.1.2 Ridge Failure Pattern I

The failure process described below generally applies for those ridges with high strength. It is believed that this would be the predominant failure pattern for multi-year ridges. The failure patterns of most of the ridges tested in the ERC's basin and the ridges of IME's tests C51, C53,

C58, and C59 fall in this category.

The interaction events described below give the sequence of the ice cracking and clearing process:

1. Cracking of the Sheet ice in Font of a Ridge

   When a ridge with its surrounding ice sheet approaches the structural model, the ice sheet in front of the ridge (between the ridge and the structure) breaks, but does not necessarily separate from the ridge. In some cases, a circumferential crack could reach the front edge of the ridge, resulting in limited local separation of part of the ice sheet from the ridge.

2. Indentation of the Structure into the Lower Edge of the Ridge

   As the ridge with the broken ice sheet moves forward, the lower part of the structure contacts the lower edge of the ridge and begins to indent into it. Both the horizontal and the vertical components of the global force increase sharply to a magnitude much higher than the sheet ice force. In the meantime, the ice sheet between the ridge and the structure, if attached to the ridge, may separate and break. The lower part of the structure (the main cone body) is usually covered with the broken ice pieces formed during the earlier ice sheet cracking process and are pushed up by the ice ridge movement.

3. Initial Cracking

   As the indentation of ice ridge progresses, the generated vertical force becomes large enough to lift the ridge slightly, and causes an initial crack. The crack usually starts at

or close to the center line of the structure's front facet or at one of the facet corners, and extends across the ridge width. Sometimes the crack even extends into the ice sheet behind the ridge. Although the lifting up of the ridge was discernible, no significant rotation was noticed up to this stage. The ice pieces riding up on the structure's surface might partly fall down when the ridge's initial crack occurs. The force associated with this cracking process kept on increasing until the crack occurred; the force history usually had a progressive increase followed by a sharp decrease. The peak value of this force could be the maximum force experienced by the structure, or just a local peak.

4. Hinge Cracking

As the ridge and sheet continued to move further forwards, the initial crack quickly widens and extends further into the ice sheet behind the ridge. In some cases, the crack propagates even into the next ridge which was several meters apart from the interacting ice ridge. The ice pieces located in the front of the structure are pushed up further. The ridge itself becomes noticeably deflected upwards. When this deformation process progresses to a certain stage, a pair of cracks, usually termed as *hinge cracks*, occur in the ridge at some distance away from the center line (or the initial crack). During this hinge cracking process, the surrounding ice sheet also cracks. The hinge cracks together with a long circumferential crack formed behind the ridge generate two large ridge fragments. In many cases, the fragments have a piece of ice sheet segment attached to their trailing edges. In other cases, the ridge segments are separated from the sheet. The global ice force continues to increase during this failure process and would reach its maximum value at the moment before or when the hinge cracks occurred. Again, a

sudden increase in the force history is associated with the hinge crack occurrence, and then the force levels off.

5. Further Cracking and Clearing Process

After the hinge cracking, the cracked ridge and ice pieces are pushed upwards to a considerable height and rotate around both X and Y axes. The ridge fragments and the attached sheet segments may crack again. As the motion continues, the ridge fragments and some sheet ice pieces are pushed further forwards and upwards to ride up on the structure. During this process, two noticeable events may occur. The first event occurs for the case in which the ridge fragments and large ice pieces are cracked into smaller pieces during the riding-up process. In this case, the pieces get cleared by sliding to the back of the structure or back on the ice in front of the structure. The force exerted on the structure for this case may be lower than the peaks for the hinge or the initial crack process. The second event occurs for the case when some ridge fragments and sheet ice pieces still remain too large to be cleared away. These large sheet ice pieces and ridge fragments ride up the structure to such a height that they reach the top of the neck (recorded highest one in ERC's Year-One tests was about a meter above the top of the neck). Under some circumstances, a few large ridge fragments and ice pieces could be jammed in front of the neck and could rest on the main cone surface for a while. This in turn prevents the clearing the ice pieces that ride up the front facets of the structure and makes the ice sheet behind more difficult to crack. As a result, this would generate the maximum force acting on the structure.

The above description is general. It does not cover some particular events for some of the particular test runs. For instance, the hinge cracks in ERC test Y1T1R3, Y1T2R3 and Y2T4R2 were followed by a secondary radial crack, but their overall failure process is different from that presented in the next subsection.

Compared with the interaction process for a ridge against a SCS described in Section 2.1.1 of Chapter 2, this ridge failure pattern has some similarities to that for the case of SCSs. This means the faceted surface may not significantly affect the failure process of a ridge.

4.1.3 Ridge Failure Pattern II

This failure pattern was mainly observed from IMD's Split Layer (SL) ridge tests. The ridges for ERC tests Y2T5R1 and Y2T5R2 and the ridge for IME's test C48 had a similar failure pattern. Before the initial cracks are formed, the interaction process for these ridges is basically similar to that described in the last subsection. The description being given here focuses on what is different, i.e. the process of ridge cracking.

When the structure starts deflecting a ridge, the ridge slightly rides up on the structure's front facet. Then, a pair of cracks begin at the two corners of the front facet and run gradually away from each other till they cross the width of the ridge. Almost simultaneously, a pair of hinge cracks are formed, each on one side of the structure, at an approximate distance of 1 meter from the corner of the front facet (in the case of IMD tests). This pair of hinge cracks

propagate and trend to converge toward one another till they meet in the sheet behind the ridge. The portion of the crack in the ice sheet is parallel to and very close to the trailing edge line of the ridge. The radial and hinge cracks break the central section of the ridge into three pieces, one with a trapezoidal shape on the front facet and the other two triangular pieces on either side of the front facet.

As the ice moves forwards further, the trapezoidal piece is pushed up on the front facet and may ride up to reach the neck. The two triangular pieces are pushed up a little, and then slide down on the two front-side facets and finally fall downstream. Although some complex riding-up and jamming events were observed in the IMD tests, the clearing process is, generally speaking, smoother than that for the Failure Pattern I.

4.1.4 Ridge Failure Pattern III

As Table 3.9 indicates, the Dump Truck ridges tested in the IMD tank were weaker than the Split Layer ridges. These weak ridges failed in a different manner. The ridge for IME test C64 may also fall in this category.

The Dump Truck ridges had a thick unconsolidated layer at the bottom. When the structure begins to contact a ridge, it indents the lower part of the ridge and the ridge bottom experiences a crushing process. This process continues till the interaction force becomes large enough to deflect the ridge upwards.

As the ridge get deflected, a pair of radial cracks form and extend from the two corners of the front facet to the trailing edge of the ridge. At almost the same moment, a circumferential crack occurs in the ridge. These cracks break three relatively small pieces away from the ridge. The remaining portion of the ridge is pushed forwards by the ice sheet behind it; the upward moving ridge in turn pushes the ridge pieces up on the structure. A little later, the structure once again contacts the new local front edge of the ridge and forms another circumferential crack which may still be within the ridge, or may extend into the interface of the ridge and the ice sheet behind. This crack breaks once again more pieces away from the ridge. This process may repeat once or twice, depending on the ridge's consolidation condition and its width. The maximum force is usually reached when the structure is fully covered by ice pieces and a fresh cracking process was about to start or is progressing.

4.2 Ridge Crack Loads and Maximum Loads

Previous SCS tests (Lewis and Croasdale 1978) indicated that *the peak (maximum) force occurred when the ridge was cracked the second time (hinge cracks) at some distance away from the first crack (center or radial crack)*. It was stated in section 4.1 that the maximum force for a MCS model, especially for those ERC tests, could occur during any of the three events: initial cracking, hinge cracking, and clearing process. To clarify the relationship between the maximum load and crack loads, the video and computer records and the plots of force history given in the test reports have been reviewed and checked. The linking of the ice failure events and their corresponding loads through the recorded test time has been recognized for the ERC tests and

the IMD tests. Because the link between load history and crack events has not been identified for the IME tests, only the results of the ERC and IMD tests will be analyzed in this section.

4.2.1 What Causes the Maximum Loads ?

Table 4.1 lists the ERC test data that show the initial (radial) crack force, hinge crack force, the maximum force as well as the interaction events which gave rise to the maximum loads. The parallel information for the IMD tests is given in Table 4.2. In these tables, X_I and Z_I represent the horizontal and vertical initial crack forces, respectively, X_H and Z_H are for the horizontal and vertical hinge crack forces, and F_{mx} and F_{mz} denote the horizontal and the vertical components of the maximum global forces, respectively.

Table 4.1 indicates that initial crack, hinge crack, and the clearing process, are all a possible source for the maximum forces. This is quite different from the results of the SCS tests (Lewis and Croasdale 1978, Abdelnour 1988).

As shown in Table 4.1, the ridge riding up (or resting on) the structure is one of the main causes for the maximum loads. For instance, in the last portion of the clearing process in test Y1T1R3, two huge ridge segments slowly slid over the side facets of the structure and a large ridge fragment sitting on the front facet with its top leaning against the front side of neck yielded a very high maximum vertical global load and high horizontal neck load (see Table 3.10). A similar situation was observed in test Y1T2R3 where a few large ridge fragments rode

up high on front and side facets and exerted extremely large forces on the structure.

Test No.	Center Crack Load (kN)		First Hinge Crack Load (kN)		Maximum Load and the Interaction Event		
					Load (kN)		The Events Resulting in the Maximum Ridge Loads
	X_I	Z_I	X_H	Z_H	F_{mx}	F_{mz}	
Y1T1R2	76	113	130	150	130	150	1st Hinge Crack
Y1T1R3	90	110	103	130	103	186	1st Hinge Crack/Ridge Riding
Y1T2R3	150	120	140	110	160	190	Ridge Riding and Resting
Y1T2R4			135	145	149	170	Ridge Riding
Y1T3R1	73	97	83	108	94.3	116	Ridge Riding and Resting
Y1T3R3	56	70	80	91	125	138	Ridge Riding and Resting
Y1T4R1	28	32	32	40	32	40	Hinge Crack
Y1T4R2	40	50	35	40	40	50	Radial Crack
Y2T2R1	20	30	25	30	63	40	Ridge Riding
Y2T2R2	32	25	28	35	72	60	Ridge Riding, Breaking Fragment
Y2T3R1	60	72	42	60	66.5	72	Ridge Riding/Radial Crack
Y2T3R2	57	68	68	83	68	83	Hinge Crack
Y2T4R1	58	68	63	75	63	75	Hinge Crack
Y2T4R2	51	63	76	97	83	100	Many Fragments Riding
Y2T5R1	7	8.5			7	8.5	Radial Crack
Y2T5R2	12	15			12	15	Radial Crack

Table 4.1 Crack Loads and Maximum Loads for the ERC Tests

Table 4.1 also shows that 7 ridges had their maximum loads associated with either radial

or hinge crack. In addition, one component of the maximum forces for each of other two ridges reached its maximum value during the hinge crack process. It is obvious that the cracking process, either for central crack or hinge cracks, is still a major interaction event to give rise to the maximum ridge load on a MCS. Even in the cases of the tests Y1T3R1 and Y2T3R1 where at least one component of the maximum force was caused by riding-up process, the crack force(s) is only slightly lower than the maximum value. All these indicate that the cracking process should still be considered at the first place for the maximum ridge load estimation.

Test No.	Initial Crack Loads (kN)		Second Crack Loads (kN)		Maximum Loads and the Interaction Events (kN)		
	X_I	Z_I	X_H	Z_H	F_{mx}	F_{mz}	Events
M33	21.07	20.75	9.8	12.8	21.07	20.75	ridge separating from sheet
M34	14.57	14.92			14.57	14.92	radial and hinge cracks
M36	6.44	7.61			9.09	10.92	ridge riding, sheet cracking
M37	10.15	10.73	12.43	12.6	12.43	12.6	radial and hinge cracks
M44	25.51	23.5			25.51	23.5	radial and hinge cracks
M45	13.96	12.29	13.46	12.69	13.69	12.69	initial and second cracks
M47	9.76	8.78	14.84	13.47	14.84	13.47	2nd radial and hinge cracks
M53	5.51	4.74	2.2	2.19	5.13	4.47	ridge separating from sheet
M54	7.68	6.05			7.68	7.60	radial & hinge / clearing
M61	10.86	10.36	6.3	6.0	10.86	10.36	radial and hinge cracks
M65	7.32	7.56	7.32	6.1	8.4	8.83	3rd radial and hinge cracks
M74	15.17	14.89	5.46	4.88	15.17	14.89	initial radial crack
M75	19.2	19.7	16.59	16.1	19.76	19.7	3rd radial and hinge crack
M77	4.64	5.17	9.14	7.68	9.14	7.98	1st crack / clearing

Table 4.2 Ridge Crack Loads and Maximum Loads for the IMD Tests

Because it was difficult to distinguish the moment of occurrence for the radial cracks from that for the hinge crack(s) for most of IMD's "dump ridge" tests, the "Initial Crack Loads" and the "Second Crack Loads" shown in Table 4.2 are forces associating with the first group and the second group of cracks, respectively. Each of these groups of cracks consist of radial and hinge cracks. The maximum force might occur when the third or fourth group of radial and hinge cracks were occurring if there were more than two groups of cracks formed.

Nine out of 14 ridges (total) for the IMD tests generated their maximum forces within the cracking process, and others showed the maximum forces during the process of either the ridge separating from the sheet or the clearing of ice pieces. Again, it indicates that the maximum forces may likely occur during the ridge cracking process.

4.2.2 Horizontal and Vertical Ridge Forces

Most analytical models for the prediction of ridge forces on a SCS (Wang 1984, Croasdale 1980, Kim and Kotras 1973) used Equation (2.1) to calculate one component of the global force from the other. Thus, validation of Equation (2.1) is of certain importance.

The ratio of the two components of the maximum forces for all the ridge tests together with those for the ERC initial and hinge crack forces were calculated and are presented in Table 4.3. "E.", used as a column head in this table, means the ratio in the column was calculated with Equation (2.1), while the definition for other symbols is the same as those for Tables 4.4

and 4.5. The angle used in the equation is the sloping angle of the main cone facet, i.e., 39.8°. Because the friction coefficients required for Equation (2.1) were not measured in the IME tests, this equation has not been applied to these tests. It should be noted that Equation (2.1) was based on a coordinate system with its z axis downwards, and the coordinate system used in this thesis and all the tests has its z axis upwards. Therefore an negative sign should be added in front of right side of the equation for the present system.

ERC'S TESTS					IMD'S TESTS			IME'S TESTS	
Test No.	X_I/Z_I	X_H/Z_H	F_{mx}/F_{mz}	E.	Test No.	F_{mx}/F_{mz}	E.	Test No.	F_{mx}/F_{mz}
Y1T1R2	0.673	0.867	0.867	0.984	M33	1.015	1.039	C45	0.883
Y1T1R3	0.818	0.792	0.554		M34	0.977		C46	0.915
Y1T2R3	1.250	1.273	0.842	1.087	M36	0.832	0.998	C47A	1.054
Y1T2R4		0.931	0.876		M37	0.987		C47B	0.912
Y1T3R1	0.753	0.769	0.813	0.896	M44	1.086		C48	1.000
Y1T3R3	0.800	0.879	0.906		M45	1.079		C49	1.154
Y1T4R1	0.875	0.800	0.800	0.900	M57	1.102		C51	1.220
Y1T4R2	0.800	0.875	0.800		M53	1.148		C52	1.200
Y2T2R1	0.667	0.833	1.575	0.961	M54	1.011		C53	1.231
Y2T2R2	1.280	0.800	1.200		M61	1.048	0.979	C58	1.342
Y2T3R1	0.833	0.700	0.924	0.975	M65	0.951		C59	1.320
Y2T3R2	0.838	0.819	0.819		M74	1.019		C63	1.076
Y2T4R1	0.853	0.840	0.840	0.988	M75	1.003		C64	1.000
Y2T4R2	0.810	0.784	0.830		M77	1.145		C65	1.065
Y2T5R1	0.824		0.824					C66	1.226
Y2T5R2	0.800		0.800						
Average	0.858	0.854	0.892	0.970		1.029	1.005		1.086

Table 4.3 Horizontal and Vertical Ridge Forces for all the Tests

Strictly speaking, the ratio should be calculated for the horizontal and vertical forces occurring at the same moment. In this sense, the ratio of the two components for the initial and hinge crack loads are appropriately calculated. However, a few ratios for some ridges' maximum force are only nominal because the maximum horizontal and the maximum vertical forces were generated during different interaction events and at different instants in the interaction history. These include ERC's Y1T1R3, Y2T3R1, and IMD's M45, M54, M75, and M77. Fortunately, the differences were not very large, except for the case of Y1T1R3.

Table 4.3 shows that the results of Equation (2.1) for the IMD tests agree well with those measured, but the calculated values for the ERC tests are significantly larger than the measured ones. Also, the data for the ERC tests are relatively scattered.

4.3 Influence of Various Parameters on Ridge Failure Process and Forces

This section presents the analysis of the effect of three tested factors which are, namely, the structure or ridge orientation, the size of the structure's neck, and ridge width. Since the structures used in the IMD tests were all in face-on orientation and the ridge widths were the same for most of its tests, this series is used only for the analysis of the effect of neck size, which is arranged in the subsection 4.3.3. The ERC and IME series tested both the orientation factor and ridge width, thus the analysis of these factors are based on these two test series. In

addition, the IME and ERC tests are also to be used in the analysis of neck size effect. The analysis of orientation factor is to be presented in the subsection 4.3.2, and the effect of ridge width will be analyzed in the subsection 4.3.1.

In the analysis of the effect of these three factors on ridge forces, the measured maximum forces are non-dimensionlized by $\sigma_{r,t} I/(z_t L_c)$ which is conventionally believed to be a combined parameter able to cover the effect of the members it contains (Abdelnour 1988). All the items in this parameter are the same as those defined in Equation (2.2). L_c and I are for the ridge only, i.e., they do not include the effect of the surrounding ice sheet. After the non-dimensionlisation, the above three factors (ridge width, structural orientation, and neck size) stand out as major parameters that might affect the dimensionless forces. There may be more factors affecting the forces, but we will focus only on the analysis of these three factors.

4.3.1 Effect of Ridge Width

Based on their widths, the IME ridges can be divided into two groups, viz., one with a width varying from 60 cm to 72 cm, the other being around 1 meter (see Table 3.5). These two groups are being referred to as "narrow ridges" and "wide ridges", respectively. In the following analysis, the ridge width, B_t, is non-dimensionlized by dividing it with the circumscribed waterline diameter of the structure, D_w.

Of the five wide ridges used in the IME tests, three experienced a local circumferential

crack. The ridges for tests C47B, C64 and C66 all of which were tested under the edge-on conditions revealed the same sequence of crack occurrence: the initial central crack was followed by a circumferential crack around the structural model. The circumferential crack broke off an arch-shaped ridge ice piece which was about 30 cm measured along the ridge width from the ridge's leading edge, and about 45 cm along the ridge leading edge with the central crack as its symmetrical axis. Another wide ridge, viz., C49, tested under the face-on condition, had an initial circumferential crack in front of the structure. In contrast to these wide ridges, the narrow ridges did not have local circumferential cracks.

In the IMD tests, only one ridge was wider than the others (see Tables 3.6 and 3.7). The ridge for test M75 was 3 meters wide, or three times wider than others (all other ridges were one meter wide). This ridge failed like a thick ice sheet. First, a pair of radial cracks and a circumferential crack formed. Then a smaller circumferential crack occurred within the first circumferential crack. A few seconds later, the third circumferential crack and another pair of radial cracks appeared. The ridge experienced a total of four circumferential cracks and five pairs of radial cracks until it failed. Other (relatively narrower) ridges, except for M45 and M65, experienced no more than two circumferential cracks. Unlike other ridges, the ridges M45 and M65 also showed a multi-circumferential crack pattern, but they failed in a mixed mode showing strong shearing failure feature. It is clear from the above that a wider ridge more likely fails through the generation of more (local) circumferential and radial cracks.

In the ERC tests, an extremely wide ridge (with width of 4.5 meters) was tested in

Y1T2R3. The widest ridge for Year Two tests was the one for Y2T2R1, with a width of 3 meters. A common crack feature for these two wide ridges is that they had multiple radial cracks (refer to Table 4.4 in the next subsection). This is very distinct from the other ridges's single radial crack pattern. The multiple radial cracks can also be considered as one type of local cracks. Thus, the wider ridges for the ERC tests also had more local cracks.

To study the influence of ridge width on the maximum ridge forces, the dimensionless forces are plotted against dimensionless ridge width (B_r/D_w) in Figures 4.1 through 4.4. The points (x and o) represent the test data, and the lines are from a linear regression analysis. Since the effect of ridge width may depend on other parameters, viz. neck size, structural orientation, and force component, the data are sorted into eight groups, and two groups are plotted in each figure. For instance, the two groups of the data plotted in Figure 4.1 are those vertical forces on large neck structure in face-on and edge-on orientations, respectively. It should also be noted that the edge-on orientation for the ERC tests is actually that in which the ridge was oblique at a 30° angle.

Since all the IMD ridges except for M75 had the same width (one meter), resulting in the identical value of B_r/D_w for all the tests except for M75, the plotting in these figures do not include the IMD tests. The data for the large neck structure are from ERC's tests, and those for the small neck structure are mainly from IME's tests. The data from ERC's two small neck structure tests, Y1T1R2 and Y1T1R3, are also included in the face-on orientation for the small neck structure (Figures 4.3 and 4.4).

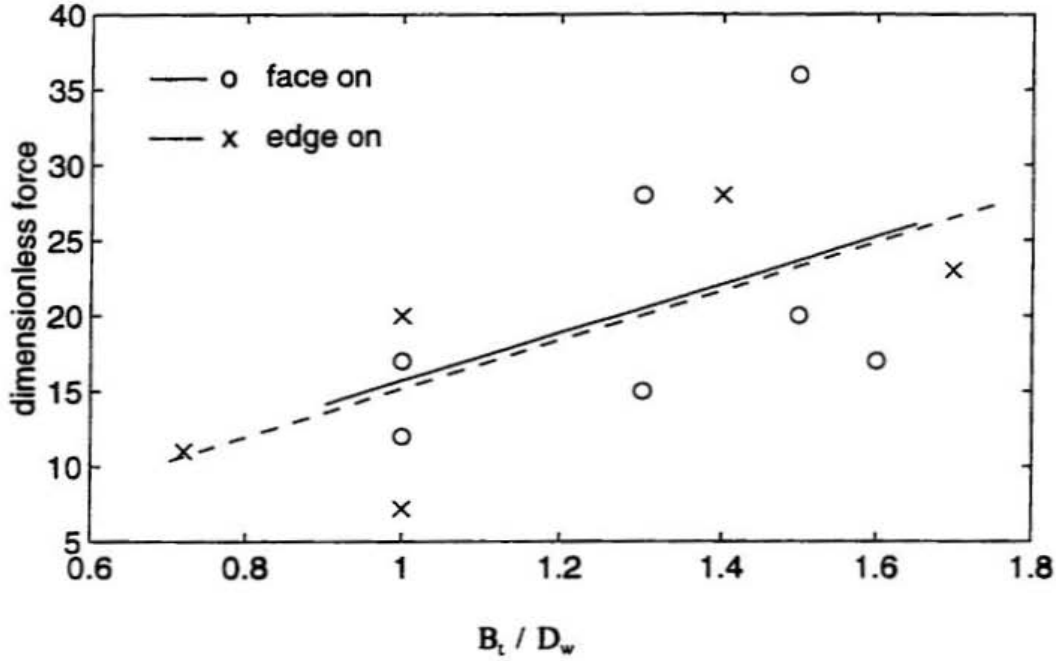

Figure 4.1 Vertical Ridge Forces on Large Neck Structures

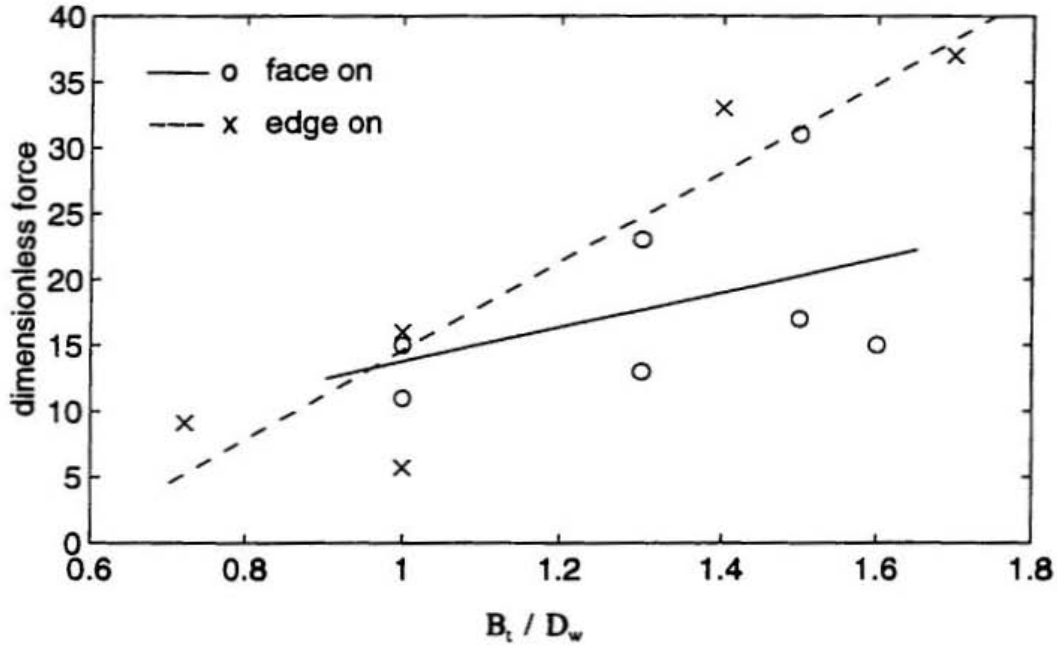

Figure 4.2 Horizontal Ridge Forces on Large Neck Structures

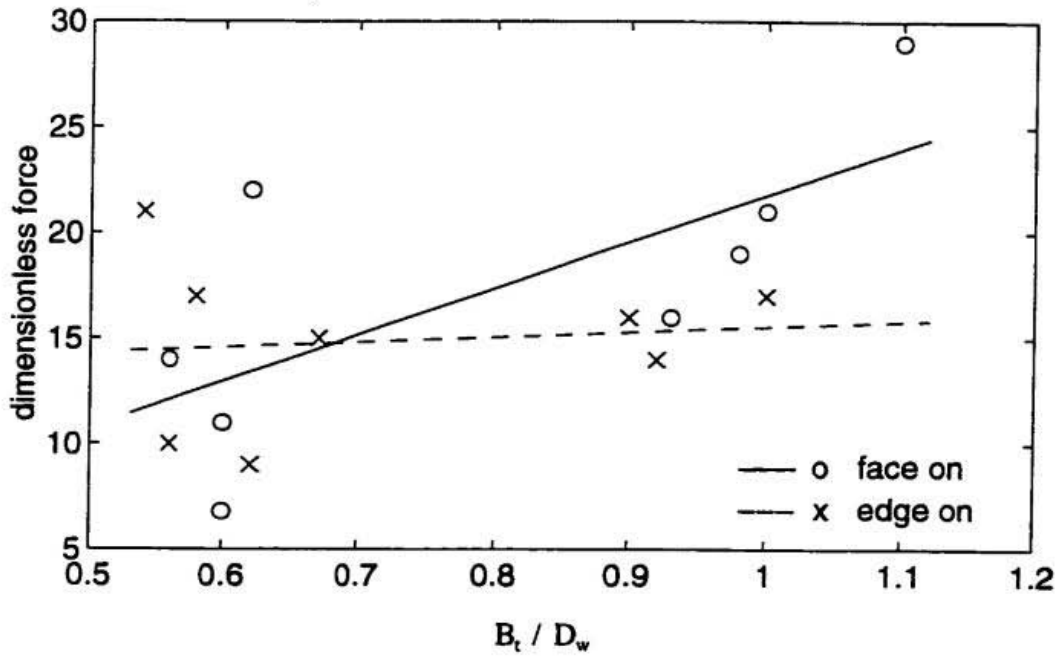

Figure 4.3 Vertical Ridge Forces on Small Neck Structures

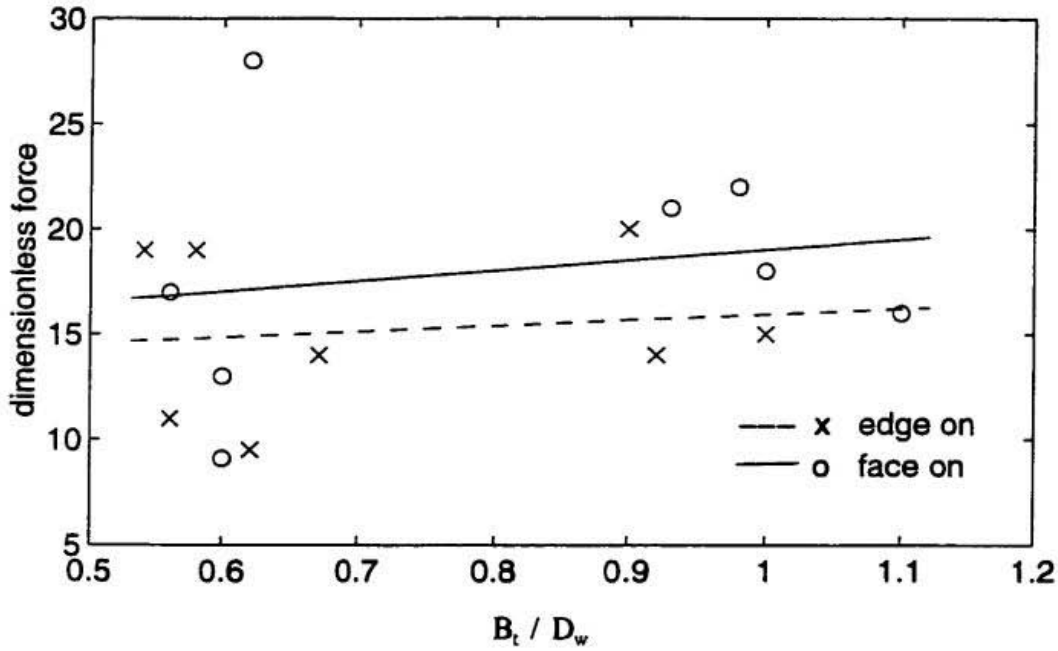

Figure 4.4 Horizontal Ridge Forces on Small Neck Structure

Because of the incompleteness in the data, test C53 in the IME series and tests Y2T5R1 and Y2T5R2 in the ERC series are excluded from this analysis and from all the other analyses to be presented in this thesis.

Generally, the effect of ridge width is quite significant for the large neck structure but less significant for the small neck structure. For both edge-on and face-on orientations of the large neck structure, both the vertical and the horizontal components of the dimensionless forces increase as the ridge width increases (Figures 4.1 and 4.2). The vertical forces for the case of a face-on orientation of a small neck structure show a similar trend (Figure 4.3), whereas this effect is nearly negligible for the other cases, viz., the horizontal forces on a small neck structure in both orientations (Figure 4.4) and the vertical forces for the edge-on orientation of the small neck structure (Figure 4.3).

A possible reason for the above trend may be that the wider ridges usually lead to large segments after their cracking, and these large segments are more likely to be stuck in front of large neck, thus resulting in large forces.

4.3.2 Effect of Structural Orientation

In the IME test series, the structure was in edge-on orientation for eight (8) ridges, and in face-on orientation for the remaining seven (7) ridges. In the ERC tests, five (5) out of sixteen (total) were oblique at a 30° angle. This ridge orientation makes one corner of the front facet contact

the ridge first, a contact situation somewhat similar to that for IME's edge-on tests. In the rest of this section, both cases will be referred to as edge-on orientation.

The location of the radial (basically, the initial crack) and the first pair of hinge cracks for the ERC and IME tests are listed in Tables 4.4 and 4.5, respectively. In these tables, the dimensionless location of the cracks are expressed as the distance from the center line of the ridge (or the center line of the structure) divided by the circumscribed waterline diameter of the structure. The direction is defined as follows: as one stands on the center line of a ridge, facing in the direction of ice motion, the crack occurring to one's left side is defined as Left; similarly for the Right. If there were two radial cracks for a test run, their locations are marked with L (or R) which means the crack appeared on the Left (or Right) defined above.

Ridge orientation has an obvious effect on the location of the initial crack(s). In the ERC tests, every oblique ridge except Y2T2R1 had a single initial crack starting from the contact point between the ridge and the structure's front corner. Even the ridge for test Y2T2R1 had one centrally located radial crack. On the other hand, only three (3) broadside ridges, out of eleven (11) in total, had initial cracks close to, but not at, the structure's front corner.

Table 4.5 shows a similar trend in the IME tests: every ridge in the edge-on tests except for C45 and C46 had a single central initial crack, whereas only four out of seven ridges, initially centrally cracked for the face-on orientation. Ridges C45 and C46 were not frozen completely. The location of the cracks were just the weak points where the ridge moulds were

joined (Irani *et al* 1992). If these two test runs are excluded from the present analysis, the initial cracks for the IME tests would all occur at the center line for the edge-on orientation.

Test No.	Ridge Orientation	Dimensionless Radial (Initial) Crack Location *			Dimensionless First Hinge Crack Location *	
		No. 1	No. 2	No. 3	Left	Right
Y1T1R2	Broadside	0.202 L	-	-	1.761	2.165
Y1T1R3	Broadside	0.029 L	0.115 R	-	2.050	1.588
Y1T2R3	Broadside	0.029 R	0.248 L	0.248 R	2.483	2.483
Y1T2R4	Broadside	0.231 L	-	-	2.454	2.511
Y1T3R1	Oblique 30°	0	-	-	2.194	2.107
Y1T3R3	Broadside	0.029 R	-	-	1.761	2.194
Y1T4R1	Oblique 30°	0	-	-	0.953	1.963
Y1T4R2	Oblique 30°	0	-	-	1.097	1.155
Y2T2R1	Oblique 30°	0	0.866 L	0.346 R	4.215	4.388
Y2T2R2	Oblique 30°	0	-	-	1.443	3.233
Y2T3R1	Broadside	0.924 L	-	-	0.924	2.598
Y2T3R2	Broadside	0.496 L	-	-	5.774	2.600
Y2T4R1	Broadside	0.288 L	-	-	2.309	3.000
Y2T4R2	Broadside	0.462 L	-	-	2.483	4.388
Y2T5R1	Broadside	0.496 R	0.496 L	-	-	-
Y2T5R2	Broadside	0.520 R	1.270 L	-	-	-
Average	Broadside	-	-	-	2.440	2.614
	Oblique	-	-	-	1.980	2.569

* the dimensionless location = CL / D_w, where CL is the distance measured from the crack to the ridge center, and D_w is circumscribed waterline diameter.

Table 4.4 Crack Location of the ERC Ridges

Test No.	Structure Orientation	Dimensionless Initial Crack Location	Dimensionless Hinge Cracks Location	
			Left	Right
C45	Edge on	0.42 R, 0	1.119	1.445
C46	Edge on	0.42 R	1.119	1.445
C47A	Edge on	0	0.560	0.811
C47B	Edge on	0	0.796	1.026
C48	Face on	0.233 R, 0.233 L	0.932	1.166
C49	Face on	0.233 R, 0.317 L	1.725	1.40
C51	Face on	0	1.212	1.40
C52	Face on	0, 0.255 L	0.932	0.932
C53	Face on	0	1.632	1.818
C58	Face on	0	1.865	1.678
C59	Face on	0	1.585	1.865
C63	Edge on	0	0.900	0.630
C64	Edge on	0	1.305	1.119
C65	Edge on	0	0.721	0.721
C66	Edge on	0	1.756	1.801
Average	Face on	-	1.412	1.466
	Edge on	-	1.035	1.125

Table 4.5 Crack Location of the IME Ridges

Another aspect of the crack, which the structure orientation seems to affect, is the distance between the two first hinge cracks. The IME tests indicate that this distance, on average, is smaller for the edge-on tests. As shown in Table 4.5, the average value of this

distance for the face-on tests is about 33% larger than that for the edge-on orientation. However, the values for the ERC tests do not strongly support this trend. Table 4.4 shows this distance for ERC's broadside ridges on average is only 11% larger than that for the oblique ridges. It should also be noted that the data are quite scattered. Indeed, the structure (or ridge) orientation is only one of many factors that may affect the hinge and radial crack locations.

To identify its effect on ridge forces, the ridge (or structure) orientation must be separated from the other two factors: viz., neck size and ridge width. The plot given in Figures 4.1 through 4.4 were arranged to show the effect of orientation factor as well. Each of the graphs is for a single neck size: viz., Figures 4.1 and 4.2 are for the large neck structure, while Figures 4.3 and 4.4 are for the small neck structure. In each of these figures, the forces for the two orientations can be directly compared for a given ridge width.

It can be seen from Figure 4.1 that the orientation, on average, rarely has any effect on the vertical forces for the large neck structure because the regression lines for the two orientations nearly coincide. However, as indicated in Figure 4.2, the edge-on orientation seems to induce larger horizontal forces on the large neck structure for $B_r/D_w > 1$.

The small neck structures show a reverse trend: the horizontal forces for the face-on orientation, on average, are larger than those for the edge-on orientation, see Figure 4.4. The case for the vertical forces on a small neck structure is a little complex. Figure 4.3 shows that the forces for these two orientations are very scattered in the vicinity of dimensionless ridge

width equal to 0.6 (narrow ridges). Though the regression line for edge-on orientation is above its counterpart for the face-on orientation, it is really hard to say which orientation experienced larger forces. In the region of $B_t/D_w = 1$ (wide ridges), the horizontal forces for the face-on orientation are obviously larger.

The orientation's effect can be roughly summarized below.

- For the small neck structure, the forces on a face-on structure are basically larger than those on the same structure in an edge-on orientation. The distance between hinge cracks are also larger for the face-on orientation.
- For the large neck structure, effect of ridge orientation is not significant. The vertical forces for these two orientations on average are fairly close, as are the average crack locations. Only the horizontal forces on the edge-on structure are larger than their counterparts for face-on orientation.

4.3.3 Effect of Neck Size

To analyze the effect of neck size, the mean values of dimensionless forces and their standard deviations are listed in Table 4.6. The data included in this table for the IMD series are those for the 1:25 scale models. The dimensionless ridge widths for these IMD tests were all the same: $B_t/D_w = 0.72$. In the ERC series, most tests were carried out with large neck structure in both face-on and edge-on orientations, and only two tests were run for the small neck structure. In the IME series, as shown, only the small neck structure (in both orientations) was tested.

Test Series	Structural or Ridge Orientation	Mean Value of Dimensionless Forces			Standard Deviation	
		Component	Large Neck	Small Neck	Large Neck	small neck
ERC	Face-on	Vertical	20.71	25.0	8.40	5.67
		Horizontal	17.71	17.0	6.60	1.41
	Edge-on	Vertical	17.84	-	8.58	-
		Horizontal	20.16	-	14.12	-
IMD	Face-on	Vertical	30.86	34.25	11.14	14.71
		Horizontal	32.29	32.25	11.00	14.59
IME	Face-on	Vertical	-	14.80	-	5.48
		Horizontal	-	18.35	-	6.77
	Edge-on	Vertical	-	14.88	-	3.91
		Horizontal	-	15.19	-	3.87

Table 4.6 Statistical Measurements on the Neck Size Effect

Because the IMD tests cover both neck sizes and had a single value in ridge width the results from this series are the most convenient and solid data for the study of neck size effect. It is shown in Table 4.6 that the mean vertical force for the large neck structure in IMD's tests is smaller than its counterpart for the small neck structure, but the horizontal mean force for the large neck structure is slightly larger (very close to the forces on the small neck structure). Exactly the same trend is also found in the ERC tests for the face-on orientation in this table.

To utilize both the IME and the ERC tests for this analysis, they are plotted in Figures 4.5 and 4.6. The comparison of the dimensionless forces from these two series tests should be

made at the same value of B_t/D_w. Since these tests share the values of B_t/D_w in the vicinity of $B_t/D_w = 1$, they are comparable in that region. These graphs show that the forces on the large neck structure in face-on orientation (average) are quite close to (slightly smaller than) those on the small neck structure in the vicinity of $B_t/D_w = 1$. It should be noted that this trend is only in average (or least square) sense and is supported by a small sample of the data. Looking at these figures more closely, one may note that the forces are quite close to each other for a few individual tests for both neck sizes.

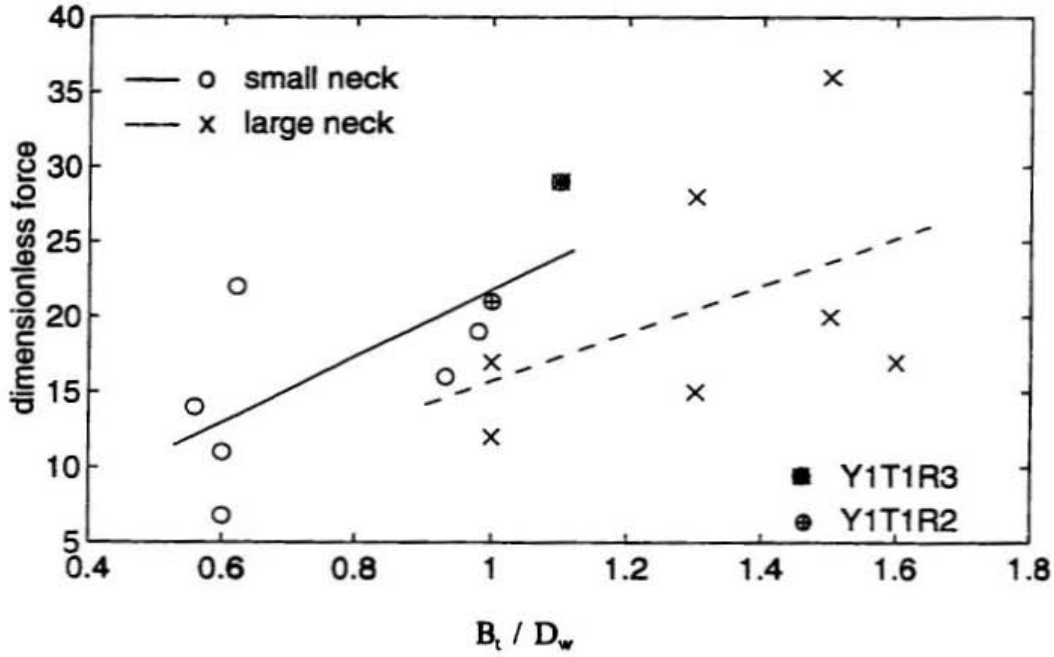

Figure 4.5 Vertical Ridge Forces on Face-on Structures

One may argue that the scale factor played a role in the difference between the forces on the structures with different neck size. Indeed, all the forces for the large neck structure were

from the ERC tests whose scale was 1:10 and 1:20, while most data for the small neck structure were from the IME tests whose structural model was at the scale of 1:50. Although one cannot be completely sure the scale factor does not play any role, the two points from tests Y1T1R2 and Y1T1R3 identified in Figures 4.5 and 4.6 are somewhat reassuring that the role is small. These two ridges were tested with small neck structure at 1:10 scale. The two points for the large neck structure (represented with x) just below those for Y1T1R2 and Y1T1R3 in Figures 4.5 and 4.6 are for tests Y1T2R4 and Y1T3R3 both of which were at 1:10 scale as well; thus they are directly comparable. It is shown in the figures that their forces are well above those for the large neck structure. The only exception is the horizontal force for Y1T1R3 which might be smaller than its counterpart for the large neck structure if there was one.

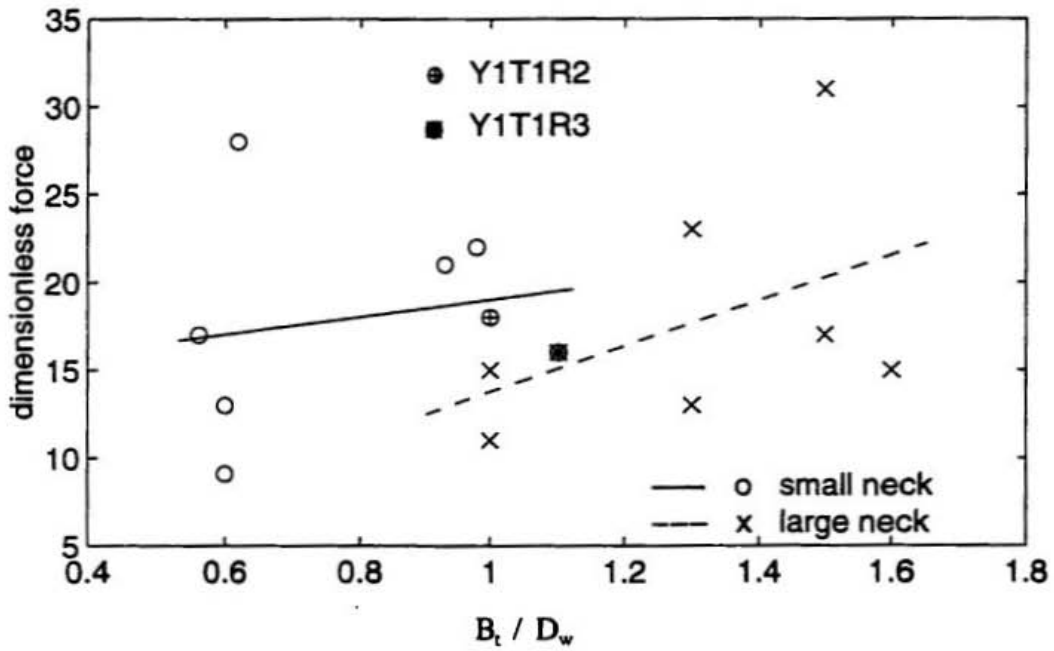

Figure 4.6 Horizontal Ridge Forces on Face-on Structures

The data for edge-on orientation are plotted in Figures 4.7 and 4.8 for vertical and horizontal forces, respectively. Within the region of $B_t/D_w < 1.01$ in Figures 4.7 and 4.8, the regression line for the small neck structure is higher than its' counterpart for the large neck structure. It is also shown in these figures that there is one case for the vertical and horizontal forces, respectively, wherein the force for the large neck structure is larger than the force for the small neck structure whose value of B_t/D_w is the same as that for the large neck structure. It should also be noted that the data are quite scattered in these figures. Considering all the above, we would say that the forces on the edge-on large neck structure and small neck structure are relatively closer to one another.

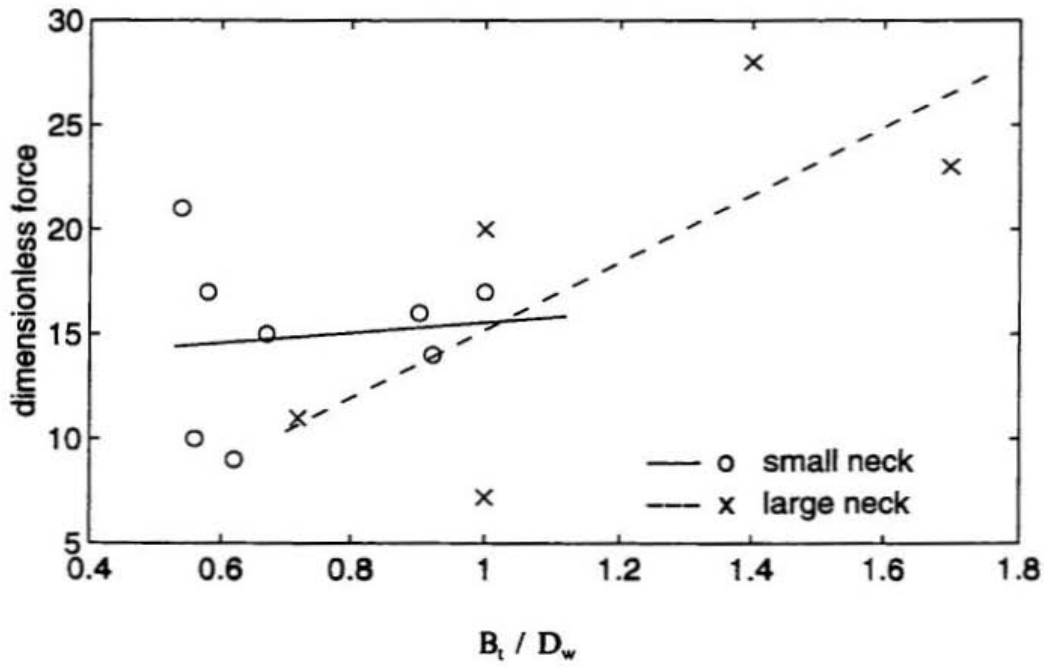

Figure 4.7 Vertical Ridge Forces on Edge-on Structures

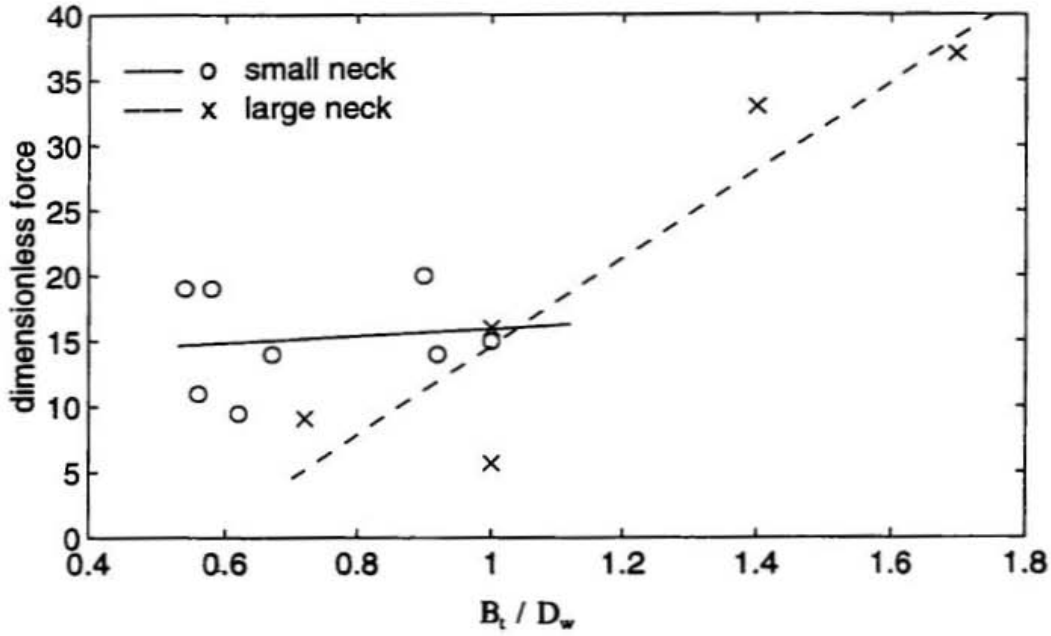

Figure 4.8 Horizontal Ridge Forces on Edge-on Structures

The effect of neck size is summarized as follows.

- For the face-on orientation, the mean horizontal force for the large neck structure is very close to (slightly larger than) the mean horizontal force on the small neck structure, while the mean vertical force on the large neck structure is smaller than its counterpart on the small neck structure.
- For the edge-on orientation, the mean forces on the small neck size structure are fairly close to those on the larger neck structure.

It should be pointed out that the data sample for the above analysis, except for the comparison in the case of the IMD tests, was quite small. In addition, the number of factors

considered here is quite limited. Therefore the effect of neck size summarized above is by no means meant to be general.

4.4 Analysis of Sheet Ice Forces

It has been made clear in Chapters 1 and 3 that a particular concern for this proposed MCS was the effect of the large neck on ice loads. This section concentrates on the analysis of this effect. For SCSs, it does not matter in which direction the ice moves towards the structure, the loads on the structure should be the same. For MCSs, it does. The effect of structure orientation on sheet ice loads, thus, is also analyzed in this section.

4.4.1 Approach for the Analysis

Since the test scales varied from 1:50 to 1:10 in our three series tests, ice mechanical properties, structure dimensions, and the ice forces all varied over a very wide range. Because the ice was not perfectly manufactured to the target scale (Croasdale and Muggeridge 1993), it is improper to directly compare the test measurements for analysis of the effects of various factors. To identify the effect of the two particular factors, viz., the neck size and structure orientation, for the tested MCSs, a dimensionless analysis is necessary.

In his analysis of sheet ice forces on SCSs, Kato (1986) assumed that the total forces (horizontal or vertical), F, can be non-dimensionlized in the form of $F/(\sigma_f h^2)$ and this

dimensionless force can be expressed as a sum of the ride-up component (the first two terms) and the breaking component (the last term) as follows:

$$\frac{F}{\sigma_f h^2} = A_n (D_w^2 - D_T^2) \frac{\rho_i g}{\sigma_f h} + B \qquad (4.1)$$

Where F, σ_f, h, ρ_i, g, D_w, and D_T are the measured force, flexural strength of ice, ice thickness, ice density, acceleration due to gravity, waterline diameter, diameter at the top of cone (there were no necks for the structures in Kato's tests), respectively. He applied linear regression approach to his test data to determine the coefficients A_n and B.

To apply this approach to the case of our MCS tests, a few modifications are required. The circumscribed waterline diameter and the circumscribed neck diameter will be used in the places of D_w and D_T, respectively. It is believed that the first two terms in Equation (4.1) do not fully (or properly) cover the effect of neck size; hence, this effect should be separated from the equation and be treated as another independent variable. Equation (4.1) can be rewritten as:

$$\frac{F}{\sigma_f h^2} = A C_p + B \qquad (4.2)$$

where B is the same as that in Equation (4.1), and C_p is defined as follows

$$C_p = D_w^2 \rho_i g / (\sigma_f h) \qquad (4.3)$$

The relation between A and A_n can be easily found by comparing Equations (4.2) and (4.3) with Equation (4.1):

$$A = A_n (1 - D_T^2 / D_w^2) \tag{4.4}$$

Kato (1986) assumed that A_n and B depend on cone slope angle. In the present case, the structures for all the tests had the same slope angle, but the ratio of D_T/D_w, which represents dimensionless neck size, and the structural orientation varied. Thus, A and B in Equation (4.2) are functions of these two parameters. It should also be noted that C_p given in Equation (4.3) is independent of D_T/D_w and structural orientation.

Generally, the dimensionless forces can be expressed as

$$\frac{F}{\sigma_f h^2} = f(C_p,\ \textit{neck size},\ \textit{orientation}) \tag{4.5}$$

For a given ratio of D_T/D_w and structural orientation, Equation (4.5) is reduced to be in the same form as Equation (4.1), but with A and B being constant and D_T included in A. Similarly, for a given C_p, the dimensionless forces are functions of structural orientation and the ratio D_T/D_w.

The basis for the analysis, to be presented in this section, can be described as follows. First, the tests are sorted into groups in each of which the tests have the same structural orientation and the same D_T/D_w. Then, use least square method to find the best fit line for each group of the tests, and plot the test groups with the same structural orientation but different ratio

of D_T/D_w together with their best fit lines in the same graph. A comparison of these data would show the effect of neck size. The effect of structural orientation is analyzed in a similar way.

4.4.2 Effect of Structural Orientation on Sheet Ice Forces

Orientation of the structure in sheet ice varied only in the IME test series with a single small neck structure. The analysis of this effect is, thus, limited to these tests. Because D_T/D_w was roughly a constant for all these tests, the dimensionless forces are a function of C_p and structural orientation itself. A total of three orientations were tested: *face on, intermediate*, and *edge on* which were defined in Subsection 3.3.1 and were identified in Table 3.4. For each of these structural orientations, the dimensionless forces are plotted against C_p in Figures 4.9 and 4.10 for the horizontal and vertical components, respectively. The points (o, +, and x) are test measurements, and the three lines are the best fit lines in a least square sense.

Generally, the dimensionless forces for all the three orientations are fairly close to each other at a given value of C_p, especially for small values of C_p. In the whole tested range of C_p, the forces for the edge-on orientation are slightly lower than the others, and the forces for face-on and intermediate orientations are quite close to each other, particularly for the vertical forces. These mean that the intermediate orientation, compared with the face-on orientation, does not significantly change the dimensionless forces, but the edge-on orientation does.

The above trend is supported by two sets of directly comparable tests, each of which

covers all the three orientations. The first set consists of tests C42 (face-on), C43 (intermediate), and C44 (edge-on), and the other set includes C60 (face-on), C61 (intermediate), and C62 (edge-on). As shown in Table 3.4, the ice thickness, flexural strength, ice speed, and structural dimensions for the three test runs in each set were either exactly the same or very close to each other. In other words, the values of C_p for the tests in each set are nearly the same. The measured forces presented in Table 3.11 show the forces for edge-on orientation to be smaller than those for other orientation. The forces for C60, the face-on orientation test run, was larger than those for intermediate orientation, C62. However, the forces for C42 (face-on) were smaller than those for C43 (intermediate).

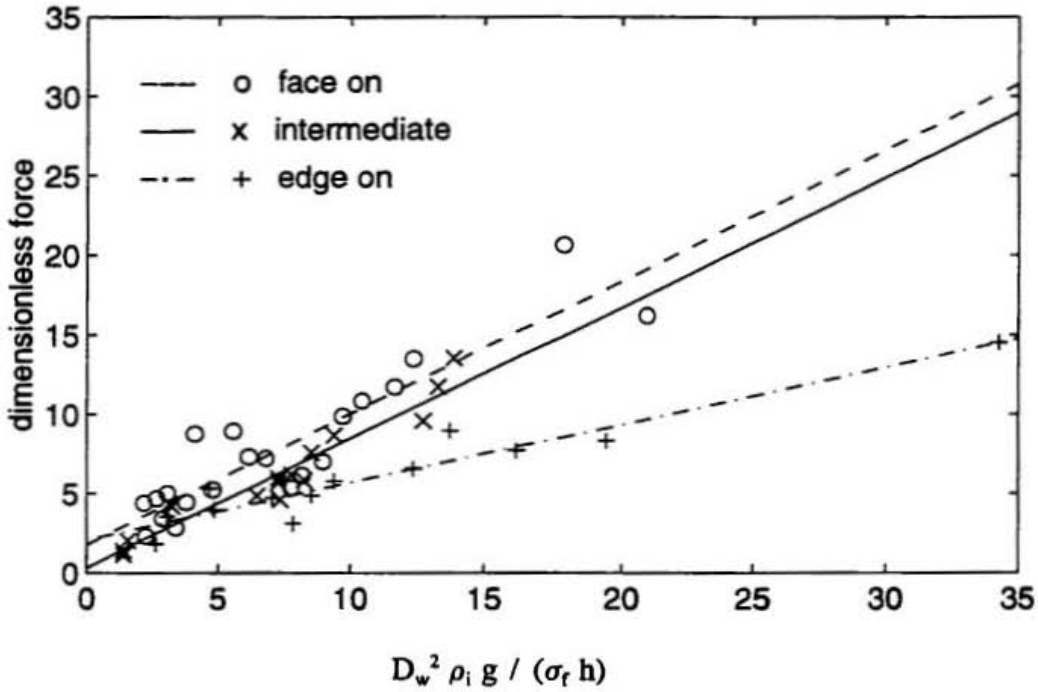

Figure 4.9 Effect of Structural Orientation on Horizontal Sheet Forces

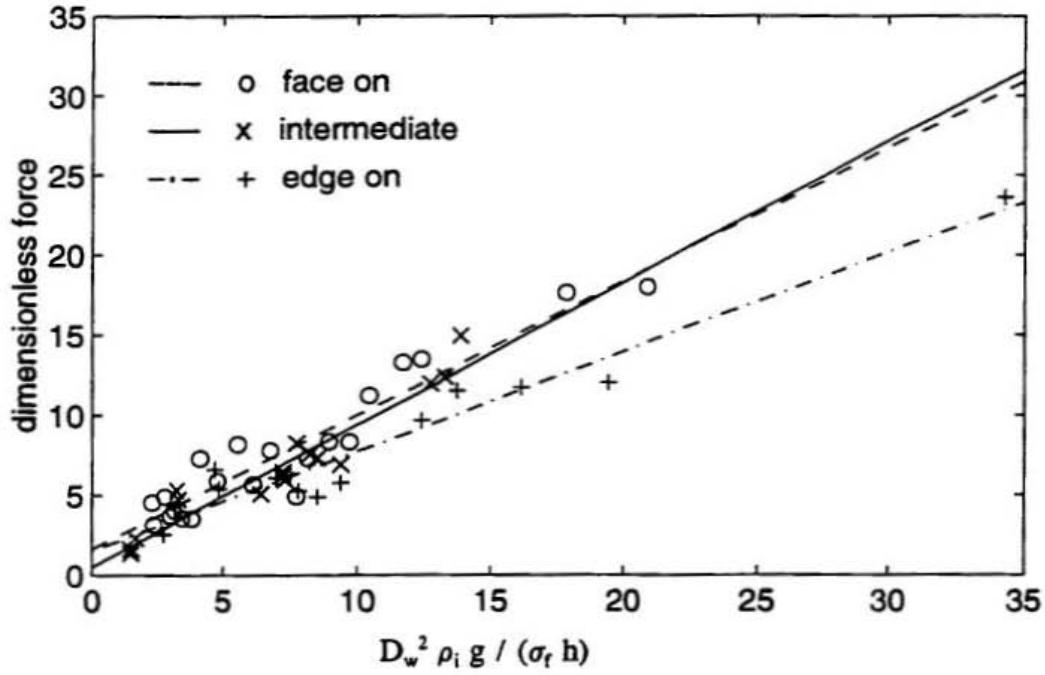

Figure 4.10 Effect of Structural Orientation on Vertical Sheet Forces

It is also shown in Figures 4.9 and 4.10 that the slope of the best fit line for the edge-on orientation is smaller than that for the face-on orientation and the slope for the face-on and intermediate orientations are very close. Because the slope, viz., the coefficient A, represents the ride-up component, we may say the ride-up forces on the edge-on structure are smaller than those on the same structure but in other orientations.

4.4.3 Effect of Neck Size on Sheet Ice Forces

To analyze neck size effect, the tests with the same structural orientation should be used. Thus,

all the ERC and IMD tests which were performed with face-on structure and those IME tests with structure in face-on orientation are to be analyzed in this subsection.

According to the values of D_T/D_w, all the face-on tests can be divided into three groups. The first group consists of those ERC and IMD tests with large neck structures and will be referred to as "large neck". The value of D_T/D_w for this group was 2/3. The second group with D_T/D_w = 1/3, "small neck" group, includes the IMD tests with small neck and the ERC's test Y1T1R1. The IME tests with face-on structural orientation comprise the third group for which 0.215 is taken as the ratio of D_T/D_w because most tests in this group had the ratio at this value (it was 0.219 only for six tests in this group). These IME tests are actually also the small neck structure with designed D_T/D_w equal to 1/3. Because the structure was raised up a bit during the test the effective waterline diameter D was increased; thus, the value of D_T/D_w was reduced. To distinguish this group from the "small neck" group, it will be referred to as "IME face-on" group.

Figures 4.11 and 4.12 presents the plotting for the vertical and horizontal dimensionless forces for these tests. Based only on the best fit lines in these figures, the effect of neck size can be summarized as follows.

- Both vertical and horizontal components of the dimensionless forces on the large neck structure are larger than others.
- The vertical forces for the "small neck" group are larger than those for the "IME face-on" group, but their horizontal forces are in a reverse order.

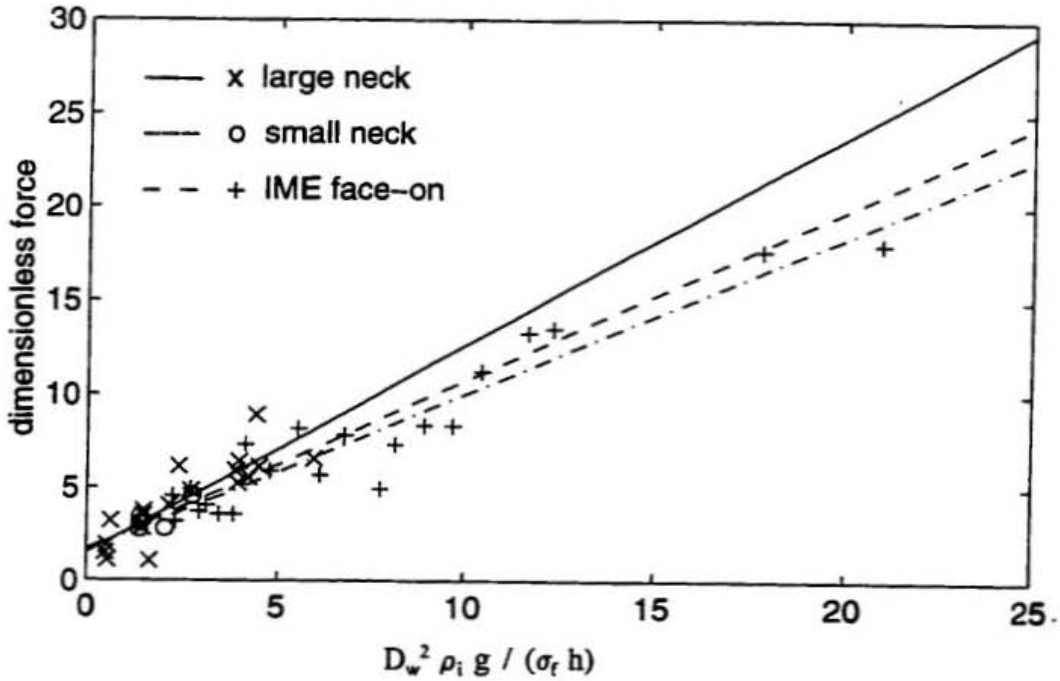

Figure 4.11 Effect of Neck Size on Vertical Sheet Ice Forces

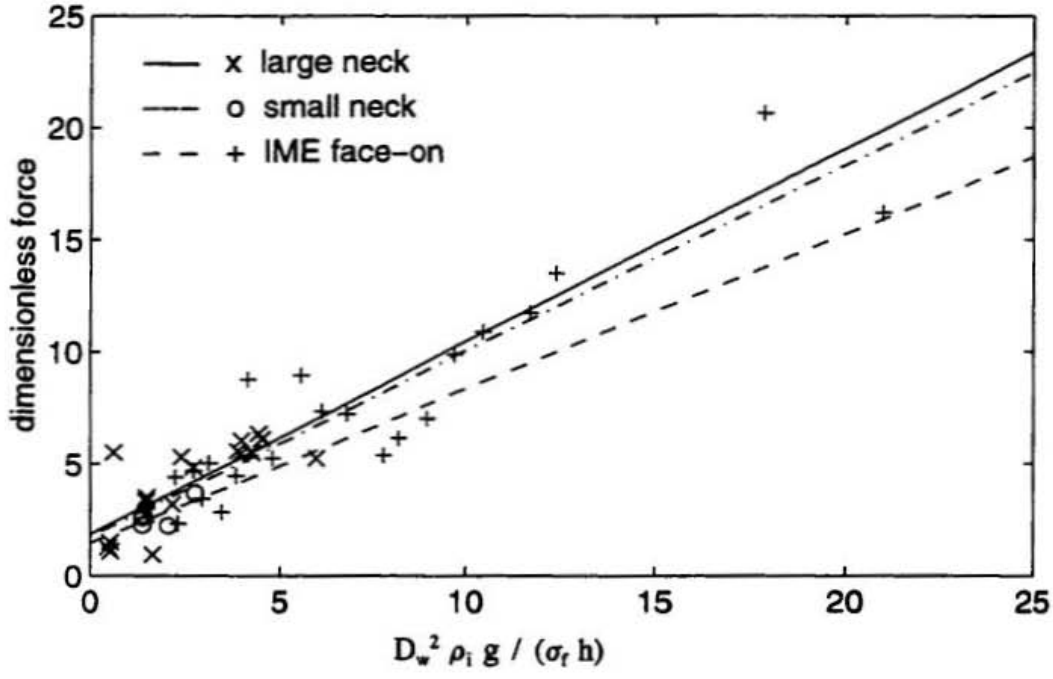

Figure 4.12 Effect of Neck Size on Horizontal Sheet Ice Force

It should be noted that the neck size effect summarized above is only in least square sense. Figures 4.11 and 4.12 show that the data are quite scattered. At certain points of C_p, the forces for the large neck are well below those for the small neck structure. To show this, a smaller window of Figure 4.11 is taken and presented in Figure 4.13 in which both the best fit lines and the test measurements are exactly the same as their counterparts in Figure 4.11. It is shown in Figure 4.13 that the forces for a few large neck tests within $C_p < 2$ are tremendously low, much lower than the best fit line and the measured forces on the small neck structure as well.

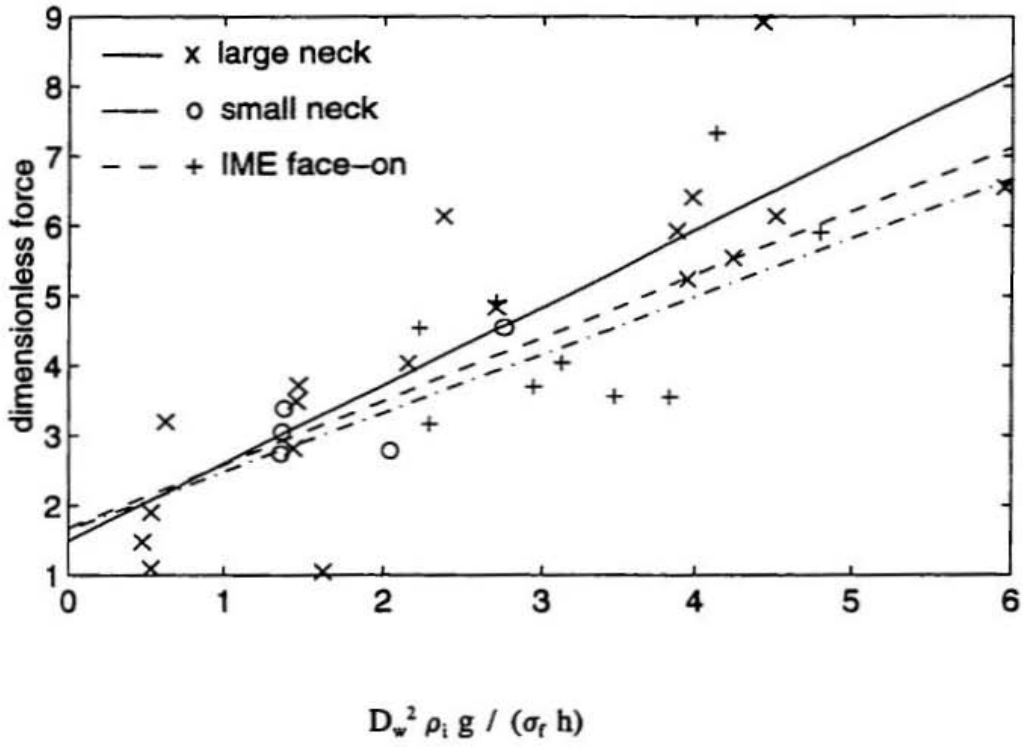

Figure 4.13 Zoomed Plotting of Vertical Forces against C_p

Chapter 5 Numerical Simulation

The ice/MCS interaction process and its relation to the generated loads described in the last chapter was a result of reviewing video records and the time history of recorded forces, which was quite general and qualitative. A quantitative understanding of the mechanisms involved in the ice/MCS interaction was offered by a series of numerical simulations that were carried out using a discrete element code, DECICE. The simulation was also used to analyze the effect of neck size on the ice forces developed since this was one of industry's major concerns.

ERC's tests Y1T1R2 and Y1T1R1 were chosen as a basis for the simulation due to the fact that Y1T1R1, Y1T1R2, and Y1T1R3 were the only tests with a small neck structure at the largest scale, namely, 1:10. Generally, if other parameters are kept the same for two tests, the larger the test scale, the closer to reality the test result will be. The first set of simulations were carried out to examine the various interaction mechanisms involved in the process. The measured geometric and mechanical properties were used as inputs to this set of simulations which are presented in Sections 5.2 and 5.3 for the sheet and the ridge, respectively.

The idea implemented in the analysis of neck size is that if only the neck size is allowed to change, the difference in the resultant ice loads and the interaction process should reflect the effect of the neck size. Thus, all the parameters used in the first set of simulations remain the same in the second set, except for the neck which is replaced by a large neck. The comparison

of the results of these two sets of simulations is expected to reveal some information on the neck size effect. These simulations are presented in Section 5.4.

5.1 The Approach for Numerical Simulation

As reviewed in Chapter 2, there exist two main methods for the numerical simulation of ice/structure interaction: Finite Element Method (FEM) and Discrete Element Method (DEM). Because of the advantage of the DEM in simulating the cracking process and the interaction of cracked ice, this method was adopted for the simulation being presented here.

5.1.1 DECICE Program and the Procedures for Problem Solving

DECICE is a large computer software based on DEM and is one of the best of its kind (refer to Section 2.5.2 of Chapter 2). By courtesy of IMD who owns a copy of DECICE, the simulation and analysis were done using this software. The formulation of the DEM implemented in DECICE as well as the capability and particular usage of the program were detailed in the Theoretical Manual, Programmer's Manuals, and User's Manual. The general procedures used in DECICE to solve a problem are briefly described below.

The first step is data input and initialization. The input data include element topology, material properties, initial and boundary conditions, etc. Using the input data, DECICE automatically does the following: forms equations for the discrete elements, determines time step

increments, and checks stability conditions for the user defined (as input) solution scheme. Then, DECICE will do the following at each time step:

1. Interaction and Applied Forces are computed for each element. The computation of interaction forces is based on the information of interaction relationship between neighbouring elements. Applied forces include buoyancy, drag, gravity, and the forces due to boundary conditions.
2. Constitutive Behaviour Matrix, for strains and stresses, is calculated using the prescribed material properties. When an element is judged to be fractured, additional new element(s) will be generated and the stresses in the plane of the fracture are relaxed.
3. Motion and State of Elements are updated. The element motion including deformation and rotation are calculated from the dynamic equilibrium equations and element strain rates. The computation also updates element coordinates, neighbouring elements, etc.
4. History Output Files are generated to record element state and geometry for post-processing.

After all the above is done, the procedure is repeated for the next time step until the prescribed "end time" is reached.

The above description is only a very brief overview of the various procedures; more details are involved during numerical solution. Some details for part of the procedures will be given in the remaining sections of this chapter.

5.1.2 Structure and Ice Modelling

In the ERC tests, as described in Chapter 3, the structure was fixed on the floor of the ice basin. The structure was designed such that it can be considered as a rigid body, i.e. no deformation and any other motions occur during its interaction with ice. The tested ice (of both the ridges and sheets) which was quite brittle was moved by a boom against the structure (see Chapter 3).

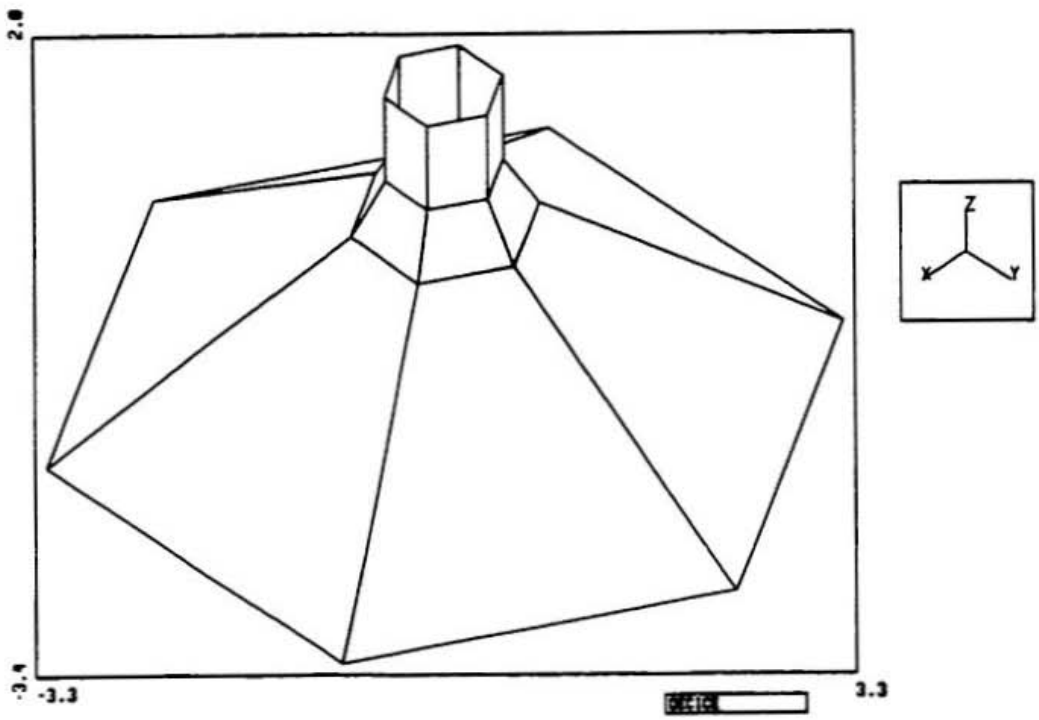

Figure 5.1 Simulated Small Neck MCS Structure

To simulate the MCS structure, a set of rigid shell elements were used as shown in Figure 5.1, which form a structure having exactly the same dimensions as those for the tested

structure. The rigid elements are connected together and fixed to ensure that the structure will experience zero deformation during the ice/structure interaction process.

The ice basin walls are simulated with two rigid bars, labelled as elements 2 and 3, respectively, as shown in Figure 5.2. These bars, like the MCS structure, are also fixed to ensure they will be motionless in the interaction process. The main function of these bars is to provide a realistic boundary condition for the ice between them. Both the sheet and ridge extend from one basin wall (the bar) to the other. Elements 4 and 1 shown in Figure 5.2 denote respectively the structure and the rigid boom used to push the ice against the structure.

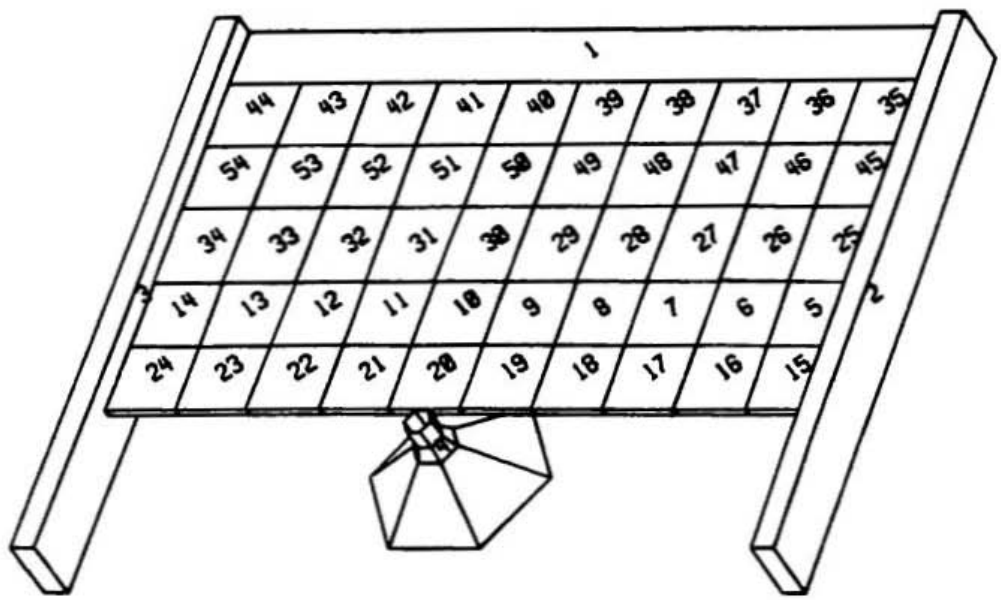

Figure 5.2 Simulated Ice, Basin Walls and the structure

As shown in Figure 5.2, both the ridge (elements 25 through 34) and the sheet are

discretized into a number of elements, prescribing the measured ice thickness. In DECICE (or any other DEM programs), each of these elements is treated as a distinct body. For instance, although the nodes of the neighbouring elements may have the same coordinates, DECICE treats them as different nodes. Before cracks occur, the ice should be a continuum. To simulate this, a "Zone Lock" provision in DECICE is applied to lock all the ice elements together. Separation occurs only when fracturing occurs which may appear either within the elements or along their mesh lines. Because the "zone lock" was applied only to the ice elements, the boundary conditions along the basin walls are not affected (viz., the deformation perpendicular to the walls is not permitted, while the deformation parallel to the walls is permitted).

The general boundary condition also includes prescribed velocity and load conditions. For all the ERC tests, the ice was pushed by a boom towards the structure at a speed of six centimetres per second. The condition is simulated by generating a push bar (element 1 in Figure 5.2) behind the ice and assigning it the above velocity. Thus, in the simulations, the ice will be pushed forward by the bar at a speed of six centimetres per second. The speed remains unchanged, no matter what interaction event occurs at the ice/MCS interface, until the bar contacts the structure. Since the bar is rigid it will not fracture when it is subjected to a very large interaction force.

The external loads acting on the ice consist of buoyancy and gravity (besides that provided by the constant velocity motion of element 1), which are simulated by assigning the measured buoyancy and gravity to all the ice elements. Because the velocity was relatively low,

the drag force exerted by the water was ignored. Before a real test starts ice freely floats on the water surface and its gravity and buoyancy balance one another. This condition is carefully simulated by sufficiently accurate computation of the correct waterline position for the ice. If the waterline is wrongly set, ice elements will experience vibrations due to the unbalanced buoyancy and gravity forces, which might not happen in real tests.

To simplify the simulation and save computer CPU time, linear elastic behaviour has been assumed for the ice. This assumption was based on the analysis presented in Appendix A of this thesis and the observations made during the ERC tests. It is also assumed further that the ice material is isotropic and homogeneous throughout the ice sheets or ridges. Appendix A shows that the error caused by this assumption is minor for the tests to be simulated.

The global coordinate system described in Section 3.2.3 is adopted for the present numerical simulation. Under this coordinate system, the waterline has a zero Z coordinate, the ice sheet, ridge, and the structure are symmetrical about X axis. Because the vertical ice loads on the structure are downward, they are negative in sign.

5.1.3 Failure Criteria and Ice Strengths

DECICE provides several criteria for judging various material failure. Because elastic brittle material behaviour was assumed for ice, the Mohr-Coulomb tension cut-off brittle failure criterion is chosen for the present simulation to judge the failure of ice elements. The elements

are allowed to fail along the mesh faces and/or through the centroid in each of the three modes: flexural, tensile, and compressive. Within DECICE the failure criterion is defined below.

An element in pure bending has the maximum tensile stress at either its upper surface fibre or its lower surface fibre, depending on its direction of bending. The elements may also be subjected to direct (or axial) stresses. The maximum total stress σ_b is a vector sum of all the stresses in the direction under consideration. When the stress condition satisfies the following relationship, the element is judged to have fractured.

$$\sigma_b \geq \sigma_f \tag{5.1}$$

where σ_f is the measured flexural strength of the ice. The crack is generated along the face perpendicular to the direction of maximum stress σ_b.

Tensile failure occurs when the minimum principal stress σ_3 is larger than or equal to the tensile strength of the ice. The crack is along a plane whose unit normal is aligned with the major principal axis (the direction of σ_1).

The compressive failure criterion is generally defined as

$$|\tau| \geq \tau_s + \mu_0 \sigma \tag{5.2}$$

where τ and σ are the shear and normal stresses on the fracture plane; τ_s is the shear strength

of ice, and μ_0 is the internal friction coefficient of ice defined by $\mu_0 = \tan \varphi$, where φ is the internal friction angle of ice.

Equation (5.2) can be directly applied to the mesh faces. However, because fracture of an element occurs through its centroid, an expression of the criterion in terms of principal stresses is required for judging the element failure. Using the relationship of the principal stresses in the Mohr-Coulomb criterion, this expression can be easily derived as follows

$$\sigma_1 \geq \sigma_c + \sigma_3 \tan^2\left(\frac{\pi}{4} + \frac{\varphi}{2}\right) \tag{5.3}$$

where σ_c is the unconfined compressive strength, and σ_1 and σ_3 are the major (maximum) and minor (minimum) principal stresses, respectively. The unconfined compression strength σ_c and the shear strength τ_s have the following relationship

$$\tau_s = \frac{\sigma_c}{2}\left(\sqrt{\mu_0^2 + 1} - \mu_0\right) \tag{5.4}$$

In other words, only two parameters are required to define this criterion. DECICE requires σ_c and φ to be input. If all principal stresses are different in magnitude, there are two equally probable fracture planes which are perpendicular to the σ_1-σ_3 plane and make angles of $\pm(45° - \varphi/2)$ with the major principal axis (the direction of σ_1).

The above Mohr-Coulomb criterion requires a total of four user-defined parameters:

flexural strength σ_f for the flexural failure, compression strength σ_c and the internal friction angle φ for compression failure, and σ_t for tension failure. In the ERC tests, only flexural strengths were measured. Therefore, the other parameters have been estimated. The estimation is presented in Appendix B.

5.2 Simulation of Sheet Ice and Structure Interaction

5.2.1 Ice Configuration and Elements

The ERC test Y1T1R1 was performed with sheet ice moving at a constant speed of 6 centimetres per second against the 1:10 small neck structure which was in "face-on" orientation (refer to Chapter 3). The test lasted for about 93 seconds with a real interaction duration of about 77 seconds which is equivalent to an ice length of 4.6 meters. At the moment when the ice began moving, the front edge of the ice was about 96 cm away from the front facet of the structure (at waterline level). At the 16th second after the test started, the structure and the ice contacted one another; hence, the 16th second will be taken as the staring time (zero second) for the comparison of the test with the simulations to be shown in Figures 5.4, 5.7, 5.8, and 5.24. In other words, the real test time is equal to the time shown in these figures plus 16 seconds.

The total length of ice sheet extended to about 9.5 meters (only 4.6 m was used in Y1T1R1) from its front edge to the first ridge which was used for the later test Y1T1R2. Because the sheet ice which was not directly involved in the interaction might also have an effect

on the interaction (by providing certain boundary condition), an ice sheet of 9 meters long has been simulated to include this effect. To reduce the simulation time (CPU time), the structure is set to nearly contact the front edge of the simulated ice, which means that the simulation begins at the 16th second of the test time. Figure 5.3 shows the configuration of ice and structure.

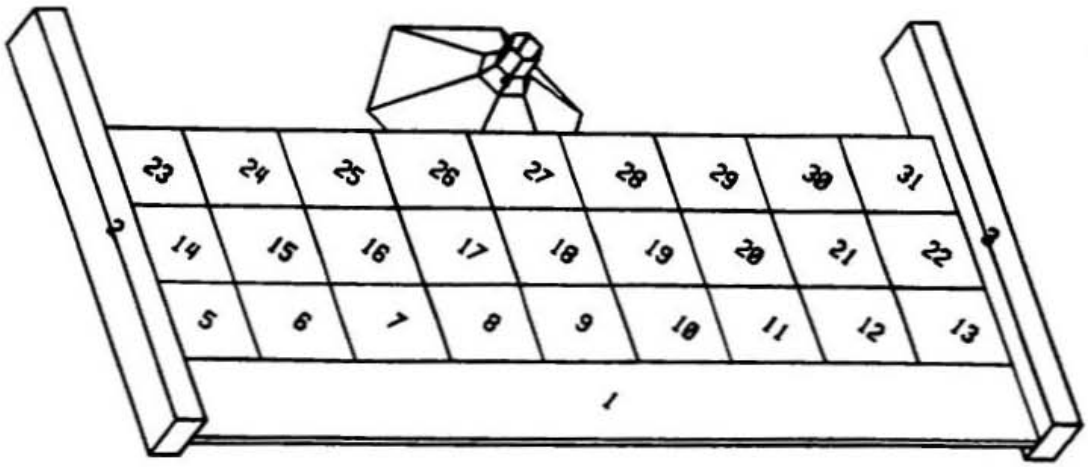

Figure 5.3 Ice Sheet and Elements

The ice sheet is discretized into 27 elements and numbered from 5 to 31. Elements 2 and 3 are rigid bars simulating the ice basin wall. Elements 1 and 4 simulate the boom and the structure, respectively. No additional restraint is applied to the boundaries of the ice sheet, which realistically simulates the boundary conditions in the physical tests.

5.2.2 Overview of Simulation Results

In the simulation, the ice sheet was set to move at 6 cm/s (ice speed in the test) towards the structure. The whole simulation lasted for 86.6 seconds which is slightly longer than the actual test duration. Time history of the global forces on the structure obtained from simulation together with the measured loads are plotted in Figure 5.4. Figure 5.5 shows the crack pattern of ice at 78th second of the simulation time.

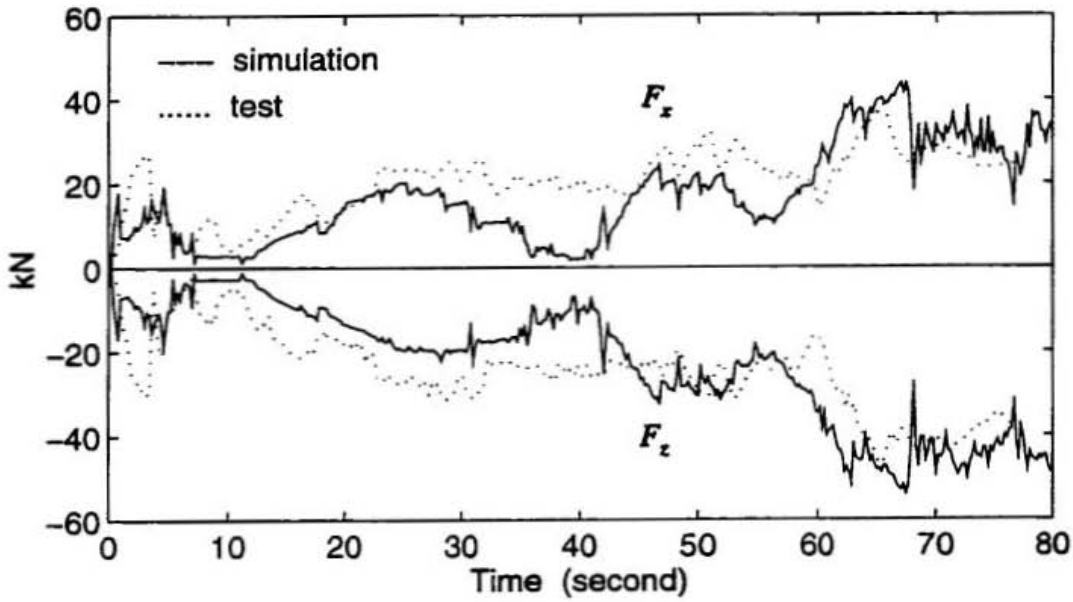

Figure 5.4 Simulated and Measured Global Sheet Loads

Under the coordinate system used in this thesis, the horizontal forces, F_x, acts along the positive direction of X axis (i.e. the direction of ice motion), thus appear above the reference line (the straight horizontal line) in Figure 5.4. The vertical force, F_z, acts downwards and is opposite to the positive direction of Z axis, and hence is located below the reference line. This

will also be applied to all the plots of F_x and F_z in the rest of this chapter.

Although there is an apparent difference in the measured and the simulated loads (Figure 5.4), the overall trend agrees well, especially in the latter portion (after 57th second) of the force time history in which both simulated and measured maximum loads occurred. During the time range the test lasted, the simulated maximum horizontal and vertical loads are 43.8 kN and 53.9 kN respectively, compared to 40 kN and 50 kN for the measured maximum horizontal and vertical loads. The simulated maximum loads occurred at 67th second after the ice first contacted the structure, while it was 65th second for the measured maximum loads. Considering the complexity in the interaction process, the closeness in both magnitude of the maximum loads and the moments that occurred are quite satisfactory.

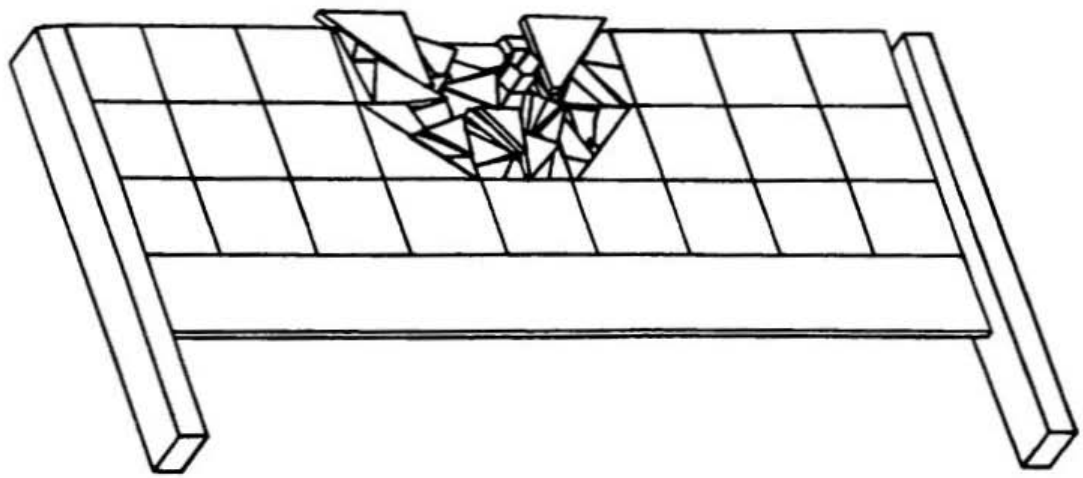

Figure 5.5 Ice Sheet/MCS Interaction Scenario at the 78th Second

5.2.3 Effect of Element Size

To study the effect of element size (mesh size), several meshes were tried. Figure 5.6 shows a very fine mesh in which the ice sheet consists of 120 elements. The results of the simulation with this fine mesh are plotted in Figure 5.7 as the dotted lines. For the purpose of comparison, the simulation with the coarse mesh (Figure 5.3) is also plotted in Figure 5.7 as solid line.

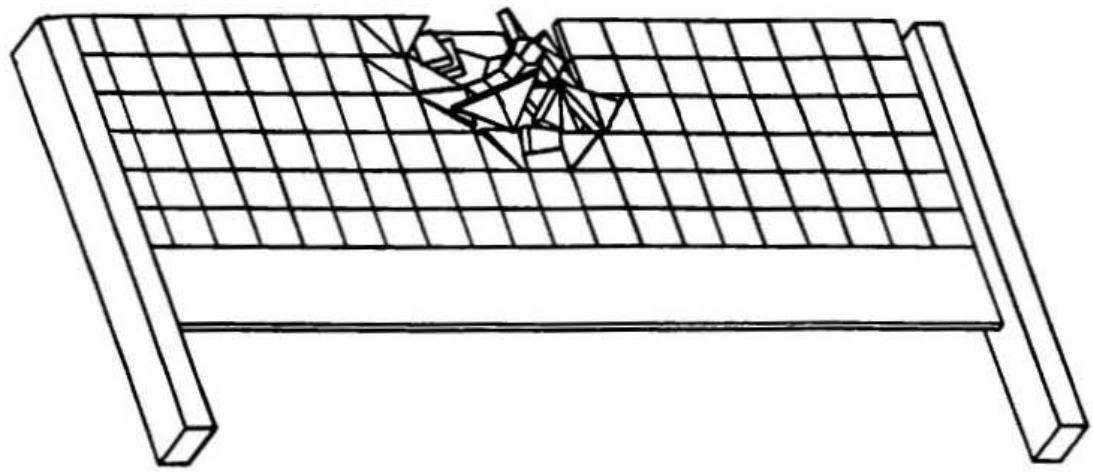

Figure 5.6 Interaction of Structure with Fine Meshed Ice Sheet at the 78th second

The crack patterns for the two meshes are also quite similar. The scenarios shown in Figures 5.5 and 5.6 are at the same moment of the interaction but for coarser and finer meshes, respectively. A comparison between them indicates the similarity in crack pattern for the different meshes. Although the initial element size of the coarser mesh is about 4.5 times larger than the element from the finer mesh, the difference in the average size of the broken ice pieces from these two meshes is relatively minor. This closeness of results in broken ice piece size

should mainly be credited to the DECICE code. Unlike the classical finite element technique, the DEM implemented in DECICE cracks an element once the stress in it reaches the prescribed failure criterion, and simultaneously, a new element is automatically generated. In this manner, a large element can be gradually cracked into many smaller elements. Consequently, the final sizes of the broken ice pieces for the coarser and finer meshes tend to be close.

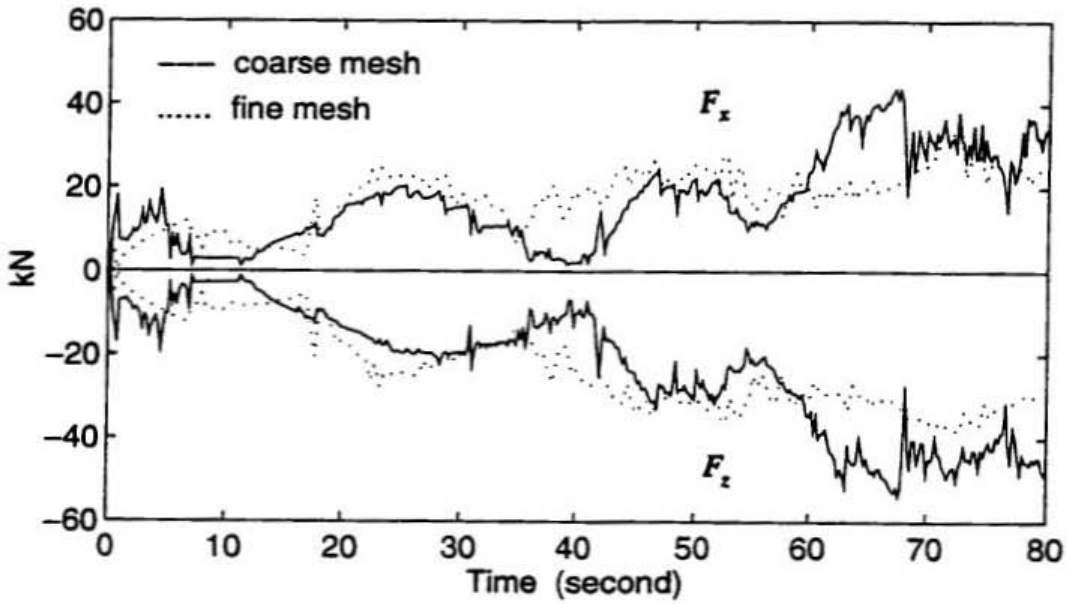

Figure 5.7 Effect of Element Mesh on Global Sheet Loads

Figure 5.7 shows that the simulated loads from these two meshes are generally quite close to each other. Considering the complexity in the interaction process, this result is quite satisfactory. On the other hand, the difference is also discernible. The fine mesh yields slightly larger loads till the 57th second and produces lower loads afterwards. Basically, the fine mesh results in a relatively mild variations in the time history of the global load, while the loads

simulated with the coarse mesh have more sharp jumps and drops. Moreover, the maximum load produced by the coarse mesh seems to be nearer the test results than the finer mesh.

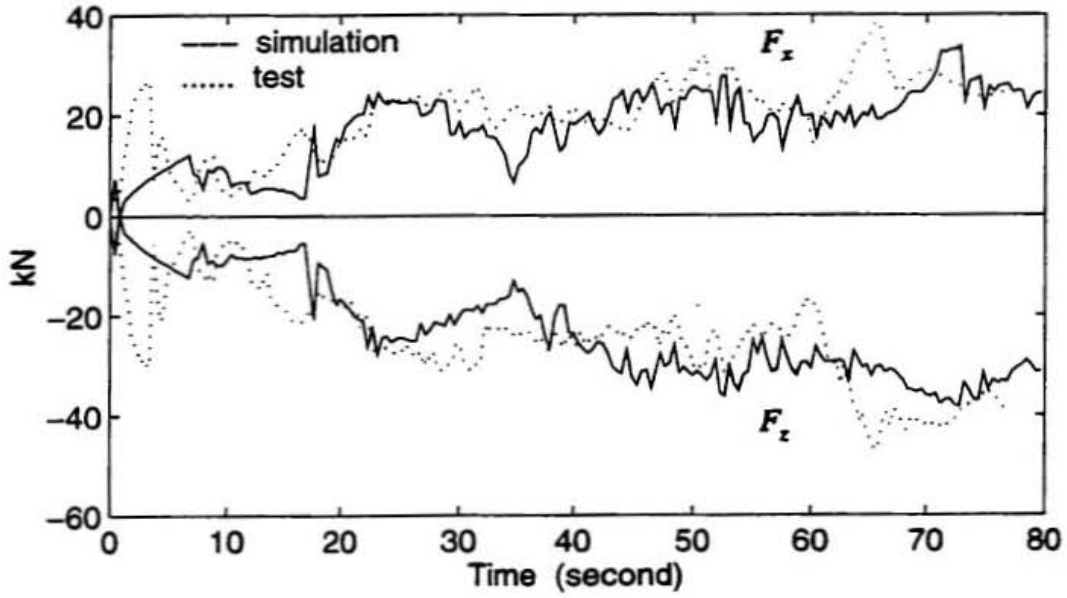

Figure 5.8 Measured Sheet Loads and the Simulation with Fine Mesh

To further examine the effect of element size, the simulation with the fine mesh together with the test measurement is plotted in Figure 5.8. From the overall appearance, this fine mesh seems to have improved the simulation result: a particularly good agreement is obtained for the middle portion of the time history record (from the 20th to the 60th second). However, the simulated loads are significantly lower in the first portion (from 0 to 20 seconds) and the last portion (from 60th to 71th second). The simulated maximum loads are significantly lower than the measured ones as well. As shown in Figure 5.4, although the simulation with the coarser mesh produces loads lower than the measured forces in the first portion, it agrees well during

the later portion of load history which contains the maximum load and may be more important in the sense of design consideration. Hence, the finer mesh may be better only for some situations and not for all.

The above problem is one of the general problems encountered in the use of the DECICE code. Before a further discussion of this problem, let's look at what happened in the actual physical test. A major crack, as seen in the recorded video tape of the physical tests, has propagated as far as a few meters away from its starting point, which has two direct results: a drop in interaction force and release of the internal stresses accumulated in ice. After each major crack, the ice around the crack became more easily deformed (because of less restraint) and exerted less forces on the structure, and it usually took a while for the ice to move further to develop a high resistance (as high as before the cracking) on the structure. This is reflected as the wavy shape in the time history of the global forces. The major crack (usually large and long) might also generate a larger size of broken ice piece in the process of ice cracking or in the interaction process that followed. These larger pieces might pile up on the structure's surface or fall down onto the top of the impinging ice, and sometimes they might get stuck between the structure and ice sheet, as observed in the ERC tests. All these actions would generally create some complex conditions for the successive ice cracking process. As a result, the peak in the global load history becomes larger than the preceding ones. The major crack or collapse could lead to sharper drops in load history because the movement of larger pieces usually results in large changes in the force history. The values of peak loads became relatively stable after the process reached a certain stage up to which enough ice pieces had accumulated in front and on

the surface of the structure. This is also one of the reasons why sufficient time duration was used for a physical test and a simulation. The measured test record of force history (the dotted lines in Figure 5.4) reflects well the trend described above.

The fracture mechanism implemented in the DECICE code is on an element-to-element basis, that is, it does not consider the propagation of a crack away from the interaction zone. Once an element is assessed to be incipient to cracking, the crack appears only within this element. The code also releases the stresses in the element just cracked, but the stresses remains unchanged in its neighbouring elements, if they are not fracturing, to which the real crack should have propagated through. Thus, if the ice mesh is very fine (such as the one shown in Figure 5.6 or even finer), i.e., the element length (or width) is much shorter than the possible crack length (of the physical test), the resultant loads on the structure may vary in a milder manner. This explanation illustrates the case of the simulation with a finer mesh, shown in Figure 5.8, in which the mean force from the simulation is relatively flat and does not fully follow those large jumps and deep drops in the time history of the measured forces.

It should also be made clear here that the above discussions and reasoning do not mean that a coarser mesh is better than a finer mesh. In fact, an extremely coarse mesh may lead to a bad (even incorrect) simulation both in crack pattern and load history. If the DECICE code allowed cracks to propagate through more than one element, a finer mesh should be chosen. With the present implementation of the element-to-element fracturing mechanism in the current version of DECICE, an appropriate discretization should be the one that allows major cracks to

occur across the full length at a certain time step of simulation. This type of mesh may lead to some exaggerated jumps and drops in load history at early stages of interaction, but it will simulate better the trend of force variation in the later portion of interaction scenario in which the maximum loads usually occur. The discretization of the ice sheet (Figure 5.3) and the ridge as well as the ice sheet surrounding it (shown in Figure 5.2 and to be presented in the next section) is based on the above considerations.

5.2.4 Interaction of Sheet with Small Neck Structure

This subsection presents a relatively detailed analysis of the interaction process and the mechanisms involved in the sheet ice interaction with the small neck structure. The analysis is based on the information from the output of the simulation.

At an early stage of interaction, only element 27 is in contact with the structure (refer to Figure 5.3). Its displacement and rotations are shown in Figures 5.9 A and B. When element 27 is being lifted upwards, it is in down bending (top fibre in tension) about the X axis and in up bending (the bottom fibre in tension) about the Y axis. At the 0.96th second, the total stress along Y direction (which is a sum of all the stresses in this direction) reaches the bending strength, and thus, the element fractures and becomes two elements (the element 27 and 32), as shown in Figure 5.10. The fracture face is perpendicular to the direction of dominant stress which is bending stress in the Y direction in this case, thus the fracture face orientates in the X direction.

In the meantime, elements 26 and 28 are also deflected upwards. Unlike element 27, these two elements are subjected to up bending in both the X and Y directions, and the bending shear stress is dominant at the moment (0.99th second) when the fracture occurs almost simultaneously in these two elements which, as a result, break into four elements labelled as 26, 28, 33, and 34 (Figure 5.10).

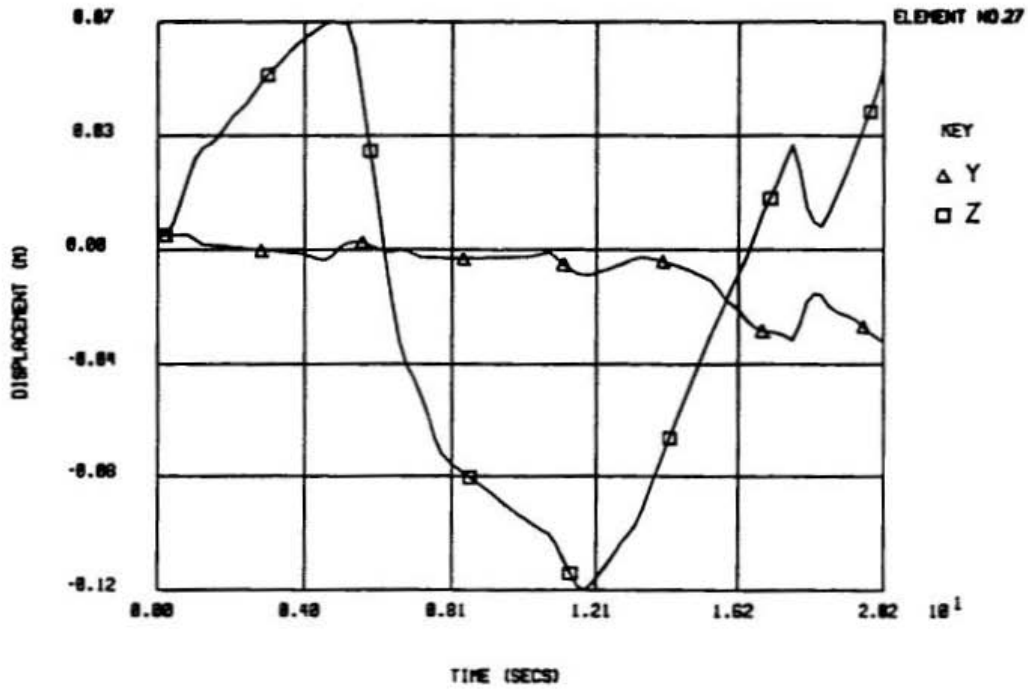

Figure 5.9 A Displacements of Element 27

The above fracture process is reflected as the first jump and the drop that follows in the time history of the global ice load shown in Figure 5.4.

After the cracks, the stresses on the fracture faces are instantaneously released, but the ice is still held in contact with the structure. As ice motion continues, the two front elements,

elements 27 and 32, are pushed farther against the structure, which gradually increases both the internal stresses and the force on the structure. At the 2.1th second, these two elements are separated from the ice sheet along the edge of element 18 (Figure 5.3). Element 27 (the new one, as shown in Figure 5.10) cracks at the 5.26th second with large bending stress being in the X direction, and symmetrically, element 32 also cracks, generating two new elements (elements 35 and 36) as shown in Figure 5.10. These cracks correspond to the second peak in the time history of the global forces.

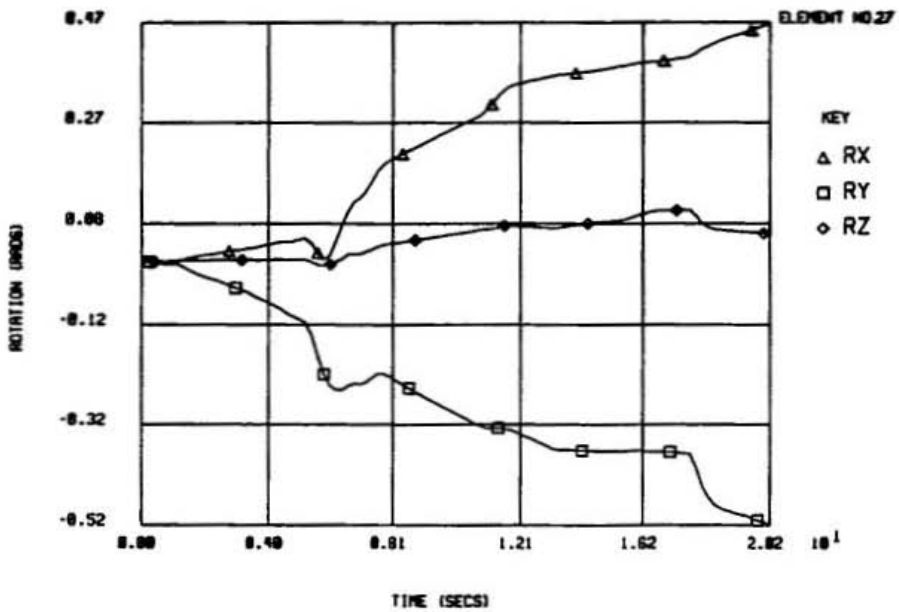

Figure 5.9 B Rotations of Element 27

The central (radial) crack along the X axis (the first crack in element 27), together with the cracks along the mesh lines of element 27 (along the X axis), reasonably simulate the radial cracks observed in the physical test. While the cracks in elements 26 and 28 together with a

separation line between element 18 and elements 35 and 36 form an approximate circumferential crack (Figure 5.10). In the tests, the time interval measured from the moment when the ice and structure contacted to the moment when the first circumferential crack occurred was in the range of 2 to 3 seconds (Metge and Weiss 1989). The simulation agrees fairly well with the test.

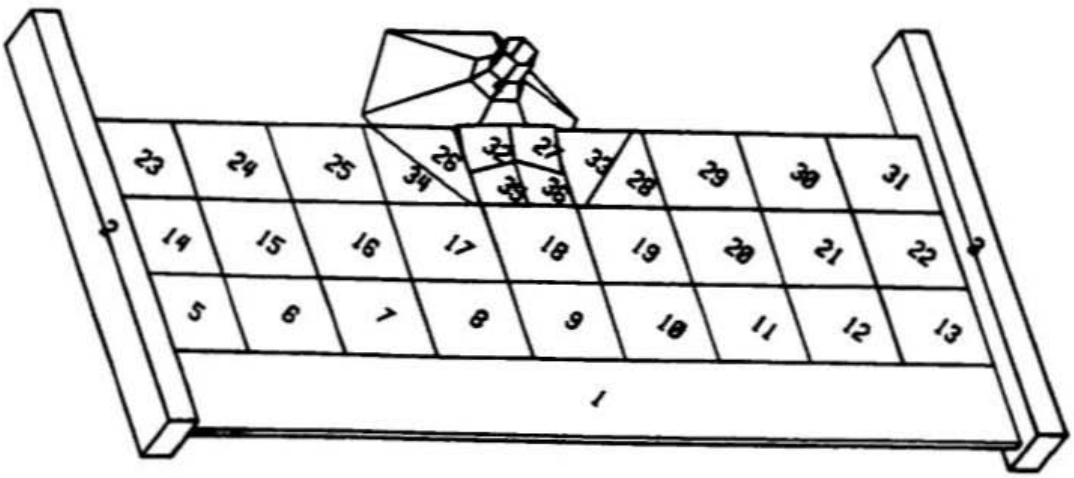

Figure 5.10 Cracks of Front Elements

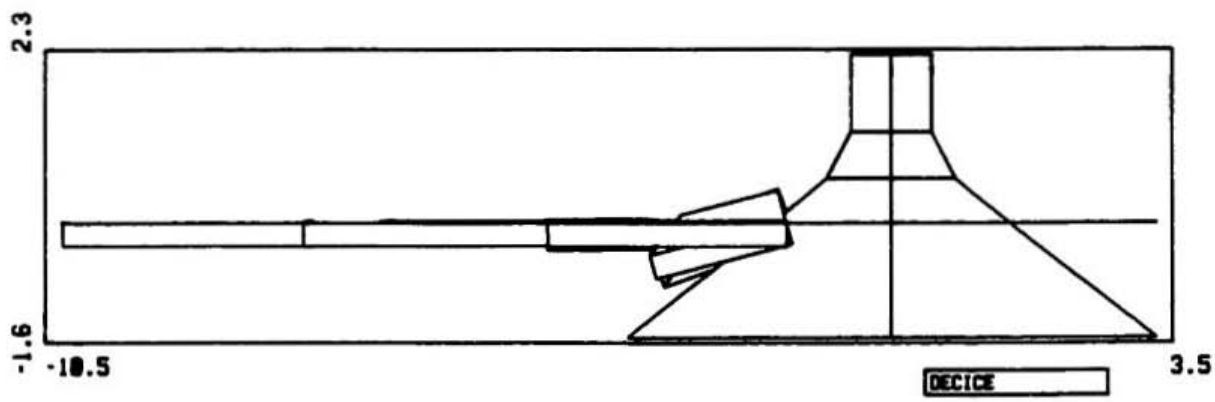

Figure 5.11 Side View of Ice Sheet/MCS Interaction Situation at the 9th Second

In the subsequent few seconds, elements 27 and 32 (Figure 5.10) gradually slide back under elements 35 and 36, and later down on the surface of the structure. Figure 5.11 shows a side view at one time step of this process. Meanwhile, the forces acting on the structure remain small (Figure 5.4).

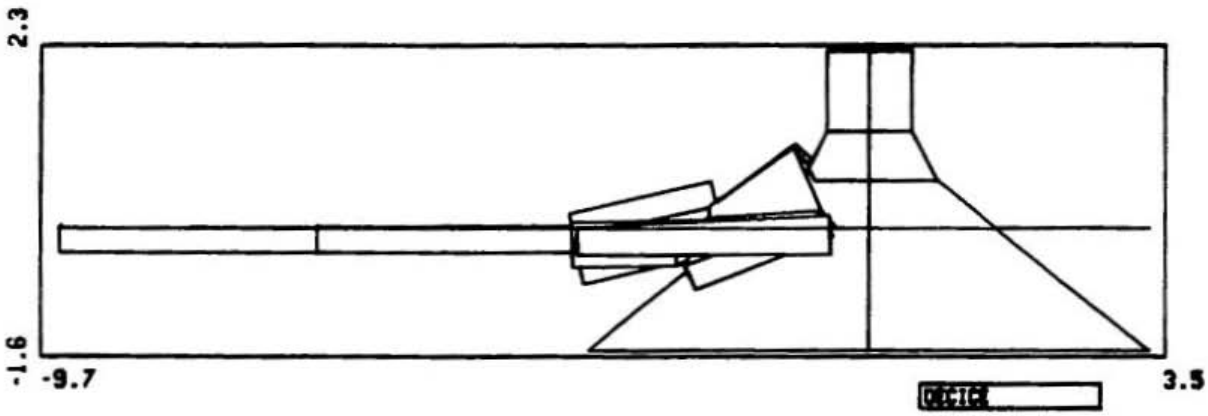

Figure 5.12 Side View of Ice Sheet/MCS Interaction Situation at the 22.5th Second

Starting at about the 12th second, ice and structure develop further firm contact, which leads to cracks in elements 27 and 32 (also fail in bending) at about the 16th second, and gives rise to a continuous increase in force history and a small drop at the moment when the crack occurs (see Figure 5.4). The horizontal force reaches its local peak when the front most pieces act against the transition between the main cone and the collar. Figure 5.12 shows a case for this portion of the interaction process.

Up to the 32th second of the interaction, the simulation generally agrees well with the test in global forces and crack pattern. In the next 10 seconds or so, the simulated forces have

a continuous decrease, and they are significantly lower than the measured forces. The decrease in force is caused by the easiness in clearing of the broken ice pieces. A closer look at the simulation data indicates that once the ice pieces pass the corners or the transition between the main cone and the upper portion, they easily slide back with little resistance. In addition, there was enough room between the structure and the un-cracked ice (element 18) to allow some ice pieces to slide down below the ice cover. These events did not happen in the test, which may be due to the disadvantage of having a coarser mesh.

The next cycle of interaction starts approximately at the 40th second and ends at about the 55th second, in which elements 17, 18, and 19 are cracked in a manner similar to that for elements 26, 27, and 28 (refer to Figures 5.3 and 5.10). However, the simulated forces follow more closely the trend of variation of the measured forces (Figure 5.4). It can be seen in Figure 5.4 that the peaks of the simulated forces as well as the measured horizontal forces are larger than those occurring during the previous cycle. The reason is that the ice pieces broken from previous interaction process play a key role in the subsequent interaction process. The broken ice pieces exert their weights as ice forces on the structure and they also introduce resistance to the ice behind to initiate a crack, Figure 5.13 shows one of those situations. In addition to the above, an extra force is also required to push the broken pieces either up or forwards on the structure surface. Test measurements have shown that the frictional resistance for ice pieces passing a corner is much higher than the sliding friction on a flat surface (Metge and Weiss 1989). Hence the clearing force may also be larger than that required for SCSs.

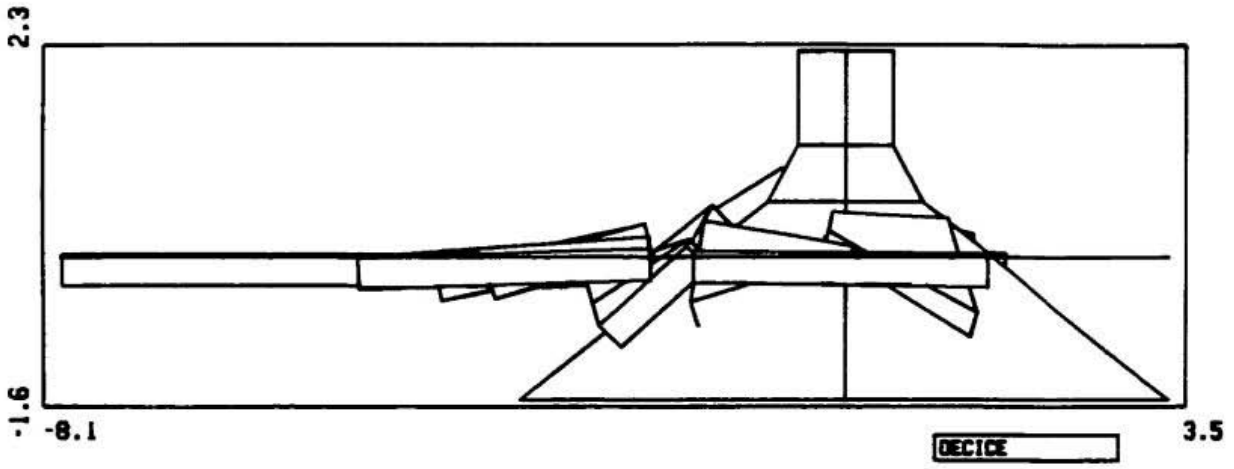

Figure 5.13 Side View of Ice Sheet/MCS Interaction Scenario at the 48th Second

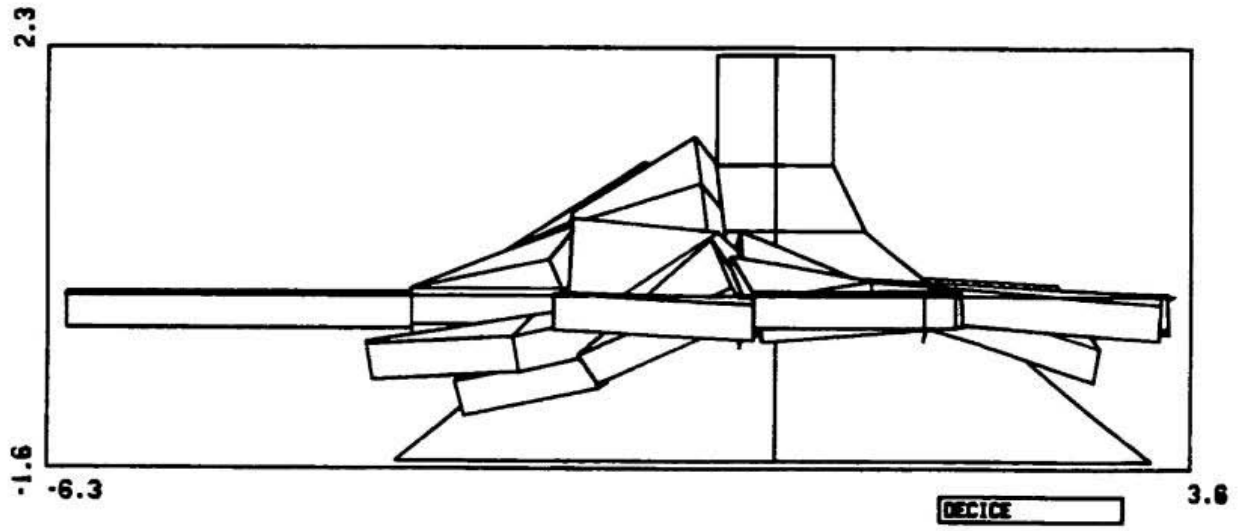

Figure 5.14 Side View of Ice Sheet/MCS Interaction Scenario at the 78th Second

The effect of the broken ice pieces becomes more significant in the next cycle (starting from the 55th second) in which the interaction becomes relatively stable. As the pieces

accumulate on the front and side facets of the structure, they form a rubble. The continuity of the interaction process keeps a certain number of ice pieces on the structure. Figure 5.14 shows a scenario of this phase of interaction. The forces for this phase, as shown in Figure 5.4, are much larger than before.

The rubble ice should be mainly responsible for this force increase. An obvious source for the force increase is the weight of the rubble ice. Because some ice pieces directly sit on or are partly supported by the structure, their weight (at least part of it) is exerted on the structure, instead of being supported by buoyancy. An additional effect of the rubble ice is that it creates more difficult situations for impinging ice sheet to fail in bending. An extreme situation may be that the advantage of a sloping structure in inducing bending failure of ice may be temporarily reduced or even lost. For instance, the intact ice in Figure 5.14 cannot contact the structure surface, rather it moves horizontally against the rubble ice. The force acting on the intact ice is mainly a horizontal force which pushes the rubble moving forwards and also upwards due to the existence of the structure's slope. At this moment, intact ice is mainly subjected to compression, instead of bending, and thus it can carry larger forces since the compression strength is much higher than the flexural strength. This situation creates a relatively large force on the structure. As the top part of the rubble is removed due to its falling down into water, the intact ice may either contact the structure or the ice pieces on it and thus the bending process may be resumed once again.

5.3 Simulation of Ridge and Structure Interaction

This section presents a simulation of ERC's test Y1T1R2 in which a ridge of 3.5 m wide and one meter thick was tested against the 1:10 small neck structure. Similar to test Y1T1R1, test Y1T1R2 was also performed with a constant ice speed of six centimetres per second.

5.3.1 The Ridge, Sheets, and Their Discretization

Figure 5.2 (in Section 5.1.2) is the ice configuration and the structure for this simulation. The three dimensional elements 25 through 34 are for the ridge to which all the mechanical properties given in Table 3.8 apply for this simulation.

Previous studies on SCSs have shown that the surrounding ice sheet can play an important role in the interaction of a ridge with a conical-shaped structure (refer to Chapter 2 of this thesis). To take account of the ice sheet effect, two pieces of ice sheet are simulated: one in front of the ridge and the other behind the ridge. Abdelnour (1981) stated that the effective width of each ice sheet is $\sqrt{2}l_s$. The characteristic length of ice sheet, l_s, is defined by

$$l_s = \left[\frac{E_s h^3}{12 \rho_w g (1 - \nu^2)} \right]^{0.25} \tag{5.5}$$

where E_s is Young's modulus of the sheet ice and equals 1136 MPa in this case (refer to Table

3.8), h is the ice sheet thickness and is 0.33 m for Y1T1R2 (see Table 3.2), ρ_w is the water density, g (=9.81 m/s^2) is gravity acceleration, and ν is Poisson's ratio which, as usual in elastic analysis, is set to be 0.33. Water density ρ_w = 1035 kg/m^3 is calculated with $\rho_w = \rho_s + \rho_b$, where ρ_s and ρ_b are ice density and buoyancy respectively and were given in Table 3.8.

With Equation (5.5), the characteristic length of ice sheet is calculated to be 4.4 meters. The calculated width of each of the ice sheets (along the X axis) is about 6 meters which was taken as the width for each of the two simulated ice sheets shown in Figure 5.2. Each sheet is discretized into two rows of elements, labelled as 5 through 24 and 35 through 54, respectively. Similar to the simulation of the sheet ice in the last section, three dimensional elements are used for the ridge and the ice sheets.

The principles for determination of element size, discussed in Section 5.2.3, are also applied to the present simulation. The factors taken into account include length of major cracks, crack pattern of the ridge and the sheets, etc. Other help came from the experience provided by Intera Technlogy Inc. (ITI) who was the developer and is the copyright owner of DECICE. ITI has applied this software to analyze ice ridge interaction with a ship (Intera Technology, 1986a) which has some similarities to the situation in our case (in their case, the ship bow width and element length were quite close, both are about 10 meters in dimension).

In the analysis being presented in this section, all the element numbers mentioned subsequently are referred to those given in Figure 5.2.

5.3.2 Comparison of Simulation with Test

The simulated time history of ridge global loads are plotted in Figure 5.15 as the solid lines. For the purpose of comparison, the measured loads are also plotted in the same figure as dot lines.

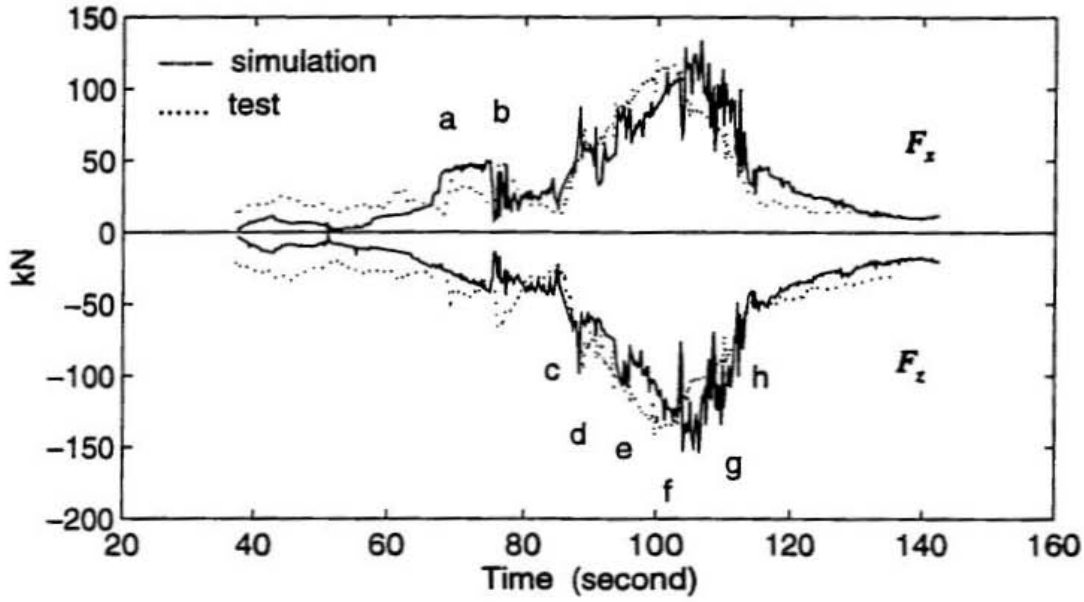

Figure 5.15 Time History of Simulated and Measured Global Ridge Loads

Figure 5.16 is a sketch of the overall ridge crack patterns from the test and the simulation. The distance is measured from the center of the ridge (along the Y axis). A interaction scenario from the simulation is shown in Figure 5.17. A picture of ridge crack pattern which was taken after the hinge cracks is shown in Figure 5.18.

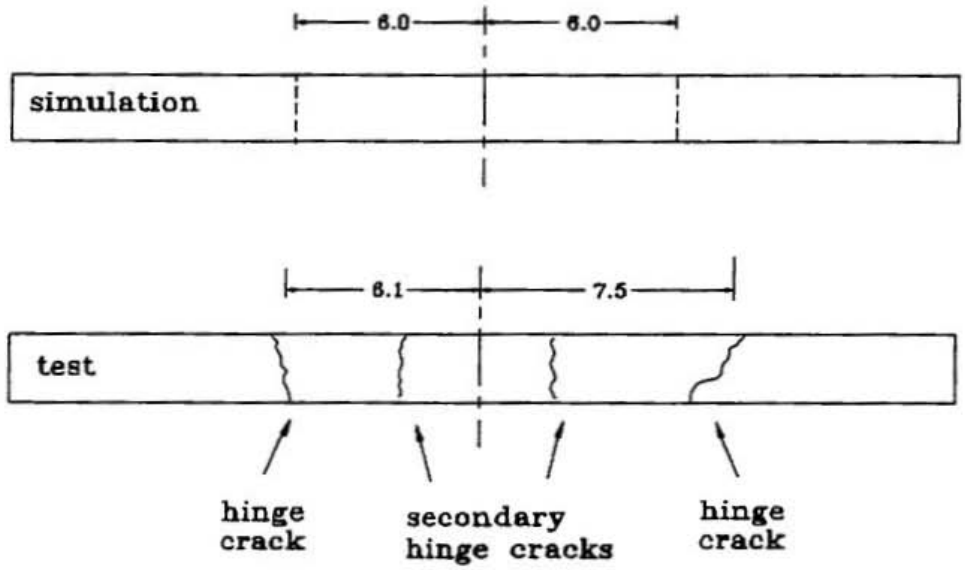

Figure 5.16 Measured and Simulated Ridge Crack Patterns

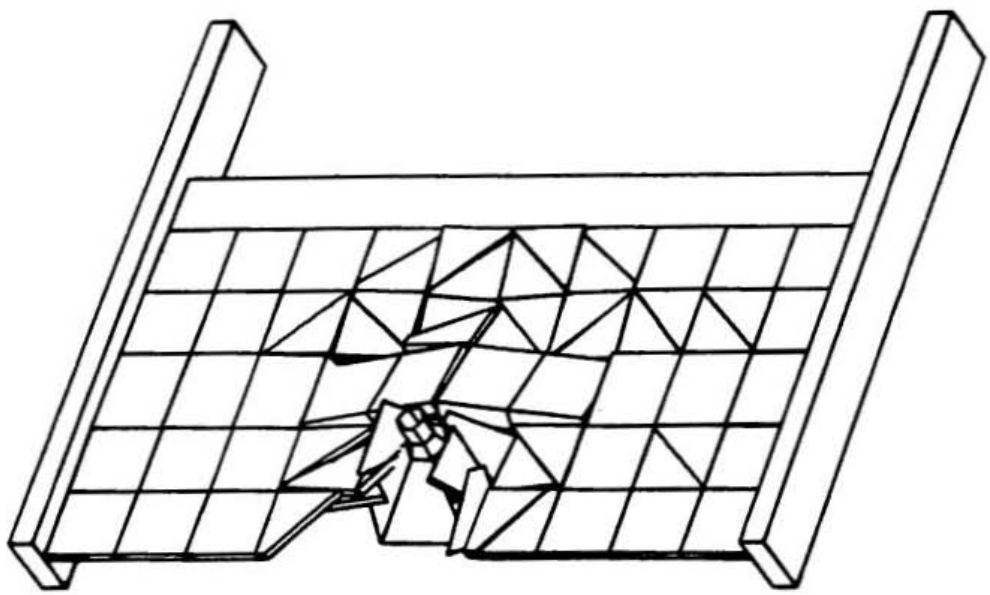

Figure 5.17 Simulated Ridge/MCS Interaction Scenario at the 116th Second

Generally, the simulated loads and crack pattern agree fairly well with those measured, as shown by Figures 5.15 and 5.16. The measured average distance from the first pair of hinge cracks to the center of the ridge was 6.8 meters, while the simulation yields a value of 6 meters for this distance. The simulated maximum vertical load (F_z) is 154 kN, compared to 150 kN for the maximum measured vertical load. The maximum horizontal loads are 134 kN and 130 kN for the simulation and the test, respectively.

Figure 5.18 Ridge Crack Pattern of Y1T1R2

On the other hand, the simulation is not perfect. The most visible difference, as shown in Figure 5.16, is that the tested ridge experienced secondary hinge cracks during its clearing process, but the simulated ridge did not. In the test, the ridge was re-cracked at the moment marked by "f" in Figure 5.15, a few seconds after the first hinge cracks. In the simulation,

however, the ridge experienced only a central crack and one pair of hinge cracks which was followed by a clearing process without further cracking in the ridge segments (refer to Figures 5.16 and 5.17). The secondary hinge cracks made the clearing easier for the test. This difference is clearly reflected in the time history of the global loads. The measured loads sharply dropped immediately after the second hinge cracks and then decreased continuously, whereas the simulated load, though it decreases at the moment "f", went through a number of increases/decreases afterwards. As a result, the maximum test loads occurred at the moment when the first hinge cracks were formed, while the occurrence of the maximum simulated forces was delayed by a few seconds.

The simulation shows that the ridge failed in bending due to the moment about the X axis, which confirms that the general mechanism for ridge failure in the case of SCSs (see Chapter 2) is still valid for this MCSs. However, the simulation also shows that the ridge's front bottom edge fully contacted the front facet of the structure at the moment when the central crack was occurring. This is different from the assumption of point contact during ridge/MCS interaction. Hence, an appropriate theory is required to account for the new feature of the interaction. The requirement will be fulfilled by the equations to be developed in Chapter 6.

5.3.3 Relation of Interaction Process and Global Forces

The process of ice sheet (in front of the ridge) interaction with the structure for this test is similar to that described in the last section. Figure 5.15 shows that the simulated loads are

lower than those measured during the early stage of this portion of interaction (from beginning to the 67th second). One of the reasons for this is that the simulation started at a totally "zero condition" in which the structure was clean of ice and the forces on the structure was zero, but the test did not start at the zero condition. In fact, the structure surface was already covered with ice pieces from the preceding test run. In the simulation, it took a while for the broken sheet ice pieces to accumulate in front and on the surface of the structure to maintain a relatively high load. All these resulted in the lower values for simulated loads.

As the interaction process during the simulation proceeds, more and more broken ice pieces accumulate on the surface of structure. These pieces directly increase the ice loads (see the analysis in the last section). One relatively larger piece of ice on each side of the structure is firmly lodged against the neck, shown in Figure 5.19. Because the slope of the neck is deeper, the horizontal component of the force becomes larger. This situation is also partly responsible for the relatively high level in the horizontal global load between the moments "a" and "b", as shown in Figure 5.15.

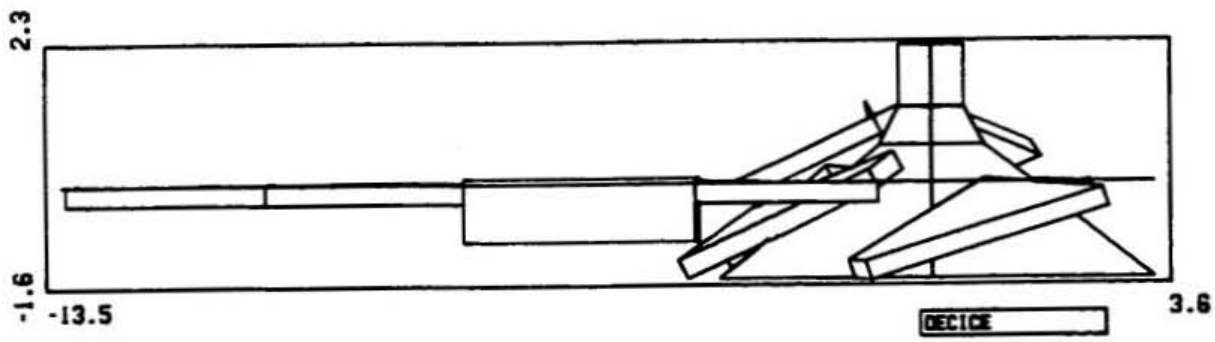

Figure 5.19 Ridge/MCS Interaction Scenario at the 72nd Second

At the moment "b" the ice pieces slide aside and then down into water, thus resulting in a drop in the force history. The remaining part of the elements 9 and 10 (their front part has broken off) begins cracking and separating from the ridge. Figure 5.20 shows a scenario for this period of the interaction.

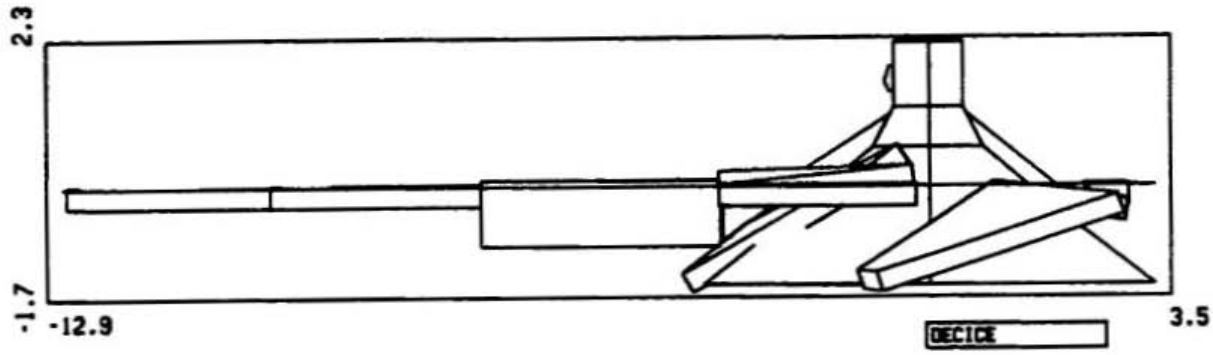

Figure 5.20 Ridge/MCS Interaction Scenario at the 82nd Second

As the motion continues, the front bottom edge of the ridge contacts the ice pieces on the lower part of the structure and causes them to slide upwards on the surface and forward to the front side facets. At the moment "c" (Figure 5.15), the ridge gains a firm contact with the structure, and begins deflecting upwards. In the mean time, small rotations about the Y axis also starts, and the global forces quickly increase. When this process develops to a certain stage the central crack forms (at the moment "d" in Figure 5.15). Figure 5.21 presents the situation at the moment just after the central crack. Up to the central crack the sheet behind the ridge is still connected to the ridge, but part of the front sheet is separated from the ridge. The central crack is accompanied or immediately followed by the cracking in elements 49, 50, 38, 47, 41, 52, etc. Figure 5.21 shows the crack pattern detected and marked by DECICE.

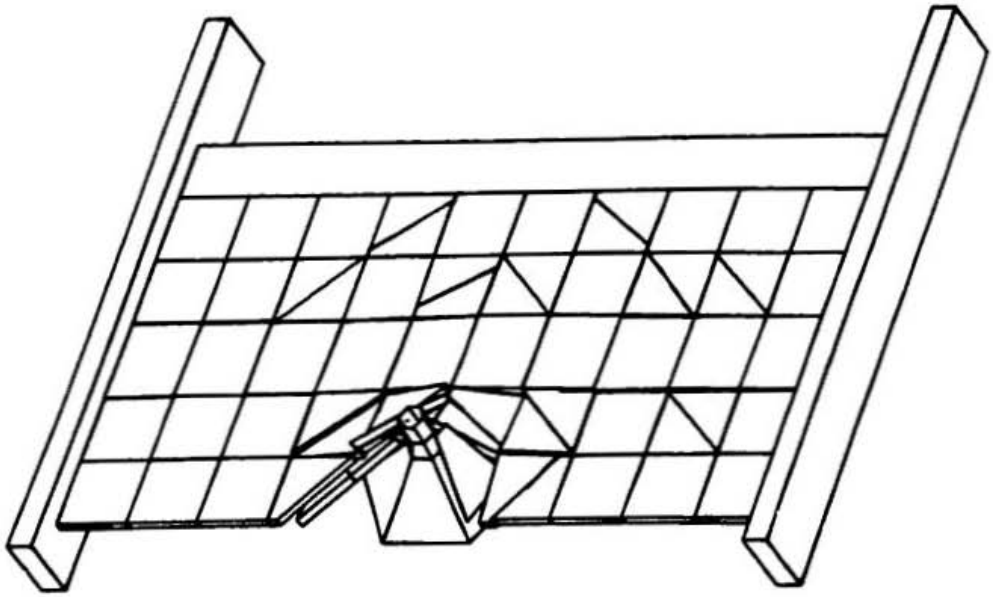

Figure 5.21 Crack Pattern immediately after Event "d"

It is worth pausing a while to examine the difference in the cracks detected by DECICE and those observed in physical tests. In the numerical simulation with DECICE, when the stress in an element or its faces reaches a prescribed failure criterion the program assesses that a crack has formed and delineates the crack immediately. The cracked ice pieces (elements), however, are still firmly in contact with one another along their fracture faces, and it appears no crack has occurred. The crack takes a while to develop to a form to be visible to human eyes. If we assume the visible crack to be half a millimetre or above (under the condition that the crack is about 10 meters away from eyes, or farther), it takes a fraction of a second to a few seconds from the moment when the crack is judged to occur to the moment at which the crack develops to this given width. The real time interval depends on the interaction situation and the distance

from the crack to the eyes. In the physical tests, such as those of the ERC tests, the cracks detected by our eyes were those at their well developed stage. Therefore, a crack seems to appear slightly earlier in the simulation than it does in the corresponding physical test.

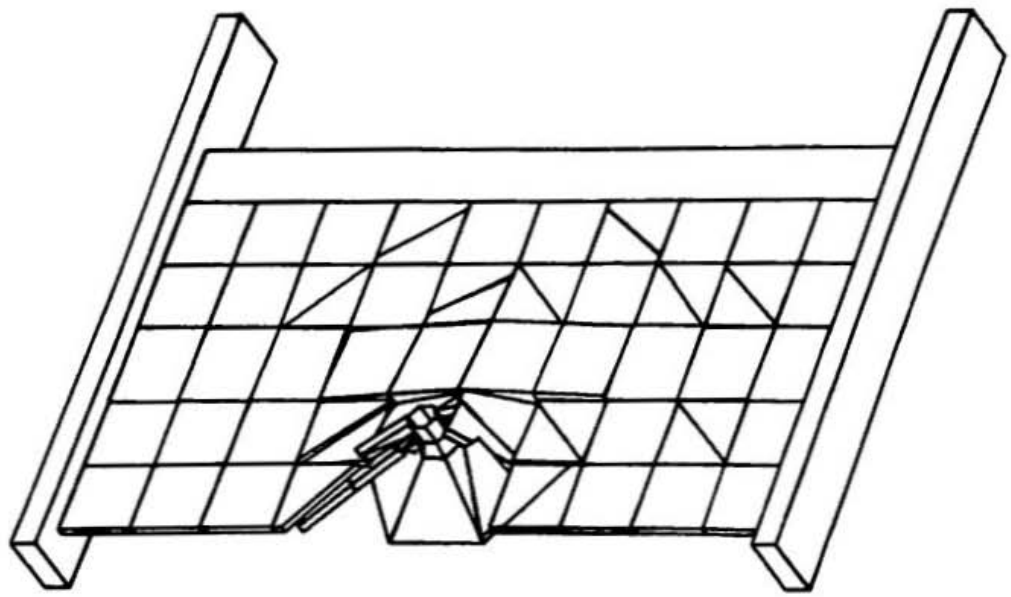

Figure 5.22 Crack Pattern during Event "e"

While the ridge continues its upward deflection and rotations after the central crack, the central crack extends into the sheet, resulting in the separation along the mesh face between sheet elements 49 and 50. Meanwhile, part of the sheet (part of element 8) in front of ridge (element 28) separates from the ridge. At the moment "e", the bending stresses in the Y direction on the mesh face between elements 31 and 32 reach the failure criterion and is judged to have separated, which is followed by the separation along the mesh face of elements 27 and 28. The ridge crack (element separation) is accompanied with the separation of a few ice sheet

elements (elements 7, 11, 47, 48, and 51) from the ridge, as shown in Figure 5.22. This event can be considered to be the beginning of the hinge crack process because this part of the hinge crack is detected only by DECICE but invisible to the human eyes (as previously explained). What is interesting is that the recorded loads from the test also has similar but milder variations just before the event "e" occurs (Figure 5.15), but no obvious hinge cracks are seen from the test video tape at that moment. It is questionable whether a crack has already occurred in the test, which might be invisible at that moment.

As the ice moves further towards the structure, the ice forces continuously increase. At the moment "f" in the simulation, the two ridge segments experience a sudden sliding back (decrease in both deformation and rotations). This results in the sharp drop in force history. The hinge cracks observed from the test should have occurred at an instant between the simulated events e and f. When they were occurring, a sharp movement (jerk) of the ridge was also observed; it was noted that the secondary hinge cracks occurred during the event marked "f".

After the event "f", the simulated ridge segments are in a long sliding (first up then down) and rotation process (the clearing process). The sheet ice behind the ridge gets gradually cracked and broken-up to give room for further sliding-down and rotation of the ridge segments. The dominant motion in this period of interaction is the rotation around the Z axis, which is mixed with motions in all the other five degrees of freedom. Figure 5.23 shows one of the scenarios after the event "h". The loads in this clearing process is eventually reduced to a level similar to that for sheet ice loads (Figure 5.15).

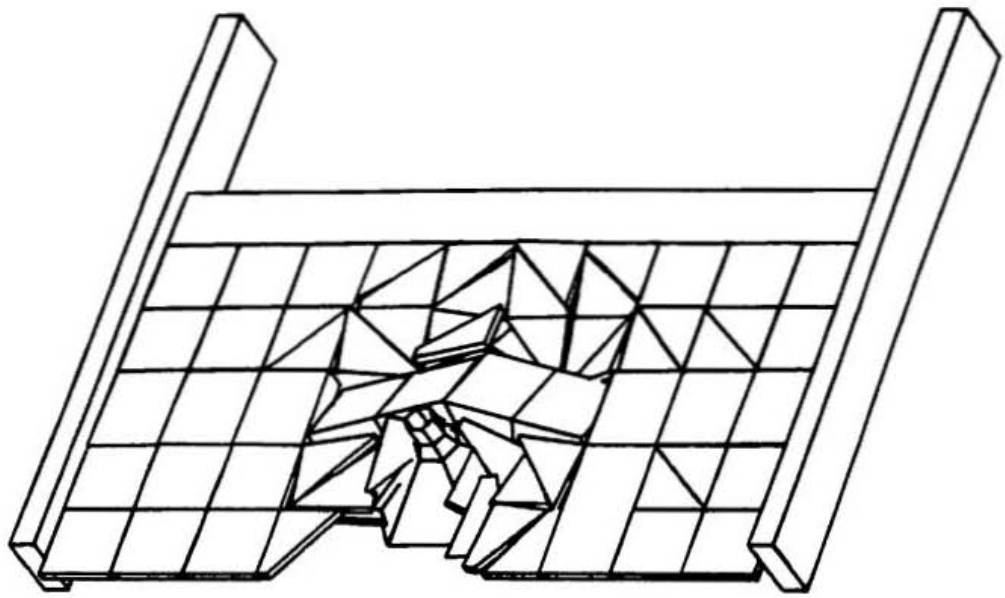

Figure 5.23 The Ridge-Sheet Ice Clearing Process

5.4 Numerical Study on the Effect of Neck Size

It was stated in previous chapters that industry has desired a large vertical neck whose diameter is only slightly smaller than the waterline diameter of the main cone, and was concerned about the possible adverse effect of this large size neck on ice loads. Although two neck sizes were tested (Chapter 3) and the data from the tests with were compared (Chapter 4), they still need further studies for the reasons given below.

For analysis of the neck size effect (or any other factors), the ideal condition in a series of physical tests should be like this: only the neck size should vary and all other parameters

should remain constant; then comparison between them would show the effect of neck size. Unfortunately, because of the limitations in the test technique, all our tests did not perfectly satisfy this strict condition, and therefore many other parameters inevitably played a role in the variation of ice forces. The problem is that no existing analytical approach can completely eliminate the effect of all the parameters other than neck size. Although the analysis given in Chapter 4 has taken many parameters into account, there were still some parameters whose effect were not eliminated. The effect of these remaining parameters might be hidden in the results of the analysis.

An alternative to the physical experiment for the study of neck size effect is to do numerical simulation. An advantage of the numerical simulation is that the parameters can be easily controlled. In the present case, two comparable sets of simulations were performed for both the sheet ice test (Y1T1R1) and the ridge ice test (Y1T1R2). The small neck structure (Figure 3.1) was used in the first set whose results have been presented in Sections 5.2 and 5.3 for tests Y1T1R1 and Y1T1R2, respectively. In the second set of simulations, the neck of the structure was replaced with a larger neck with other parameters remaining unchanged, i.e., the structure shown in Figure 3.2 was used in the second set of simulations. These results are presented in Subsection 5.4.1 for sheet ice and Subsection 5.4.2 for ridge ice. Comparison of the results from these two sets of a simulations are expected to show the effect of large neck on ice forces.

5.4.1 Ice Sheet Interaction with a Large Neck Structure

Similar to the simulation presented in Section 5.2, the ice dimensions and mechanical properties measured in test Y1T1R1 (Tables 3.2 and 3.8) were taken as inputs for this simulation. The only difference is the neck of the structure, i.e., the large neck structure (Figure 3.2) is used for this simulation. The loads from this simulation, together with those from the simulation for the small neck structure (Figure 5.4), are plotted in Figure 5.24.

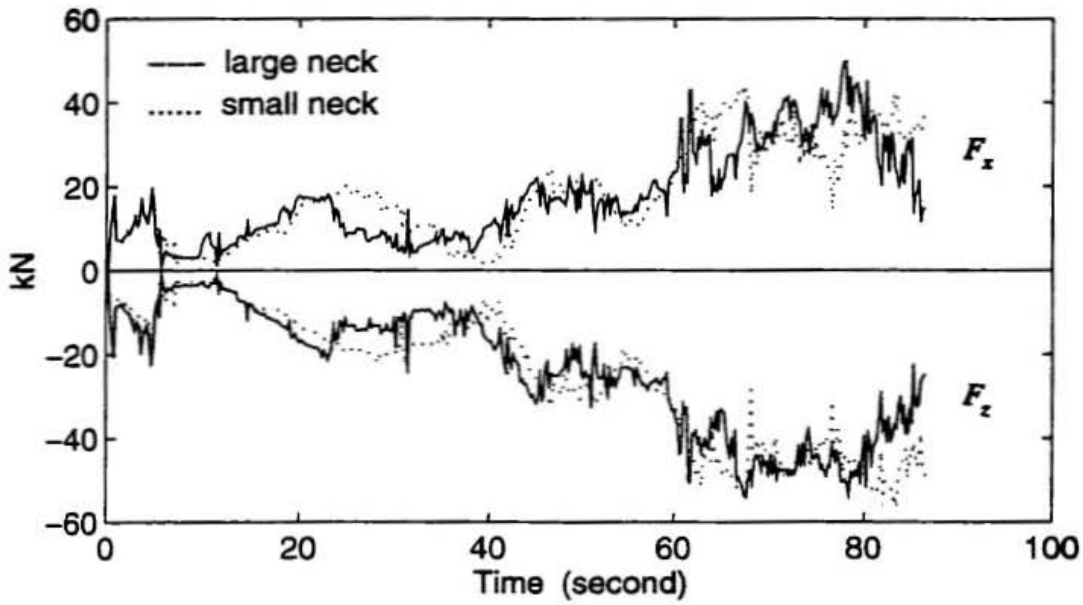

Figure 5.24 Simulated Sheet Loads for Large and Small Neck Structures

Figure 5.24 indicates that the difference in forces from the two simulations are noticeable but not very big. As discussed in Section 5.2, the later portion of the interaction is of greater importance because both simulated and measured maximum loads occurred in this part.

Therefore, the analysis and comparison of results are focused on this portion (after 57th second of the simulation). The overall trend for this portion is that the simulation with large neck structure yields larger horizontal peak force but smaller vertical force (see Figure 5.24). The maximum horizontal and vertical forces simulated with the large neck structure are 49.8 kN and 51.1 kN, respectively. Compared with the maximum simulated loads for the small neck structure (43.8 kN and 53.9 kN for the horizontal and vertical maximum forces, respectively), the counterparts for the large neck structure increase by 13.7% for the horizontal load component and decreases by 5.2% in the vertical load component.

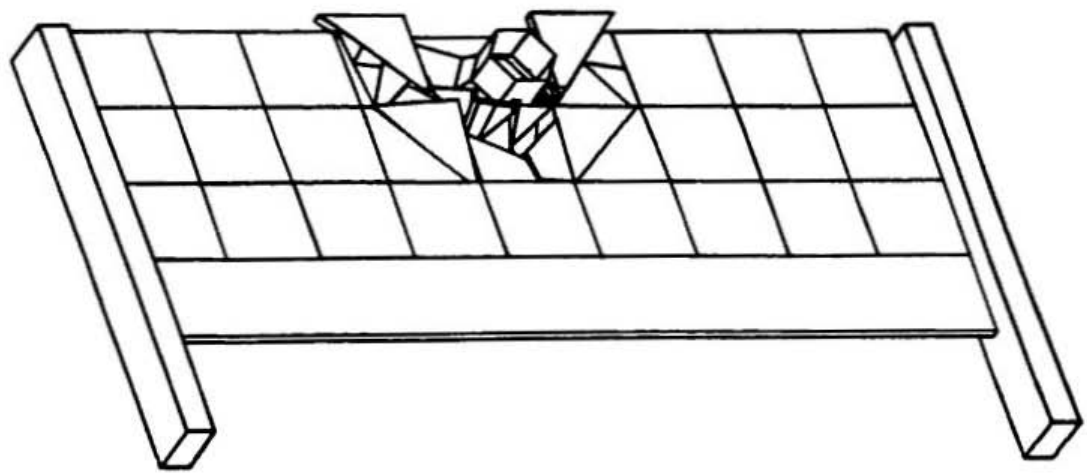

Figure 5.25 A Scenario of Sheet Ice Interaction with the Large Neck Structure

The above results reflect two aspects of the effect of the larger neck on sheet ice loads. The wider neck partly prevents the ride-up of the broken ice pieces, which increases the difficulties in deflection and bending of the impinging ice sheet. This gives rise to certain increase in the horizontal load. On the other hand, the large neck reduces the length of main

cone slope, or the area of structure surface between waterline and the neck (refer to Figure 3.2). Hence, less amount of ice pieces can sit on (or ride up) on the main cone. As a result, the vertical load to which ride-up component contributes a large portion becomes less than that for the small neck structure. Figure 5.25 presents a typical situation for this case.

The sheet ice crack pattern for this large neck structure is essentially the same as that for the small neck. The time history of the simulated loads for these two structure follow the same overall trend as well.

5.4.2 Ice Ridge Interaction with Large Neck Structure

Similar to the ice sheet interaction study presented in Section 5.4.1, the interaction of the ice ridge (Y1T1R2) with the large neck structure was investigated. The geometric configuration, mechanical properties, and element mesh size, etc., remained the same as those in the simulation for the small neck structure, while the structure was replaced by the large neck structure, shown earlier in Figure 3.2 of Chapter 3.

It is shown in Figure 5.26 that the ridge loads for structures with different neck sizes are quite close to one another. The simulation for the large neck structure yields a maximum horizontal load of 154 kN, and a maximum vertical load of 161 kN. Compared with the maximum simulated horizontal load (134 kN) and vertical load (154 kN) for the small neck structure, the large neck increases the horizontal load by 14.9%, and the vertical load by 4.5%.

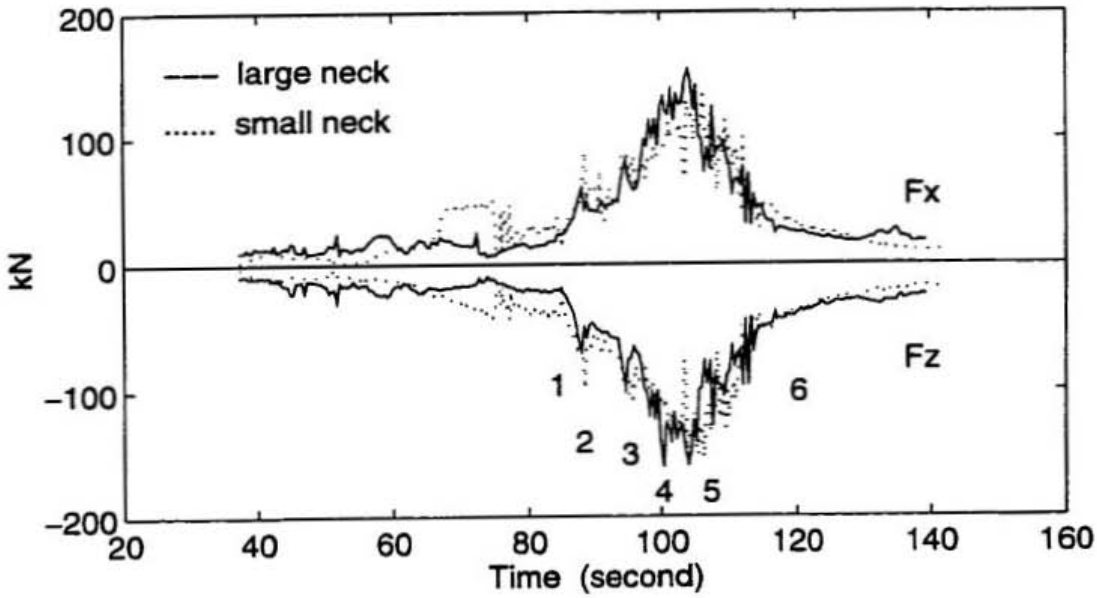

Figure 5.26 Simulated Ridge Ice Loads on the Large and Small Neck Structures

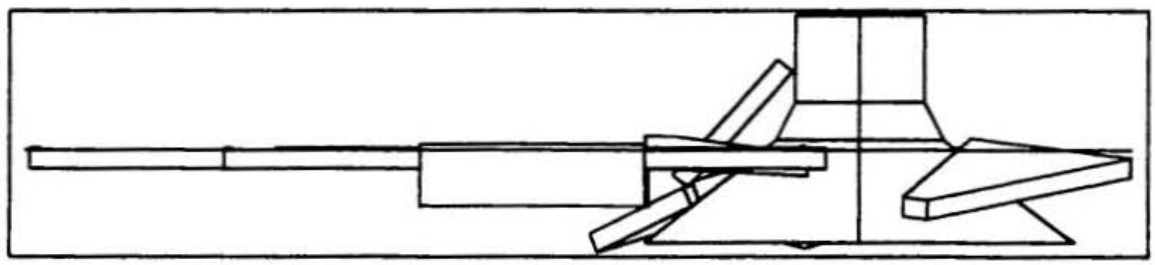

Figure 5.27 An Interaction Scenario of the Ridge Interacting with the Large Neck Structure

Similar to the case of sheet ice, the mechanism and process of ridge cracking exhibited for the large neck structure are essentially the same as those for the small neck structure. Because the large neck significantly reduces the area of the main cone slope, fewer sheet ice

pieces can accumulate on the cone. As a result, the sheet ice loads for the period of interaction just before the ridge contacts the structure are much lower than those for the small structure. Figure 5.27 is a typical scenario for this period of interaction, which shows that there are fewer ice pieces on the cone and some pieces have slid off the structure.

There is a notable difference in the effect of neck size on sheet ice loads and ridge ice loads. The large neck increases the maximum horizontal sheet ice load, but reduces the vertical load component. However, the large neck increases both maximum horizontal and vertical ridge loads even though the increase in vertical load is at a much lower rate. The main reason is that the ridge segments are more difficult to be cleared off the structure. Because of their large size, the ridge segments are subjected to greater resistance than the sheet ice. This larger resistance combined with the pushing forces from the ice sheet behind the ridge segments creates an unfavourable situation as shown in Figure 5.28: movement of the ridge segments are partly blocked and larger portion of ridge segments' weight is supported by the structure instead of the water buoyancy. Since the loads exerted by the ridge segments dominate the total ice loads, the overall vertical ice loads have, thus, increased.

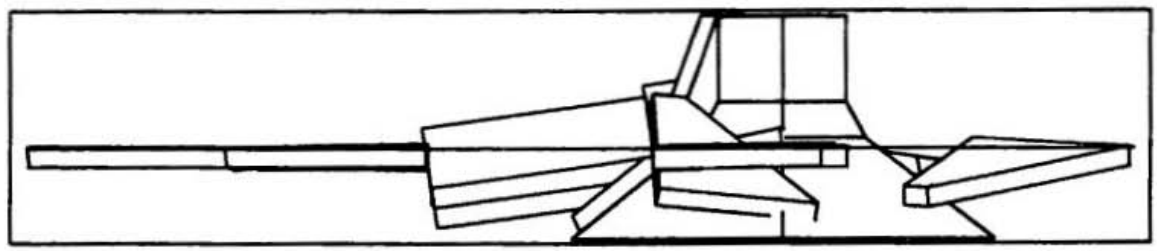

Figure 5.28 Side View of a Scenario of Ridge Clearing Process

5.4.3 Discussions of Neck Size Effect

The effect of neck size on ice loads from the present simulations can be summarized as follows.

1. The maximum horizontal ridge loads acting on the small neck structure and the large neck structure are 134 kN and 154 kN, respectively. Compared with the small neck structure, the large neck structure increases the maximum horizontal ridge load by 14.9%.
2. The maximum vertical ridge loads acting on the small neck structure and the large neck structure are 154 kN and 161 kN, respectively. Compared with the small neck structure, the large neck structure increases the maximum vertical ridge load by only 4.5%.
3. The maximum horizontal sheet ice loads exerted on the small neck structure and the large neck structure are 43.8 kN and 49.8 kN, respectively. The large neck increases the maximum horizontal sheet ice load by 13.7%.
4. The maximum vertical sheet ice forces exerted on the small neck structure and the large neck structure are 53.9 kN and 51.1 kN, respectively. The large neck decreases the maximum vertical sheet ice load by 5.2%.

The trend given in items #1 and #3 above agree with the results from the analysis of the physical tests given in Table 4.6 (Section 4.3.3) and Figure 4.12 (Section 4.4.3), i.e., the large neck increases the maximum horizontal forces for both ridges and sheets. However, the analysis of the physical tests show that large neck decreases the maximum vertical ridge load (Table 4.6) but increases the maximum vertical sheet ice loads (Figure 4.11); these trends of the neck

influence on the maximum vertical forces do not agree with the results of the numerical simulation given in items #2 and #4 above.

The disagreement could be caused by many factors; the major ones may be the errors in the analysis of the tests, the tests themselves, and the numerical analysis. As mentioned at the beginning of this section, the analysis of the tests does not eliminate all the factors other than neck size, which might be one source of the error. If an error of 10% (or even more) in the physical tests and the numerical simulations is found, it won't surprise an engineer. Besides, the trend given in Table 4.6 and Figure 4.12 is in a least square sense. As shown in Figure 4.13, there are indeed a few cases of large neck tests giving maximum vertical sheet ice forces significantly lower than the best fit values for the small neck structure.

Chapter 6 Analytical Studies

The ridge loads on a structure, as shown in Chapter 3, are usually much higher than the sheet ice loads. The International Association for Hydraulic Research (IAHR) Working Group on Ice Forces (Wessels and Kato 1989) has recommended: "at least similar (to those for sheet ice) efforts should be made to study the ice forces exerted on the offshore structures by pressure ridges, as they may present the worst load case". This recommendation has also been appreciated by industry (Chao 1992b). Indeed, an appropriate method for determining the ridge load is of utmost importance. All the existing analytical models were based on the tests with SCSs, and they did not account for the particular features of the MCSs.

An analytical model is being developed in this chapter for practical use in the calculation of the maximum ridge loads on a MCS. Sections 6.2 through 6.4 develop an analytical model for computing ridge ice forces exerted on a MCS by infinite length ridges. Section 6.5 presents equations for the computation of the forces exerted by ridges of finite length. A brief but quite intensive discussion of the analytical model is given in Section 6.6. Section 6.7 deals with the issue of ride-up force computation.

6.1 The Problem and Its Simplification

As shown by the analysis in Chapter 4, ridge cracking is one of the interaction events which is

likely to give rise to the maximum ridge load. Hence, the ridge loads generated due to the initial and hinge cracks will be considered as possible maximum loads on a MCS. As shown in Figures 4.1 through 4.4, the ridge loads on the tested face-on MCSs in most cases (except the case of Figure 4.2) are larger than those on edge-on MCSs. Hence, the structure is assumed to be in face-on orientation and the ridge in broadside orientation so that the forces exerted on the structure would be a maximum. The ridge is assumed to behave as an elastic beam on an elastic foundation, subjected to vertical loads. To be conservative, the surrounding ice sheet is assumed not to separate from the ridge until the hinge cracks occur.

The attached ice sheet significantly affects ridge deformation and load. Its effect has two different consequences: (i) increase of foundation modulus; and (ii) participation in the ridge bending. According to Kim and Kotras (1973), the attached ice increases the foundation modulus by $2\sqrt{2}\rho_w g l_s$, making the total foundation modulus per unit length of the ridge to be:

$$k = \rho_w g (B_t + 2\sqrt{2}\, l_s) \tag{6.1}$$

where l_s is the characteristic length of the ice sheet and is defined by Equation (5.5). During the ridge bending process, the attached ice sheet also contributes to total rigidity. This effect of the sheet can be taken into account by adding two flanges, each with a width B_e, to the ridge beam. B_e can be approximately determined with the following equation:

$$B_e = \sqrt{2}\, l_s \tag{6.2}$$

Thus, the combination of the ridge and its surrounding ice sheet can be treated as an

elastic beam on an elastic foundation. Figure 6.1 shows the overall cross section of this beam whose foundation modulus per unit length is given by Equation (6.1). The characteristic length of this beam (ridge plus sheet) is given by

$$L_c = \sqrt[4]{\frac{4 E_r I}{k}} \tag{6.3}$$

where I is the moment of inertia of the beam, which is sum of the moment of inertia of the flanges, I_f, and the moment of inertia of the isolated ridge, I_r, i.e.

$$I = I_r + I_f \tag{6.4}$$

From here on, this beam will be referred to as *ridge* for short, whereas the ridge without ice sheet attached will be identified as an *isolated ridge*.

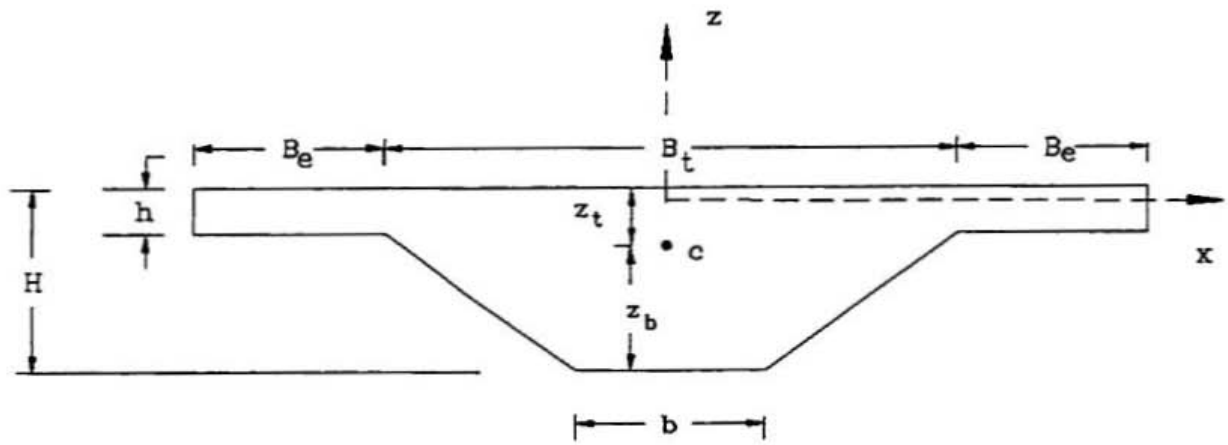

Figure 6.1 Cross Section of Ridge Beam with Ice Sheet Flanges

The positive sense of x, y, and z axes of the Cartesian coordinate system being used in the following analysis is coincident with that defined in Chapter 3, but its origin shifts to the intersection of the ridge's two central planes at the water surface where the weight and buoyancy of the ice are balanced (see Figure 6.1). The upward-acting shearing force and upward convex bending moment (which makes the bottom layer of the beam to be in tension) are considered positive. Using this coordinate system, the equation governing deformation of the above beam is of the form:

$$E_r I \frac{d^4 z}{dy^4} = -kz + q \tag{6.5}$$

where q, the intensity of a distributed load, will be given according to the interaction condition. This equation was derived for the loaded portion of the beam. Outside the loaded portion, this equation is still valid if q is set to zero.

In Equation (6.5), the ice ridge beam is considered to be a constant stiffness beam under vertical flexural loads only; this idealization has been widely accepted by industry and research community (Kim and Kotras 1973, Wang 1979, Croasdale 1980, American Petroleum Institute 1988, Schreiber *et al* 1989). Additional calculations carried out to show sufficiency of considering vertical loads only are given in Appendix C. One question that needs to be answered is the error due to application of elementary bending theory on which Equation (6.5) is based. From the results of an elasticity solution reported by Higdon *et al* (1967, p. 257), it is found that bending stress (in y direction) from elementary theory is very close to that from more exact

theory of elasticity. The difference between using the elementary theory and the elasticity theory is less than 0.2 percent. The vertical stress (in z direction) calculated from elasticity theory is much less than the stress in y direction computed from elementary beam theory, for a beam whose length is several times the depth. Shear stress is the same for both the elementary beam bending theory and the elasticity theory; it has a zero value at top and bottom fibres and reaches its maximum value at beam's neutral axis. In this analysis, the ice ridge is considered to be a brittle material, i.e., once its maximum stress equals ridge strength the ridge cracks across its entire cross section. Since the maximum stress for this bending problem occurs at the top or bottom fibre, shear stress does not affect the maximum bending stress, and consequently does not affect accuracy of calculation of maximum loads on a MCS.

The ridge cracking loads can be obtained by solving Equation (6.5) by the superposition method (Hetenyi 1946). The approach to be used consists of three steps:

1. Choose a reasonably simplified loading condition(s) for initial (central) cracking and hinge cracking process.
2. Under each given loading condition, the bending moment $M(y)$ will be derived. And then, the location of the maximum bending moment, Y, will be determined by solving the following equation:

$$\frac{dM(y)}{dy} = 0 \tag{6.6}$$

This location is considered as the section where the crack will appear. The maximum bending moment $M_{max} = M(Y)$ can be found out by substituting Y back into the expression of the bending moment.

3. Once the maximum bending moment M_{max} is determined, the maximum ridge load for that particular cracking process will be given by the equation:

$$M_{max} = -\frac{\sigma_r I}{z_n} \tag{6.7}$$

where $z_n = z_t$ and $\sigma_r = \sigma_{rt}$ if the top layer of the ridge is in tension, and $z_n = z_b$ and $\sigma_r = \sigma_{rb}$ for the bottom layer of the ridge in tension (see Figure 6.1). σ_{rt} and σ_{rb} are the ridge flexural strength with top layer and bottom layer in tension, respectively. The negative sign in Equation (6.7) is due to the definition of the coordinate system and the positive sense of the bending moment. If absolute value of M_{max}, z_t, and z_b are used, the negative sign should be ignored.

6.2 Loading Conditions

For the predominant failure mode of ridges (the failure pattern I, see Section 4.1), a ridge usually undergoes an initial (central) cracking followed by a pair of hinge cracks. It is assumed here that the maximum force occurs during either the central crack or the hinge crack, depending on whichever generates a larger load.

For a face-on MCS and a broadside ridge, we assume they have an ideal firm contact

along the contact interface during the central cracking process. Figure 6.2 A is a sketch showing the top view of this contact condition. The force on the ridge under this contact condition can be simulated with a uniformly distributed load as shown in Figure 6.2 B. For the convenience of derivation of equations, the load length which equals the length of structure's facet at water line is represented by $2l$. This definition will be used throughout the remaining parts of this chapter.

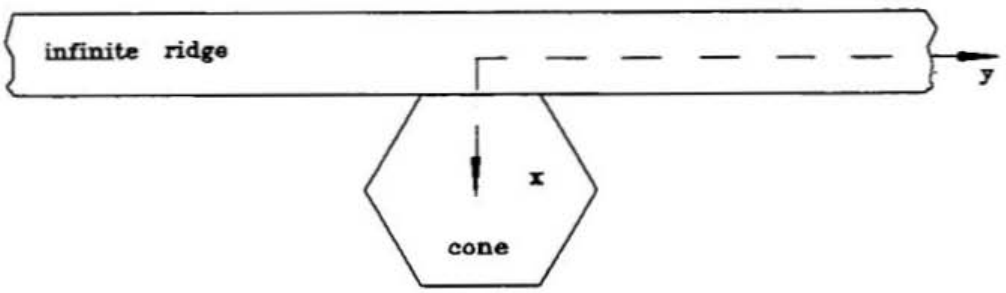

Figure 6.2 A Contact Condition for Initial Crack

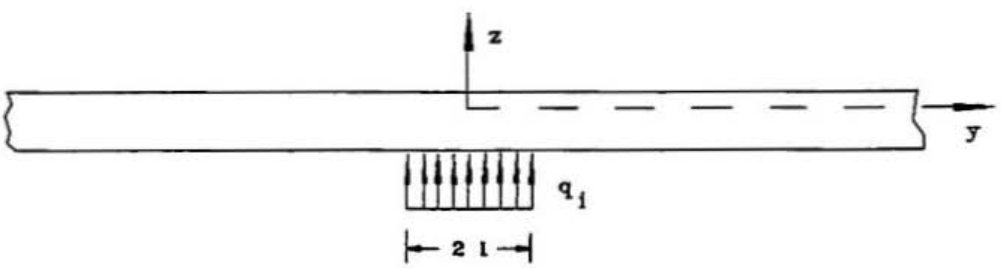

Figure 6.2 B Loading Condition for Initial Crack

After the initial (central) crack has formed, a pair of hinge cracks will occur at a certain distance away from the central crack. The contact condition for the hinge crack can vary from firm contact along the whole interface to point contact on the two corners of the front facet, depending on ridge and sheet ice rigidity, structure size, previous interaction condition, and many other factors. These two extreme contact conditions can be represented by a uniformly distributed load and a pair of concentrated loads, respectively. The corner contact and the concentrated loads are shown in Figure 6.3 A and 6.3 B, respectively, while the uniformly distributed load and the corresponding contact condition are similar to those for the initial crack shown in Figures 6.2A and 6.2 B except for the fact that the central crack already exists in the ridge for this case. Between these extreme contact conditions, an intermediate condition could be considered such that the contact is quite complete at the facet corners and gradually reduces to zero at the center line of the facet. This condition can be simulated by a triangular load, as shown in Figure 6.4.

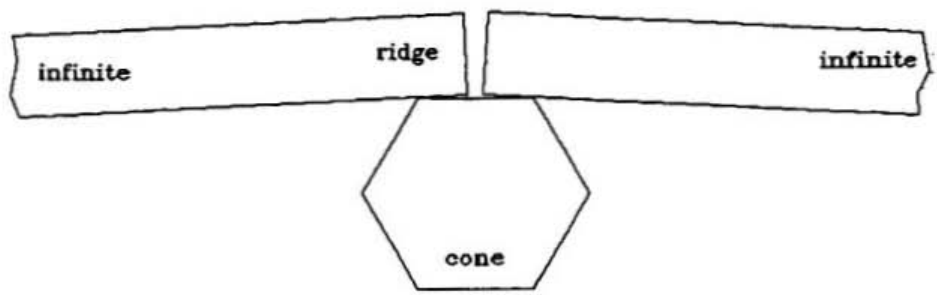

Figure 6.3 A Corner Contact for Hinge Crack

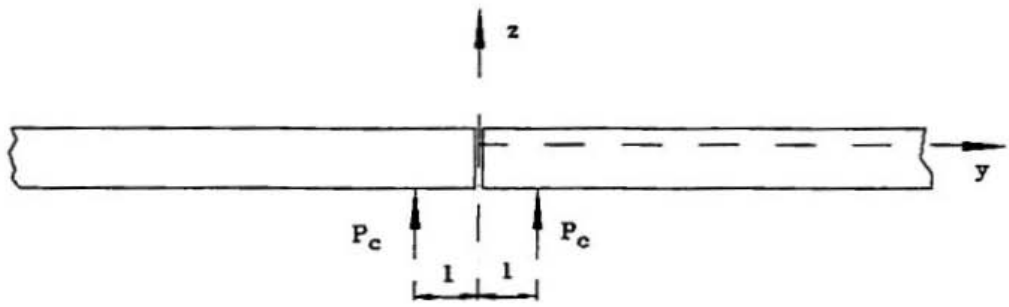

Figure 6.3 B Concentrated Loads for Hinge Crack

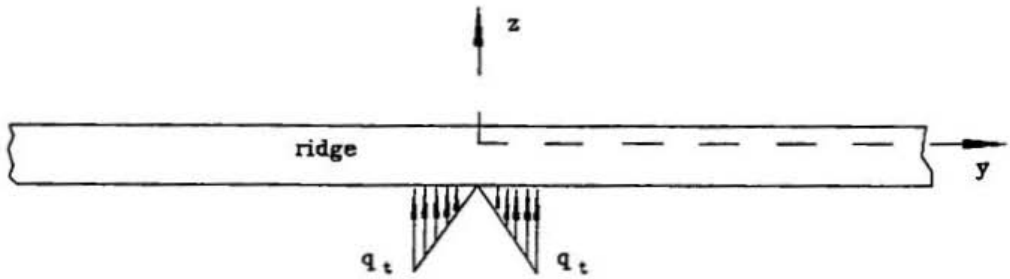

Figure 6.4 Triangular Loads for Hinge Crack

Of course, the real contact condition could be anything between the two extreme conditions or even outside them. Any of the three conditions chosen here may be applicable only for a few interaction scenarios, but together they can cover most of the contact conditions observed during the tests.

6.3 Bending Moment and Crack Locations for Infinite Ridges

Following the procedures given in Section 6.1, this section will present the derived bending moment. The material is organized into four subsections: the moments and crack locations for the initial crack are shown in subsection 6.3.1, and those for hinge cracks under uniformly distributed, concentrated, and triangularly distributed loads are presented in subsections 6.3.2, 6.3.3, and 6.3.4, respectively.

6.3.1 Bending Moment and Crack Location for Initial Crack

For the loading condition given in Figure 6.2 B, the bending moment in the ridge for the part where $y \geq 0$ is given as

$$\begin{aligned} M_i(y) &= -\frac{1}{4} q_i L_c^2 [B(y+l) + B(l-y)] \qquad 0 \leq y \leq l \\ M_i(y) &= -\frac{1}{4} q_i L_c^2 [B(y+l) - B(y-l)] \qquad y \geq l \end{aligned} \tag{6.8}$$

where q_i is intensity of the uniform load per unit length, and L_c is characteristic length of the ridge defined in Equation (6.3). $B(y+l)$, $B(y-l)$, and $B(l-y)$ are functions of y, l, and L_c, and given in Appendix D. Since both the ridge and the load are symmetrical about the x-z plane, the bending moment in the part of $y \leq 0$ is also symmetrical with respect to those given in the Equation (6.8).

Application of Equation (6.6) to Equation (6.8) yields:

$$\begin{aligned} C(y+l) - C(l-y) &= 0 \qquad 0 \le y \le l \\ C(y+l) - C(y-l) &= 0 \qquad y \ge l \end{aligned} \tag{6.9}$$

where $C(y+l)$, $C(y-l)$, and $C(l-y)$ are also given in Appendix D.

Solving equation (6.9) for y gives y_i that defines the location of the section where the crack occurs and the bending moment $M_i(y)$ reaches its maximum value M_i, i.e., $M_i(y_i) = M_i$. The solution of Equation (6.9) can be expressed in a dimensionless form as follows

$$\frac{y_i}{L_c} = g_i(2l/L_c) \tag{6.10}$$

Part of its numerical values are plotted in Figure 6.5.

In Figure 6.5, the dotted line represents $y=l$, the corner of the structure's facet. The values of y/L_c above this line would mean that the crack occurs outside the ice-structure interface area. When y/L_c is below this line the crack will occur within the interface area.

Figure 6.5 shows that the initial crack theoretically occurs at $y = 0$. Thus, it is reasonable to assume that the initial crack occurs at the center of the contact area. In the rest of this thesis, the analysis for hinge cracks which occur after the initial crack will be based on this assumption.

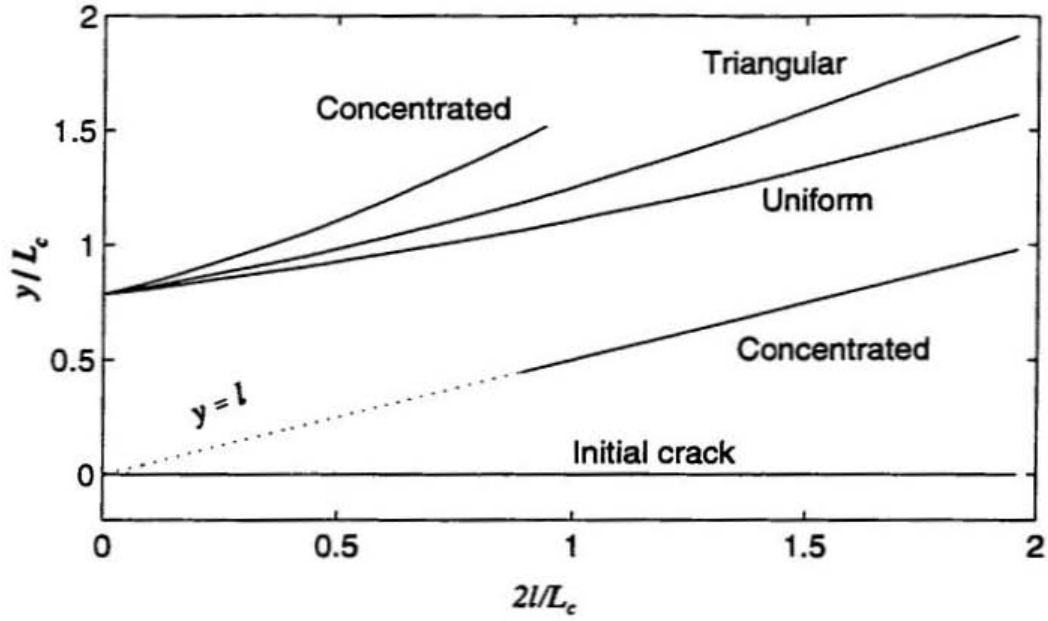

Figure 6.5 Normalized Crack Location of Initial and Hinge Cracks

The physical tests and the numerical simulations well support the above results. Tables 4.4 and 4.5 (in Chapter 4) showed the initial crack of many ridges tested with face-on structure occurred at or near the center of the contact area. The numerical simulation also showed an initial crack at the center of the ridge.

After obtaining y_i, one can determine the maximum moment M_i by substituting y_i into equations (6.8). In general, M_i can be expressed as

$$M_i = q_i f_i(l, L_c) \tag{6.11}$$

where $f_i(l,L_c)$ is a function of l and L_c and will be addressed in Section 6.4.

6.3.2 Bending Moment and Crack Location for Hinge Crack under Uniformly Distributed Load Condition

After the occurrence of the central (initial) crack, the ridge breaks into two semi-infinite segments; it is assumed that the loads and the sectional profile are symmetrical about the x-z plane. Thus, one needs to consider one segment only. Under the uniformly distributed load, the bending moment, $M_d(y)$, along the semi-infinite ridge can be written as

$$\begin{aligned} M_d(y) &= -\frac{1}{4} q_d L_c^2 \left[u_1 C(y) - u_2 D(y) + B(y) + B(l-y)\right] \qquad 0 \le y \le l \\ M_d(y) &= -\frac{1}{4} q_d L_c^2 \left[u_1 C(y) - u_2 D(y) + B(y) - B(y-l)\right] \qquad y \ge l \end{aligned} \tag{6.12}$$

where q_d is the intensity of the uniform load, and u_1 and u_2 are defined by

$$\begin{aligned} u_1 &= 1 + B(l) - C(l) \\ u_2 &= 1 + 2B(l) - C(l) \end{aligned} \tag{6.13}$$

$B(l)$, $B(y)$, $B(l-y)$, $B(y-l)$, $C(l)$, $C(y)$, and $D(y)$ are given in Appendix D.

Applying Equation (6.6) to Equation (6.12) leads to

$$\begin{aligned} 2u_1 D(y) - u_2 A(y) - C(y) + C(l-y) &= 0 \qquad 0 \le y \le l \\ 2u_1 D(y) - u_2 A(y) - C(y) + C(y-l) &= 0 \qquad y \ge l \end{aligned} \tag{6.14}$$

where u_1 and u_2 are the coefficients defined by Equation (6.13).

Solving Equation (6.14), one would obtain a solution of the form

$$\frac{y_d}{L_c} = g_d(2l/L_c) \tag{6.15}$$

where y_d represents the location of the section where $M_d(y)$ reaches its peak value M_d, and hence is the location of the hinge crack. The function $g_d(2l/L_c)$ is also plotted against $2l/L_c$ in Figure 6.5. The figure indicates that the hinge crack caused by a uniformly distributed load appears outside the ridge/structure contact area. Since the two semi-infinite ridge segments are symmetrical about x-z plane, there is also a crack in the other segment (the part where $y < 0$), at a distance y_d away from the center crack.

Substituting $y = y_d$ back into Equation (6.12) gives the maximum bending moment M_d for the hinge cracks under the uniformly distributed load. M_d can be expressed in the form

$$M_d = q_d f_d(l, L_c) \tag{6.16}$$

where $f_d(l,L_c)$ is a function of l and L_c and will be addressed in Section 6.4.

6.3.3 Bending Moment and Crack Location for Hinge Crack under Concentrated Load Condition

If each of the two semi-infinite ridges is subjected to a concentrated load at the contact points

at the facet corners as shown in Figure 6.3 A, the bending moment for the ridge within $y > 0$ can be derived as

$$\begin{aligned} M_c(y) &= -\frac{1}{4} p_c L_c [s_2 C(y) + C(l-y) - 2 s_1 D(y)] \qquad 0 \le y \le l \\ M_c(y) &= -\frac{1}{4} p_c L_c [s_2 C(y) + C(y-l) - 2 s_1 D(y)] \qquad y \ge l \end{aligned} \tag{6.17}$$

where p_c is the concentrated load on the semi-infinite ridge. Functions $C(y)$, $C(l-y)$, $C(y-l)$, and $D(y)$ are given in Appendix D. s_1 and s_2 are functions of l and are defined as

$$\begin{aligned} s_1 &= C(l) + D(l) \\ s_2 &= C(l) + 2 D(l) \end{aligned} \tag{6.18}$$

Applying Equation (6.6) to Equation (6.17), we have:

$$\begin{aligned} s_2 D(y) - s_1 A(y) - D(l-y) &= 0 \qquad 0 \le y \le l \\ s_2 D(y) - s_1 A(y) + D(y-l) &= 0 \qquad y \ge l \end{aligned} \tag{6.19}$$

Function $A(y)$ is given in Appendix D. s_1 and s_2 are defined in Equation (6.18). The location for the maximum bending moment or the hinge crack, y_c, thus can be obtained by solving Equation (6.19), and it can be expressed in the following general form:

$$\frac{y_c}{L_c} = g_c(2l/L_c) \tag{6.20}$$

The function $g_c(2l/L_c)$ is plotted also in Figure 6.5.

Figure 6.5 shows that the hinge cracks caused by concentrated load could have occurred

at three pairs of locations. Firstly, a pair of cracks will appear at the sections at a distance varying from $0.79L_c$ (at $2l/L_c = 0$) to $1.52L_c$ (at $2l/L_c = 0.89$) away from the center of the contact area when $2l/L_c$ is less than 0.891. Secondly, within the range of $0.89 < 2l/L_c < 0.94$ two pairs of cracks may appear: one pair occurs following the above regularity, the other pair may appear just at the contact points (i.e. the loading points). At these two pairs of locations, the bending moments are very close, with the maximum difference less than 10%. When the ratio $2l/L_c$ increases further, say larger than 0.941, the cracks will occur at the loading points only.

If a ridge/structure combination had a value of $2l/L_c > 0.94$, the ridge after the occurrence of hinge cracks cannot still pass the structure because the width of the structure is larger than $2l$ whereas the distance between the two cracks is only $2l$. This means that other cracks must occur to let the ridge pass beyond the structure. The approach for a semi-infinite beam under a concentrated force at its one end can be applied to this problem.

Fortunately, the combination of a ridge and a structure which has a value of $2l/L_c > 0.8$, does not occur under realistic condition. Based on the information compiled by Cammaert and Muggeridge (1988), the calculation presented in Appendix E of this thesis shows that the range of ridge characteristic lengths for the Beaufort Sea and the Chukchi Sea is between 55 and 370 meters. If this limitation is applied to the prototype structure shown in Figure 3.1, the range of $2l/L_c$ varies between 0.05 and 0.31 which is much below 0.94 or 0.89. The maximum value for the ridges and the structural models used in the present tests was 0.47 which is also much smaller than 0.89. Hence, one can say that considering the situations for $2l/L_c < 0.89$ is good

enough for real life situations. Thus, only one pair of crack locations (the part above the dashed line) will be considered for concentrated loading conditions.

Substituting y_c for y in equations (6.17), we have the expression of the maximum bending moment M_c as follows

$$M_c = p_c f_c(l, L_c) \tag{6.21}$$

where $f_c(l,L_c)$ is a function of l and L_c and will be addressed in Section 6.4.

6.3.4 Bending Moment and Crack Location for Hinge Crack under Triangular Load Condition

For the triangular distributed loading condition given in Figure 6.4, the bending moment can be written as

$$\begin{aligned} M_t(y) &= -\frac{1}{4}P_0 L_c C(y) - \frac{1}{2}M_0 D(y) + \frac{q_t L_c^3}{8l}[A(y) - A(l-y) - \frac{2l}{L_c}B(l-y)] \qquad 0 \le y \le l \\ M_t(y) &= -\frac{1}{4}P_0 L_c C(y) - \frac{1}{2}M_0 D(y) + \frac{q_t L_c^3}{8l}[A(y) - A(y-l) + \frac{2l}{L_c}B(y-l)] \qquad y \ge l \end{aligned} \tag{6.22}$$

where q_t is the maximum value of the load intensity. $A(y)$, $A(y-l)$, and $B(y-l)$ are given in Appendix C. M_0 and P_0 are the resultant moment and force, respectively, and they are

independent of y and are defined as follows

$$P_0 = -\frac{q_t L_c^2}{2l}\left[1-A(l)-\frac{2l}{L_c}B(l)-2B(l)+\frac{2l}{L_c}C(l)\right]$$
$$M_0 = -\frac{q_t L_c^3}{2l}\left[1-A(l)-\frac{2l}{L_c}B(l)-B(l)+\frac{l}{L_c}C(l)\right] \qquad (6.23)$$

Applying Equation (6.6) to Equation (6.22) yields the following equations:

$$P_0 D(y)+\frac{M_0}{L_c}A(y)-\frac{q_t L_c^2}{2l}\left[B(y)+B(l-y)-\frac{l}{L_c}C(l-y)\right] = 0 \qquad 0\le y\le l$$
$$P_0 D(y)+\frac{M_0}{L_c}A(y)-\frac{q_t L_c^2}{2l}\left[B(y)-B(y-l)-\frac{l}{L_c}C(y-l)\right] = 0 \qquad y\ge l \qquad (6.24)$$

The solution of Equation (6.24) is the location of the maximum bending moment or the location of the hinge crack under a pair of triangular distributed loads. The solution can be expressed in the following general form:

$$\frac{y_t}{L_c} = g_t(2l/L_c) \qquad (6.25)$$

where $g_t(2l/L_c)$ is a dimensionless function and is also plotted in Figure 6.5.

Substituting y_t for y in Equation (6.22) gives maximum bending moment M_t which can be expressed as follows

$$M_t = q_t f_t(l, l_c) \tag{6.26}$$

where $f_t(l, L_c)$ is a function of l and L_c and will be addressed in Section 6.4.

6.4 Formulae for Estimation of the Loads Exerted by Infinite Ridges

The maximum bending moments M_i, M_d, M_c, and M_t given in Equations (6.11), (6.16), (6.21), and (6.26) are for the occurrence of initial crack and hinge cracks under uniform, concentrated, and triangular loading, respectively. The maximum loads for cracking can be determined by applying Equation (6.7) to these maximum moments. Substituting Equations (6.11), (6.16), (6.21), and (6.26) into (6.7), one obtains the following equations:

$$2l q_i \frac{f_i(l, L_c)}{2l} = -\frac{\sigma_{rt} I}{z_t} \tag{6.27}$$

$$\begin{aligned} 2l q_d \frac{f_d(l, L_c)}{2l} &= \frac{\sigma_{rb} I}{z_b} \\ 2p_c \frac{f_c(l, L_c)}{2} &= \frac{\sigma_{rb} I}{z_b} \\ l q_t \frac{f_t(l, L_c)}{l} &= \frac{\sigma_{rb} I}{z_b} \end{aligned} \tag{6.28}$$

In above equations, $2lq_i$, $2lq_d$, $2p_c$, and lq_t are the ultimate loads for initial crack and hinge cracks under uniform, concentrated, triangular loads, respectively. It should also be noted that σ_{rt}, the ridge flexural strength with its top in tension, and z_t, the distance from ridge's centroidal axis to its top surface, are used in Equation (6.27) which is valid only for initial crack. On the other hand, σ_{rb}, the ridge flexural strength with its bottom in tension and, z_b, the distance from the centroidal axis to the bottom surface, are used in Equation (6.28). This is due to the fact that the initial crack breaks the ridge with its top in tension, whereas the hinge cracks break the ridge with its bottom in tension. It should also be noted that z_t and z_b are the absolute values of the corresponding distance because their signs have already been taken into account in the equations.

Equations (6.27) and (6.28) can be rewritten in a neater form as:

$$P_I = \frac{\sigma_{rt} I}{z_t L_c} F_I(\frac{2l}{L_c}) \tag{6.29}$$

$$P_D = \frac{\sigma_{rb} I}{z_b L_c} F_D(\frac{2l}{L_c}) \tag{6.30}$$

$$P_C = \frac{\sigma_{rb} I}{z_b L_c} F_C(\frac{2l}{L_c}) \tag{6.31}$$

$$P_T = \frac{\sigma_{rb} I}{z_b L_c} F_T(\frac{2l}{L_c}) \tag{6.32}$$

where P_I, P_D, P_C, and P_T are the maximum initial crack load and the hinge crack load under

uniform, concentrated, and triangular loading conditions, i.e.,

$$P_I = 2lq_i\ ,\quad P_D = 2lq_d\ ,\quad P_C = 2p_c\ ,\quad P_T = lq_t \tag{6.33}$$

$F_I(2l/L_c)$, $F_D(2l/L_c)$, $F_C(2l/L_c)$, and $F_T(2l/L_c)$ are dimensionless load functions, which can be considered to be normalized vertical ridge load for infinite ridges, defined as follows:

$$F_I(\frac{2l}{L_c}) = -\frac{2lL_c}{f_i(l, L_c)} \tag{6.34}$$

$$F_D(\frac{2l}{L_c}) = \frac{2lL_c}{f_d(l, L_c)} \qquad F_C(\frac{2l}{L_c}) = \frac{2L_c}{f_c(l, L_c)} \qquad F_T(\frac{2l}{L_c}) = \frac{lL_c}{f_t(l, L_c)} \tag{6.35}$$

These load function are functions of $2l/L_c$ (the dimensionless structural facet length at waterline level), and are shown in Figure 6.6.

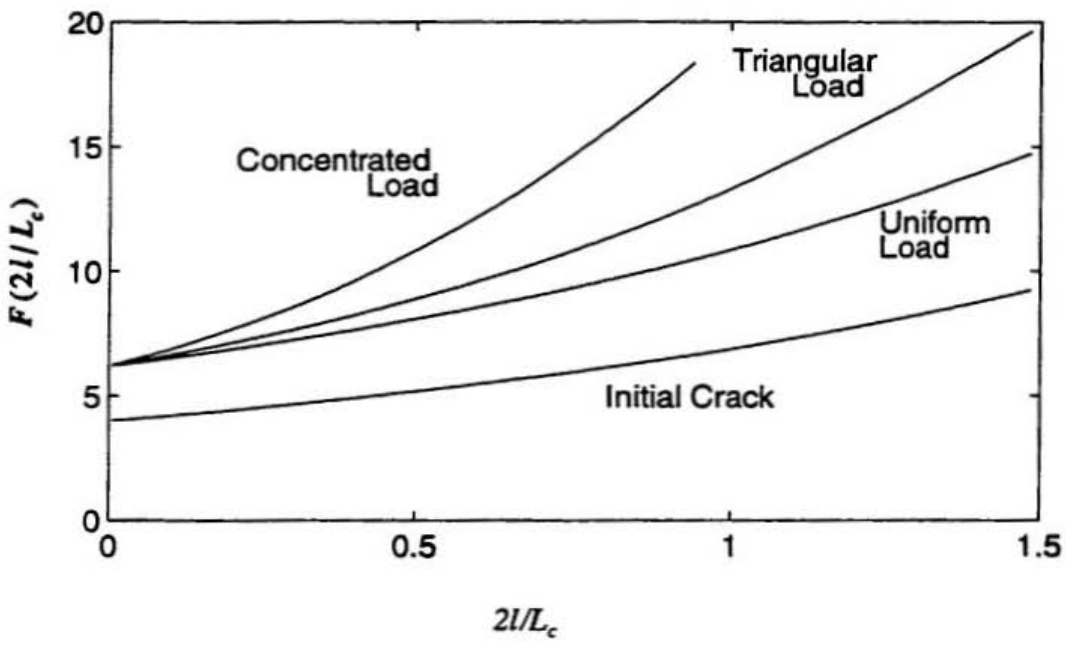

Figure 6.6 Load Functions of Infinite Ridges

These functions can be approximated in a general form by the following quadratic function:

$$F(\frac{2l}{L_c}) = a_0 + a_1 \frac{2l}{L_c} + a_2 (\frac{2l}{L_c})^2 \qquad (6.36)$$

The coefficients a_0, a_1, and a_2 were determined using the linear regression approach and are listed in Table 6.1.

Crack	Loading	a_0	a_1	a_2
Initial Crack	Uniform Load (F_I)	4.0	1.7	1.2
Hinge Crack	Uniform Load (F_D)	6.2	2.7	2.0
	Concentrated Load (F_C)	6.2	5.2	8.1
	Triangular Load (F_T)	6.2	3.4	3.8

Table 6.1 Coefficients of $F(2l/L_c)$

Thus, the initial crack load can be calculated with Equations (6.29) and (6.36). The hinge crack load, theoretically speaking, should be calculated with one of the equations, (6.30), (6.31), or (6.32), depending on which loading condition is most appropriate. Generally, designers would appreciate a single simple equation for ridge load estimation rather than a number of equations as given in Equations (6.30) through (6.32). To be conservative, the concentrated loading condition should be used for hinge crack load estimation. Since the concentrated load is one of extreme loading conditions and the $F_C(2l/L_c)$ envelops the other two load function curves, the

equation for the concentrated loading condition, viz., Equation (6.31) will predict a larger ridge load.

It should be noted that formulae presented above are only valid for the vertical ridge loads. The horizontal load can be calculated using Equation (2.1).

6.5 Consideration of Ridge Length Effect

So far, the ridges considered are infinitely long. Many researchers have pointed out that the ridge length could significantly affect the load if the ridges are short (Ralston 1978, Wang 1979, Abdelnour 1988). This effect will be investigated in this section.

Similar to the simplification made in section 6.1, the ridge is still assumed to be an elastic beam on an elastic foundation, but with finite length $2L$ (L is the half ridge length). Uniformly distributed load is also assumed to be the loading condition for initial crack formation in this finite ridge. Among the three loading conditions considered for hinge cracks, the concentrated loading condition has been chosen as the critical one for the formation of hinge crack in this finite ridge. Again, this choice would lead to a prediction of larger ridge crack loads. Figure 6.7 is a sketch showing the interaction scenario and the loading condition for the hinge crack formation in a finite ridge. Similar to the derivation for infinite ridges, the formulae given below are also valid only for the estimation of maximum vertical ridge loads. The horizontal component of a finite length ridge can be estimated with the help of Equation (2.1).

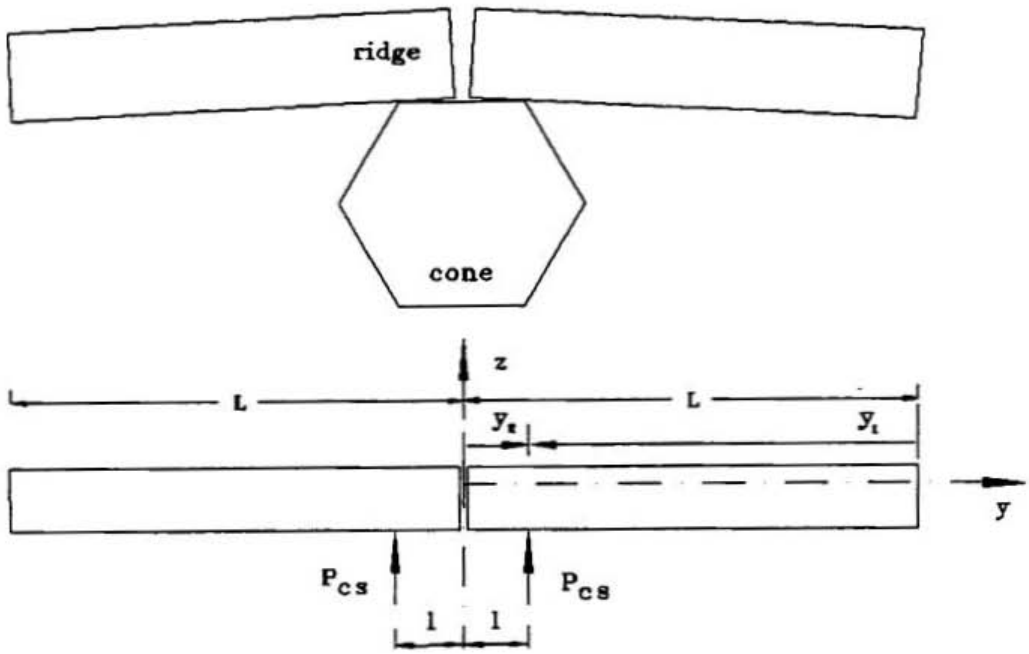

Figure 6.7 Contact and Loading Conditions for Hinge Cracks in a Finite Ridge

6.5.1 Initial Crack Load of a Finite Length Ridge

Using the results and the assumption that initial crack occurs along center plane of the ridge used earlier (see Section 6.3.1), one can directly derive an equation for the computation of initial crack formation load for a finite ridge. At the center of the ridge, the bending moment for the initial crack can be written as

$$M_o(L_n, l_n) = q_{is} L_c^2 \left[\frac{\sin l_n \sinh L_n \sinh(L_n - l_n) + \sinh(L_n - l_n) \sin L_n \sin(L_n - l_n)}{\sinh 2L_n + \sin 2L_n} \right] \quad (6.37)$$

where q_{is} is intensity of the uniform load, L_n and l_n are normalized half ridge length and half

facet length, respectively.

$$L_n = L / L_c \qquad l_n = l / L_c \tag{6.38}$$

Applying Equation (6.7) to this case, one can express the initial crack load, P_{IS}, as

$$P_{IS} = 2 l q_{is} = \frac{\sigma_{rt} I}{z_t L_c} F_o(L_n, l_n) \tag{6.39}$$

The load function, $F_o(L_n, l_n)$, is defined by Equation (6.40) and is plotted in Figure 6.8.

$$F_o(L_n, l_n) = \frac{2 l_n (\sinh 2L_n + \sin 2L_n)}{\sin l_n \sinh L_n \sinh(L_n - l_n) + \sinh l_n \sin L_n \sin(L_n - l_n)} \tag{6.40}$$

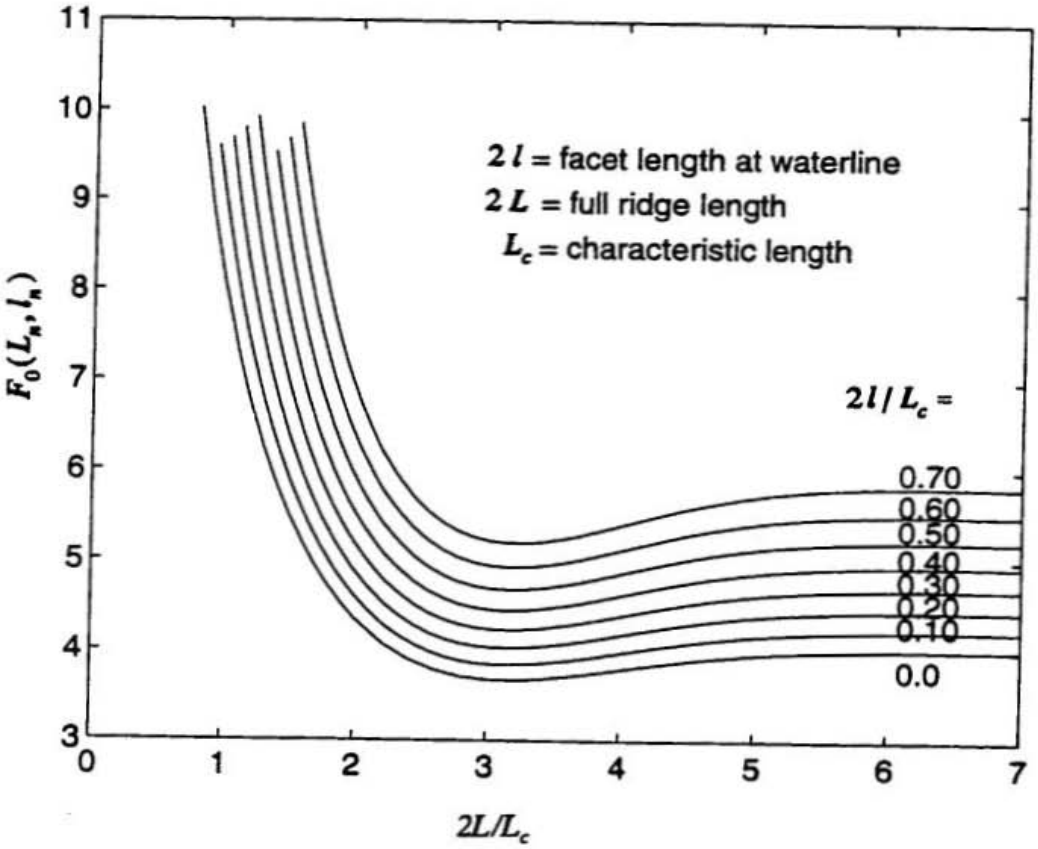

Figure 6.8 Load Function for the Central Crack in a Finite Length Ridge

6.5.2 Hinge Crack Load of a Finite Length Ridge under a Concentrated Load

For convenience in derivation of equations, two local coordinates (for y and its origin only) y_1 and y_2 are defined in this section (see Figure 6.7).

For a finite length ridge under a pair of concentrated loads, P_{cs}, (Figure 6.7), the bending moment along its length is given by

$$\begin{aligned} M(\bar{y}_1) &= P_{s0}[2C_1\sinh\bar{y}_1\sin\bar{y}_1 + D_1(\cosh\bar{y}_1\sin\bar{y}_1 - \sinh\bar{y}_1\cos\bar{y}_1)] \qquad 0 \le \bar{y}_1 \le (L_n - l_n) \\ M(\bar{y}_2) &= P_{s0}[2C_2\sinh\bar{y}_2\sin\bar{y}_2 + D_2(\cosh\bar{y}_2\sin\bar{y}_2 - \sinh\bar{y}_2\cos\bar{y}_2)] \qquad 0 \le \bar{y}_2 \le l_n \end{aligned} \tag{6.41}$$

Coefficients P_{s0}, C_1, C_2, D_1, and D_2 are functions of L_n and l_n and are given as follows

$$P_{s0} = \frac{P_{cs}\, L_c}{2\,(\sinh^2 L_n - \sin^2 L_n)} \tag{6.42}$$

$$\begin{aligned} C_1 &= \sinh L_n \cos(L_n - l_n)\cosh l_n - \sin L_n \cosh(L_n - l_n)\cos l_n \\ D_1 &= \sinh L_n [\sin(L_n - l_n)\cosh l_n - \cos(L_n - l_n)\sinh l_n] \\ &\quad + \sin L_n [\sinh(L_n - l_n)\cos l_n - \cosh(L_n - l_n)\sin l_n] \\ C_2 &= \sinh L_n \cos l_n \cosh(L_n - l_n) - \sinh L_n \cosh l_n \cos(L_n - l_n) \\ D_2 &= \sinh L_n [\sin l_n \cosh(L_n - l_n) - \cos l_n \sinh(L_n - l_n)] \\ &\quad + \sin L_n [\sinh l_n \cos(L_n - l_n) - \cosh l_n \sin(L_n - l_n)] \end{aligned} \tag{6.43}$$

The normalized coordinates are defined as

$$\bar{y}_1 = \frac{y_1}{L_c} \qquad \bar{y}_2 = \frac{y_2}{L_c} \tag{6.44}$$

Application of Equation (6.6) to Equation (6.41) gives the following:

$$\begin{aligned} C_1(\cosh\bar{y}_1 \sin\bar{y}_1 + \sinh\bar{y}_1 \cos\bar{y}_1) + D_1 \sinh\bar{y}_1 \sin\bar{y}_1 &= 0 \\ C_2(\cosh\bar{y}_2 \sin\bar{y}_2 + \sinh\bar{y}_2 \cos\bar{y}_2) + D_2 \sinh\bar{y}_2 \sin\bar{y}_2 &= 0 \end{aligned} \tag{6.45}$$

Their solution can be generally presented as

$$\bar{y}_1 = \bar{Y}_1 \qquad \bar{y}_2 = \bar{Y}_2$$

Substitution of the solutions of Equation (6.45) into (6.41) gives the local maximum values of the bending moments for the two portions of the ridge, respectively. The overall maximum bending moment is the larger of these two local maximum moments. After a detailed investigation, it was observed that the overall maximum bending moment is most likely to occur in the portion $l < y < L - l$, i.e. the portion outside the loading area.

Again, application of Equation (6.7) to the present case gives an equation for the estimation of the vertical hinge crack load of a finite ridge, P_{HS}, as follows:

$$P_{HS} = 2\,P_{cs} = \frac{\sigma_{rb}\,I}{z_b\,L_c}\,F_H(L_n, l_n) \tag{6.46}$$

where the load function $F_H(L_n, l_n)$ is given below and is plotted in Figure 6.9.

$$F_H(L_n, l_n) = \frac{4(\sinh^2 L_n - \sin^2 L_n)}{2C_1 \sinh \bar{Y}_1 \sin \bar{Y}_1 + D_1(\cosh \bar{Y}_1 \sin \bar{Y}_1 - \sinh \bar{Y}_1 \cos \bar{Y}_1)} \quad (6.47)$$

$F_H(L_n, l_n)$ represents the dimensionless load exerted by the ridge for hinge crack formation and is a function of L_n and l_n (defined earlier in Equation (6.38)). The figure is based on a detailed computation considering a number of combination of these two variables.

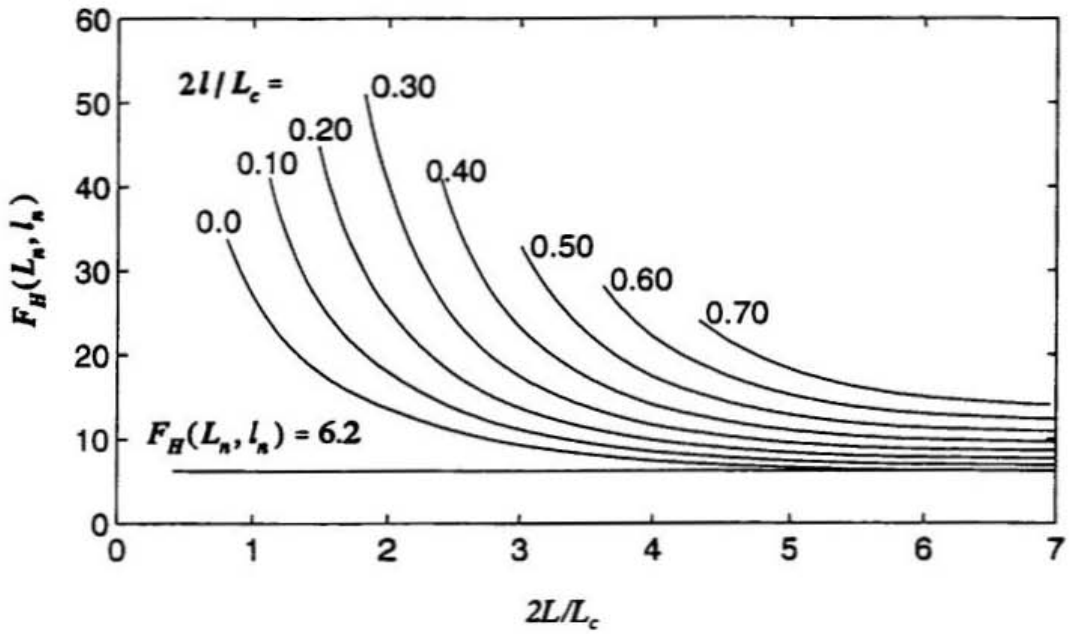

Figure 6.9 Load Function for Hinge Cracks in a Finite Length Ridge

6.6 Discussion about the Analytical Model

The main difference of a SCS and a MCS is in their surface configuration. Since the surface of

a MCS comprises several flat facets, the width of contact area for the ridge with a MCS equals the facet length if the structure is in face-on orientation and the ridge is in broadside orientation. On the other hand, the contact area for a SCS and a ridge may be much narrower.

The analytical models presented in this chapter may be used to compute the maximum ridge loads exerted on a MCS, while the Croasdale-Abdelnour model (refer to Section 2.2.1 of Chapter 2) was derived for SCSs. Both of these models are based on the theory of an elastic beam on an elastic foundation (Hetenyi 1946). Because local crushing is ignored, the loading condition for the present model is a line load with three types of load distribution along the interface line (equal to the facet length), whereas the Croasdale-Abdelnour model used a point load as the loading condition, with the load at the point of contact between the ridge and the SCS (at the center of the ridge). Thus, it is obvious that the main difference in Croasdale-Abdelnour model and the present model is the effect of the length of the load, or the effect of the facet length. In this sense, Equation (2.2) is a counterpart of Equations (6.29) through (6.32). A discussion of their similarities and differences are given in Section 6.6.1. Similarly, Equation (2.3) is a counterpart of Equations (6.39) and (6.46). These equations show the effect of ridge length on crack loads, which will be discussed in Section 6.6.2.

6.6.1 Effect of Facet Length on the Loads and Crack Locations of Infinite Ridges

Comparing Equations (6.29) through (6.32) with Equation (2.2), one can see that the coefficient

4.0 in Equation (2.2) is analogous to the load function $F_I(2l/L_c)$ given in Equation (6.29), and the coefficient *6.2* in Equation (2.2) is analogous to the load functions given in Equations (6.30) through (6.32).

The load functions plotted in Figure 6.6 show that both the initial crack load and the hinge crack load increase steadily as the dimensionless facet length $2l/L_c$ increases. The starting point (where $2l/L_c = 0$) of the functions for initial crack and hinge crack loads are the very values of the coefficients for Equation (2.2), 4.0 and 6.2, respectively. This clearly shows that the Croasdale's (Equation (2.2)) is only a particular case of the present models. In other words, a SCS is the particular case of a MCS with its facet length equal to zero.

From the above discussions, a conclusion may be drawn as follows: For a given ridge and a MCS, the more facets it has, the lower the ridge load will be exerted on it. The lower bound is the case of a SCS, or a MCS with facet length equal to zero.

A glance at the curves in Figure 6.6 may give one an impression that the ridge load, especially the hinge crack load, on a MCS may be twice or even three times as large as the load on a SCS if the $2l/L_c$ is large (let's say larger than 1.0). It is not true in real cases. As mentioned in section 6.3.3, the range of $2l/L_c$ for the Chukchi and Beaufort Seas where this type of structures were proposed to be used, is 0.05 to 0.31. For the largest value of $2l/L_c$, viz., 0.31, $F_I(0.31) = 4.65$, and $F_C(0.31) = 8.6$. Compared with the coefficients 4.0 and 6.2, these values of F_I and F_C are only 15% and 38.6% higher. The largest value of $2l/L_c$ of all the tests

presented in Chapter 3 was 0.472. For this extreme value, the hinge crack load predicted with the present model is about 69% larger than that from Equation (2.2), and it is about 27% for the initial crack.

The effect of facet length (or the number of facets) on crack location can be seen from Figure 6.5. The initial crack for both SCS and MCS occurs at the center of the ridge (or the center of the front facet at waterline level). The hinge crack for SCSs, if Equation (2.2) is applied, is always located at

$$\frac{y}{L_c} = \frac{\pi}{4} + 2\,i\,\pi \qquad \textit{where } i = 0, 1, 2, \ldots \qquad (6.48)$$

It is rarely possible to have $y/L_c \geq 2.25\,\pi$. Thus, we can let $i = 0$ and obtain the crack location $y/L_c = 0.785$. This, as shown in Figure 6.5, is the location where all the curves for hinge crack locations begin. This, again, shows that Croasdale's equation is only a special case of the present model.

Because the values represented by curves in Figure 6.5 steadily increase as $2l/L_c$ increases, the crack location for MCS is farther away from the ridge center, but it will not be too far since the value of $2l/L_c$ under actual conditions is usually less than 0.31.

6.6.2 Effect of Ridge Length on Crack Loads

Ralston (1978) pointed out that a decrease in ridge length, according to Hetenyi's (1946) description of finite beams, will increase the ridge load if the ridge length is relatively short. His plotting of ridge vertical force, predicted with Hetenyi's theory, against dimensionless ridge length clearly showed this trend.

Figure 6.8 shows the effect of ridge length on vertical central crack load for various facet lengths. Basically, the curves of load function can be divided into two regions by a critical value around $2L/L_c = 2.9$ which also to a certain extent depends on the value of dimensionless facet length ($2l/L_c$). When the ridge's dimensionless length is lower than these critical values, the load function and thus the load decreases sharply as the dimensionless ridge length increases. As the dimensionless ridge length increases to values larger than these critical values, the load function slowly increases until $2L/L_c$ reaches an upper threshold value about 5.8. Within the range of $2L/L_c = 2.9$ to 5.8, the value of load function is lower than its value when the ridge length is infinity. Hence, the effect of ridge length on vertical central crack load, according to Figure 6.8, can be stated as follows:

1. For ridges with lengths shorter than 2.9 times of their characteristic length, the load increases as the length decreases.
2. For ridges whose lengths fall in the range of 2.9 to 5.8 times of their characteristic length, the load will be lower than that of an infinite length ridge with other properties remaining same. The load slowly increases as ridge length increases.

3. If a ridge's length is longer than 5.8 times of its characteristic length, it can be approximately treated as an infinite ridge.

Figure 6.8 also shows that an increase in facet length gives rise to an increase in vertical central crack load for a ridge with a given length and characteristic length. This is similar to the trend shown in Figure 6.6. The values of the load function beyond $2L/L_c = 5.8$ in Figure 6.8 are in complete agreement with those in Figure 6.6 at corresponding points of dimensionless facet lengths $2l/L_c$. It is worth mentioning here that the line with facet length equal to zero in Figure 6.8 is exactly the same as that obtained with Equation (2.4), which is the vertical load function obtained for a finite length ridge.

The effect of ridge length on the vertical hinge crack load can be seen in Figure 6.9. It shows that the load function decreases as the ridge length increases for all possible facet lengths. Generally speaking, if the ridge length is longer than about 6.8 times of its characteristic length, neglecting the effect of the ridge length results only in a negligible error. In other words, a ridge can be treated as infinitely long if its dimensionless length is larger than 6.8. The value of this critical point depends on the value of the dimensionless facet length, as shown in Figure 6.9. For instance, for a SCS (i.e. $l = 0$), the critical point can be lowered to a value of $2L/L_c = 5.8$.

In addition, Figure 6.9 also shows that facet length plays a significant role in the effect of ridge length on hinge crack load. Basically, for a ridge with given length and characteristic length, the larger is the dimensionless facet length, the higher the load will be.

6.6.3 Short, Finite, and Long Ridges

According to Wang (1979), Semeniuk (1975) has divided the ridges (for the cases of SCSs) into three groups in his modification of APOA project 87 (Semeniuk, 1975) that implemented the Kim and Kotras method (see Chapter 2 of this thesis). The first group consists of those ridges whose dimensionless length is less than 0.835. These so-called *short ridges* were considered to be the ridges that do not fail as they move against a cone. The second group comprises of the ridges with dimensionless lengths in the ranges of 0.835 to 5.0. These ridges were considered to be finite and their load should be computed using Hetenyi's finite beam theory. The ridges with dimensionless lengths greater than 5.0 fell in the third group that can be treated as infinite beams.

The curve for zero dimensionless facet lengths (i.e., a smooth cone) in Figures 6.8 and 6.9 well support the above classification. It shows that the load required to fail a very short ridge ($2l/L_c < 0.835$) is unbelievably high. This ridge, as described by Ralston (1978), may slide over the surface of the structure without cracking because the force needed for this may be lower than that for developing a crack in the ridge. In the case of SCSs, the effect of ridge length, as previously pointed out, is negligible if the dimensionless ridge length is greater than 5.8. This value is quite close to the one (i.e., 5.0) chosen by Semeniuk (1975). In fact, when the dimensionless ridge length is greater than 5.0, its effect on the vertical load on a SCS (both initial and hinge cracks) becomes insignificant.

In the case of MCSs, the values of the points which divid ridges into the three groups should be increased because the load required to fail a ridge increases as the dimensionless facet length increases. The detailed computation shows that ridges with $2L/L_c$ lower than a certain value and $2l/L_c$ greater than 0.1 do not experience hinge cracks at all. The critical value of $2L/L_c$ can be roughly expressed as $6(2l/L_c)$, i.e., for $2l/L_c > 0.1$, if a ridge's $2L/L_c < 6(2l/L_c)$ no cracks would occur. For example, if $2l/L_c = 0.2$, the ridge will not have hinge crack if its $2L/L_c < 1.2$. The upper bound values below which the short ridges are defined should be no lower than the values given by the above rule. That is the reason why the curves with $2l/L_c$ larger than 0.3 in Figure 6.9 begin with very high values of $2L/L_c$. This is another aspect of the ridge length effect.

6.6.4 The Maximum Ridge Crack Loads

With the present analytical model, the maximum ridge crack load on a MCS is the larger of the initial and hinge crack loads predicted with equations (6.39) and (6.46), or (6.29) through (6.32) if the ridge length is long enough.

For a given ridge and structure (i.e. the dimensionless ridge length and facet length are given), it is obvious that the value of hinge crack load function is larger than that for the central crack. However, this does not mean that the hinge crack load is always larger than the central crack load. The reasons are given below.

For a central crack, the ridge ice strength is the one with its top surface layer in tension, which is usually higher than the ice strength with its bottom surface layer in tension, and the latter is used in equations for hinge cracks. Also, z_t is used in the equations for central crack load, i.e. Equations (6.29) and (6.39), and z_b is used in the equations for hinge crack load, i.e., Equations (6.46) and (6.30) through (6.32). Because the attached sheet is included in the ridge beam, the modified cross section has a centroidal axis closer to the top, which results in a smaller z_t and a larger z_b. The combined effect of all these parameters together can lead to the prediction of the vertical central crack load higher than that for the hinge crack. Thus, it can be said that whether the hinge crack or central crack produces the maximum load depends not only the value of load function but also on the relative value of two flexural strengths and the condition of the surrounding ice sheet.

If the hinge crack governs the maximum crack load, the load predicted with Equation (6.46) is larger than that obtained for infinite length ridges (i.e., Equations (6.30) through (6.32)). If the initial crack induces a larger load, the load predicted with Equation (6.39) is possible to be smaller than that obtained from Equation (6.29) for $2.9 < 2L/L_c < 5.8$.

6.7 Ride-up Forces and Total Forces

So far, the formulation and discussions are given only for ridge crack loads. As stated in Chapters 3 and 4, the ridge cracking is usually accompanied by the sheet ice pieces riding up on the cone surface. This ride-up process also generates ice loads on the structure. The total

maximum forces should include both the ridge crack forces and the forces due to the ice pieces riding up.

As reviewed in Section 2.4.3, the analytical model developed by Nevel (1992) is capable of computing the ride-up forces on SCSs with multiple conical sections including a vertical neck. It is just suitable for the cases of the MCSs dealt within this thesis. The Nevel model separately computes the breaking component and the ride-up component of the total sheet ice forces. The part for the computation of the ride-up forces is adopted here.

The Nevel model assumes that the broken ice pieces completely cover the front half of the structure. To apply the Nevel model to the case of the present MCSs, it is assumed that the front facet and the two front side-facets be completely covered with ice pieces for the face-on orientation; for the edge-on orientation, the two front side-facets (no front facet in this case) are assumed to be fully covered by the ice pieces and the side facet behind the front side-facet on each side is only half covered, from its front edge (the behind edge of the front side-facet) to its center line (symmetrical axis).

Large variation in the height of the ride-up was observed during the tests. To be general, the ice can be assumed to reach the middle of the neck (in the vertical direction). In the computation for the comparison of the present model with the Wang and Croasdale-Abdelnour models to be presented in Section 7.2, the ice pieces ride-up height was taken only to the top of the collar because the Wang model can account for the ride-up ice only to the top of sloped

sections (the Wang model uses part of the Ralston model to compute the ride-up component).

Adding up the ride-up forces computed with the Nevel model to the forces given by Equations (6.39) and (6.46) or Equations (6.29) through (6.32) will give the total forces acting on a MCS due to the process of ridge cracking.

Chapter 7 Validation of Analytical Models

This chapter consists of three main parts: (i) verifying the models developed in the last chapter, (ii) checking the suitability of Wang's model (Wang, Y.S., 1979 & 1984) and the Croasdale-Abdelnour model to estimate the ridge loads on MCSs, and (iii) examining the validity of the Ralston model, the Nevel model, and the Croasdale model for the prediction of sheet ice load on MCSs. These three parts will be arranged in Sections 7.1 through 7.3. The analytical models to be validated in Sections 7.2 and 7.3 were reviewed in Chapter 2. The verification and validation will be performed by comparing the prediction from the analytical models with the test results compiled in Chapter 3.

A few ridges are not used in the comparison and analyses in this chapter, mainly due to their incompleteness in data. These include ERC's tests Y2T5R1 and Y2T5R2, and IME's C53.

7.1 Verification of the Present Analytical Model

The method given in Chapter 6 has been coded into a computer program to compute the loads on the MCSs for the given test conditions. The ice properties and structural dimensions shown in Chapter 3 were used as inputs.

In the ERC test series, the ridges Y1T3R1, Y1T4R1, Y1T4R2, Y2T2R1, and Y2T2R2

orientated at an oblique angle of 30°. In the IME test series, the structure was in edge-on orientation for the ridge tests C45, C46, C47A, C47B, C63, C64, C65 and C66. Basically, a point contact, just like that for SCSs, can be assumed for these tests. Thus, the parameter $2l$ (the length of the loading) is set to be zero for the above tests for input.

For the structures in face-on orientation, it was assumed that each of the front facet and two front side-facets were covered with broken ice pieces. Similarly, the two front side-facets of a structure in edge-on orientation were also assumed fully covered with ice pieces, but only a half of the two side-facets (behind the front side-facets) were assumed loaded with ice pieces. This latter part of the assumption can help to properly account for the contribution of ride-up process to the total load on an edge-on structure. The ice pieces were assumed to have reached the top of the collar.

7.1.1 Comparison of Computed and Measured Loads

The computed vertical and horizontal loads using Equations (6.39) and (6.46) are plotted in Figure 7.1 and Figure 7.2, respectively. Since Equations (6.39) and (6.46) were derived for finite ridges, the effect of ridge length on ridge loads for these tests were taken into account.

Because the measured and predicted forces are in three different orders for the tests in three facilities, Figures 7.1 and 7.2 give a log-log plot which is expected to provide an overall view. The detailed and finer plots will be given in the next subsection.

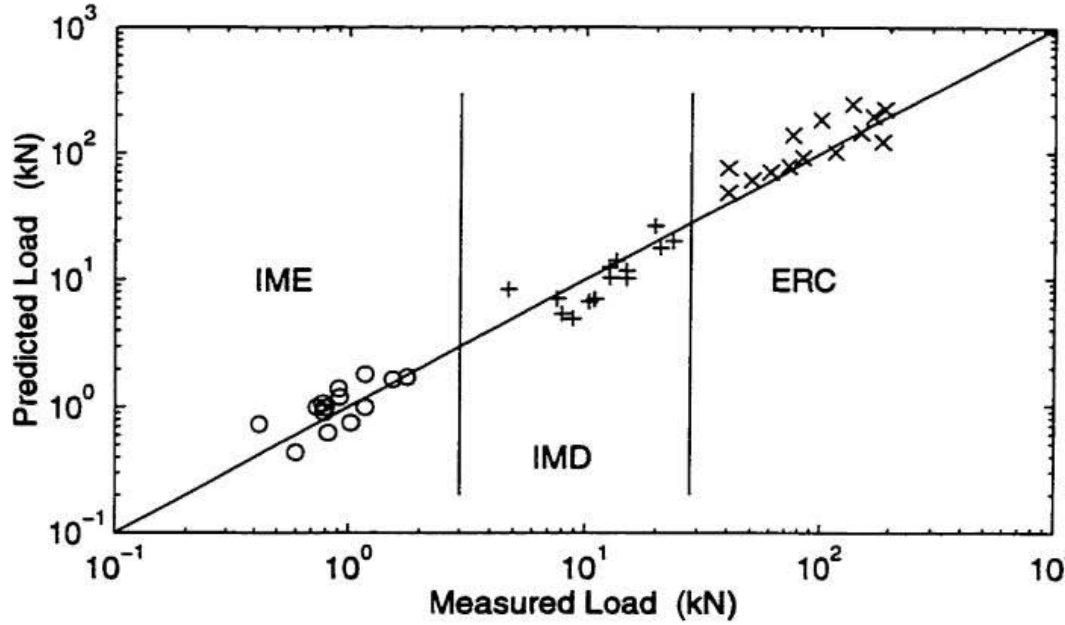

Figure 7.1 Vertical Predicted and Measured Ridge Loads

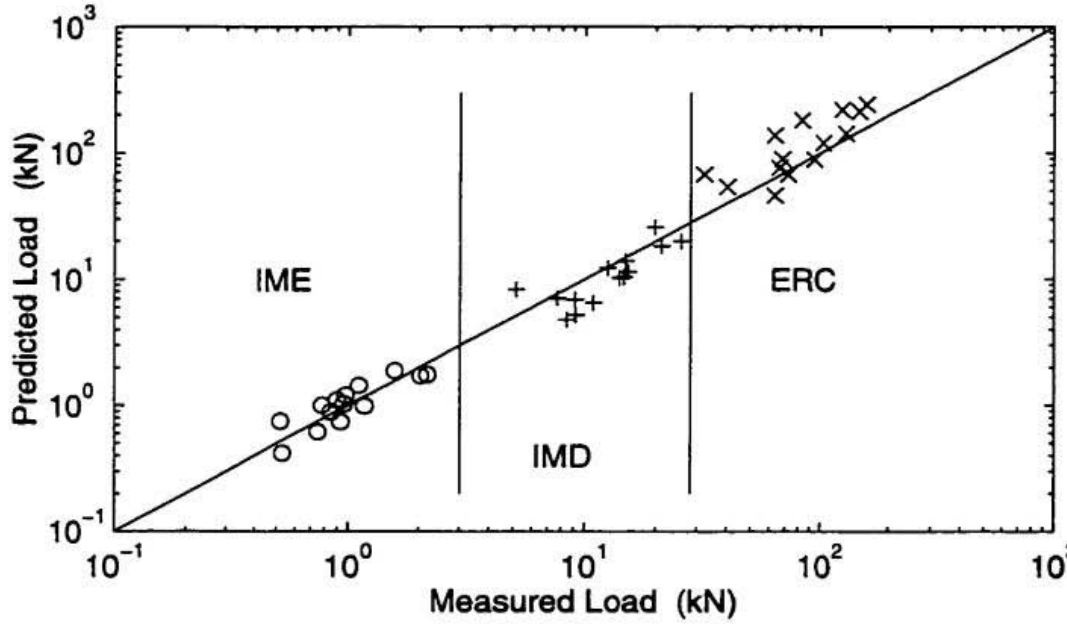

Figure 7.2 Horizontal Predicted and Measured Ridge Loads

The vertical and horizontal coordinates of each point in the figures are the measured and predicted values of the force for an individual ridge. The inclined solid line is at a 45° slope. A point above this line means the predicted force is greater than the measured value. In other words, an over prediction gives a point above the 45° line. The points under the line, of course, means an under-prediction.

For quantitative evaluation of the analytical model, a set of statistical measures are adopted. These include the mean of the force ratios of predicted to measured forces (R_P), the standard deviation of force ratios (S_P), the root mean square of relative errors of the prediction (RMS), and the correlation coefficient (R), as defined below:

$$R_P = \frac{1}{N} \sum_{i=1}^{N} \frac{F_{pi}}{F_{mi}}$$

$$S_P = \sqrt{\frac{1}{N} \sum_{i=1}^{N} \left(\frac{F_{pi}}{F_{mi}}\right)^2 - R_P^2} \qquad (7.1)$$

$$RMS = \sqrt{\frac{1}{N} \sum_{i=1}^{N} \left(\frac{F_{pi} - F_{mi}}{F_{mi}}\right)^2}$$

$$R = \frac{1}{N S_M S_C} \sum_{i=1}^{N} \left[(F_{pi} - \bar{F}_P)(F_{mi} - \bar{F}_m)\right]$$

where F_{mi} and F_{pi} are ith measured and predicted forces, respectively, N is number of the tests analyzed (or the number of points in Figures 7.1 or 7.2), and

$$S_M = \sqrt{\frac{1}{N}\sum_{i=1}^{N} F_{mi}^2 - \bar{F}_m^2} \qquad S_C = \sqrt{\frac{1}{N}\sum_{i=1}^{N} F_{pi}^2 - \bar{F}_p^2} \tag{7.2}$$

$$\bar{F}_m = \frac{1}{N}\sum_{i=1}^{N} F_{mi} \qquad \bar{F}_p = \frac{1}{N}\sum_{i=1}^{N} F_{pi}$$

B_S in Table 7.1 is the slope of the best fitting line through the origin.

Statistical Measures		OVERALL		ERC TESTS		IMD TESTS		IME TESTS	
		finite	infinite	finite	infinite	finite	infinite	finite	infinite
R_P	Vert.	1.12	1.06	1.29	1.20	0.90	0.84	1.16	1.14
	Hori.	1.11	1.06	1.42	1.32	0.86	0.81	1.05	1.04
S_P	Vert.	0.37	0.33	0.38	0.34	0.31	0.21	0.31	0.31
	Hori.	0.41	0.37	0.46	0.43	0.28	0.18	0.22	0.23
R_{MS}	Vert.	0.39	0.34	0.46	0.40	0.33	0.26	0.35	0.34
	Hori.	0.42	0.37	0.62	0.54	0.31	0.26	0.23	0.23
B_S	Vert.	1.15	1.02	1.15	1.02	0.90	0.84	1.10	1.00
	Hori.	1.39	1.22	1.40	1.23	0.87	0.82	0.98	0.93
R	Vert.	0.93	0.93	0.75	0.75	0.85	0.93	0.77	0.73
	Hori.	0.95	0.94	0.84	0.77	0.86	0.94	0.88	0.83

Table 7.1 Statistical Measures of the Predicted Ridge Loads

These statistical measures for the ridge load computation based on the finite ridge model (Equations (6.39) and 6.46)) are listed in Table 7.1. For the purpose of comparison, the

statistical measures for the computation based on the infinite ridge model (Equations (6.29) through 6.32)) are also listed in Table 7.1.

Both Table 7.1 and Figures 7.1 & 7.2 indicate that the prediction of maximum ice ridge loads with the present analytical model agrees well with the test measurements. The overall ratio of the predicted to the measured forces is 1.12 for vertical force and 1.11 for horizontal force, respectively. These numbers show that the prediction is only slightly higher than the measurement. The relatively low values of S_P and R_{MS} also indicate the low error level of the prediction.

7.1.2 Analysis of the Prediction

The predicted and measured maximum ridge forces for the ERC, IMD and IME tests are separately plotted in Figures 7.3 through 7.8, for a closer look. The vertical coordinates of the plus signs (+) in these figures represent the prediction with Equations (6.39) and (6.46), which will be referred to as finite ridge model in the following analysis, i.e., the effect of ridge length is taken into account (identified with "finite" in Table 7.1). Vertical coordinates of the circles (o) represent the forces predicted with Equations (6.29) and (6.32) which will be referred to as infinite ridge model in the analysis below, i.e., without considering the ridge length effect (labelled as "infinite" in Table 7.1). The points (o and +) in Figures 7.3, 7.5, and 7.7 are labelled with abbreviated test number that are obtained simply by omitting the letter(s) in the full test numbers. For instance, 241 shown in Figure 7.3 denotes the ERC test Y2T4R1.

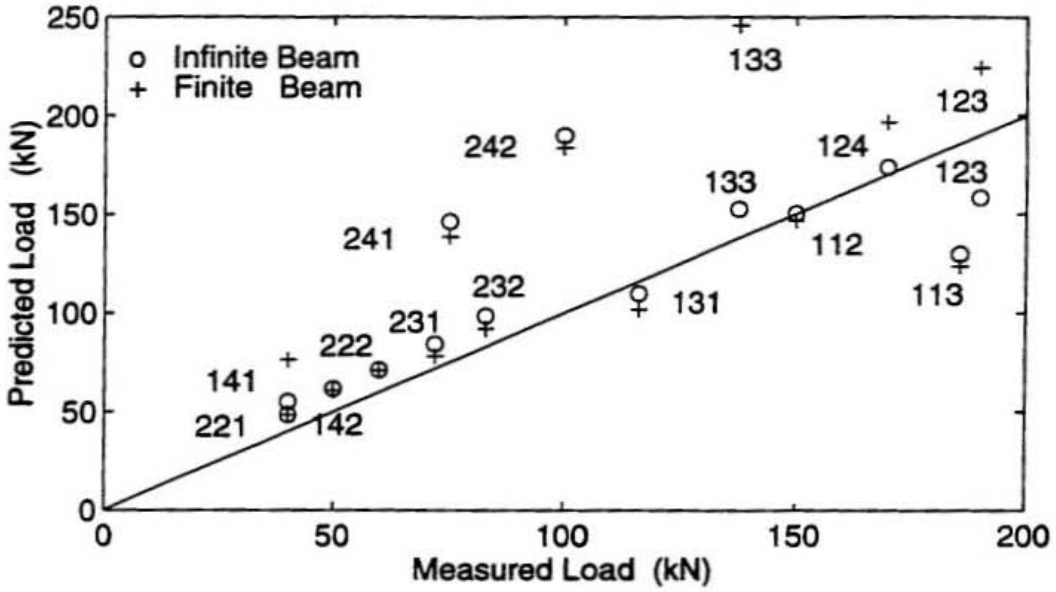

Figure 7.3 Vertical Ridge Loads of the ERC Tests

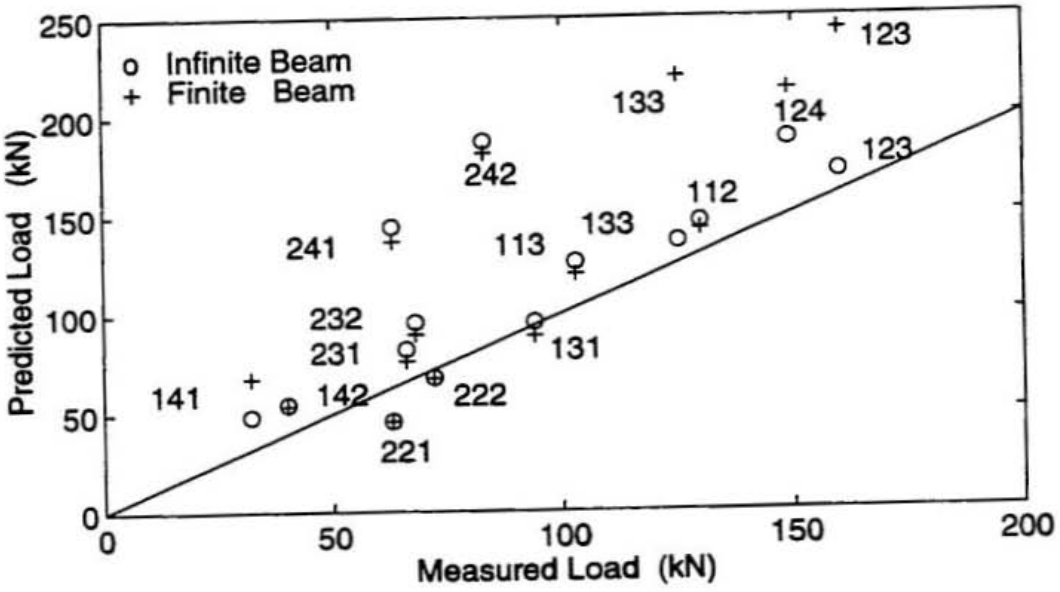

Figure 7.4 Horizontal Ridge Loads of the ERC Tests

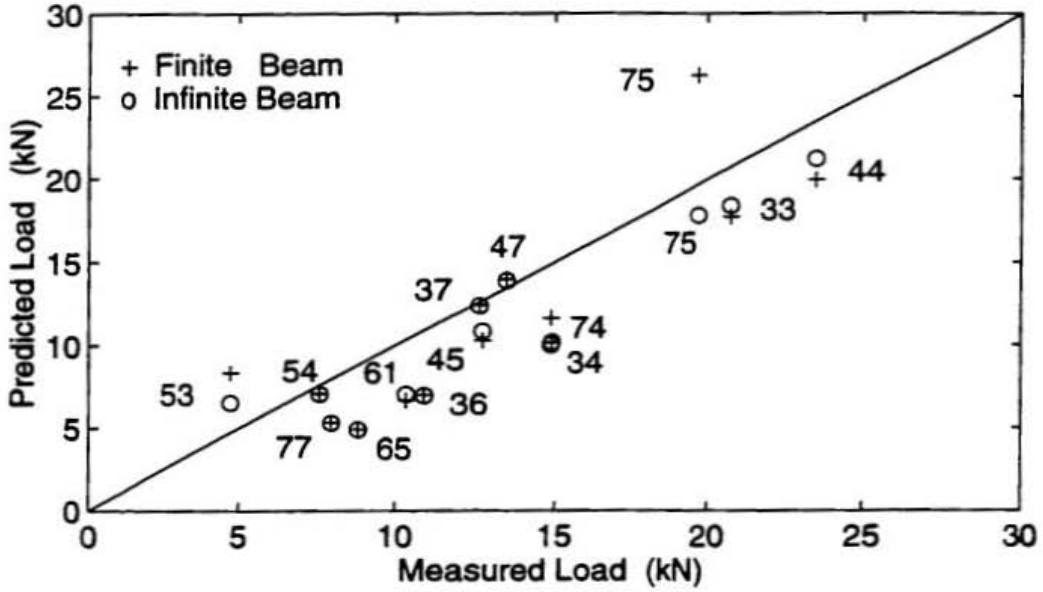

Figure 7.5 Vertical Ridge Loads of IMD Tests

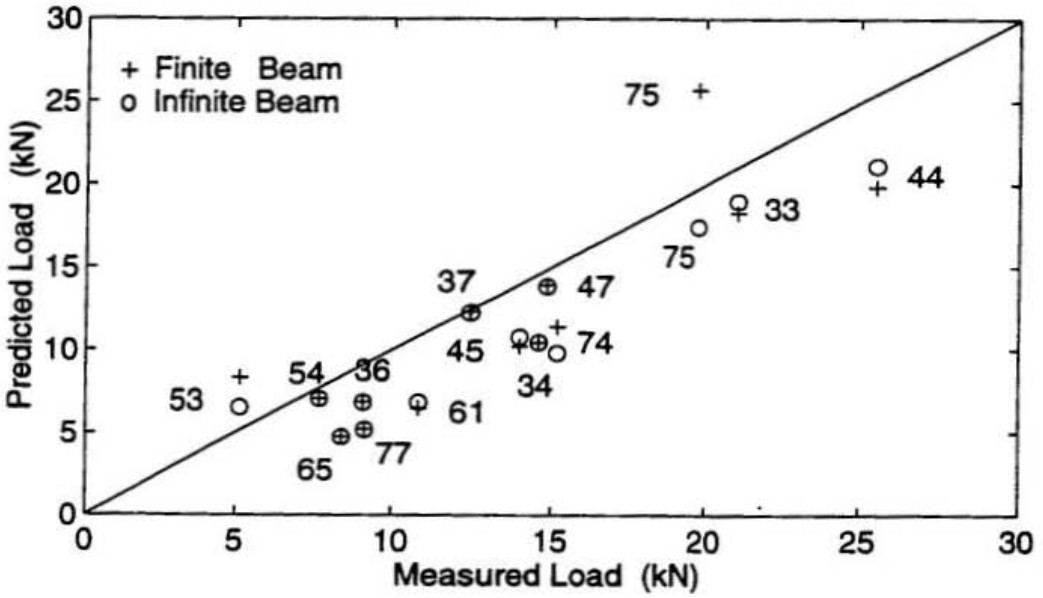

Figure 7.6 Horizontal Ridge Loads of IMD Tests

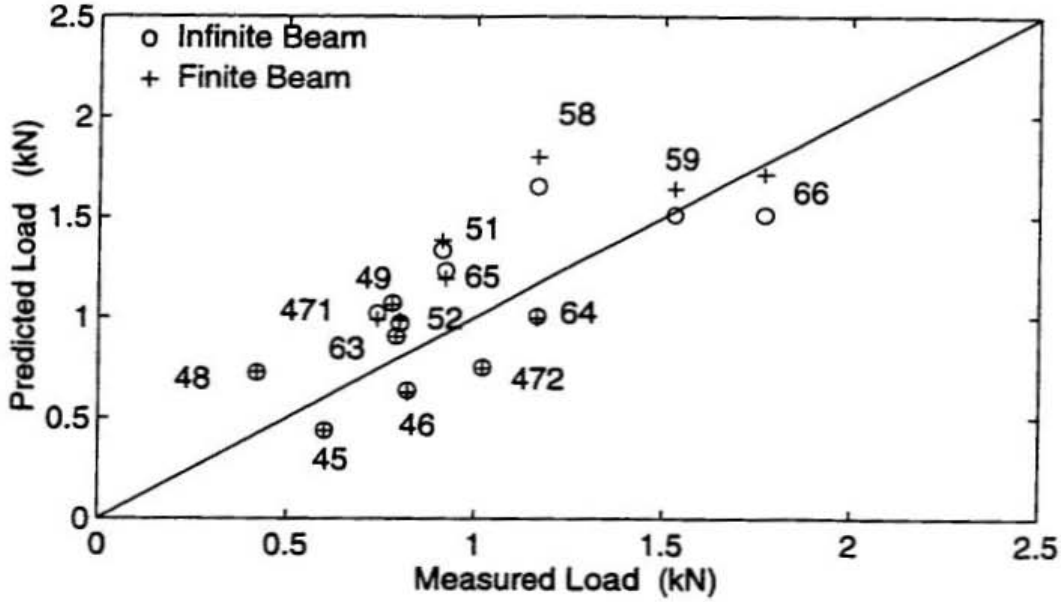

Figure 7.7 Vertical Ridge Loads of the IME Tests

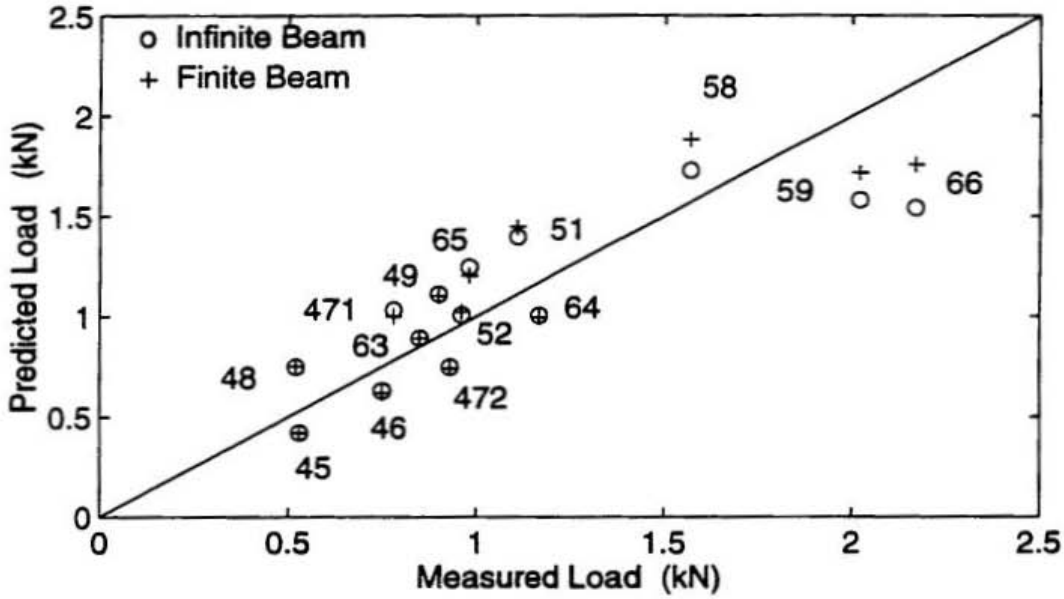

Figure 7.8 Horizontal Ridge Loads of the IME Tests

Figures 7.3 and 7.4 show that most points are above the 45° line, which means both the infinite and finite ridge models overpredict the ridge loads for the ERC tests. The numbers in Table 7.1 also statistically show the same trend: R_p and B_s for both infinite and finite ridge models are larger than 1. They also indicate that the degree of over-prediction for the horizontal loads is higher than that for the vertical loads. As discussed in Chapter 4 (shown in Table 4.3), Equation (2.1) does not correctly represent the relation between the vertical and horizontal loads. In the case of the ERC tests, the numbers in Table 4.3 showed that applying Equation (2.1) to the tests will incorrectly increase the horizontal load by 8.7% on average. In other words, even if an analytical model can perfectly predict those vertical loads (with zero error), use of Equation (2.1) may result in an average over prediction by about 8.7%. This may be part of reason for the over-prediction of the horizontal loads.

Compared with the measured vertical load of 185.8 kN for ridge 113 (ERC test Y1T1R3), the prediction with the finite ridge model is quite low, only 123.7 kN or 33% under-prediction of the load. One of the factors responsible for this large error may be the extraordinarily large vertical load. The ratio of the vertical (185.8 kN) to the horizontal loads (103 kN) for Y1T1R3 is 1.8, the largest of all the measured loads shown in Table 3.10. This large vertical load was primarily caused by the extremely heavy ride up. Unfortunately, the present analytical model does not cover these ride-up events. If the vertical hinge crack load (130 kN) is taken as the maximum vertical load (as wrongly presented in the summary of ERC' test report) the prediction would agree well with the measurement.

At the other end, the analytical model significantly overpredicted both vertical and horizontal loads for ridges 241 and 242 (the tests Y2T2R1 and Y2T2R2). The ratio of the flexural strength σ_{rt}/σ_{rb} (top in tension to bottom in tension) for ridges 241 and 242, as shown in Table 3.8, were 1.97 and 3.38, respectively. These unusually large ratios together with the strong sheet ice led to the higher predicted initial crack loads. There were two factors that might have played a role in the relatively low measured loads. Firstly, the days before the test day were extremely cold. The mean temperature for the two preceding days was -25°, which could make the ice more brittle. In fact, the video tape showed that the crack propagated quite far and fast. Secondly, ridge 241 had a crack near its center before the test began. Although no pre-crack was reported for ridge 242, the sheet ice in front of the ridge was damaged by the propagated cracks from the preceding test; these could have resulted in low measured loads.

Figures 7.5 and 7.6 present the predicted and measured ridge forces for the IMD tests. It is obvious, as shown by the graphs and the values of R_p and B_s for the IMD tests in Table 7.1, that the present analytical model significantly underpredicted the loads. It will be shown in the next section of this chapter that applying the plasticity model (Wang 1979 & 1984) also seriously underpredicts the ridge loads for the IMD tests. Table 4.6 has shown that the dimensionless ridge loads for the IMD tests are significantly larger than those for the ERC and IME tests. Moreover, Section 7.3 will also show that the analytical models predicting sheet ice loads also underestimate the sheet ice forces for the IMD tests. The reason for these is not clear. The complexity in failure mode of the IMD ridges may be one, if not all, of the reasons. Although the analytical models underpredict the loads, there is less scatter in the predicted loads for the

IMD tests than that for the ERC tests. This can be seen from the figures, the low values of S_p, and the relatively high values of correlation coefficient R.

Figures 7.7 and 7.8 give the prediction and the measurements for IME's tests. Generally, the prediction agrees well with the measurements, as shown by the figures and by the fact that R_p given in Table 7.1 is very close to (slightly higher than) unity with a small value of standard deviation. The prediction for the IME tests yields the best overall agreement of all the three series tests. The largest error, 73% over-prediction, occurs for the vertical load of ridge 48.

The effect of ridge length is shown by the difference in values identified by + and o in Figures 7.3 through 7.8. On the whole, the ridge length does not affect the ridge loads very much. This is due to the fact that the mean dimensionless ridge length ($2L/L_c$) for all these three series tests (with effect of sheet ice included) was 4.74, a value quite close to the critical value above which the effect of ridge length is negligible (refer to Section 6.62).

The effect for each individual test is different, depending on its dimensionless ridge length. As shown in the figures, the ridge length almost does not affect the ridge force for ridges 34, 36, 37, 47, 54, 65, and 77 in the IMD tests, and 45, 472, 48, 63, and 64 in the IME tests, 221 and 222 in the ERC tests. The dimensionless ridge lengths for these ridges vary in the ranges of 5.5 to 8.2. On the other hand, the effect is significant for the following ridges: ERC's ridge 123, 124, 133, and 141, IMD's 44, 53, 74, and 75, and IME's 58, 59, and 66. The dimensionless ridge length for these ridges fall in the ranges of 3.1 to 4.4.

The degree of the ridge length effect also depends on which crack governs the maximum ridge force. If the initial crack results in the maximum force, the effect may only slightly reduce the ridge load usually. Ridges that belong to this category include: 112, 113, 131, 142, 231, 232, 241 and 242 for the ERC tests, 33, 45, and 61 for the IMD tests, and 46, 471, 49, 51, and 64 for the IME tests. If the hinge crack gives rise to the maximum force, the effect usually increases inversely proportional to the dimensionless ridge length. The cases in which the effect of the dimensionless ridge length is insignificant includes ridges 53 and 74 in the IMD tests and ridges 51 and 52 in the IME tests. Ridges 141, 123, and 133 in the ERC tests, 58, 59, and 66 in the IME tests, and 75 in the IMD tests belong to the cases in which the ridge length effect is significant.

7.2 Validation of Other Analytical Models for Ridge Load Estimation

One of the concerns on the MCSs was the validity of those analytical models which were widely accepted for SCSs. This section evaluates two typical analytical models, Wang's model (1979 & 1984) and the Croasdale-Abdelnour model (Croasdale 1980, Abdelnour 1981 & 1988), by comparing their predictions with the test results presented in Chapters 3 and 4. Moreover, comparison between the analytical models and the present model (given in Chapter 6) will also be carried out to further evaluate them.

Wang's model and the present model include the ride-up forces, but the Croasdale-Abdelnour model does not. To make the predictions comparable between the analytical models, the ride-up forces computed with the Nevel model (the same as those for the present model) are added to the prediction using the Croasdale-Abdelnour model as the total ridge ice loads. Since Wang's model is incapable of accounting for the effect of ice ride-up on the vertical neck, the height of ice ride-up is taken from the waterline to the top of the collar for all three models.

7.2.1 The Load Predictions

The predicted loads with the three analytical models together with those measured are plotted in Figures 7.9 through 7.14. Although both the finite ridge and the infinite ridge formulations for the present analytical model and the Croasdale-Abdelnour model were applied to predict the ridge loads, only those from finite ridge formulations (i.e. with ridge length taken into account) are presented in these figures. However, the results of the prediction with infinite ridge formulations will also be discussed in the next subsection.

In these figures, the symbols "o", "+", and "x" represent the predictions of the present model, Wang's model, and the Croasdale-Abdelnour model (labelled as C-A in the figures), respectively. Their best fit lines through the origin of the coordinate are given by dash line, dash-dot line, and dotted line, respectively. The solid line in these figures has a slope of 45°. The points and lines above this solid line mean that the analytical model over-predicts the loads, otherwise, the analytical model under-predicts the loads.

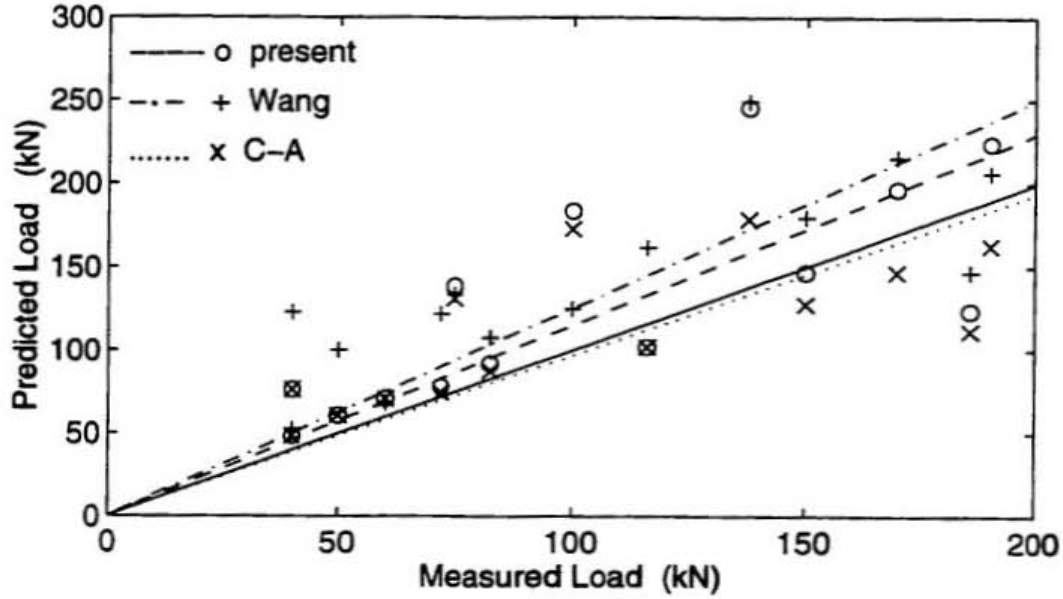

Figure 7.9 Vertical Loads from Three Models for the ERC Tests

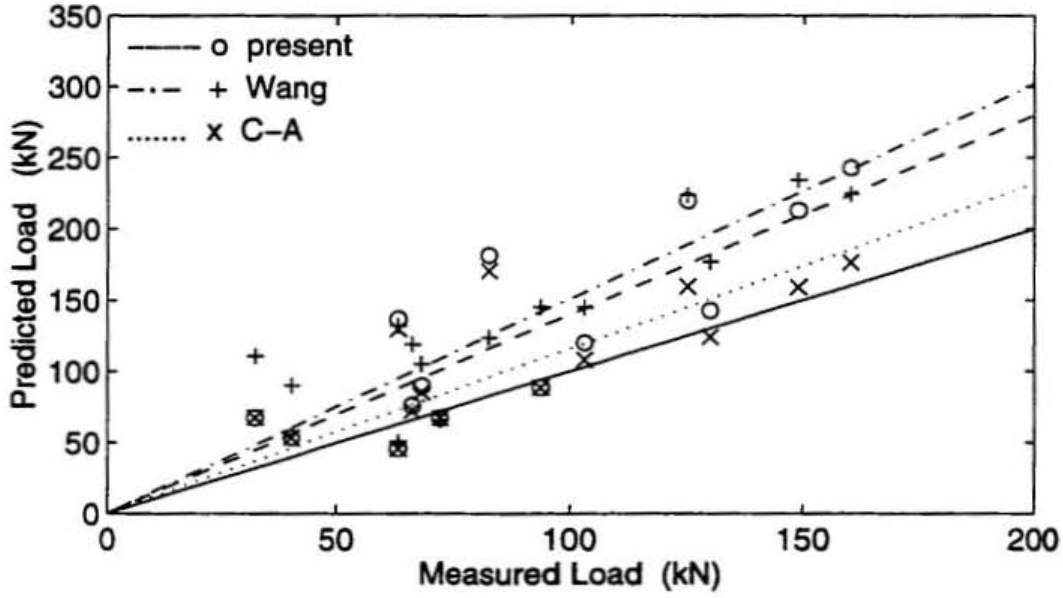

Figure 7.10 Horizontal Loads from Three Models for the ERC Tests

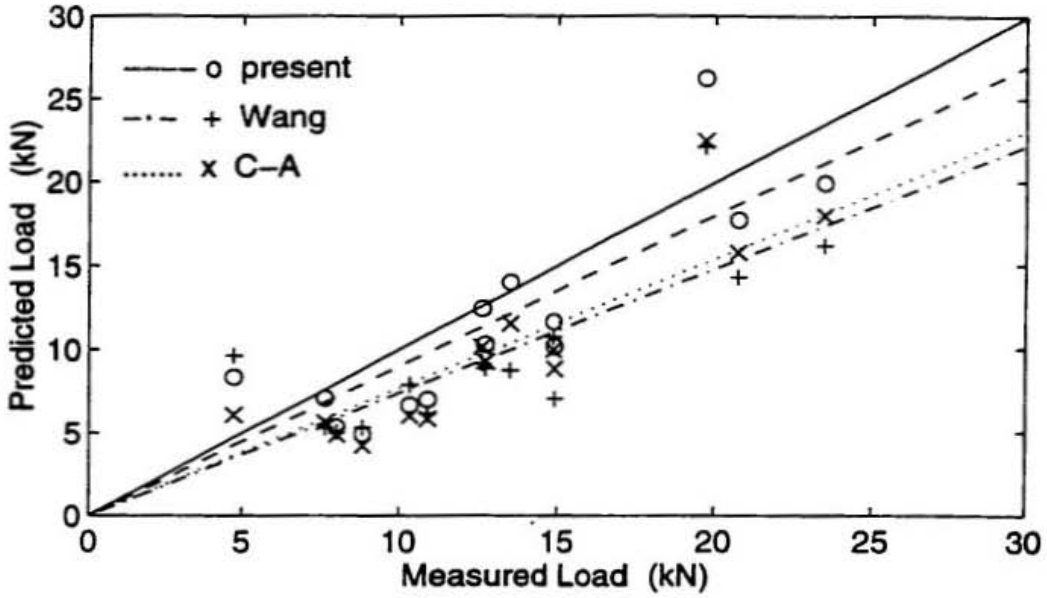

Figure 7.11 Vertical Loads from Three Models for the IMD Tests

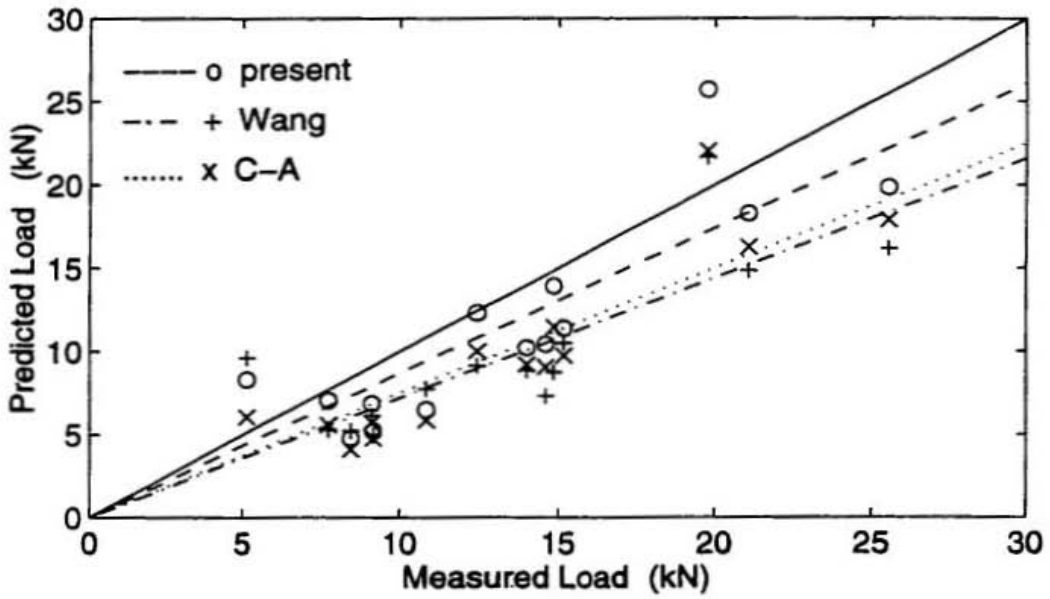

Figure 7.12 Horizontal Loads from Three Models for the IMD Tests

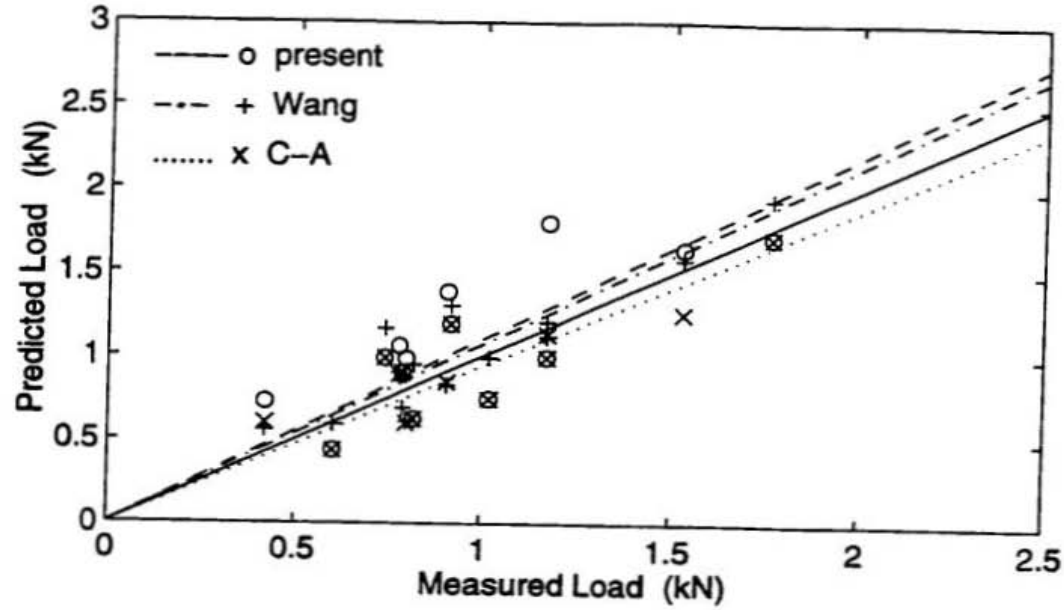

Figure 7.13 Vertical Loads from Three Models for the IME Tests

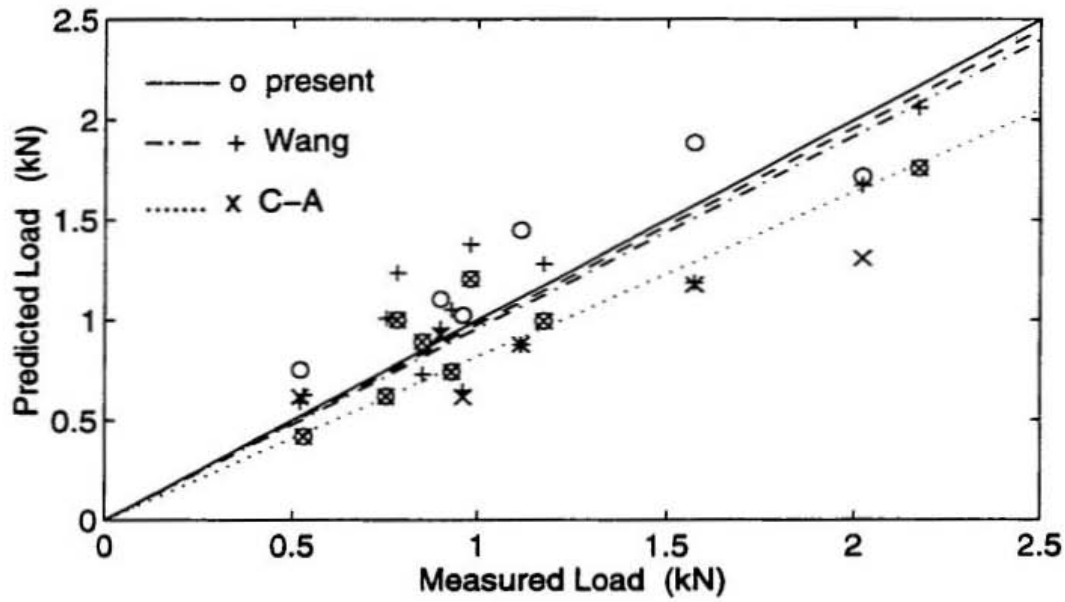

Figure 7.14 Horizontal Loads from Three Models for the IME Tests

7.2.2 Evaluation of the Analytical Models

Although the graphs in Figures 7.9 through 7.14 show the difference in the predictions from three analytical models, it is still difficult to quantitatively evaluate them. Again, the statistical quantities given in Equation (7.1) are used to help the evaluation. The computed statistical quantities for the vertical and the horizontal loads of each of the three facilities' tests are given in Tables 7.2 and 7.3, respectively.

MODEL		TESTS	R_P	S_P	RMS	R	B_S
Wang's Model		ERC	1.51	0.54	0.74	0.79	1.25
		IMD	0.79	0.37	0.43	0.78	0.74
		IME	1.09	0.22	0.23	0.90	1.07
the Croasdale and Abdelnour Model	Finite Beam Theory	ERC	1.17	0.37	0.41	0.71	0.96
		IMD	0.75	0.22	0.33	0.89	0.78
		IME	0.99	0.23	0.23	0.85	0.94
	Infinite Beam Theory	ERC	1.13	0.34	0.37	0.69	0.92
		IMD	0.74	0.19	0.32	0.94	0.75
		IME	0.98	0.24	0.24	0.82	0.92
The Present Analytical Model	Finite Beam Theory	ERC	1.29	0.38	0.48	0.75	1.15
		IMD	0.90	0.31	0.33	0.85	0.90
		IME	1.16	0.31	0.35	0.77	1.10
	Infinite Beam Theory	ERC	1.20	0.34	0.40	0.75	1.02
		IMD	0.84	0.21	0.26	0.93	0.84
		IME	1.14	0.31	0.34	0.73	1.00

Table 7.2 Statistical Measures of Vertical Load Predictions for the Three Models

MODEL		TESTS	R_p	S_p	RMS	R	B_s
Wang's Model		ERC	1.67	0.62	0.92	0.86	1.51
		IMD	0.76	0.34	0.41	0.79	0.72
		IME	1.06	0.26	0.26	0.85	0.96
the Croasdale and Abdelnour Model	Finite Beam Theory	ERC	1.28	0.44	0.52	0.77	1.16
		IMD	0.73	0.20	0.34	0.89	0.75
		IME	0.91	0.20	0.22	0.87	0.82
	Infinite Beam Theory	ERC	1.24	0.42	0.48	0.70	1.11
		IMD	0.71	0.16	0.33	0.96	0.72
		IME	0.90	0.22	0.24	0.84	0.80
The Present Analytical Model	Finite Beam Theory	ERC	1.42	0.46	0.62	0.84	1.40
		IMD	0.86	0.28	0.31	0.86	0.87
		IME	1.05	0.22	0.23	0.88	0.98
	Infinite Beam Theory	ERC	1.32	0.43	0.54	0.77	1.23
		IMD	0.81	0.18	0.26	0.94	0.82
		IME	1.04	0.23	0.23	0.83	0.93

Table 7.3 Statistical Measures of Horizontal Load Predictions for the Three Models

To quantitatively evaluate the analytical models, the rules for judging the quality of their predictions are defined as : A model is considered to be better if its' prediction yields i) R_p closer to or slightly larger than unity with smaller S_p, ii) relatively smaller RMS, iii) a larger R, closer to unity, and iv) B_s closer to or slightly larger than unity.

Let's first look at the Wang model. This model, on an average, over-predicted the loads

by 51% for vertical loads and by 67% for horizontal loads of the ERC tests, as shown in Tables 7.2 and 7.3. Figures 7.9 and 7.10 as well as the corresponding values of the statistical measures in Tables 7.2 and 7.3 show that the prediction had a large scatter, resulting in large values of root mean square (''RMS'' in the tables). On the other hand, the Wang model significantly under-predicted both the vertical and horizontal loads for the IMD tests, and the data are less scattered. Its prediction for the IME tests yielded a very good agreement with the measurements. The average ratio R_P is very close to unity with relatively smaller S_P.

Croasdale-Abdelnour's finite ridge theory given in Equation (2.3) significantly under-predicted the vertical and horizontal loads for the IMD tests and slightly under-predicted both loads for the IME tests. However, its predictions for the ERC tests were quite good, especially those for the vertical loads of the ERC tests.

If comparing the predictions of the three models, it can be seen from both the figures and the tables that the present model is the best one. Both the Wang model and the present model over-predicted the loads of the ERC tests, but the present model yields a lower prediction. For the IMD tests all three models under-predicted, but the present model gives a highest prediction whose R_P is 0.9. The predictions of Wang's model and the present model for the IME tests are very close and are better than the Croasdale-Abdelnour model. The Croasdale-Abdelnour model shows a better performance for the prediction of the ERC tests.

The Croasdale-Abdelnour model is based on elastic theory and was supported by the

saline ice tests. The Wang model, as previously pointed out, was based on plasticity theory and was supported by the test with model ice ridges (Wang 1979). The ice ridges used in the ERC tests were also constructed with saline ice and seem to behave in an elastic and brittle manner. On the other hand, the ice ridges used in the IMD and IME tests (especially the IMD tests) were made of model ice which seems to behave more or less in an elastic-plastic manner. Thus, it is understandable that Wang's model did well for the IMD and IME tests but significantly over-predicted the ERC tests, and the Croasdale-Abdelnour model shows the best performance with the ERC tests. Although the present model is also based on elastic theory, it takes the special features of the faceted cone into account. Hence as expected it gives a better accuracy for the prediction.

To provide an overall assessment of the accuracy of predictions of these models, their overall statistical measures for all the tests in the three facilities are listed in Table 7.4. Although the numbers in this table still show that the Croasdale-Abdelnour model under-predicts the loads, it appears as if all three models are acceptable for the prediction of ice ridge loads on the tested MCSs. These overall values of the statistical measures give a general idea about the models' predictions, but cover over the large errors for tests at each individual facility. For instance, the significant over-prediction for the ERC tests and under-prediction for the IMD tests by the Wang model are partly cancelled to give a R_p close to 1. Similar charges also occurred to the Croasdale-Abdelnour and the present models. The effect of the cancellation is to a lower degree in the present model.

	MODEL		R_P	S_P	RMS	R	B_S
VERTICAL LOAD	Wang's model		1.13	0.49	0.51	0.94	1.24
	Croasdale-Abdelnour model	finite	0.97	0.33	0.33	0.92	0.96
		infinite	0.95	0.31	0.31	0.92	0.92
	the Present model	finite	1.12	0.37	0.39	0.93	1.15
		infinite	1.06	0.33	0.34	0.93	1.02
HORIZONTAL LOAD	Wang's model		1.16	0.58	0.60	0.97	1.50
	Croasdale-Abdelnour model	finite	0.97	0.38	0.38	0.95	1.15
		infinite	0.95	0.36	0.37	0.93	1.10
	the Present Model	finite	1.11	0.41	0.42	0.95	1.39
		infinite	1.06	0.37	0.37	0.94	1.22

Table 7.4 Overall Statistical Measures of Predictions of the Three Models

A noticeable feature of the predicted loads, plotted in Figures 7.9 through 7.14, should be pointed out and explained, that is the overlaps of the "o" and "x" for some of the ERC tests and the IME tests. These occur on those ridges that were oblique at a 30° angle for the ERC tests and those tested with the structure in an edge-on orientation for the IME tests. In all these cases, the contact area was assumed to be a point; in other words, a point load at the center line of the ridges was assumed. As previously stated, the difference between the present model and the Croasdale-Abdelnour model is the loading condition, and the Croasdale-Abdelnour model is identical to the present model when the contact area becomes a point. Hence the point loading condition of the tests that was used as an input to these two models has made their prediction

identical to one another.

7.3 Validation of the Theoretical Models for Sheet Ice Load Prediction

Another part of the concern three, stated in Chapter 1, was the validity of those theoretical models for prediction of floe ice loads on MCSs. These models were all developed for SCSs and widely used or accepted for such structures. Their validity will be examined in this section.

7.3.1 The models and the Inputs

Ralston's model (1978 & 1980) has been most widely used for the prediction of sheet ice loads on SCSs and is recommended by the American Petroleum Institute (1988). Croasdale's (1980) three dimensional model (to be abbreviated as Croasdale's model) was another widely accepted earlier model. These two models can be considered as representatives of their kind based on plasticity theory and elasticity theory, respectively. Therefore, these two models together with the Nevel model (Nevel, 1992) will be evaluated in this section.

The recently developed Nevel's model is considered to be conceptually more suitable for application to MCSs because of its characteristics:

A. It divides the ice floe into several wedges that act against a cone and ride up on the

cone's surface. The forces are exerted on the cone through the cone/ice contact lines or points. Thus, if the ice is divided into the number of wedges which is equal to the number of facets of a half cone, this model is capable of being directly applied to MCSs.

B. Nevel's model considers multi-section characteristics of the cone and its effect on ice loads. Thus, theoretically speaking, it is able to account for the effect of the vertical neck and the transition from the main cone to the collar.

Due to the characteristics of the tested MCSs and the requirement of Ralston's model and Croasdale's model, part of the inputs to these two models were not so certain. The parameters needed for determining ice forces include waterline diameter, cone slope angle, and height of ice ride-up. All these are presented and discussed as follows:

1. Waterline diameter. Only one waterline diameter exists for a smooth cone, but there are two for a MCS: an inscribed diameter and a circumscribed diameter and the latter is about 1.155 times larger than the former. To show the effect of this parameter, a separate computation for each of these diameters will be carried out with both Ralston's and Croasdale's models. The coordinates for the cone geometry used in Nevel's model are those along the center line of the ice wedge. Since this line is the center line (symmetrical axis) of a facet, thus the inscribed diameter is chosen as a reasonable value for Nevel's model.
2. Cone slope angle. Again the six-sided cone has two slope angles: one is its facet angle which is 39.8°, and the other is its corner slope angle which is about 35.8°. Since the ice floe exerted its forces mainly against the facet and rode up on it, the facet slope angle

has been used as the main cone slope angle for all three models.

3. Height of ice ride up. Strictly speaking, Ralston's and Croasdale's models are only capable of accounting for the height to the top of the main cone. However, tests have shown that ice pieces rode up at least to the top of the collar which was up to 60 centimetres (for 1:10 structural models) above the main cone top. Thus, the ride-up height was measured from the waterline to the top of the collar. The freeboard of the main cone, measured from the waterline to the top of the main cone, is also taken as the input of another ride-up height for studying the effect of this parameter. Although Nevel's model is capable of including the effect of the neck, the input ride-up height for it is also taken as the distance from the waterline to the collar top to make the computation comparable.

7.3.2 Computation Results

Computation for a total of 40 sheet ice tests using face-on structures were conducted. These tests are: Y1T1R2, Y1T3R2, Y1T4R1, Y2T1R2, Y2T2R2, Y2T3R1, and Y2T4R1 for the ERC tests, M31, M32, M33, M35, M41, M42, M43, M46, M51, M52, M53, M62, M63, M64, M71, M72, M73, and M76 for the IMD tests, and C16 through C30 (15 tests), C42, C50, C54 through C57, and C60 for the IME tests.

The predicted loads are plotted against those measured in Figures 7.15 through 7.20. The keys in these figures have the following meanings:

NIL Nevel's model with cone's inscribed diameter and the ride-up height measured from the waterline to the top of the collar,

RIL Ralston's model with inscribed diameter and ride-up hight to the collar top,

RCL Ralston's model with circumscribed diameter and ride-up height to the collar top,

RCN Ralston's model with circumscribed diameter and ride-up height to main cone top,

CIL, CCL, and CCN are for Croasdale's model with diameter and ride-up height the same as RIL, RCL, and RCN, respectively.

Because of the wide range of the loads, the plots are given in log-log format to make this section more compact. The disadvantage of log-log plotting is that it may hide the scatter of the data. This will be overcome by listing the statistical measures shown in the next subsection. These graphs are only expected to provide a general idea as to how the data are distributed.

Nevel's model is capable of handling two ride-up interaction conditions one of which is termed as ''passive action'' and the other as ''active action'' (refer to Section 2.4.3). Compared to passive action, the active action generates an additional force between the structure and ice Thus, the active action may result in a larger overall force. The active action was assumed for all the computations shown in this subsection. It will be shown in the next subsection that the effect of assuming the active action is insignificant for vertical load prediction compared with the passive action, but it slightly increases the horizontal load.

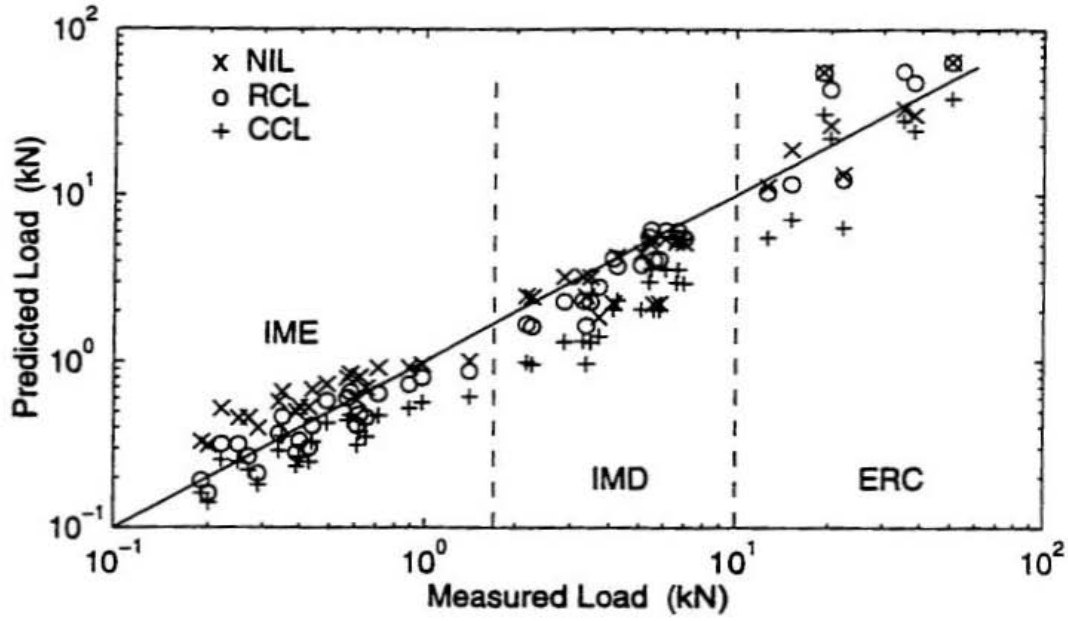

Figure 7.15 Vertical Sheet Ice Loads, NIL, RCL, and CCL

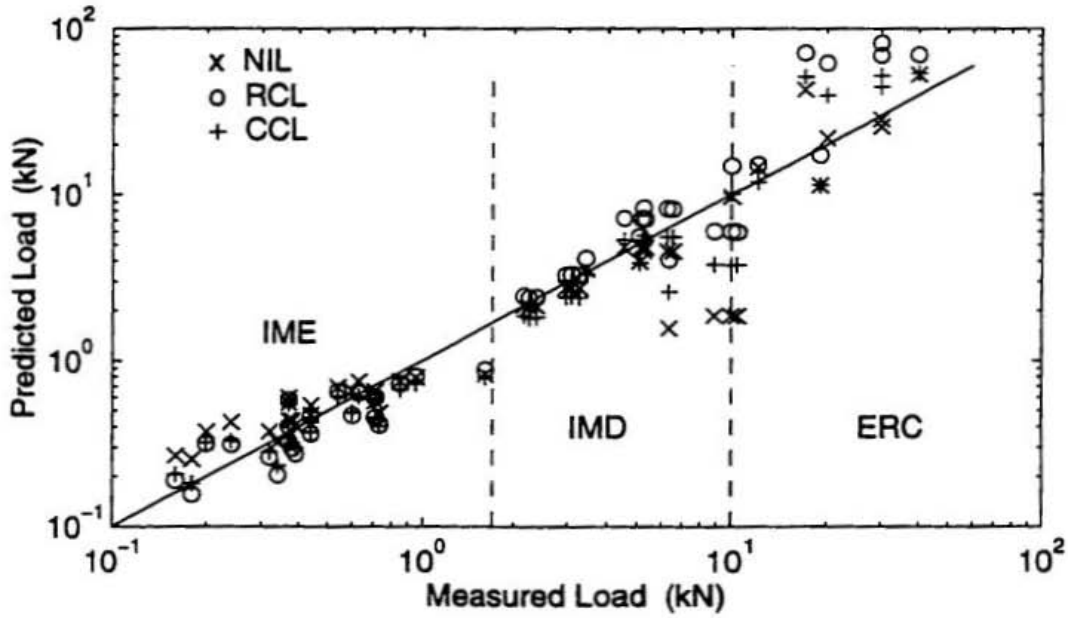

Figure 7.16 Horizontal Sheet Ice Loads, NIL, RCL, and CCL

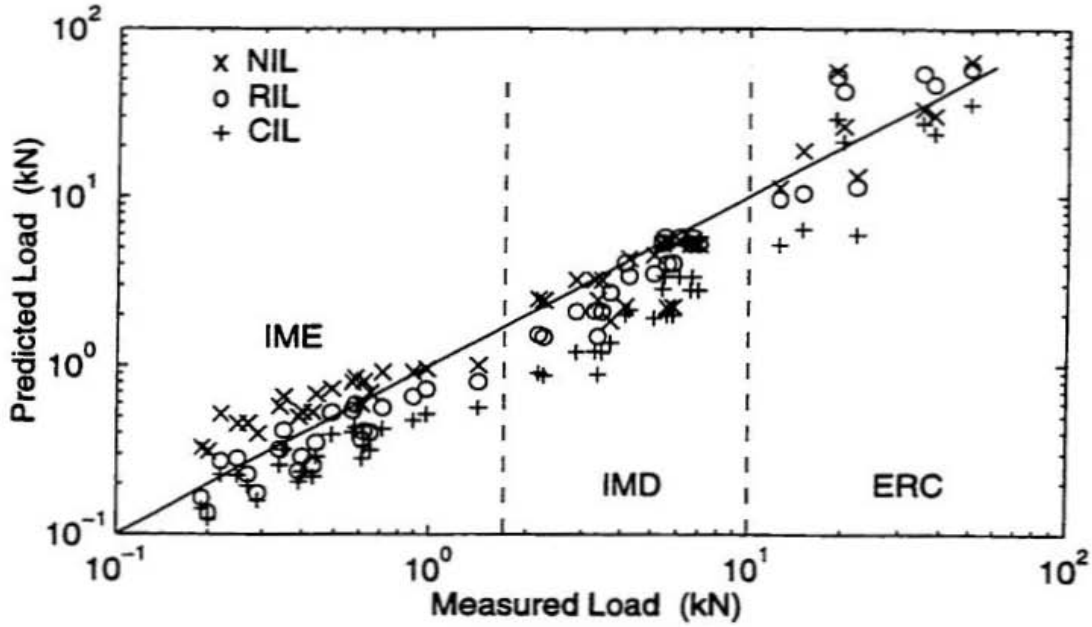

Figure 7.17 Vertical Sheet Ice Loads, NIL, RIL, and CIL

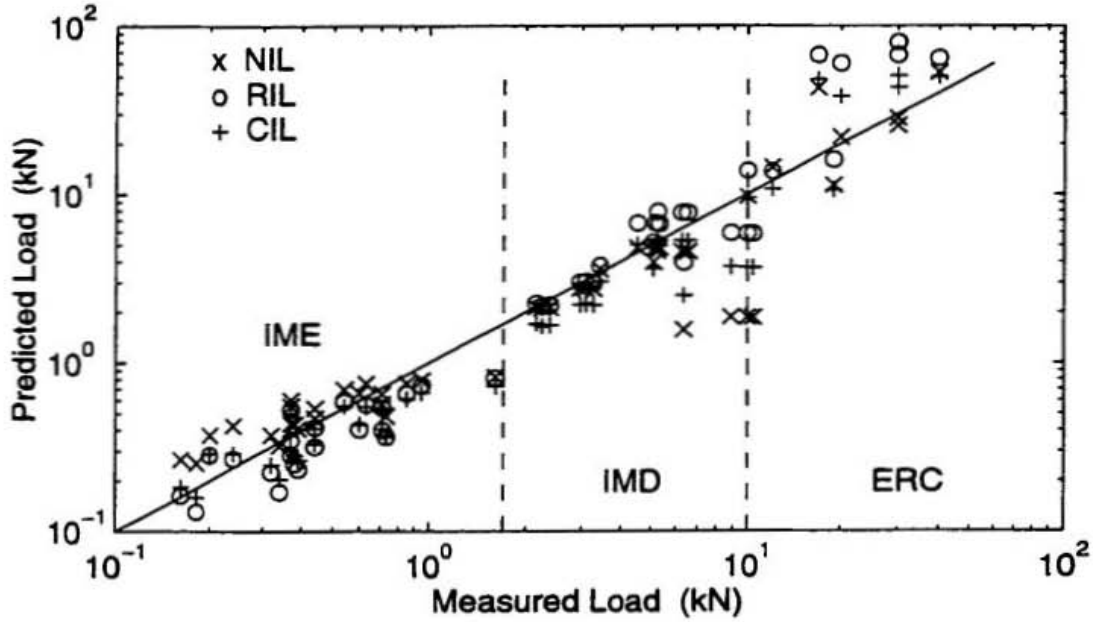

Figure 7.18 Horizontal Sheet Ice Loads, NIL, RIL, and CIL

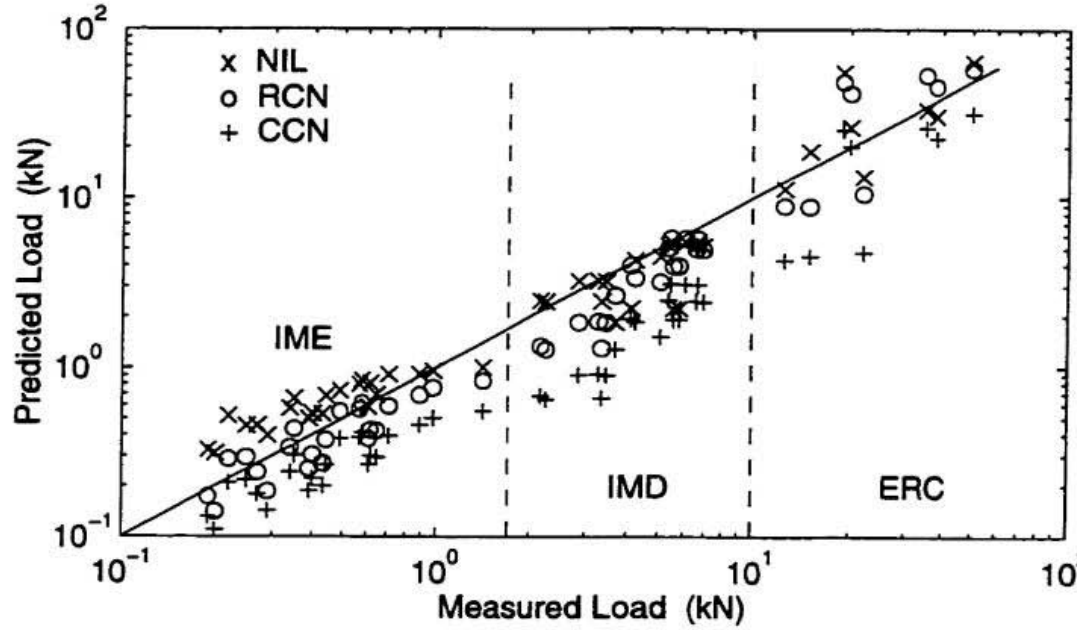

Figure 7.19 Vertical Sheet Ice Loads, NIL, RCN, and CCN

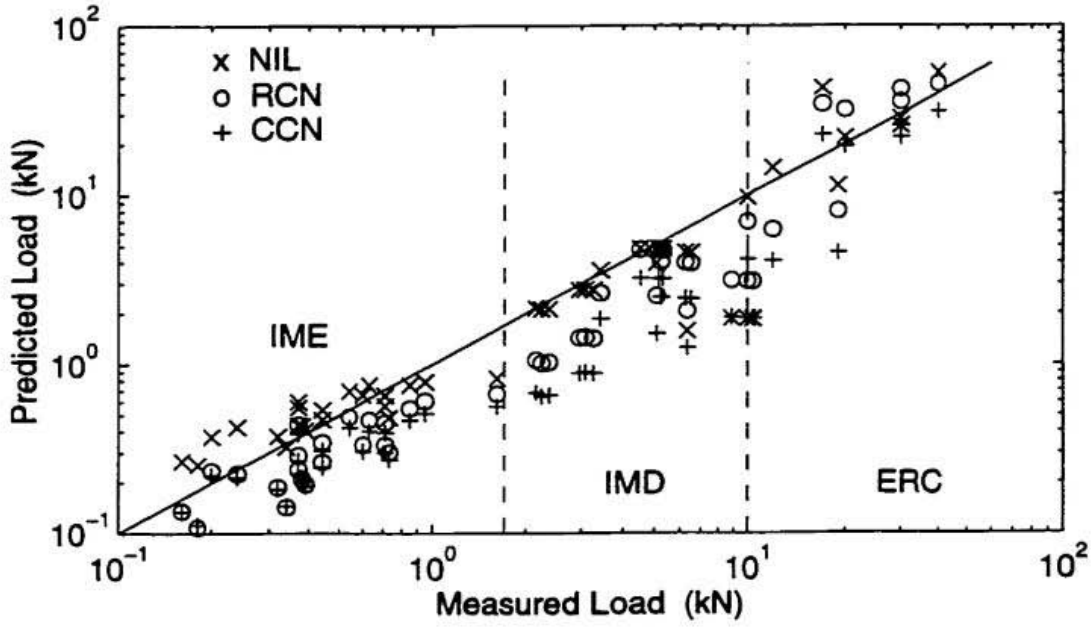

Figure 7.20 Horizontal Sheet Ice Loads, NIL, RCN, and CCN

7.3.3 Analysis of Prediction

First of all, let's look at the overall performance of each model for all the tests. The statistical measures for all the tests are listed in Table 7.5. The numbers in the table show that Nevel's model (NIL), on average, provides the best prediction of all the models with all the chosen parameter (i.e., the diameter and ride-up height) combinations. RCL gives the second best average prediction with vertical loads slightly under-predicted and horizontal loads significantly over-predicted. RIL also yields reasonable prediction on average. All others including CCL, CIL, CCN, and RCN significantly under-predict the loads.

Model	R_P		S_P		RMS		R	
	Ver.	Hori.	Ver.	Hori.	Ver.	Hori.	Ver.	Hori.
NIL	1.17	1.01	0.48	0.43	0.51	0.43	0.90	0.90
RIL	0.89	1.11	0.39	0.66	0.41	0.66	0.92	0.91
CIL	0.58	0.90	0.23	0.43	0.48	0.44	0.93	0.92
RCL	0.97	1.21	0.41	0.67	0.41	0.71	0.93	0.91
CCL	0.63	0.98	0.25	0.45	0.45	0.45	0.93	0.92
RCN	0.88	0.71	0.39	0.35	0.40	0.45	0.92	0.93
CCN	0.53	0.54	0.22	0.26	0.53	0.53	0.93	0.93

Table 7.5 Overall Statistical Measures of Sheet Ice Load Prediction

As pointed out in the last section, the overall statistical measures give a general idea about a model's prediction but hide errors which may be presented for individual test series.

Therefore, a detailed list of those statistical measures for each series tests are given in Table 7.6 for vertical load prediction and in Table 7.7 for horizontal load prediction.

Model	ERC			IMD			IME		
	R_p	S_p	RMS	R_p	S_p	RMS	R_p	S_p	RMS
NIL	1.26	0.68	0.73	0.83	0.23	0.29	1.42	0.36	0.55
RIL	1.35	0.71	0.79	0.77	0.15	0.28	0.82	0.20	0.28
CIL	0.73	0.38	0.47	0.43	0.09	0.58	0.65	0.16	0.38
RCL	1.42	0.74	0.85	0.82	0.15	0.24	0.93	0.23	0.24
CCL	0.77	0.40	0.46	0.46	0.09	0.55	0.73	0.18	0.33
RCN	1.29	0.69	0.75	0.73	0.17	0.32	0.86	0.21	0.26
CCN	0.65	0.36	0.50	0.37	0.10	0.64	0.61	0.15	0.42

Table 7.6 Statistical Measures for Vertical Sheet Load Prediction

Model	ERC			IMD			IME		
	R_p	S_p	RMS	R_p	S_p	RMS	R_p	S_p	RMS
NIL	1.19	0.55	0.58	0.74	0.30	0.40	1.17	0.35	0.39
RIL	2.10	0.99	1.49	1.01	0.28	0.28	0.82	0.26	0.32
CIL	1.44	0.67	0.80	0.73	0.22	0.35	0.85	0.26	0.30
RCL	2.22	1.02	1.59	1.09	0.30	0.32	0.94	0.29	0.29
CCL	1.52	0.70	0.87	0.78	0.24	0.32	0.95	0.28	0.29
RCN	1.13	0.52	0.54	0.57	0.22	0.49	0.68	0.22	0.38
CCN	0.71	0.34	0.45	0.36	0.16	0.66	0.63	0.20	0.42

Table 7.7 Statistical Measures for Horizontal Sheet Load Prediction

It is shown from the tables that Ralston's model (RCL, RIL, and RCN) and Nevel's model (NIL) over predicted both the vertical and horizontal loads for the ERC tests, while Croasdale's model (CIL and CCL) significantly under-predicted the vertical loads and over-predicted the horizontal loads; CCN model under-predicted both the horizontal and vertical loads. It seems that Croasdale's model is better than Ralston's model for horizontal load prediction but worse for vertical load prediction. Of all the models, Nevel (NIL) and RCN of Ralston model give the best predictions.

For IMD's tests, all the models under-predicted the vertical loads with NIL and RCL giving the highest prediction. RCL and RIL predict the horizontal loads very well but all the others under-predict the horizontal loads. Generally, Ralston model's prediction is slightly better than that from Nevel's model which, however, performed better than Croasdale's model. If the IMD tests alone are used to judge the models, RCL may be the best choice. There are four tests, M71, M72, M73, and M76, in the IMD series for which NIL considerably under-predicted the horizontal loads. The data given in Table 3.12 of Chapter 3 showed the ratio of the measured horizontal force to the vertical to be near 2 for these four tests which is unreasonably large, while the ratio for the rest of the tests was either smaller than or very close to 1.

In the IME tests, it turns out that NIL is the only one which over-predicted the loads. Compared with the prediction by Croasdale's model and the other cases of Ralston's model, RCL of Ralston model gave a good prediction for the IME tests.

Combining the analyses given above along with all the information gleaned out from graphs shown in Figures 7.15 through 7.20 and the numbers listed in Tables 7.5 through 7.7, we may draw the conclusion as follows: Nevel model (NIL) is fairly suitable for application to prediction of sheet ice loads on MCSs such as those tested. If proper parameters are chosen, Ralston's model is also applicable to MCSs, like RCL or RIL. Croasdale's three dimensional model generally under-predicted the loads even though it yielded some good prediction for the ERC tests.

To further test Nevel's model and examine the effect of the choice of passive action and active action, another two input conditions are applied to the model. Both of these conditions consider the ice ride-up on the vertical neck, and active action is assumed for the first one, which is being labelled as NNA, while the second one considers the passive action and is termed as NNP. The prediction of Nevel's model for these two conditions are plotted in Figures 7.21 and 7.22. The corresponding statistical measures are given in Table 7.8.

TESTS		NNA			NNP		
		R_p	S_p	RMS	R_p	S_p	RMS
ERC	Ver.	1.45	0.79	0.91	1.45	0.79	0.91
	Hori.	1.52	0.69	0.86	1.29	0.59	0.66
IMD	Ver.	0.95	0.25	0.26	0.94	0.25	0.26
	Hori.	0.91	0.34	0.36	0.78	0.31	0.37
IME	Ver.	1.46	0.37	0.59	1.46	0.37	0.59
	Hori.	1.24	0.37	0.44	1.19	0.35	0.40
OVERALL	Ver.	1.27	0.50	0.57	1.27	0.50	0.57
	Hori.	1.16	0.48	0.51	1.05	0.44	0.44

Table 7.8 Statistical Measures of NNA and NNP Predictions

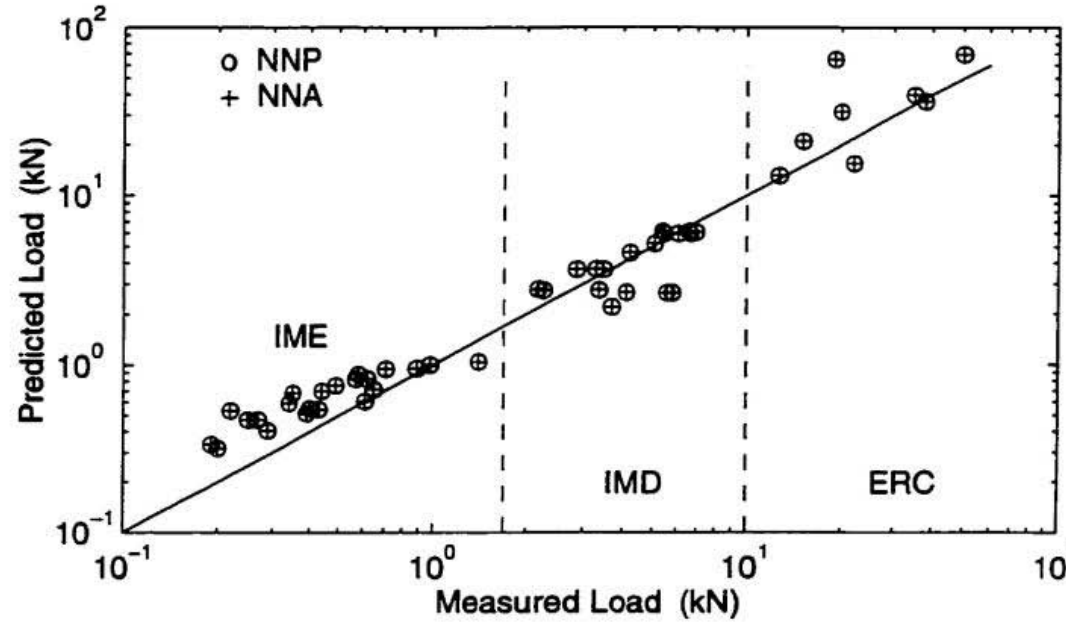

Figure 7.21 Predicted Vertical Sheet Ice Loads with NNA and NNP

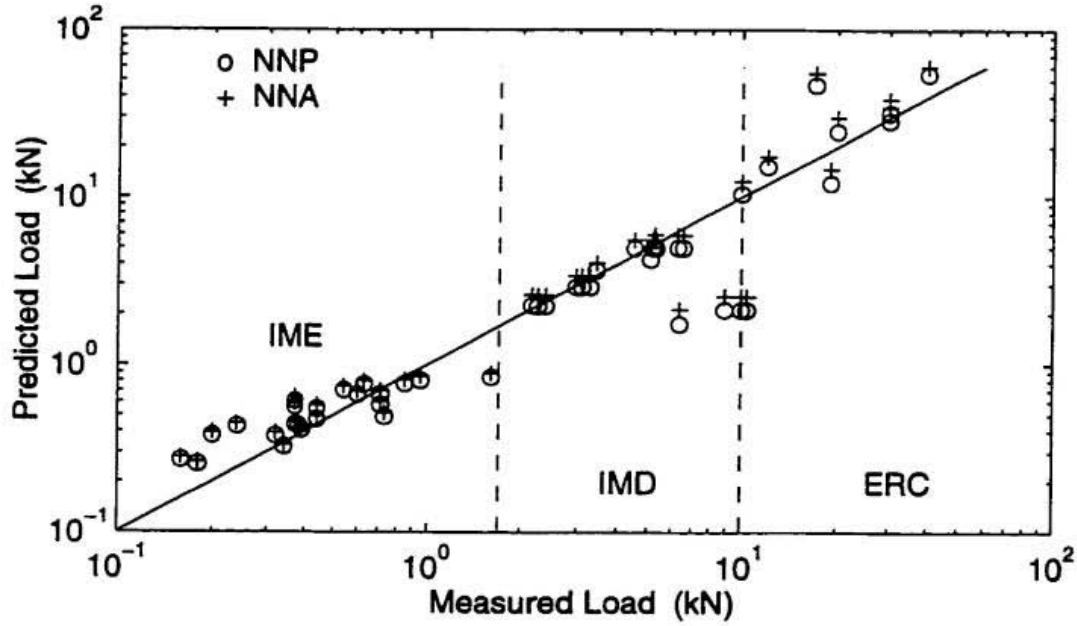

Figure 7.22 Predicted Horizontal Sheet Ice Loads with NNA and NNP

Figure 7.21 shows that the predicted vertical loads vs. the measured vertical loads for the ERC and IME tests were mainly located above the 45° line, which means that the model gives a conservative prediction for these two series tests. Although some points for the IMD tests are below the line, most points are basically fairly close to the line. The numbers in Table 7.8 give quantitative description of this trend. R_P has a value of 1.45 for the ERC test with relatively large value of S_P and RMS which means the data are quite widely spread, and an almost the same value of R_P, 1.46, for the IME tests accompanied by smaller values of S_P and RMS representing a better prediction. R_P drops to 0.95 (for NNA, and 0.94 for NNP) for the IMD tests but is still close enough to the perfect value of 1, indicating a slightly less under-prediction for these tests.

A similar trend is reflected in Figure 7.22 and by the numbers for horizontal load prediction in shown Table 7.8. The exception is the tremendous under-prediction for four of the IMD tests (M71, M72, M73, and M76) for which the reason has been previously explored in this section. From the above discussion and the information extracted from the overall statistical measures in Table 7.8, it is seen that Nevel's model considering the ride-up on the neck gives a good prediction of sheet ice loads on the tested MCSs.

An interesting feature of these prediction is that NNA and NNP give almost the same value of the vertical loads (Figure 7.21) but slightly different for horizontal load prediction (Figure 7.22). The reason for this is quite simple. The active action applied in NNA generates additional forces on the collar and the vertical neck sections and these additional forces only take

a small portion of total loads on the structure. Since the neck was vertical and the slope of collar facet was steeper (compared to the slope of the main cone, see Figure 3.1), the additional forces mainly contributed to the horizontal component of the total force.

Chapter 8 Conclusions and Recommendations

The study presented in this thesis covers quite a wide range of topics on ice loads exerted on the newly proposed MCS. The results are summarized in such a manner that the industry's concerns are addressed in the order given in Chapter 1, and are presented in three sections (8.1 through 8.3). Section 8.4 is arranged to summarize the main contributions made during the course of the present investigations. Some recommendations for further work are also given in Section 8.5.

8.1 Conclusions Regarding Ice Failure Mechanisms and Maximum Loads

Both the tests and numerical simulations show that ice ridges and ice sheets failed in bending modes; this is quite similar to the failure mechanisms obtained for ice interaction with SCSs. Conclusions regarding ice crack patterns, events causing the maximum ice loads, and the effect of structural orientation on crack pattern and ice loads are given in this section. These results and conclusions are expected to address concern # 1 (Section 1.1).

8.1.1 Ice Ridge and Ice Sheet Crack patterns

Three ridge failure patterns were identified (presented in subsections 4.1.2, 4.1.3, and 4.1.4). The predominant pattern is pattern I which is quite similar to the pattern observed for ridge/SCS interaction. A common feature for the other two crack patterns is the closer distance between cracks and also more the presence of local cracks.

Ice sheet crack patterns (subsection 4.1.1) are also similar to those for SCSs, but two simultaneous radial cracks extending from the corners of the front facet occurred as initial cracks in a number of tests which have been rarely seen in the case of SCSs.

8.1.2 Events Generating Maximum Loads

Besides the initial and the hinge cracking, large ice pieces riding-up or accumulating on the structure's surface were also events which caused the maximum ridge loads (subsection 4.2.1). The maximum sheet ice loads occurred after sufficient broken ice pieces accumulated in front of the structure and covered the structure's surface (subsections 4.1.1, 5.2.4, and 5.4.1).

8.1.3 Effect of Structural Orientation

Compared to face-on orientation, edge-on orientation resulted in a smaller distance between two hinge cracks in the ridges. The initial cracks in the ridges for the edge-on MCSs occurred at the

centre of the ridge (the contact point) for nearly all the tests, while a few of the initial cracks for face-on MCSs occurred near to but not at the centre of the ridges (refer to subsection 4.3.2). In the interaction with an ice sheet, the front edge of an edge-on MCS acted like a inclined rigid wedge to initiate a radial crack extending from the edge and to separate ice sheet into two wedges (subsection 4.1.1).

Compared to the face-on orientation, the edge-on orientation generally reduced both the vertical and the horizontal maximum sheet ice loads; the maximum sheet ice loads on the MCSs in intermediate orientation were closer to those for the MCS in face-on orientation (refer to subsection 4.4.2).

The effect of structural orientation on maximum ridge ice loads depended on neck size, load components, and ridge width. For the small neck MCSs, the horizontal loads on the face-on MCSs were larger than their counterparts on the edge-on MCSs; and the vertical loads on the face-on MCSs were larger for wide ridges and they were closer to the vertical loads on the edge-on MCSs for narrow ridges. For the large neck MCSs, the vertical loads on face-on MCSs were slightly larger than those on edge-on MCSs; but the horizontal forces on the face-on MCSs were smaller than their counterparts on the edge-on MCSs for wide ridges, and they were closer to one another for narrow ridges (subsection 4.3.2).

8.2 Conclusions Regarding the Effect of Neck Size

The effect of neck size was industry's major concern, and it was experimentally and numerically examined in this thesis. A general conclusion is that the effect of neck size is not very big, at least it is not as significant as expected (at the time the MCS prototype was proposed). Relatively detailed conclusions for this effect on the maximum ridge loads and sheet ice loads are given in two separate subsections below. These address concern # 2.

8.2.1 Effect of Neck Size on Ice Ridge Loads

Both the analyses of experimental results (subsection 4.3.3) and the numerical simulations (subsection 5.4.3) showed that the large neck increased the maximum horizontal ridge loads. The analyses of the test results indicated that the large neck reduced the maximum vertical loads, but numerical simulation yielded a very small increase in the vertical maximum loads. For the conservative (safer) consideration in design, an increase due to the large neck may be considered.

8.2.2 Effect of Neck Size on Ice Sheet Loads

Similar to the ridge loads, both the analyses of the tests and the numerical simulation showed that the large neck increased the maximum horizontal sheet ice loads. The analyses of the tests

also showed the large neck tended to increase the maximum vertical sheet ice loads, however the numerical simulation resulted in a small decrease in the maximum vertical load when the small neck was replaced by the large neck. For a safer design, it is recommended that designers should consider an increase in both the horizontal and the vertical loads due to the change of the neck size from the small to the large.

8.3 Conclusions Regarding Validation of Load Equations

The conclusions summarized in this section address concern # 3.

8.3.1 Validation of Ridge Ice Load Equations

Of the three analytical models (Wang's model, Croasdale-Abdelnour model, and the model presented in Chapter 6), the present model gives the best prediction for all the three series of tests. As a second choice, Wang's model may also be used for the maximum ridge load estimation, but Croasdale-Abdelnour model could seriously underestimate the maximum ridge loads (sections 7.1 and 7.2).

8.3.2 Validation of Sheet Ice Load Equations

Nevel's model for the maximum sheet ice load estimation is recommended for use in the case of a MCS since it gave the best overall prediction for the sheet ice loads on the tested MCSs and is also capable of accounting for the particular features of multiple-sectioned MCSs with a vertical neck (section 7.3). The widely used Ralston model can also be used in the case of MCSs, but it's performance may not be as good as the Nevel model.

8.4 Contributions of This Work

The present research work contributes to the study of ice loads on MCS in four different ways as summarized below.

1. **An extensive analysis of all the tests to identify the effect of various parameters.**
   The analysis of tests results presented in Chapter 4 is the first one covering the data from all test series. The analysis partly addresses two of the industry's concerns, viz., (i) failure patterns and mechanisms of multi-year ridge ice in front of this new MCS and the causes that generate the maximum ridge ice loads; and (ii) effects of various model parameters on ice loads and ice/structure interaction. Effects of relative orientation between the structure and the ice ridge, width of the ice ridges, and size of the vertical neck on ice loads on the MCS have been studied. The analysis covers both the ice ridge and sheet tests. Although these parameters were tested in the test program, their effects

were hidden due to the variations of other parameters. By non-dimensionalizing the results, the present analysis has successfully identified their effects.

2. **A set of numerical simulations with a discrete element computer code.**

The numerical analysis presented in Chapter 5 models the ice and structure using the experimentally determined values of ice properties and simulates realistically the entire process of ice/structure interaction, including the effects of rubble ice and riding-up process. Influence of the ice pieces lodged under ice cover and ridge are recognized. An insight into the mechanism of ice sheet breaking is gained by studying ice deformations and interaction forces. All these cannot be obtained from physical tests done due to difficulties encounted in instrumentation. More importantly, the effect of neck size is investigated under an ideal condition. Since so many parameters can affect ice/structure interaction process and ice loads, the effect of neck size recognized from the analysis of physical tests may still contain the effect of other parameters. In the present numerical simulations, all other parameters are kept exactly the same and only the neck size is varied for the two runs. Thus, the comparison of the results of these two runs has revealed the effect of neck size more accurately.

3. **Development of an analytical model to predict ice ridge cracking loads on a MCS**

The analytical models presented in Chapter 6 are new and are found to be immensely useful for predicting ice ridge cracking loads on a MCS with an accuracy better than any other existing models (the assessment is presented in Chapter 7). The development

involved recognizing and simplifying ridge's loading conditions (or ridge/structure contact conditions), obtaining relevant analytical solutions for various loading conditions, implementing the analytical model in a computer program, simplifying the equations to an easily usable form, and computation of ice forces for various possible values of the parameters (facet length, ridge characteristic length, etc.). The simplified form of the equations are quite easy to be used and should be a helpful and convenient tool for MCS designers.

4. **Evaluation of widely used analytical models**

Industry wanted to examine whether the analytical models widely accepted for SCS design could also be used for MCS. These earlier models were developed for SCSs and were based on tests with SCS structural models. A total of six (6) analytical models were evaluated in this study using the test data obtained for MCSs. It is found that Nevel's model and Ralston's model give reasonable load prediction if proper parameters are chosen. Conclusions drawn from this evaluation will provide a reference basis for designers involved in MCS designs to decide which analytical model could be better used and what geometrical dimensions would be appropriate for input in their ice load estimation.

8.5 Recommendations for Future Work

As shown in Section 4.2, the maximum ice ridge loads experienced by a MCS could be

generated either during the ridge cracking process or during the ridge segment clearing process. A question that is left unanswered in this study is about the conditions under which the maximum ridge loads are generated by the cracking process and the conditions under which the ride-up process generates the maximum ridge loads. Indeed, this is a very complicated problem and verifications of these aspects would greatly help the further understanding of the mechanism involved in the maximum load generation.

In addition, the equations for estimating the maximum ridge loads generated during the clearing process need to be developed. Since the ride-up process has been one of the events causing the maximum ridge loads, the development of this type of equations would be of great use importance for the total coverage of all possible events generating the maximum ridge loads.

References

Abdelnour, R and Teh, D., 1976, *Modelling the Interaction between Pressure Ridges and Conical Structures — Assessment of the Effects of Ridge Length, Ice Cover Thickness and Angle of Encounter*, Arctec Canada Limited Report 193C, for Exxon Production Research, January, 1976.

Abdelnour, R., 1981, *Model Tests of Multi-year Pressure Ridges Moving onto Conical Structures*, Proceedings of IAHR Ice Symposium, Quebec, pp. 729 - 749.

Abdelnour, R., 1988, *Assessment of the Effect of Length and Orientation of a Multi-year Ridge on the Force Acting on Conical Structures*, Proceedings of IAHR Ice Symposium, Sapporo, pp. 59 - 75.

American Petroleum Institute (API), 1988, *Recommended Practice for Planning, Designing, and Constructing Fixed Offshore Structures in Ice Environments*, first edition, 50 p.

Applied Mechanics Inc., 1985, *Mechanical Analysis of Spray Ice Platform*, Report for Standard Oil Company (Indiana), Oct. 9.

Bercha, F. G., 1973, *Ice Adhesion Study*, APOA project 57(2), by Acres Consulting Service Ltd.

Cammaert, A.B. and Muggeridge, D.B., 1988, *Ice Interaction with Offshore Structures*, Van Nostrand Reinhold, New York, 432 p.

Chao, J.C., 1992a, *Comparison of Sheet Ice Load Prediction Methods and Experimental Data for Conical structures*, Proceedings of 11th International Conference on Offshore Mechanics and Arctic Engineering (OMAE), Calgary, Vol. IV pp 183 - 193.

Chao, J.C., 1992b, *Comparison of Ridge Load Prediction Methods and Experimental Data for Conical structures*, Proceedings of 11th International Conference on Offshore Mechanics and Arctic Engineering (OMAE), Calgary, Vol. IV, pp. 195 - 203.

Coon, M.D. and Pizzano, B.A., 1985, *Ice Loads on Structures with Compound Slopes*, Proceedings of Arctic's 85, American Society of Civil Engineers, San. Francisco, pp. 267 - 275.

Cox, G.F.N., Richter, J.A., Weeks, W.F., and Mellor, M., 1984, *A Summary of the Strength and Modulus of Ice Samples from Multi-Year Pressure Ridges*, Proceedings of 3rd International Conference on Offshore Mechanics and Arctic Engineering (OMAE), Calgary, pp. 126 - 133.

Croasdale, K.R., 1975, *Ice Forces on Marine Structures*, Third International Symposium on Ice Problems, pp. 315 - 337.

Croasdale, K.R., 1980, *Ice Forces on Fixed, Rigid Structures*, Working Group on Ice Forces on Structures, a State-of-the-Art Report, pp. 34 - 106.

Croasdale, K.R., 1991, *Structures in Ice: Past Experience and Future Challenges*, Proceedings of 11th International Conference on Port and Ocean Engineering under Arctic Conditions (POAC'91), St. John's, Newfoundland, pp. 1 - 27.

Croasdale, K.R. and Muggeridge, D.B., 1993, *A Collaborative Research Program to Investigate Ice Loads on Multifaceted Conical Structures*, Proceedings of the 12th International Conference on Port and Ocean Engineering under Arctic Conditions (POAC'93), Hamburg, August 17 - 20, pp 475 - 486.

Croasdale K.R. and Cammaert, A.B., 1993, *Improved Method for the Calculation of Ice Loads on Sloping Structures in First-year Ice*, Proceedings of the First International Conference on Development of the Russian Arctic Offshore, St. Petersburg, September 21 - 24, pp. 161 - 168.

Croasdale, K.R., Cammaert, A.B. and Metge, M., 1994, *A Method for the Calculation of Sheet Ice Loads on Sloping Structures*, IAHR 94, Proceedings of 12th International Symposium on Ice, Vol II, pp. 874 - 885.

Derradji-Aouat, A., 1994a, *Ice Loads on Conical Piers --- A Finite Element Investigation*, International Journal of Offshore and Polar Engineering, Vol. 4, No. 1, pp. 11 - 19.

Derradji-Aouat, A., 1994b, *Ice Forces on Conical Piers --- Numerical Analysis and Development of Design Equations*, Proceedings of 7th International Cold Regions Engineering Specialty Conference, Edmonton, March 6 - 9, 1994, pp. 243 - 262.

Edwards, R.Y., Jr., and Abdelnour, R., 1977, *Modelling the Interaction between Pressure Ridges and Conical Structures*, Arctec Canada Limited Report 193C, for Exxon Production Research, February, 1977.

Evgin, E. and Sun, L., 1990, *Review of Analytical Modelling of Ice Cover Evolution*, Report from Finnish/Canadian Joint Research Project No. 5, Interim Report on Task 1B.

Hetenyi, M., 1946, *Beams on Elastic Foundation*, The University of Michigan Press.

Higdon, A., Ohlsen, E.H., Stiles W.B., and Weese J.A., 1967, *Mechanics of Materials*, John Wiley and Sons Inc., second edition, 591 p.

Hocking, G., Mustoe, G.G.W., and Williams, J.R., 1985a, *Validation of the CICE Code for*

Ice Ride-Up and Ice Ridge Cone Interaction, Proceedings of the Conference Arctic'85, San Francisco, pp. 962 - 970.

Hocking, G., Mustoe, G.G.W., and Williams, J.R., 1985b, *Influence of Artificial Island Side-Slopes on Ice Ride-Up and Pile-Up*, Proceedings of the Conference Arctic'85, San Francisco, pp. 185 - 192.

Hocking, G., Williams, J.R., and Mustoe, G.G.W., 1985c, *Dynamic Global Forces of an Offshore Structure from Multi-Year Ice Floe Impact*, Proceedings of the Conference Arctic'85, San Francisco, pp. 202 - 210.

Intera Information Technologies, *DECICE Theoretical Manual*.

Intera Technology Inc., 1986a, *Quantification of First-Year and Multi-Year Ice Ridge Properties*, Report for Alaskan Oil and Gas Association, AOGA **305**, July 7.

Intera Technology Inc., 1986b, *Ice Sheet Ridging Loads for Limit Force Design*, Final Report for Joint Industry Study, Oct. 31.

Irani, M.B., Timco, G.W. and Muggeridge, D.B., 1992, *Ice Loading on a Multi-faceted Conical Structure*, NRCC Report IME-CRE-TR-005, 615 p.

Izumiyama, K., Irani, M.B. and Timco, G.W., 1994, *Influence of a Rubble Field in Front of a Conical Structure*, Proceedings of the 4th International Offshore and Polar Engineering Conference, Osaka, pp. 553 - 558.

Kamesaki, K.and Yoshimura, N., 1988, *Multi-year Ridge Load on a Conical Structure*, Proceedings of 9th International Conference on Port and Ocean Engineering under Arctic Conditions (POAC'87), Fairbanks, pp. 307 - 316.

Kato, Kazuyuki, 1986, *Experimental Studies of Ice Forces on Conical Structures*, IAHR Ice Symposium, pp 185 - 196.

Kawai, T., 1977, *New Element Models in Discrete Structural Analysis*, Journal of the Society of Naval Architects of Japan, Vol. 141, pp. 174 - 180.

Kawai, T., 1979, *Collapse Load Analysis of Engineering Structures by Using New Discrete Element Models*, IABSE Colloquium, Copenhagen.

Kim, J.K. and Kotras, T.V., 1973, *Mathematical Model to Describe the Behaviour of a Moving Ice Field Encountering a Conical Structure*, Report for APOA project **57**(1), 108 p.

Krankkala, T. and Maattanen, M.P., 1984, *Methods for Determining Ice Forces due to First and Multi-year Ridges*, Proceedings of IAHR Ice Symposium, Vol. IV, pp 263 - 287.

Lau, M., Tucker, J.R., Jones, S. and Muggeridge, D.B., 1993, *Model Ice Forces on an Upward Breaking Multi-faceted Cone*, NRC's IMD Report, TR 1993-07, 225 p.

Lewis, J.W. and Croasdale, K.R., 1978, *Modelling the Interaction between Pressure Ridges and Conical Shaped Structures*, Proceedings of IAHR Ice Symposium, Part 1, pp. 165 - 196.

Maattanen, M.P. and Mustamaki, E.O., 1985, *Ice Forces Exerted on a Conical Structure in the Gulf of Bothnia*, Proceedings of Offshore Technology Conference, Vol. 4, Houston, pp. 313 - 320.

Maattanen, M.P., 1986, *Ice Sheet failure against an Inclined Wall*, Proceedings of IAHR Ice Symposium, Iowa City, pp. 149 - 158.

Maattanen, M.P. and Hoikkanen, J., 1990, *The Effect of Ice Pile-up on the Ice Forces of a Conical Structure*, Proceedings IAHR Ice Symposium, Espoo, pp. 1010 - 1021.

Marcellus, R.W., Morrison, T.B., Allyn, N.F.B., Croasdale, K.R., Iyer, H.S. and Tseng, J, 1988, *Ice Forces on Marine Structures: Volume 2 --- Discussion*, Public Works Canada.

McKenna, R.F. and Spencer, D., 1994, *Ice Rubble Buildup on Conical Structures*, Proceedings of IAHR Ice Symposium 1994, Trondheim, Norway, pp. 177 - 186.

Metge, M. and Weiss, R.T., 1989, *Multifaceted Cone Tests, 1988-1989*, ERCL.RS.89.14.

Metge, M. and Tucker, J.R., 1990, *Multifaceted Cone Tests, Year Two: 1989-1990*, ERCL.RS.90.11.

Mustoe, G. W. W., Henriksen and Huttelmaier (editors), 1989, *Proceedings of 1st U.S. Conference on Discrete Element Methods*, Golden, Oct. 17-19.

Nevel, D.E., 1991, *Wang's Equation for Ice Forces from a Pressure Ridge*, Proceedings of the Sixth Cold Regions Engineering Specialty Conference, West Lebanon, NH, edited by D.S. Sodhi, pp. 666 - 672.

Nevel, D.E., 1992, *Ice Forces on Cones from Floes*, IAHR Ice Symposium 1992, Banff, 1992, pp 1391 - 1404

Nessim, M.A., Chung, M.S. and Jordaan, I.J, 1987, *Ice Action on Fixed Offshore Structures: a State-of-the-Art review*, Canadian Journal of Civil Engineering, Vol. 14, pp. 381 - 407.

Nordgren, R.P. and Winler, M.M., 1989, *Dynamic Ride up and Crushing of Short Ice Ridges on Conical Structures*, Proceedings of 8th International Conference on Offshore Mechanics and Arctic Engineering (OMAE), Hague, pp. 287 - 291.

Pande, G.N., Beer, G. and Williams, J.R., 1990, *Numerical Methods in Rock Mechanics*, John Wiley and Sons Ltd., p327.

Ralston, T.D., 1978, *Ice Force Design Considerations for Conical Offshore Structures*, Proceedings of 4th International Conference on Port and Ocean Engineering under Arctic Conditions (POAC'77), St. John's, pp. 741 - 752.

Ralston, T.D., 1980, *Plastic Limit Analysis of Sheet Ice Loads on Conical structure*, Physics and Mechanics of Ice (Proceedings of IUTAM Symposium Copenhagen), Editor: Per Tryde, pp. 289 - 308.

Roark, R. J., 1965, *Formulas for Stress and Strain*, McGraw-Hill Book Company, Fourth Edition, 432 p.

Robins, R.J., Metge, M. Taylor, T.R. and Verity, P.H., 1975, *Test Techniques for Study of Ice Structure Interaction*, Proceedings of 3rd International Conference on Port and Ocean Engineering under Arctic Conditions (POAC'75), Fairbanks, Vol II, pp. 911 - 924.

Sanderson, T.J.O., 1988, *Ice Mechanics*, Graham and Trotman, 253 p.

Schreiber, R.W., Ralston, T.D. and Egging, D.E., 1989, *Multi-year Ridge Force Variability*, Proceedings of 10th International Conference on Port and Ocean Engineering under Arctic Conditions (POAC'89), Lulea, pp. 147 - 155.

Semeniuk, A., 1975, *Computer Program to Evaluate the Forces Generated by a Moving Ice Field Encountering a Conical Structure*, Report for APOA Project **87**, 59 p.

Shibue, T. and Kato, K., 1988, *A Numerical Simulation Method for Failure Analysis and Load Estimation*, Proceedings of 9th International Conference on Port and Ocean Engineering under Arctic Conditions (POAC'87), pp. 413 - 425.

Shibue, T., Kato, K. and Kumakura, Y., 1994, *Numerical Simulation of Ice Failure Problems*, Proceedings of 4th International Offshore and Polar Engineering Conference, Osaka, pp. 442 - 448.

Sinha, N.K., 1978, *Rheology of Columnar-Grained Ice*, Journal of Experimental Mechanics, Vol. 18, No. 12, pp. 464 - 470.

Sinha, N.K., 1979, *Grain Boundary Sliding in Polycrystalline Material*, Philosophical Magazine A, Vol. 40, No. 6, pp. 825 - 842.

Sinha, N. K., 1983, *Creep Model of Ice for Monotonically Increasing Stress*, Cold region Science and Technology, Vol 8, pp 25 - 33.

Sinha, N.K., 1984, *Intercrystalline Cracking, Grain Boundary Sliding, and Delayed Elasticity at High Temperature*, Journal of Material Science, 1984 No. 19, pp. 359 - 376

Sinha, N.K., 1988, *Crack Enhanced Creep in Polycrystalline Material: Stress-Strain Sensitive Strength and Deformation of Ice*, Journal of Material Science, 1988, No. 23, pp 4415 - 4428.

Sodhi, D.S., 1987, *Flexural and Buckling Failures of Floating Ice Sheet against Structures*, IAHR Working Group on Ice Problems, 3th State-of-the Art Report, pp. 53 - 73.

Timco, G.W., 1986, *EG/AD/S: a New Type of Model Ice for Refrigerated Towing Tanks*, Journal of Cold Regions Science and Technology, Vol. 12, pp. 175 - 195.

Wang, Y.S., 1979, *Analysis and Model Tests of Pressure Ridges Failing against Conical Structures*, Report for AOGA Project **96**, 61p.

Wang, Y.S., 1984, *Analysis and Model Tests of Pressure Ridges Failing against Conical Structures*, Proceedings of IAHR Ice Symposium, Hamburg, pp. 67 - 76. [The derivation of the equation was presented on pages 483 - 491 of the same proceedings. This work was described in detail in the report of AOGA Project 96].

Watanabe, M. and Kawai, T., 1980, *Simulation of the Bending Collapse of Ice Plate Using a New Discrete Model*, Journal of the Society of Naval Architects of Japan, Vol 147, pp 306 - 315.

Weiss, R.T., 1988, *Proposed Ice Basin Model Test Program for Multifaceted Conical Structure, To Be Conducted by Exxon Production Research Co.*, EPR 4/5/88, 24 p.

Wessels, E. and Kato, K., 1989, *Ice Forces on Fixed and Floating Conical Structures*, Working Group on Ice Problems, 4th State-of-the Art Report, pp. 231 - 257.

William, J.R., Hocking, G., and Mustoe, G.G.W., 1985, *The Theoretical Basis of the Discrete Element Method*, Presented at International Conference on Advances in Numerical Methods, University College of Swansea, Jan. 7-11.

William, J.R. Mustoe, G.G.W., 1993, *Proceedings of the 2nd International Conference on Discrete Element Methods (DEM)*, the Massachusetts Institute of Technology, March 18-19.

Winkler, M.M. and Nordgren, R.P., 1986, *Ice Ridge Ride-up Forces on Conical Structures*, Proceedings of 8th IAHR Ice Symposium, Iowa City, Iowa, pp. 171 - 183.

Winkler, M.M. and Reece, A.M., 1986, *Probabilistic Model for Multi-year Ice Ridge Loads on Conical Structures*, Proceedings of 8th IAHR Ice Symposium, Iowa City, pp. 159 - 170.

Wright, B.D., Hnatiuk, J., and Kovacs, A., 1979, *Multi-Year Pressure Ridges in the Canadian Beaufort Sea*, Proceedings of 5th International Conference on Port and Ocean Engineering under Arctic Conditions (POAC'79), Trondheim, pp. 107 - 126.

Yoshimura, N. and Kamesaki, K., 1981, *The Estimation of Crack Pattern on Ice by the New Discrete Model*, IAHR International Symposium on Ice, Quebec City, pp. 663 - 672.

Appendix A Assumption for Ice Behaviour

The material behaviour of ice is quite complicated, but under certain circumstances, its behaviour can be well approximated by simple theory. The analysis presented in this appendix will show that an elasticity theory is acceptable for description of the material behaviour of ice for the tests presented in this thesis.

Sanderson (1988) has compiled research results about ice behaviour which he states as "when ice is subjected to a stress it initially deforms in three distinct ways: it undergoes an immediate elastic strain ε_e, a transient time-dependent delayed elastic strain ε_d, and a time-dependent nonlinear viscous creep strain ε_v." There are well verified constitutive equations describing this stress-strain behaviour (Sinha, 1978, 1979, 1983).

The true elastic strain ε_e follows Hooke's law:

$$\varepsilon_e = \frac{\sigma}{E} \tag{A.1}$$

where E is Young's modulus and σ is a stress applied. The time-dependent delayed elastic strain ε_d, which has also been termed as primary creep strain, is defined by

$$\varepsilon_d = c_1 \left(\frac{d_1}{d}\right)\left(\frac{\sigma}{E}\right)^s \left[1 - \exp\left(-(a_T t)^b\right)\right] \tag{A.2}$$

where d is actual grain size and t is time (in seconds). The meanings of parameters c_1, d_1, a_T, s, and b together with their values are listed in Table A.1.

The viscous creep strain ε_v is expressed as follows:

$$\varepsilon_v = \dot{\varepsilon}_{v1}\, t \left(\frac{\sigma}{\sigma_1}\right)^n \tag{A.3}$$

where $\dot{\varepsilon}_{v1}$ is a reference viscous strain rate at the reference stress σ_1 and n is a constant. Their values are also listed in Table A.1.

The total strain ε_t is sum of all the strains expressed in the above equation. Thus ε_t is given by:

$$\varepsilon_t = \varepsilon_e + \varepsilon_d + \varepsilon_v \tag{A.4}$$

For a given ice with constant Young's modulus, the true elastic stain ε_e is a constant value while both ε_d and ε_v are time dependent; hence the total strain is also time dependent. Basically, the total strain gradually increases as the time continues to increase. Within the range of a small amount of time after the stress has been applied, the elastic strain ε_e usually dominates. For instance, if ice with a Young's modulus E = 9.5 GPa is subjected to a constant

stress of 2.5 MPa, the stains ε_e, ε_d, ε_v, and ε_t at time t = 10 seconds are (in s^{-1}) 2.63 x 10^{-4}, 0.10 x10^{-4}, 0.28 x 10^{-4}, and 3.01 x 10^{-4}, respectively. The elastic strain is 87% of the total strain.

Parameters	Value	Unit	Meaning of the parameter
d_1	1.0	meter	reference grain size
c_1	9 x 10^{-3}		a constant for the reference grain size d_1
a_T	2.5 x 10^{-4}	s^{-1}	inverse relaxation rate
s	1		a constant
b	0.34		a constant
n	3		a constant
σ_1	1.0 x 10^6	Pa.	reference stress
ε_{v1}	1.76 x 10^{-7}	s^{-1}	reference viscous strain rate at stress σ_1

Table A.1 Parameters for Sinha's Model

To estimate the strain condition of the tested ice, the ice strength and measured modulus are used as a constants in Equations (A.1) through (A.4). The computed strains are plotted against time in Figures A.1 and A.2 for the ERC test T1Y1R1 and TY1T1R2, respectively. The computed time is up to 120 seconds, this duration is much longer than the duration of the interaction for each ice crack in the physical tests. The viscous creep strains for these two tests are very small, such that they emerge in the bottom border line of the graphs in Figures A.1 and A.2 (hence, they cannot be seen in these figures).

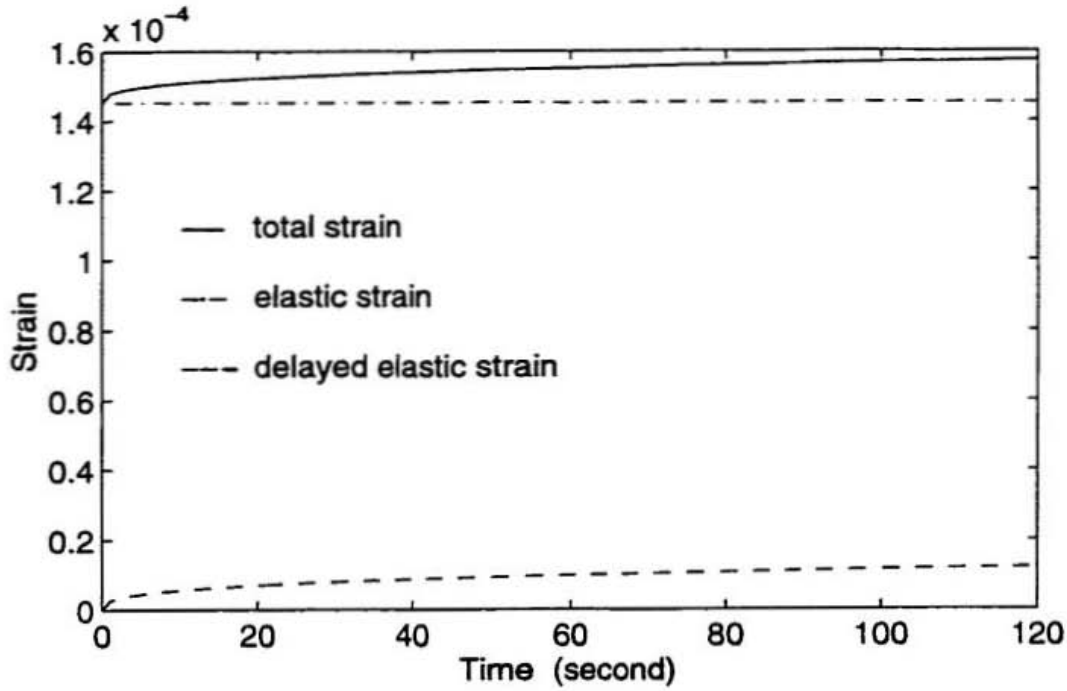

Figure A.1 Strains for the ERC test Y1T1R1, computed with Equation (A.4)

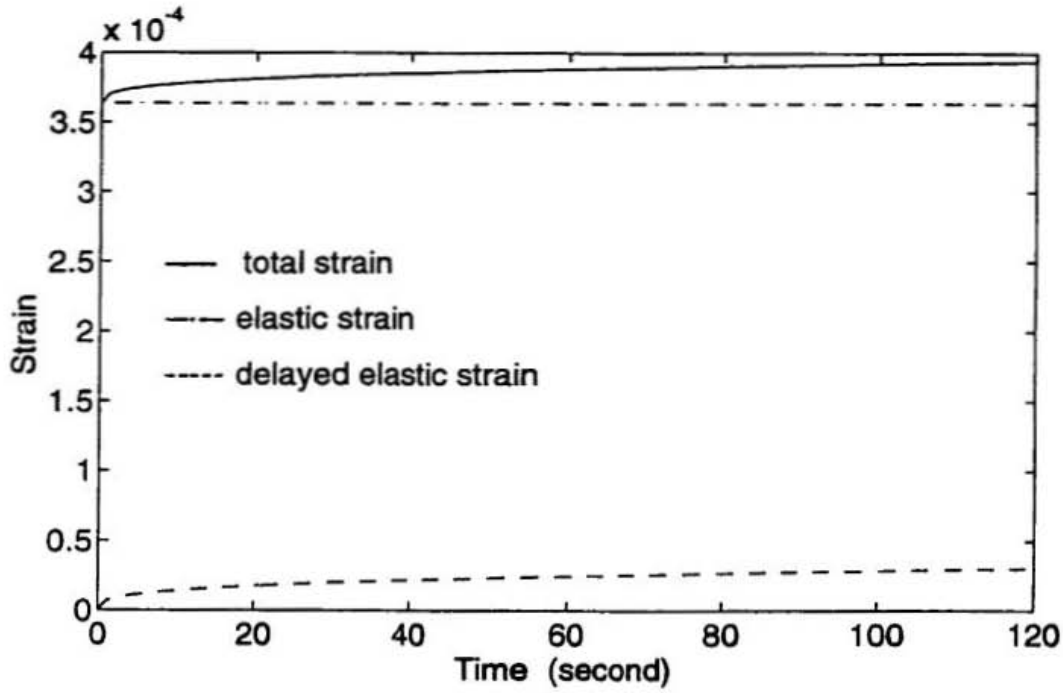

Figure A.2 Strains for the ERC test Y1T1R2, computed with Equation (A.4)

Figures A.1 and A.2 clearly show the two features of the ice used in these tests:

i) total strain gradually increases as time increases, and

ii) elastic strain dominates.

Because the estimated compressive strength is much higher than the measured flexural strength, strain computation was also performed with the compressive strengths, σ_c, which are estimated using Equations (3.1) and (3.13) in the book by Cammaert and Muggeridge (1988). The strains at time t = 20 seconds together with those computed using the flexural strengths are listed in Table A.2

Strain	Y1T1R1	E = 1.136 GPa	Y1T1R2	E = 352 MPa
	σ_c = 892 kPa	σ_f = 165 kPa	σ_c = 865 kPa	σ_f = 128 kPa
ε_e	7.85×10^{-4}	1.45×10^{-4}	2.46×10^{-3}	3.64×10^{-4}
ε_t	8.26×10^{-4}	1.52×10^{-4}	2.57×10^{-3}	3.81×10^{-4}
$100 \times \varepsilon_e/\varepsilon_t$	95.0	95.4	95.7	95.5

Table A.2 Strains For Y1T1R1 and Y1T1R2 at 20th Second of Loading

The numbers in Table A.2 show that the elastic strain is about 95% of the total strain. Computations with stresses as low as one tenth of the flexural strength also give similar values of the ratio of elastic stain to total strain.

The above analysis quantitatively shows that elastic strain (thus the deformation) is

dominant for both the sheet ice test Y1T1R1 and the ridge test Y1T1R2. Therefore, elastic behaviour of ice is assumed for the analysis of these tests.

Appendix B Estimate of Parameters for Mohr-Coulomb Criterion

The Mohr-Coulomb criterion implemented in DECICE requires four parameters: flexural strength σ_f, compressive strength σ_c, tensile strength σ_t, and the internal friction angle of ice φ. Out of the four parameters only the flexural strength was measured for each of the ERC tests. Because no direct relationship between flexural strength and compression or tensile strength has been found, an alternate approach for the strength estimation was used. The main idea of this approach is that the unknown parameters can be estimated using available empirical formulae and then scaled down to the test scale.

B.1 Estimate of Compressive and Tensile Strength

Cammaert and Muggeridge (1988) have compiled most of the empirical formulae for the estimation of compression and tensile strengths of ice. Three formulae for the estimation of compressive, tensile, and flexural strengths are quoted in Equations (B.1), (B.2), and (B.3), respectively (Cammaert and Muggeridge 1988, p83, 89, and 91).

$$\sigma_c = 1.65 \left(1 - \sqrt{\frac{v_b}{275}}\right) \tag{B.1}$$

$$\sigma_t = 0.82 \left(1 - \sqrt{\frac{\nu_b}{142}}\right) \tag{B.2}$$

$$\sigma_f = 0.75 \left(1 - \sqrt{\frac{\nu_b}{202}}\right) \tag{B.3}$$

where the strengths are in MPa, the brine volume ν_b is in ‰ and can be estimated using Equation (B.4) (Cammaert and Muggeridge 1988, p77).

$$\nu_b = S_i \left(0.532 + \frac{49.185}{|T|}\right) \tag{B.4}$$

where S_i represents the ice salinity, in ‰; and T, the temperature, in °C.

It is assumed that the above equations are consistent, that is, if Equation (B.3) predicts the correct flexural strength, then Equations (B.1) and (B.2) also should predict the correct compressive and tensile strengths respectively.

In Table B.1, the strengths directly calculated using the above equations are listed in the first row for each test. Within the column of σ_f, the second row of each test gives the measured value of the flexural strength. It is clear the predicted flexural strength is much larger than the value measured. To use measured flexural strength (σ_{fm}) in the failure criterion means that the

calculated flexural strength (σ_{fc}) is scaled down by the ratio η which is defined as follows:

$$\eta = \frac{\sigma_{fc}}{\sigma_{fm}} \tag{B.5}$$

The values of η for the tests are listed in the extreme right column of Table B.1.

According to the assumption made above, the calculated compressive and tensile strength which are given in the first row for each of the tests, thus, should be divided by the ratio η to make them corresponding to the measured flexural strength. The values of the scaled compressive and tensile strength are given in the second row of each test.

Test	T (°C)	S_i (‰)	ν_b (‰)	Strength (KPa)				Strength Scale Factor
				Source	σ_c	σ_t	σ_f	
Y1T1R1	-5	5.6	58.1	Calculated	892	296	348	2.11
				Scaled	423	140	165	
Y1T1R2	-5	6.0	62.2	Calculated	865	277	334	2.61
				Scaled	331	106	128	

Table B.1 Estimated Compressive and Tensile Strengths

In its API Recommended Practice 2N (RP-2N), American Petroleum Institute (1988) also recommended some plotted data for use in ice strength estimation. Some of these data are different from those on which the equation (B.1) through (B.3) were based. However, it is found

that these data also support the above calculation. For a brine volume of 60‰, the ratio of tensile strength to flexural strength given in RP-2N is about 0.75 which is fairly close to the ratio for the above calculations (the ratio is 0.83 for the test Y1T1R2, and 0.85 for Y1T1R1, which can be calculated from the numbers given in Table B.1). The ratio of calculated compressive strength to flexural strength is near 2.6 which is slightly lower than the ratio of 3.2 (lower bound) for the API's data.

B.2 Internal Friction Coefficient

Another parameter required for Mohr-Coulomb criterion is the internal friction coefficient μ_0. As shown in Chapter 5 of this thesis, the following relationship holds good for the Mohr-Coulomb criterion:

$$\tau_s = \frac{\sigma_c}{2} \left(\sqrt{\mu_0^2 + 1} - \mu_0 \right) \tag{B.6}$$

where τ_s and σ_c are shear and compressive strengths, respectively. The internal friction coefficient, μ_0, can be expressed in terms of internal friction angle φ:

$$\mu_0 = \tan \varphi \tag{B.7}$$

Equation (B.6) can be rewritten to express the internal friction coefficient in terms of compressive and shear strength, shown in Equation (B.8).

$$\mu_0 = \frac{1}{4}\frac{\sigma_c}{\tau_s} - \frac{\tau_s}{\sigma_c} \tag{B.8}$$

If the ratio of compressive strength to shear strength is found, the internal friction coefficient, or the friction angle, can be determined.

Unfortunately, relatively little information is available on the shear strength. The data compiled by Cammaert and Muggeridge (1988) including those given in RP-2N (American Petroleum Institute 1988) show quite a wide scatter. The ratio of compressive strength to the shear strength, thus, varies over a wide range. For the brine volume of 60‰ (the value for the ERC tests), the data indicates that 2.2 to 4.5 may be a reasonable range for the ratio σ_c/τ_s. Corresponding to this range is the range of 0.095 to 0.903 for internal friction coefficient μ_0. Thus, the internal angle calculated using Equation (B.7) is in the range of 5.4° to 42.1°.

Appendix C Simplification of Ridge Crack Problem

This appendix is arranged to demonstrate the sufficiency of considering the vertical loads only in analysis of ice ridge cracking loads on MCSs. In fact, many researchers (Croasdale 1980; Abdelnour 1981, 1988; Schreiber *et al* 1989) have already used this simplified loading condition for analysis of ice ridge cracking loads on SCSs, including a number of important research projects supported by Arctic Petroleum Operators Association: APOA projects No. 57 (Kim and Kotras 1973), No. 87 (Semeniuk 1975), No. 96 (Wang 1979, 1984), etc. In all these analyses except for the plasticity analysis by Wang (1979, 1984), the ridge was treated as an elastic beam with constant stiffness, resting on elastic foundation, subjected to a vertical concentrated load at the contact point. These analytical models based on elementary bending theory and the above idealizations are also recommended for engineering use by industry (American Petroleum Institute 1988, Croasdale 1980).

In addition to the vertical force acting on the ridge, which all the above analytical models have considered, more forces would be acting on the ridge. Could the effects of theses forces be neglected and if so, what is the degree of error caused ? These concerns will be addressed in this appendix.

C.1 Modelling of Loading Condition

The cross section of the ridge is idealized to be rectangular, as shown in Figure C.1. In the test program presented in Chapter 3, most of the ridges had a rectangular cross section; hence this idealization is fairly reasonable for these tests. A pair of flanges are included in the ridge cross section to account for the effect of attached ice sheet. According to Equations (6.2) and (5.5), width of the flange depends on ice sheet's Young's modulus E_s, thickness h, and Poisson's ratio ν. For the ice ridges and sheets used in the MCS test program, typical values of parameters of an ice ridge and its flanges are given in Table C.1. In Table C.1, Z_t is calculated using dimensions a, h, and B_e and their relationships to ridge height H, defined in other columns of this table.

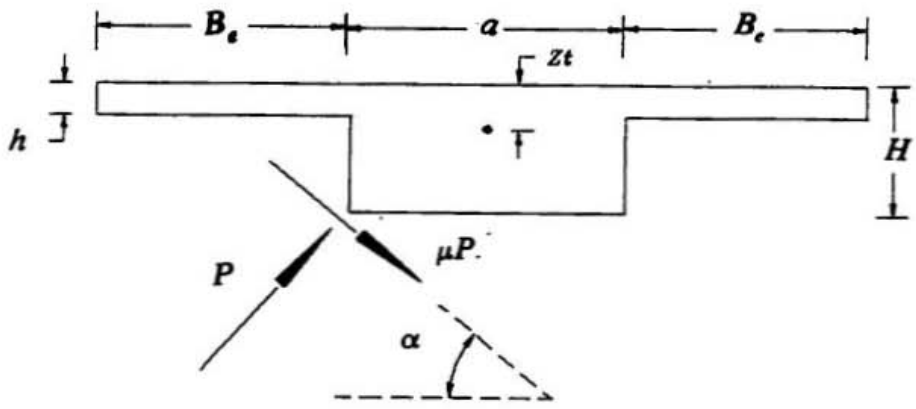

Figure C.1 Forces on a Ridge

Symbols	a	B_e	h	Z_t
Meaning of the Symbol	Ridge Width	Flange Width	Ice Sheet Thickness	Distance from Neutral Axis to Top Fibre of the Ridge
Expression in Terms of Ridge Height H	3.3 H	4.5 H	1/3 H	0.34 H

Table C.1 Ridge Dimension

When a ridge comes into contact with the MCS, it is subjected to a normal force P and a tangential force μP, where μ is coefficient of friction between ice ridge and MCS surface. The direction of P is perpendicular to the contact interface and μP is along the contact surface; Figure C.1 shows the directions of these forces.

Due to the applied load P, crushing usually occurs at the contact interface before the ridge cracking occurs. The crushing may change the location of forces P and μP. To simplify analysis, this effect is also ignored, as earlier researchers have done in analysis of ridge loads on SCSs (Croasdale 1980, Abdelnour 1981, 1988). Action of forces P and μP can be replaced by a vertical force P_V, a horizontal force P_H, and two torques, M_V and M_H. Figure C.2 shows these forces and torques.

P_V and P_H can be expressed in terms of the normal force P, friction coefficient μ, and slope angle of the front facet of the MCS, α:

$$P_V = P(\cos\alpha - \mu \sin\alpha) \quad \text{(C.1)}$$

$$P_H = P(\sin\alpha + \mu \cos\alpha) \quad \text{(C.2)}$$

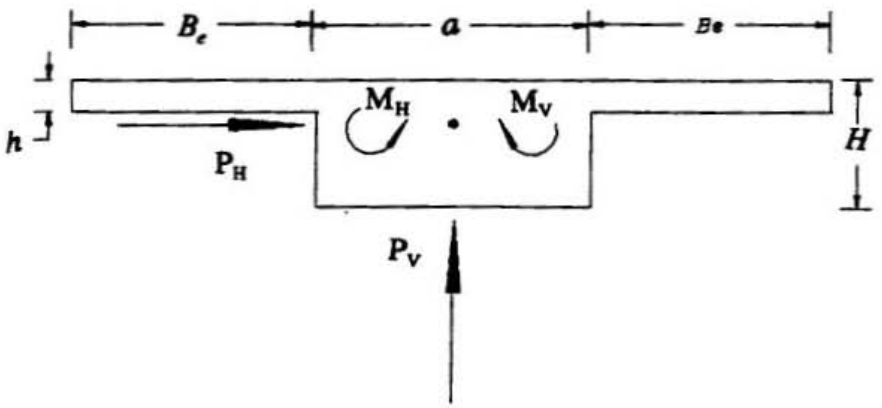

Figure C.2 Equivalent Forces on the Ridge

The total torque, m, acting at the centroid of the ridge and its flanges, can be expressed as:

$$m = M_V - M_H \quad \text{(C.3)}$$

where M_V and M_H are the torques generated due to the shifting of location of P_V and P_H,

respectively.

Values of P_V and P_H vary with a number of factors. For a given friction coefficient μ and slope angle α, P_V and P_H are functions of normal force P. For the MCS tests, in which the average values of μ can be approximately taken as 0.1 and $\alpha \approx 40°$, $P_V = 0.704P$ and $P_H = 0.717P$. Thus, we obtain the following relation for these MCSs:

$$P_H = \frac{0.717}{0.704} P_V \sim 1.02 P_V \qquad \text{(C.4)}$$

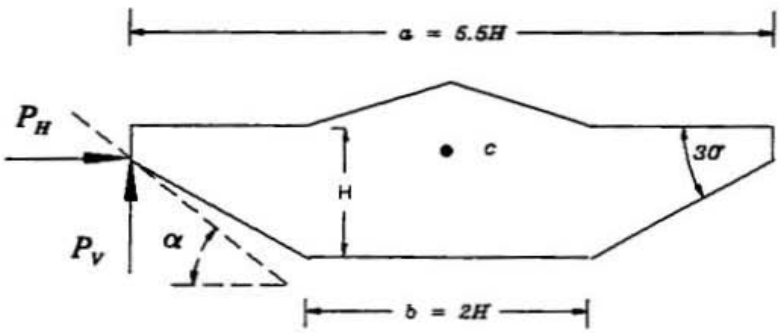

Figure C.3 Idealized Geometry of Multi-year Ridges

Value of m is strongly dependent on shape of ridge cross section, slope angle of the structure, and interaction process; hence it is more difficult to determine it exactly. Here only two idealized extreme cases are discussed: *Case 1* (represented by Figure C.2) in which the forces act at the lower front edge of the ridge; and *Case 2* (shown in Figure C.3) where the

forces act near the top front edge of the ridge. For *case 1*, the total torque, m_1, can be calculated as:

$$m_1 = \frac{1}{2} a P_V - P_H(H - Z_t) = 1.65 H P_V - 0.66 H P_H = 0.977 H P_V \qquad \text{(C.5)}$$

where a is ridge width, H is ridge height, and Z_t is the distance from the neutral axis to the top fibre of the ridge (refer to Figure C.2).

The ridge cross section shown in Figure C.3 is the idealized geometry of multi-year ridges defined by Wright *et al* (1979). Due to the existence of the flanges (they are not shown in Figure C.3) that accounts for the influence of attached ice sheet, the centroid of entire cross section of ridge and flanges is usually located quite close to the lower surface of attached ice sheet such that the contact point B is nearly along the same horizontal axis as centroid c. In this case, P_H does not generate any significant torque. The total torque for this case (case 2), m_2, is approximately the one generated by P_V:

$$m_2 \approx 0.5\, a\, P_V = 2.75\, H\, P_V \qquad \text{(C.6)}$$

It is obvious that the total torque given by equation (C.6) is greater than the one given by Equation (C.5). If this torque is ignored in analysis, the larger the torque, the higher the error will be. Thus, to consider the worst condition, Equation (C.6) will be used in the analysis of error made due to ignoring the effect of torque.

C.2 Simplification of Loading Condition

The combined action of forces P_V and P_H and torque m will lead to very complicated equations for estimation of ice ridge loads on a MCS. Magnitudes of stresses due to these forces and torque will be analyzed below to determine which one is dominant and to estimate the degree of error that will be generated if one or more of these force components are ignored. Strictly speaking, the ridge geometry shown in Figure C.3 should be used in this analysis. Since the purpose of this appendix is to demonstrate the sufficiency of considering the vertical load in ridge cracking load analysis, the simplified geometry shown in Figure C.2 is used to make the analysis simple.

If the vertical bending moment m_V (about the neutral axis parallel to x axis) for the location y is given, the maximum normal stress at bottom fibre, σ_V, due to m_V can be written as:

$$\sigma_V = \frac{m_V (H - Z_t)}{I_x} \tag{C.7}$$

where I_x is the moment of inertia about neutral axis parallel to coordinate axis x and is given by:

$$I_x = \frac{1}{3}[(2B_e+a)Z_t^3 - 2B_e(Z_t-h)^3 + a(H-Z_t)^3] \approx 0.48H^4 \tag{C.8}$$

Similarly, if horizontal bending moment m_H (about the neutral axis parallel to z axis) for the same location y is given, the normal stresses at the left and right edges of the ridge, due to

m_H, can be written in the following form:

$$\sigma_H = \frac{\frac{1}{2} a\, m_H}{I_z} \tag{C.9}$$

where I_z is the moment of inertia about the neutral axis parallel to z axis,

$$I_z = \frac{1}{12}[h(a+2B_e)^3+(H-h)a^3] \approx 53.7\, H^4 \tag{C.10}$$

Bending moments m_V and m_H are linear functions of P_V and P_H, respectively. Accounting for the relation $P_H = 1.02\, P_V$, we have the following relationship for the bending moments at given location y:

$$\frac{m_H}{m_V} = \frac{P_H}{P_V} = 1.02 \tag{C.11}$$

Thus, the ratio of σ_H to σ_V can be derived as:

$$\frac{\sigma_H}{\sigma_V} = \frac{a}{2(H-Z_t)} \frac{m_H}{m_V} \frac{I_x}{I_z} = \frac{1.02\times 3.3H}{2\times\frac{2}{3}H} \frac{0.48H^4}{53.7H^4} = 0.0226 \tag{C.12}$$

Equation (C.12) shows that σ_H is much smaller than σ_V. If P_H is neglected, it affects the normal stress by less than 2.3 percent.

The maximum shear stress due to the torque m is very difficult to calculate. To simplify the problem, we can ignore the flanges, i.e., consider the ridge only. This simplification could

tremendously enlarge the shear stress. If the maximum shear stress for the ridge only is still smaller than σ_V, the vertical bending is dominant loading condition.

According to Roark (1965), the maximum shear stress in a rectangular beam can be expressed as:

$$\tau_{max} = \frac{m\ (1.5a+0.9H)}{a^2 H^2} = \frac{1.07\,m}{H^3} \qquad \text{(C.13)}$$

The ratio of τ_{max} to σ_V can be expressed as:

$$\frac{\tau_{max}}{\sigma_V} = \frac{1.07\,m\,I_x}{m_V H^3 (H-Z_t)} = \frac{m}{m_V}\,\frac{1.07\times0.48\times3}{2} = \frac{0.77\,m}{m_V} \qquad \text{(C.14)}$$

Bending moment m_V is larger than torque m. For instance m_V for hinge crack could be $7\,H\,P_V$ which, compared to Equation (C.6), is nearly three times m. Hence it can be seen from Equation (C.14) σ_V is much larger than τ_{max}. Recalling that we have considered the ridge only in the above analysis, the real shear stress can be much smaller than that obtained above.

In Equation (C.7) we used $(H-Z_t)$, which means that we considered the upward bending (hinge crack). For upward crown bending, $(H-Z_V)$ should be replaced by Z_t, resulting in a smaller σ_V which is about half the upward bending (hinge crack) stress. From the data presented above, we can see this bending stress to be still dominant. Hence the neglecting of the effect of horizontal load and the torque are justified by the results shown above.

Appendix D Functions A(y), B(y), C(y), D(y) and Their Operations

D.1 A(y), B(y), C(y), D(y)

The functions $A(y)$, $B(y)$, $C(y)$, and $D(y)$, are functions of y and L_c. They are defined as follows:

$$\begin{aligned} A(y) &= e^{-\bar{y}}(\cos\bar{y}+\sin\bar{y}) \\ B(y) &= e^{-\bar{y}}\sin\bar{y} \\ C(y) &= e^{-\bar{y}}(\cos\bar{y}-\sin\bar{y}) \\ D(y) &= e^{-\bar{y}}\cos\bar{y} \end{aligned} \tag{D.1}$$

where

$$\bar{y} = y/L_c$$

y is a variable (is the y coordinate in our case) and L_c is the characteristic length of a ridge.

$A(l)$, $B(l)$, $C(l)$, and $D(l)$ can be obtained by substituting y with l in Equation (D.1).

The functions defined in Equation (C.1) are related as follows:

$$\begin{aligned} D(y)+B(y) &= A(y) \\ D(y)-B(y) &= C(y) \end{aligned}$$

The relationships were helpful in deriving the equations given in Chapter 6.

D.2 Derivatives and Integrations of A(y), B(y), C(y), and D(y)

The derivatives of these functions, expressed in any of the four functions, $A(y)$, $B(y)$, $C(y)$, and $D(y)$, are given as follows

$$\begin{aligned}
\frac{dA(y)}{dy} &= -\frac{2}{L_c}B(y) & \frac{d^2A(y)}{dy^2} &= -\frac{2}{L_c^2}C(y) \\
\frac{dB(y)}{dy} &= \frac{1}{L_c}C(y) & \frac{d^2B(y)}{dy^2} &= -\frac{2}{L_c^2}D(y) \\
\frac{dC(y)}{dy} &= -\frac{2}{L_c}D(y) & \frac{d^2C(y)}{dy^2} &= \frac{2}{L_c^2}A(y) \\
\frac{dD(y)}{dy} &= -\frac{1}{L_c}A(y) & \frac{d^2D(y)}{dy^2} &= \frac{2}{L_c^2}B(y)
\end{aligned} \tag{D.2}$$

The integrations can also be expressed in terms of $A(y)$, e.t.c.:

$$\begin{aligned}
\int A(y)\,dy &= -L_c D(y) \\
\int B(y)\,dy &= -\frac{L_c}{2}A(y) \\
\int C(y)\,dy &= L_c B(y) \\
\int D(y)\,dy &= -\frac{L_c}{2}C(y)
\end{aligned} \tag{D.3}$$

In these equations, the integral constants were ignored.

D.3 A(l-y), B(l-y), C(l-y), D(l-y) and Their Derivatives

Substituting $(l\text{-}y)$ for y in Equations (D.1) gives

$$\begin{aligned} A(l-y) &= e^{-(\bar{l}-\bar{y})}[\cos(\bar{l}-\bar{y})+\sin(\bar{l}-\bar{y})] \\ B(l-y) &= e^{-(\bar{l}-\bar{y})}\sin(\bar{l}-\bar{y}) \\ C(l-y) &= e^{-(\bar{l}-\bar{y})}[\cos(\bar{l}-\bar{y})-\sin(\bar{l}-\bar{y})] \\ D(l-y) &= e^{-(\bar{l}-\bar{y})}\cos(\bar{l}-\bar{y}) \end{aligned} \tag{D.4}$$

where

$$\bar{l} = l / L_c$$

and l, in our case, is one half of a facet length at waterline.

The derivatives of these functions can be expressed as follows

$$\begin{aligned} \frac{dA(l-y)}{dy} &= \frac{2}{L_c}B(l-y) \\ \frac{dB(l-y)}{dy} &= -\frac{1}{L_c}C(l-y) \\ \frac{dC(l-y)}{dy} &= \frac{2}{L_c}D(l-y) \\ \frac{dD(l-y)}{dy} &= \frac{1}{L_c}A(l-y) \end{aligned} \tag{D.5}$$

D.4 A(y-l), B(y-l), C(y-l), D(y-l) and Their Derivatives

Substituting *(y-l)* for *y* in Equations (D.1) gives

$$\begin{aligned} A(y-l) &= e^{-(\bar{y}-\bar{l})}[\cos(\bar{y}-\bar{l})+\sin(\bar{y}-\bar{l})] \\ B(y-l) &= e^{-(\bar{y}-\bar{l})}\sin(\bar{y}-\bar{l}) \\ C(y-l) &= e^{-(\bar{y}-\bar{l})}[\cos(\bar{y}-\bar{l})-\sin(\bar{y}-\bar{l})] \\ D(y-l) &= e^{-(\bar{y}-\bar{l})}\cos(\bar{y}-\bar{l}) \end{aligned} \tag{D.6}$$

The derivatives of these functions can be expressed as follows

$$\begin{aligned} \frac{dA(y-l)}{dy} &= -\frac{2}{l_c}B(y-l) \\ \frac{dB(y-l)}{dy} &= \frac{1}{l_c}C(y-l) \\ \frac{dC(y-l)}{dy} &= -\frac{2}{l_c}D(y-l) \\ \frac{dD(y-l)}{dy} &= -\frac{1}{l_c}A(y-l) \end{aligned} \tag{D.7}$$

Appendix E Multi-Year Ice Characteristics for Beaufort and Chukchi Sea

Cammaert and Muggeridge (1988) compiled data available in the open literature about multi-year ice characteristics for the Canadian Beaufort Sea, the Alaskan Beaufort Sea and the Chukchi Sea. Some of these data are listed in Table E.1.

Region	Ridge Sail Height (m)		Maximum Sheet Thickness (m)	Floe Thickness (m)		Ridge frequency (No. of Ridges /km)
	Mean	Max.		Mean	Max.	
Canadian Beaufort Sea	3.3	8.9 (14.3)	(4.0)	2.2	5.2	12
Alaskan Beaufort Sea	1.7	(9.4)	1.8			3 to 7
Chukchi Sea	1.6		1.6			3 to 10

Numbers in brackets denote extreme ice features

Table E.1 Multi-Year Ice Characteristics

The data for the Canadian Beaufort Sea given in Table E.1 apply to the southern region of the sea, where the continental shelf extends to about 150 kilometres from shore. The area

that has been explored for hydrocarbons extends to approximately the 60-m water depth contour. Some additional data have been recorded in the deeper water area (Polar Ice Zone). The deepest multi-year ridge keel ever measured was about 47 meters below sea level (Cammaert and Muggeridge 1988, page 7), and multi-year ice thickness could reach as high as 4 meters. Because the multi-year ice in this region could drift to as far south as the 5-m water depth, it should be considered in determining the design loads. Similarly, some extreme ice features were also measured in the Alaskan Beaufort Sea. For instance, a maximum ridge keel of about 31 meters has been recorded. The ridge sail heights corresponding to these extreme keel heights are also included in Table E.1 (the numbers in brackets).

The target ice dimensions for the test program presented in Chapter 3, which was considered as "one in 100 years in the Beaufort or Chukchi Seas", were: 27 meters for ridge thickness, and 8 meters for sheet thickness (Weiss, 1988).

With a given sail height, the remaining dimensions of a ridge can be approximately determined using the idealized cross section profile given by Wright *et al* (1979). Cox *et al* (1984) reported Young's modulus values for samples obtained from multi-year ridges in the Alaskan Beaufort Sea. Mean values of 5.02 and 6.99 GPa were obtained at a strain rates between 10^{-5} and 10^{-3} s^{-1} and at a temperature of -5°C. Corresponding values of 5.95 and 7.62 GPa were obtained at strain rates of 10^{-5} and 10^{-3} s^{-1} at a temperature of -20°C.

The characteristic length of a ridge with flanges can be calculated with Equation (6.3)

which can also be used for calculation of the characteristic length for a ridge without sheet ice by ignoring the contribution of the sheet to the foundation modulus and the moment of inertia. The calculation results together with the values of ice dimensions and modulus used are listed in Table E.2.

Region	Sail Height (m)	Sheet Thickness (m)	L_r (m)		L_c (m)	
			E_r=5.02 (GPa)	E_r=7.62 (GPa)	E_r=5.02 (GPa)	E_r=7.62 (GPa)
Canadian Beaufort Sea	3.3	2.2	111.9	124.2	95.5	104.9
	8.9	2.2	235.5	261.4	217.3	239.5
	14.3	4.0	336.1	373.0	310.9	342.7
Alaskan Beaufort Sea	1.7	1.8	68.0	75.5	57.6	63.5
	9.4	1.8	245.3	272.3	228.9	252.4
Chukchi Sea	1.6	1.6	65.0	72.2	54.5	60.0
Test Target	6.3	8.0	181.7	201.7	163.9	181.2

Table E.2 Ridge Characteristic Length

In Table E.2, L_r and L_c are the characteristic length for a ridge without and with attached flanges, respectively. The mean floe thickness were used in place of the mean sheet thickness and the maximum sheet thickness for a ridge in the Canadian Beaufort Sea since no sheet thickness was available. Also the mean sheet thickness for the Alaskan Beaufort Sea was used for the extreme ridges due to the same reason. Two extreme values of modulus, the lowest and the highest, given by Cox *et al* (1984) were used.

The data in Table E.2 indicate that

1. The highest characteristic length could be 373 meters for a ridge without ice attached, and 342.7 meters for a ridge with ice sheet attached, under the condition of the Canadian Beaufort Sea. The corresponding lowest values are 111.9 and 95.5 meters, respectively.
2. The lowest characteristic lengths for Alaskan Beaufort Sea could be 68 meters and 57.6 meter, respectively. The highest characteristic length could exceed 272.3 meters for a ridge without sheet attached, and 252 meters for a ridge with sheet attached because the sheet thickness used in the calculation was the mean sheet thickness for the extreme ridge. The maximum sheet thickness is expected to be much higher.
3. For the target ridge and sheet modelled in the MCS test program, the minimum characteristic length could be 181.7 and 163.9 meters for a ridge without and with ice sheet attached, respectively.